Rheology of Fault Rocks - an experimental Study on the Brittle-Viscous Transition in Mafic Rocks

Inauguraldissertation

zur
Erlangung der Würde eines Doktors der Philosophie
vorgelegt der
Philosophisch-Naturwissenschaftlichen Fakultät
der Universität Basel

von

Sina Marti

aus Willisau (Luzern, Schweiz)

Basel, 2019

Genehmigt von der Philosopisch-Naturwissenschaftlichen Fakultät
auf Antrag von:

Prof. Dr. Renée Heilbronner
(Fakultätsverantwortliche und Dissertationsleiterin)

Prof. Dr. Misha Bystricky
(Korreferent)

Basel, den 19.9.2017

Prof. Dr. Martin Spiess
Dekan der Philosophisch-
Naturwissenschaftlichen Fakultät

Acknowledgements

First and foremost I would like to thank Renée Heilbronner and Holger Stünitz for their time, patience, advise and friendship over the past years. They always and openheartedly shared their knowledge and experience about rocks, science, life, decent food, splendid movies and much more with me, and I'm very greatful for this. I was always looking up to their curiosity, enthusiasm and particularly to Renées so very refreshing ways of boldly questioning all our rigid views and theories. Rüdiger Kilian is much thanked for his patience and support with everything, for endless hours of joyful beers, good music, great coffe and long discussions about science and geology, garlic harvest and much more - I couldn't wish for a better friend.
The financial support by the Swiss National Funds (SNF) over the duration of my project has been more than generous. Further tanks go to the Freiwillige Akademische Gesellschaft, Basel, for their financial support during the last stages of finishing this thesis.
I'm deeply grateful to all the technical support I received from a number of people - special thanks go to Willy Tschudin, the SNI team, Oliver Plümper, Tom-Ivar Eilertsen, Trine Dahl and Aurelien Canizares. The inhabitants of the Bernoullianum and the geological institute and Deformation Lab at Tromso University are much thanked for their support, expertise, coffee breaks and joyful evening beers.
Wholeheartedly, a thousand thanks to my friends for their kindness, support, shared hardship and endless hours of laughter, which made these past few years a most dear memory to me. Special thanks go to Chregu and Simon for ski- and climbing adventures. To Rüdiger, Adrian, Simon & Simon, Annika and Lea for their long-lasting friendship, Rhine swims, nightlife explorations, music and the best vibes in town. Carly, Hanne, Henry and Andrea for taking me to the mountains and all the discussions about life, love, boats and climbing - seldom did I shed so many tears of laughter as with you guys. To Yann and Naxo for guitar jams and for taking me sailing. And to Alun, who more than anyone else inspired me to continue to follow my nose. And with his out-of-the-ordinary ways encourages me to keep on trusting in the good of my own odd ways too. Thanks to you Alun, for the hours of laughter, disputes, boat-maintenance, sashimi feasts and your kindness and company.
And finally to my parents Bruno and Luzia and my sisters Michèle and Jana, for their unwavering support ever since.

"I know not all that may be coming, but
be it what it will, I'll go to it laughing!"
Herman Melville, The Whale

Abstract

In this thesis, the rheology, deformation mechanisms and microstructural evolution of a mafic fault rock are investigated, over a range of conditions where a transition from dominant brittle to dominant viscous deformation is observed.
A Griggs-type deformation apparatus was used to perform experiments at elevated confining pressures (Pc) of 0.5 to 1.5 GPa, and over a temperature (T) range from 300 - 900 °C. The sample material is a 'simulated' fault rock of mafic composition, fabricated from pre-crushed plagioclase-pyroxene mixtures. 0.18 or 0.11 wt.-% H_2O is added to the samples to allow for solution-mass transport and mineral reactions during the experiments. Most experiments were performed in a general shear set-up, at constant displacement rates of $\sim 10^{-4}$ down to 10^{-6} mm/s. Mechanical data and microstructural observations are used to determine the rheology and identify the deformation mechanisms. Microstructural descriptions mainly base on observations made from scanning electron microscopy (SEM) and transmission electron microscopy (TEM). Different methods of image analysis were used for microstructural quantifications.

In the experiments, the brittle-viscous transition (BVT) occurs within the temperature range of 600 °C $\leq$ T $\leq$ 800 °C, at confining pressures of 0.5 GPa $\leq$ Pc $\leq$ 1.5 GPa. The transition is effected by a switch from brittle fracturing and cataclastic flow, to dissolution-precipitation creep and grain boundary sliding (GBS). Viscous flow is enabled by intense grain size refinement resulting from heterogeneous nucleation during syn-kinematic mineral reactions. The reaction products are fine-grained (< 1 μm) neocrystallized plagioclase and the new mineral phases amphibole, quartz and zoisite. In the BVT regime, the mechanical response of the sample is a mixed-mode between brittle and viscous rheology and microstructures associated with both brittle and viscous deformation are observed.
Microstructural evolution is seen to be a crucial factor determining the bulk sample rheology, highlighting the importance of considering strain dependent rheological changes for natural fault zones. Especially in the BVT regime, the initially more brittle dominated rheology is suggested to be only transient, evolving with increasing strain to a more viscous rheology.

In the viscous dominated 800 °C experiments, the following findings are furthermore made:

1) A method was developed to study amphibole reaction corona thicknesses as a function of direction around their pyroxene host clasts. During the initial $\sim$ hydrostatic stage of the experiments (during lead run-in) reaction coronas grow isotropically in all directions. Upon applying a differential stress however, corona thicknesses decrease in directions correlating with high stress sites and increase in low stress sites. The results are interpreted to show the ability of amphibole to deform by dissolution-precipitation creep - a mechanism that is frequently described for naturally deformed amphibole but so far has seldom been reproduced in deformation experiments.
2) Electron backscatter diffraction (EBSD) orientation mapping revealed a weak but consistent crystallographic preferred orientation (CPO) of fine-grained albite within shear bands. No indicators for the activity of dislocation glide or creep are observed and the CPO is interpreted to form during deformation by dissolution-precipitation creep and GBS.

In the low-T experiments at T of 300 - 600 °C, samples deform in a dominant semi-brittle manner by cataclastic flow. Within these experiments, the syn-kinematic formation of amorphous material in high strain zones was observed. The amorphous material is interpreted to evolve from an ultra-cataclastic pre-stage by mechanical wear, where plagioclase is seen to be particularly susceptible to this form of amorphisation. Flow structures within the amorphous material indicate its potential viscous flow behaviour. The mechanical data does show significantly lower strengths for samples deformed at higher temperatures and based on microstructural observations and Brillouin spectroscopy measurements it is seen as likely that the amorphous material is causing this temperature sensitivity. The occurrence of amorphous material in natural brittle fault zones might thus bear the potential to introduce a viscous contribution to fault rock rheology.

Kurzfassung

Diese Arbeit untersucht die Rheologie, Verformungsmechanismen und die mikrostrukturelle Entwicklung eines mafischen Störungszonen Gesteins bei Bedingungen wo ein Übergang von dominant bruchhafter zu dominant viskoser Verformung beobachtet werden kann.
Ein Griggs-Typ Verformungsapparat wurde benutzt, um Experimente bei erhöhten Umschliessungsdrucken (Pc) von 0.5 bis 1.5 GPa, und über einen Temperaturbereich von 300 - 900 °C durchzuführen. Das Probenmaterial ist ein 'simuliertes' Störungszonen Gestein mit einer mafischen Zusammensetzung, fabriziert aus einer zertrümmerten Plagioklas-Pyroxen Mischung (Gesteinspulver). Um Lösungs-und-Massentransport und Mineralreaktion zu ermöglichen wurde dem Probenmaterial jeweils entweder 0.18 oder 0.11 Gewichts-% H_2O hinzugefügt. Die Mehrheit der Experimente sind Scher-Experimente bei konstanter Versatzrate von $\sim 10^{-4}$ bis hinunter auf 10^{-6} mm/s. Anhand der mechanischen Daten und der Mikrostrukturen wurde die Rheologie der Proben und die aktiven Verformungsmechanismen ermittelt. Die Mikrostrukturellen Beschreibungen stammen mehrheitlich aus Beobachtungen welche mit Rasterelektronenmikroskopie (REM) und Transmissionselektronenmikroskopie (TEM) gemacht wurden. Verschiedene Methoden der Bildanalyse wurden benutzt um die Mikrostrukturen zu quantifizieren.

Der spröd-viskos Übergang ('brittle-viscous transition', BVT) in den Experimenten konnte innerhalb des Temperaturbereiches von 600 °C $\leq$ T $\leq$ 800 °C, bei Umschliessungsdrucken von 0.5 GPa $\leq$ Pc $\leq$ 1.5 GPa beobachtet werden. Der übergang findet dabei von sprödem Zerbrechen und Kataklastischem Fliessen, zu Lösungs-Ausfällungs Kriechen und Korngrenzgleiten statt. Heterogene Nukleierung neuer Körnern während syn-kinematische Mineral Reaktionen verursacht intensive Kornverkleinerung und ermöglicht dadurch viskoses Fliessen. Die Reaktionsprodukte sind feinkörnige (< 1 μm), neu-kristallisierte Plagioklas Körner und die neu-auftretenden Mineralphasen Amphibol, Quarz und Zoisit. Im Bereich des spröd-viskos Übergangs ist das mechanische Verhalten der Proben ein Mischung aus bruchhafter und viskoser Rheologie. Weiter sind auch die beobachteten Mikrostrukturen assoziiert mit sowohl bruchhafter als auch viskoser Verformung.
Es wurde erkannt dass die mikrostrukturelle Entwicklung einen entscheidenden Einfluss auf das rheologische Verhalten einer Probe einnimmt. Dies hebt hervor wie wichtig es ist, verformungsabhängige Änderungen in der Rheologie von natürlichen Störungszonen in

Betracht zu ziehen. Vor allem im Bereich des spröd-viskos Übergangs ist es wahrscheinlich, dass eine initiale, eher bruchhaft-dominierte Rheologie nur vorübergehender Natur ist und, dass mit zunehmender Verformung, viskose Prozesse zunehmends an Einfluss auf die Rheologie gewinnen.

In den mehrheitlich viskos verformenden 800 °C Experimenten konnten weiterhin folgende Befunde erbracht werden:
1) Eine Methode wurde entwickelt, welche es erlaubt, die Dicke von Amphibol-Reaktionssäumen als eine Funktion ihrer Richtung um ihre jeweiligen Pyroxen-Klasten zu analysieren. Während der Anfangsstufe eines Experiments befindet sich die Probe bei $\sim$ hydrostatischen Bedingungen und die Reaktionssaäume wachsen isotrop in alle Richtungen. In den darauffolgenden Abschnitten des Experiments, in denen eine Differentialspannung einwirkt, verkleinert sich die Dicke der Reaktionssäume in Richtung von Flächen mit hoher Normalspannung und vergrössert sich in Richtung von Flächen mit niedriger Normalspannung. Anhand dieser Resultate wird interpretiert, dass sich Amphibol mit Lösungs-Ausfällungs Kriechen verformt - ein Mechanismus, welcher oft in natürlich verformten Amphiboliten beschrieben ist, bisher aber nur selten in Experimenten reproduziert werden konnte.
2) Elektronenrückstreubeugungs-Analysen ('electron backscatter diffraction', EBSD) offenbarten eine schwach ausgeprägte aber konsistente Vorzugsorientierung der Kristallachsen ('crystallographic preferred orientation', CPO) feinkörnigen Albit Materials in Scherbändern. Es wurden keine Hinweise auf Dislokations-Kriechen gefunden und es wird interpretiert, dass die CPO während der Verformung durch Lösungs-Ausfällungs Kriechen und Korngrenzgleiten entstand.

In den niedrig-Temperatur Experimenten zwischen 300 - 600 °C verformen sich die Proben semi-spröde ('semi-brittle') durch kataklastisches Fliessen. In diesen Experimenten wurde die syn-kinematische Entstehung von amorphem Material in stark verformten Zonen beobachtet. Es wird interpretiert, dass sich das amorphe Material aus einer ultra-kataklastischen Vorstufe durch mechanische Abration entwickelt, wobei Plagioklas speziell auf diese Form der Amorphisierung anfällig zu sein scheint. Fliesstrukturen innerhalb des amorphen Materials weisen auf potentiell viskoses Fliessverhalten hin. Die mechanischen Daten zeigen dabei klar niedrigere Stärken für Experimente bei höheren Temperaturen. Basierend auf mikrostrukturellen Beobachtungen und Brillouin Spektroskopie Messungen wird es als wahrscheinlich angesehen, dass die Temperaturabhängigkeit der Stärke durch Fliessverhalten des amorphen Materials verur-

sacht wird. Das Vorkommen von amorphen Materialien in natürlichen spröde verformenden Störungszonen könnte deshalb potentiell dazu führen, dass die Rheologie des Störungszonen-Gesteins einen viskosen Anteil enthält.

Contents

Chapter 1

Introduction

1.1 General aspects

Deformation of the earths lithosphere is often not taking place homogeneously but is observed to localise into fault zones of various scales. Whereas the term 'fault zone' herein is not meant to imply any specific deformation mechanism, rather than describing a zone where displacement of rock volumes past each other is accommodated. Lithospheric scale fault zones operate over a wide range of pressures and temperatures, within a variety of rock types and whereas the upper crust is generally seen to deform brittlely, the increasing temperatures and pressures with depth will eventually favour viscous deformation. This change in dominant deformation mechanisms from brittle to viscous has significant implications on the rheology and structure of a fault zone.

Fault zone structures can be studied from field observations of exhumed fault zones (e.g. Sibson, 1977; Sibson et al., 1981; Mancktelow, 1985; Handy et al., 2005). From outcrop- and microstructural observations, relative strengths of fault rocks and their constituent minerals can be made in comparison to the surrounding host rock. However, the history of exhumed fault zones can be complicated by overprinting during exhumation and rheology and absolute strengths of fault rocks and minerals cannot be determined in the field. Our knowledge about the development and strength of fault rocks has thus been greatly aided by laboratory studies on rock deformation over a wide range of crustal and upper-mantle P-T conditions, as well as on a wide variety of rock types.

Noting that the strength of the lithosphere cannot be greater than that of the rocks it is composed of, strength envelopes are constructed, which plot laboratory derived strength or flow laws for minerals (or rocks) versus depth (e.g. Brace and Kohlstedt,

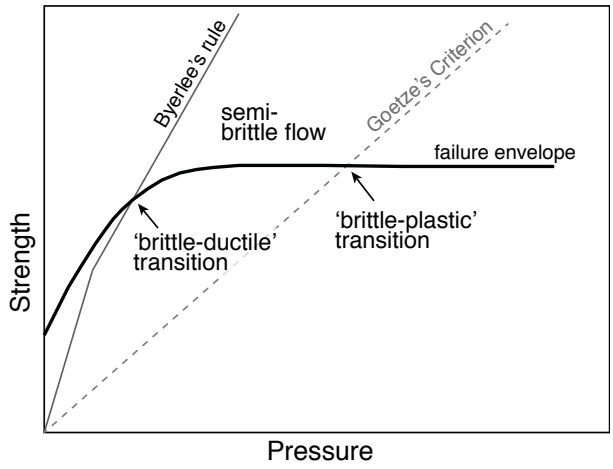

Figure 1.1: *Rock strength approximation, figure after (Kohlstedt et al., 1995). Theoretical 'brittle-ductile' and 'brittle-plastic' transitions are indicated. Failure envelope includes Mohr-Coulomb and Von Mises envelope.*

1980; Kohlstedt et al., 1995; Burov, 2011, and references therein) and provide a model for strength variations within the lithosphere. Following the general consensus that the upper crust deforms dominantly by brittle fracturing and frictional sliding, and the lower crust by viscous creep, these strength envelopes were initially constructed with a simple two mechanism approach of plotting Byerlee's rule (Byerlee, 1978) with depth, until temperatures and pressures are high enough for viscous deformation to set in at lower stresses than does brittle deformation and frictional sliding. Since their introduction, the limitations of these strength profiles have been pointed out. Extrapolating Byerlee's rule down to mid-crustal conditions is expected to overestimate rock strength (Brace and Kohlstedt, 1980; Carter and Tsenn, 1987) and initially, viscous strength of the whole continental crust (in absence of an available creep flow law for feldspars) was estimated with a dislocation creep flow law for quartz. Since then, advances in rock deformation studies yielded viscous creep flow law parameter for minerals such as feldspar and pyroxene (e.g. Kirby and Kronenberg, 1984; Bystricky and Mackwell, 2001; Dimanov et al., 2003; Rybacki and Dresen, 2000; Rybacki et al., 2006; Wang et al., 2012; Zhou et al., 2012), allowing to construct strength envelopes approximated by the viscous flow strength of these minerals which are more typical for the mid- to lower crust than quartz.
The transition from brittle-frictional faulting to viscous flow in the classical strength profiles is a sharp transition, were rock strengths reach relatively high differential stresses. However, as seen e.g. from laboratory studies, rocks failing in the brittle field change their mode of failure from highly localised faulting along a discrete plane, to distributed microcracking and cataclastic flow (e.g. Karman, 1911; Kirby and Kronenberg, 1984). This change from discrete to distributed ('ductile') failure mode was also observed to frequently coincide with a decrease in pressure sensitivity of strength, and was attributed to a field of semi-brittle deformation (e.g. Kohlstedt et al., 1995), truncating Byerlee's rule

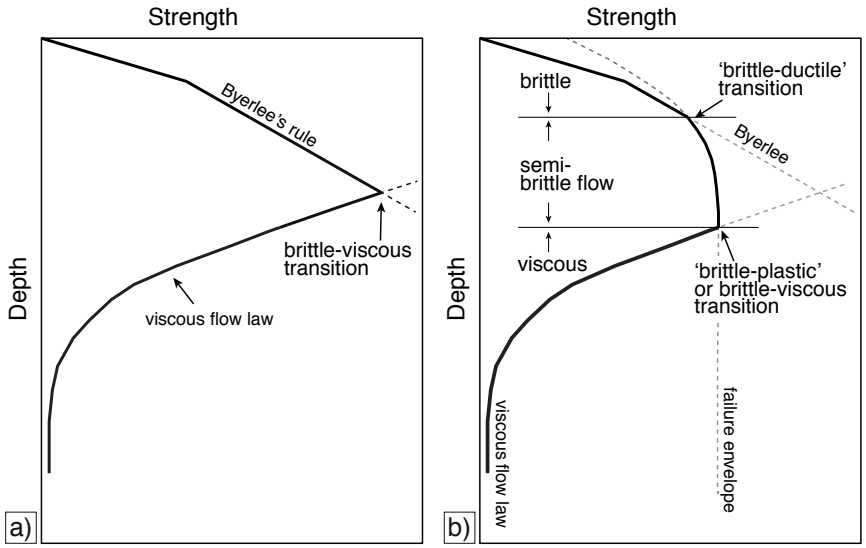

Figure 1.2: *Schematic crustal strength envelopes. a) simple two-mechanism envelope constructed from Byerlee's rule and a viscous flow law. The intersection of the two is termed the 'brittle-viscous' transition. b) Same as (a) but including a semi-brittle field, truncating Byerlee's rule at the 'brittle-ductile' transition and change into the field of viscous flow at what is either termed the 'brittle-plastic' or 'brittle-viscous' transition.*

at the 'brittle-ductile' transition (Figure 1.1). At higher pressures, the semi-brittle field then is terminated by the transition to the 'plastic' field. The term 'plastic' here is being used to describe the pressure-independence of strength of the failure envelope. In terms of failure mode the 'brittle-plastic' transition is usually observed to correlate with the onset of viscous deformation, and thus the term 'brittle-viscous' transition (thereafter shorted as BVT) is preferred and will be used in the following. The introduction of a semi-brittle field to the classical strength envelope leads to the prediction of a broad transitional field from dominant brittle to dominant viscous deformation, whereas expected strengths at the BVT still remain high (Figure 1.2).

1.2 From brittle to viscous deformation

1.2.1 The brittle-frictional field

1.2.1.1 Fracturing

Brittle deformation is accommodated by fracturing, frictional sliding and cataclastic flow. Cracks in minerals and rocks are thought to nucleate at stress-concentration points such as impurities or pores. Above a certain threshold density, these initial micro-cracks will interact and link to eventually lead to macroscopic failure. Brittle failure can thus

be approximated by describing the critical stress state controlling crack propagation (Brantut et al., 2013). What is known as the *stress intensity factor, K_i,* describes the magnitude of the local driving stress close to the crack tip. For the simplified case of uniform loading, K_i is given as (Brantut et al., 2013):

$$K_i = B\ \sigma_r\ \sqrt{\pi l} \tag{1.1}$$

where B: dimensionless parameter describing the crack and loading geometry, σ_r: remotely applied tensile stress, l: crack half-length.
The *fracture toughness, K_{ic}*, describes the resistance of a rock to dynamic fracture propagation (e.g. Meredith, 1990; Brantut et al., 2013) and where $K_i < K_{ic}$, pre-existing cracks should remain stable and stationary (Brantut et al., 2013). Equation (1.1) predicts no influence of temperature on the stress intensity factor. However, in the case of stress-corrosion cracking, subcritical crack growth can occur, where the velocity of stress corrosion crack growth does show an activation energy and is temperature dependent (Brantut et al., 2013, and references therein).

1.2.1.2 Frictional sliding

To a first approximation, frictional sliding of rocks obeys the empirical observation that (i) resistance to shear (i.e. frictional sliding) is proportional to the normal stress acting on the sliding surface, and (ii) the shear resistance is independent of the area of the sliding surface. Thus simply formulated as:

$$\tau = \mu \cdot \sigma_n \tag{1.2}$$

where τ: shear stress, μ: friction coefficient, and σ_n: normal stress. In an empirical approach, Byerlee (1978) formulated his rule for the frictional sliding of rocks as:

$$\tau = 0.85\sigma_n \qquad for\ \sigma_n < 2\ kb \tag{1.3}$$

$$\tau = 0.5 + 0.6\sigma_n \quad for\ 2\ kb < \sigma_n < 20\ kb \tag{1.4}$$

For frictional sliding, the observation had been made that 'static friction' (i.e. the resistance to shear at slip initiation) is not necessarily equal to 'dynamic friction' (i.e. the shear resistance during the slip at constant velocity) and that friction coefficient evolves and changes as a function of applied displacement rate (e.g. Scholz et al., 1972; Scholz and Engelder, 1976). Empirical *rate-and-state friction laws* were formulated, to describe the time and velocity dependent evolution of friction properties (e.g. Dietrich, 1978; Scholz,

1998). Rate-and-state theory proposes the predictability of potentially seismic to potentially aseismic faults by determining if a fault zone shows either velocity strengthening or velocity weakening behaviour. Rate-and-state friction laws have several forms - the one presented here was summarised in Beeler et al. (e.g. 1994) as:

$$\tau = \left[\mu_0 + a\ ln\left(\frac{V}{V_0}\right) + b\ ln\left(\frac{V_0\ \theta}{D_c}\right) \right]\ \sigma' \tag{1.5}$$

with μ_0: steady state friction at V = V_0, V: slip velocity, V_0: a reference velocity, a and b: empirical variables denoting material properties, D_c: critical slip distance, θ: critical state variable describing the evolution with slip distance and velocity, and σ': effective normal stress.

Although rate-and-state friction laws greatly enhanced our understanding of fault behaviour, they are largely formulated on the data of experiments performed under low normal stress conditions. The physical explanation to the dependency of friction coefficient on slip velocity, slip distance and inter-slip time intervals is largely based on the state and evolution of asperity contacts along the fault plane. Furthermore, as friction is occurring on a pre-existing fault, the process of fracturing is usually not considered in rate-and-state friction laws. In the semi-brittle flow regime, displacement is not localised on a single fault plane but usually accommodated by cataclastic flow in a fault zone of a certain width. Pervasive fracturing occurs, as the stress needed to overcome friction on pre-existing discontinuities is higher than the resistance to form new fractures. Marone et al. (1990) performed experiments on simulated fault gouge at somewhat elevated normal stresses of up to 190 MPa, showing that shearing of gouge is accompanied by dilatancy and shows different friction coefficient evolution compared to simulated bare-surface faults. It is likely that for semi-brittle deformation, rate-and-state frictional laws will not be simply applicable and that different physical explanations are needed to explain fault strengths in the semi-brittle regime.

1.2.2 The viscous field

Viscous deformation mechanisms in rocks are most commonly either intragranular (i.e. lattice) processes, or intergranular (i.e. boundary) processes.

Intragranular deformation in rock forming minerals is often described as being dominated by recovery controlled dislocation glide (generally termed 'dislocation creep') and the experimentally derived mechanical data is generally fitted to a flow law of the general form:

$$\dot{\varepsilon} = A\ \Delta\sigma^n\ d^{-m}\ exp(-Q/RT) \tag{1.6}$$

with A: constant, $\Delta\sigma$: differential stress, n: stress exponent, d: grain size, m: grain size exponent, Q: activation energy, R: universal gas constant, T: temperature.
Dislocation creep is generally described to be grain size independent, thus with $m = 0$. Strain rate however is seen to depend exponentially on stress, with reported stress exponent values in the range of 3 - 6 (e.g. Glen, 1955; Kirby and Kronenberg, 1984; Gleason and Tullis, 1995; Rybacki and Dresen, 2000; Bystricky and Mackwell, 2001).

Intergranular deformation in rocks is mainly accommodated by grain boundary diffusion creep (for vacancy diffusion also termed 'Coble creep' after Coble (1963)) accompanied by grain boundary sliding. Diffusion creep involves the serial processes reaction at the source, transport, and deposition (i.e. reaction) at the sink. Depending on the rate limiting step, which can either be reaction at the source and/or sink, or transport, diffusion creep is either 'reaction controlled' or 'transport controlled' respectively. Depending on the rate limiting step, the grain size exponent m varies between 1 to 3 (e.g. Paterson, 2013). Diffusion creep is generally described with a Newtonian rheology, that is, a stress exponent $n = 1$, and is always interrelated with grain boundary sliding (e.g. Ashby and Verrall, 1973; Elliott, 1973; Gifkins, 1976; Langdon, 2006), as neighbour switching and/or grain shape changes occur.
For crustal conditions, where a hydrous fluid layer is often assumed to be present along grain- and phase boundaries during deformation, diffusion in rocks can be accommodated by fluid-transport diffusion creep (referred to with various terms such as 'pressure-solution creep' or 'dissolution-precipitation creep'. The latter term is used in the following). The rate of dissolution-precipitation creep is depending on the grain size, state of the fluid layer (geometry, width etc.), the concentration of the dissolving material in the fluid, as well as transport and reaction rates. The latter two, as already mentioned previously, are potential rate controlling factors. As e.g. proposed by Paterson (2013), the rate of dissolution-precipitation creep in the transport controlled case can be described as:

$$\dot{\varepsilon} = C\ \frac{V_m\ c\ D\ \delta\ \Delta\sigma^n}{R\ T\ d^3} \tag{1.7}$$

with C: constant, V_m: molar volume of the material in solution, c: molar concentration of solute, δ: mean thickness of the intergranular fluid film, D: diffusion coefficient.
The stress exponent thereby is assumed to be $n = 1$. However, as discussed in Gratier et al. (2009, 2013) this might not always be true and somewhat higher n values are likely for dissolution-precipitation creep, depending on the driving force or chemical potential gradient along the grain contact area.

1.2.3 Summary

The above listed equations give an insight on the spectrum of parameters determining the rate of the competing deformation mechanisms. Brittle deformation is usually approximated as being largely temperature insensitive but strongly pressure sensitive (e.g. equations (1.2) - (1.5)). As has been observed from frictional sliding experiments, the friction coefficient and its evolution differ for bare-surface faults and faults with a sufficiently thick gouge layer. Thus, the 'morphology' of fault zones is seen to be an additional factor influencing fault rock rheology in the brittle field.
Viscous deformation mechanisms are temperature activated and stress depends strongly on temperature and strain rate (e.g. equations (1.6) and (1.7)). Whereupon flow law parameters differ for different minerals. Additionally, the mechanism of fluid-transfer diffusion creep incorporates parameters such as grain size and state of fluid layer, influencing the rate at which the process accommodates strain. It becomes thus clear that the brittle-viscous transition is a complex system governed by not only the most obvious parameters such as pressure and temperature, but also by fluid availability, fault geometry and fault rock composition (i.e. mineral assemblage), microstructure and chemical environment.

1.3 Polymineralic rock deformation

This study presents the result of deformation experiments performed on plagioclase-pyroxene mixtures, representative for large parts of mid- to lower crustal rock compositions. As friction coefficients for a wide range of silicate minerals and rock types are observed to show similar values (e.g. Byerlee, 1978), brittle deformation is generally assumed to be relatively independent on mineral or rock type. Flow law parameters in the viscous field however show pronounced differences for different minerals. Furthermore, the dominant deformation mechanism is likely different in monomineralic than in polymineralic aggregates. Viscous deformation in monomineralic aggregates at mid-

to lower crustal conditions is often described as being dominated by dislocation creep. Although diffusion creep would be favoured by the expectedly low differential stresses, grain growth in monomineralic aggregates at the elevated T of the mid- to lower crust is extensive, rendering diffusion creep less efficient than dislocation creep. In polymineralic mixtures there are several processes acting, which influence the deformability and the dominating deformation mechanism. The occurrence of mineral reactions and nucleation entail grain size reduction (e.g. Brodie and Rutter, 1987; Fitz Gerald and Stünitz, 1993; Newman et al., 1999; de Ronde et al., 2005), grain pinning due to secondary phases will impede grain growth (e.g. Olgaard and Evans, 1986; Berger and Herwegh, 2004; Linckens et al., 2011), and diffusion is expected to be faster along phase boundaries compared to grain boundaries (e.g. Hickman and Evans, 1991; Wheeler, 1992; Sundberg and Cooper, 2008). Factors, which will enhance diffusion creep rates and can possibly lead to a switch in dominant deformation mechanism from dislocation creep in monomineralic layers, to diffusion creep in polymineralic layers (e.g. Etheridge and Wilkie, 1979; Mehl and Hirth, 2008; Linckens et al., 2011; Kilian et al., 2011). There is thus certainly a need to extend the database of deformation experiments on polymineralic systems, in spite of facing the difficulties of an increasingly complex system.

1.3.1 Previous work

Available experimental data on the minerals plagioclase and pyroxene exist for high-temperature creep deformation (for plagioclase, e.g. Tullis and Yund, 1985; Shaocheng and Mainprice, 1987; Tullis and Yund, 1991; Dimanov et al., 1999; Rybacki and Dresen, 2000; Stünitz and Tullis, 2001; Stünitz et al., 2003; Ji et al., 2004; Barreiro et al., 2007) (and for pyroxene, e.g. Lallemant, 1978; Kolle and Blacic, 1982; Raterron and Jaoul, 1991; Mauler et al., 2000; Bystricky and Mackwell, 2001; Hier-Majumder et al., 2005; Chen et al., 2006; Zhang et al., 2006). Some studies are published on experimental deformation of plagioclase and pyroxene mixtures (either synthetic mixtures or natural samples with a gabbroic composition). Of these, focusing on the high-temperature creep regime there are the experiments performed by Dimanov et al. (e.g. 2003); Dimanov and Dresen (e.g. 2005); Dimanov et al. (e.g. 2007); Zhou et al. (e.g. 2012).
In water-added experiments on plagioclase, Stünitz and Tullis (2001) used the plagioclase hydration reaction to zoisite to study the influence of syn-kinematic mineral reactions on the deformation. Similarly, Rutter et al. (1985) and Getsinger and Hirth (2014) performed deformation experiments on basaltic starting materials under hydrous conditions in the viscous field, and observed the syn-kinematic mineral reactions to amphibole. The

authors of Rutter et al. (1985); Stünitz and Tullis (2001); Getsinger and Hirth (2014) all suggest some form of diffusion creep + grain boundary sliding as the dominant deformation mechanism in their polymineralic samples.
Kronenberg and Shelton (1980) and Caristan (1982) present results from deformation experiments on Maryland Diabase deformed under a range of pressure and temperatures, crossing the brittle-viscous transition of their sample material. In these experiments, the brittle-viscous transition was described to occur from fracturing to viscous flow by dislocation glide or creep. No syn-kinematic mineral reactions were observed by the authors. Studies on the brittle-viscous transition from either monomineralic plagioclase or pyroxene materials also frequently describe the brittle-viscous transition to occur from fracturing to viscous flow by intracrystalline mechanisms such as dislocation glide, dislocation creep or mechanical twinning (e.g. Kirby and Kronenberg, 1984; Boland and Tullis, 1986; Tullis and Yund, 1987; Tullis et al., 1987; McLaren and Pryer, 2001). In contrast to experimental results, natural observations on brittle-viscous transitional behaviour of mafic rocks are frequently described to happen from fracturing to grain size sensitive diffusion creep and grain boundary sliding (e.g. Hanmer, 2000; Brander et al., 2012; Getsinger et al., 2013; Okudaira et al., 2015; Viegas et al., 2016). In these cases, initial fracturing is usually accompanied by fluid infiltration and mineral reactions, leading to grain size refinement caused by reaction and enhanced diffusional transport rates due to the presence of a grain boundary fluid film.

1.4 Aim of this thesis

Complementing to previous studies, this thesis is aimed to increase our understanding of the behaviour of fault zones in mafic rocks over the brittle-viscous transition. Focus is set on identifying the active deformation mechanisms and rheology controlling factors in the brittle, the brittle-viscous and the dominantly viscous field. Additionally, performing experiments at the same conditions but to different amounts of total displacement allows to study microstructural evolution and changes in processes acting during fault zone initiation and maintenance. Microstructural observations thereby can be correlated to the mechanical data, helping to understand the effect of microstructural evolution on fault zone rheology.
In the viscous field, a focus will be set on trying to incorporate and understand the effects of syn-kinematic mineral reactions on the onset and maintenance of viscous deformation. The susceptibility of mafic rocks to hydration reactions presents an ideal attribute for this study. Whereas high-temperature viscous creep under $\sim$ 'dry' conditions is relatively

well studied for both pyroxene and plagioclase, lower-temperature deformation experiments at 'wet' conditions are scarce. However, as shear zone formation is often observed to be accompanied by fluid infiltration and hydration reactions, there is a profound need to further our understanding of the rheology of fault zones in polyphase materials, deforming by viscous creep mechanisms during fluid-present conditions.
And last but not least: in a previous study on semi-brittle deformation of granitoid fault rock by Pec (2014), the formation of amorphous material had been observed during aseismic (i.e. slow displacement rate) deformation experiments. In our study, a set of experiments was performed, imposing the same experimental conditions on our mafic starting material to see if amorphisation is like-wisely observed. It has in recent years become evident, that amorphous material along fault zones might not always be caused due to frictional melting during seismic rupture, but can form during aseismic creep (Goldsby and Tullis, 2002; Janssen et al., 2010; Pec et al., 2012b; Hayward et al., 2016). As amorphous materials are likely to deform by a viscous creep mechanism, the occurrence of amorphous material along fault zones in the brittle field has the potential to introduce a temperature and rate dependent rheology to these fault zones. A fact that would greatly influence the way we model the behaviour and strength of brittlely deforming fault zones.

1.5 Thesis structure

This thesis is structured as following:

- The following second chapter contains a description of the methods, which are of relevance to all of the three main results chapters. These are descriptions of the deformation apparatus, experimental procedure, starting material, data treatment, microscopy and image analysis. Methods, which are only relevant to specific results chapters will be presented in their relative chapters.

- The third chapter (first of the 'results' chapters) reports mechanical data and microstructures developed in the mafic fault rock deformed at a range of pressure-temperature conditions where a transition from dominant brittle to dominant viscous deformation is observed. This chapter is submitted to **Journal of Structural Geology** as:

  ***Marti, S.**, Stünitz, H., Heilbronner, R., Plümper, O., Drury, M. (2017). Experimental investigation of the brittle-viscous transition in mafic rocks - interplay between fracturing, reaction and viscous deformation.*

- The fourth chapter (second of the 'results' chapters) focuses on the higher temperature experiments and describes how deformation by viscous flow is accommodated. This chapter is in preparation as:

  ***Marti, S.**, Heilbronner, R., Stünitz, H., Plümper, O., Drury, M.*
  Dissolution precipitation creep and grain boundary sliding in experimentally deformed plagioclase - pyroxene mixtures.
  To be submitted in: ***Journal of Structural Geology***

- The fifth chapter (third of the 'results' chapters) focuses on the low-temperature experiments and the formation of amorphous material during the aseismically deformed mafic fault rock. This chapter is in preparation as:

  ***Marti, S.**, Heilbronner, R., Stünitz, H.*
  Low temperature deformation of mafic fault rock and the influence of amorphisation on fault rock strength.
  To be submitted in: ***Journal of Structural Geology***

- Chapter six contains a general discussion, summary and conclusions, and suggestions for future work.

- Appendix A contains a list of all performed experiments.

- Appendix B presents the result of a new calibration of the displacement correction factors for Rig 1 and Rig 2 at Tromsø University.

- Appendix C contains the MATLAB code that calculates the 'elastic salt correction' applied to the mechanical data.

- Appendix D contains the MATLAB code used to determine the amphibole corona thickness as a function around pyroxene clasts.

- Appendix E gives a short overview on results and the problems faced when using thermodynamic modeling to predict the stable mineral assemblages for the samples at the experimental conditions.

Chapter 2

Methods

2.1 Experimental setup

2.1.1 Deformation apparatus

Experiments were performed using two modified Griggs type deformation apparatus at the University of Tromsø, Norway (Figure 2.1). The Griggs apparatus used have a confining pressure ram controlled by a hydraulic oil pump system, and a load ram controlled by a servo-controlled motor. The load system can either be run in a constant displacement rate or in a constant load setup. Temperatures during pumping and experimental runs are automatically controlled via a Eurotherm proportional-integral-derivative (PID) controller.

2.1.2 Data recording

During an experiment, confining pressure (Pc), vertical displacement of the load piston, and axial load are recorded in parallel with an analogue chart recorder (sampling frequency 50 Hz) and a digital data-logging system (LabView) with a sampling frequency of 1 Hz. Vertical displacement of the load piston is measured with two external devices: a direct current displacement transducer (DC-DT, resolution ≈ 1 μm) and a noiseless

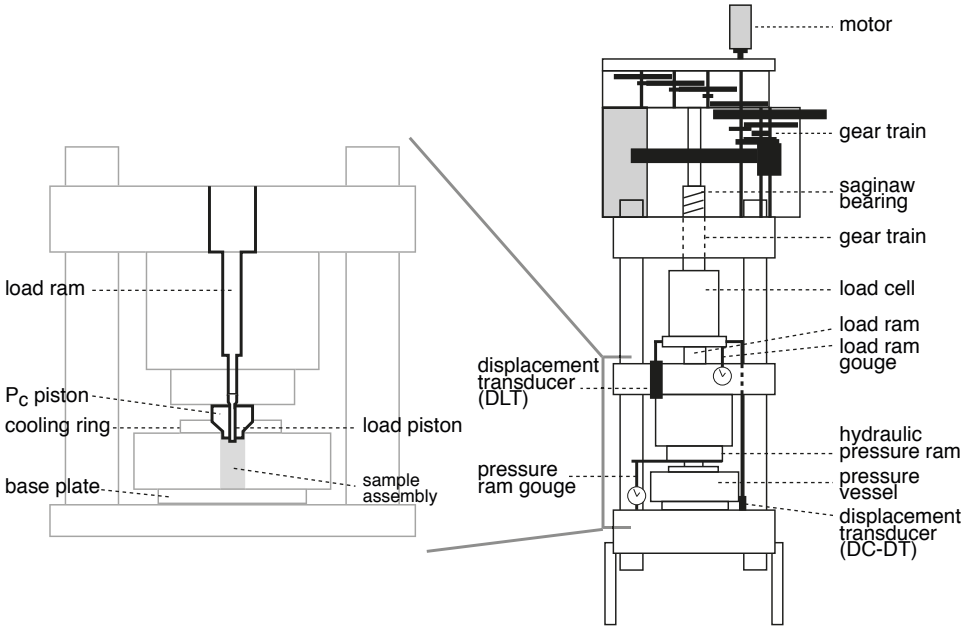

Figure 2.1: *Schematic sketch of the modified Griggs-type deformation apparatus 'Rig 2' at the University of Tromsø. Sketch modified after Holyoke III and Kronenberg (2010)*

digital linear transformation measurement (DLT) system (resolution = 0.1 μm). Pc is measured via the oil pressure in the hydraulic pumping system and axial load is measured with an external load cell (Figure 2.1).

2.1.3 Sample assembly

The sample assembly is composed of the following pieces (Figure 2.2; Figure 2.3):
A top lead (Pb) piece to protect the sample during pressurisation. The Pb piece was fabricated with an inner salt ring, which provided better piston guidance especially during higher-T experiments. Heating of the graphite resistance furnace is achieved by electric current flowing in from the base plate via the WC carbide plug, through the lower Cu-disc, furnace and the upper Cu-disc, and from there onto the pressure vessel and the rig. To prevent a short circuit between the base-plate and the pressure vessel, the two were insulated from each other by putting an insulating paper disc between them. The thermocouple is insulated against the furnace with an Al_2O_3 ring fitted into the furnace. The sample column consists of three different parts, a lower Al_2O_3 piston, the sample and an upper Al_2O_3 piston. Most of the experiments were run in a setup where the rock sample is placed between Al_2O_3 forcing blocks pre-cut at 45° with respect to the load axis (i.e. load-piston). Forcing blocks and all other Al_2O_3 pistons are cylindrical and 6.33 mm in diameter. The sample is encapsulated in a platinum jacket (0.15 mm

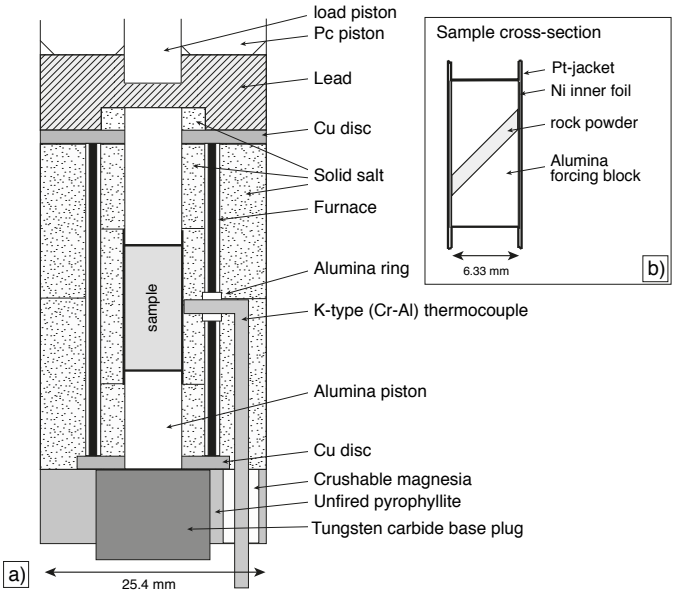

Figure 2.2: *Sample assembly. a) Schematic cross-section of the sample assembly, modified after Tarantola et al. (2010). b) Close-up view sample: Shear zone from rock powder + H_2O, between alumina forcing blocks pre-cut at 45°. The sample and forcing blocks are wrapped in an inner Ni-foil sleeve and are encapsuled in a weld-sealed Pt-jacket.*

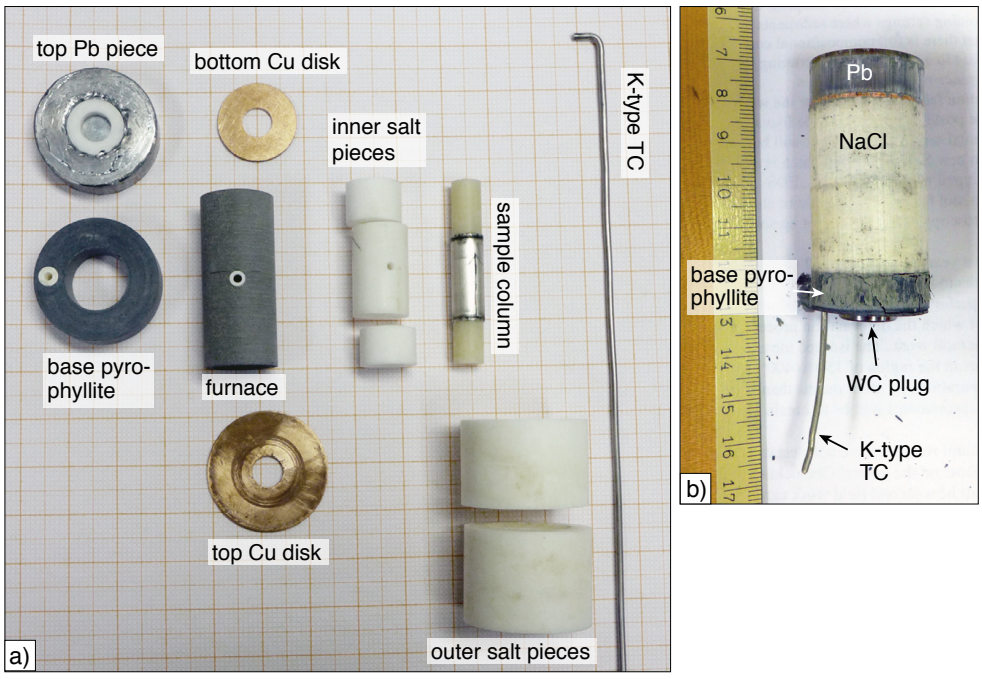

Figure 2.3: *Sample assembly. a) Photograph of the individual pieces of the sample assembly. The 'sample column' is made from the upper alumina piston, the sample (in the Pt-jacket) and the lower alumina piston. TC = thermo couple. b) The sample after the experiment when retrieved from the pressure vessel.*

wall thickness) with an inner Ni-foil sleeve (0.025 mm foil thickness). The jacket then is weld-sealed with a Lampert welding apparatus, with the sample encased in a cooled (T $\approx$ 4°C) brass piece to minimise heating and potential water loss.
Solid salt was used as confining medium. Inner salt pieces are either fabricated from potassium iodide (KI) for experiments at T $\leq$ 600 °C and NaCl for experiments at T $\geq$ 700 °C. KI is mechanically weaker than NaCl but shows partial melting at T $>$ 600 °C (at the pressures of the experiments), which leads to thermal convection in the salt cell, corrosion of the thermocouple and resulting experiment abortion. Outer salt pieces are always fabricated from NaCl.
A chromel-alumel thermocouple (K-type) was used for most experiments. Only for long-duration experiments at 800 °C, Pt-Pt(10%Rh) (S-type) thermocouples with wires in mullite tubing were used. The mullite tubing is fragile and S-type thermocouples are delicate to handle during sample fabrication and pressurisation. However, they are more durable in the corrosive environment of the heated salt during the experiment and proved to be the better choice for long-duration experimental runs. The thermocouple is held in place by a crushable magnesia ring fitted into the base pyrophyllite.

2.1.3.1 Sample material

Experiments were performed on five different starting materials (Table 2.1):

(1) Maryland Diabase (Kronenberg and Shelton, 1980).
(2) Synthetic mixture of Sonora Labradorite ($\sim An_{60}$) and Damaping Enstatite.
(3) Synthetic mixture of Sonora Labradorite and Damaping Diopside.
(4) Synthetic mixture of Sonora Labradorite and Cranberry Lake Diopside.
(5) Synthetic mixture of Alpe Rischuna Albite and Damaping Enstatite.

The Maryland Diabase material was kindly provided by Terry Tullis. Except for one experiment, experiments on Maryland Diabase were performed using a rock powder fabricated by crushing Maryland Diabase pieces with a hand-press and subsequently with an alumina hand-mortar. The resulting powder was dry-sieved to extract a grain size fraction $\leq$ 125 μm. Only one experiment (nr. 475) was performed as axial shortening experiment on a Maryland Diabase whole rock cylinder. The Maryland Diabase starting material has a modal composition (by volume) of $\sim$ Pl: 57%, Cpx: 32%, Opx: 8%, accessories (Qz, Kfs, Ilm, Mag, Bt, Ap): 3% (Mineral abbreviations after Whitney and Evans (2010)). The Pl shows a relatively homogeneous composition except for a thin rim with lower anorthite component (Table 2.1). The core to rim area ratio is $\sim$ 83 : 17

Table 2.1: *Representative mineral measurements as normalised oxide wt.-% and as calculated stoichiometric mineral composition for the different starting materials. All Fe is taken as Fe^{2+} due to the reducing environment in the sample assembly.*

	Alpe Rischuna Albite	Sonora Labradorite	Maryland Diabase plagioclase			Cranberry lake Diopside	Damaping Diopside	Damaping Enstatite	Maryland Diabase Cpx	Maryland Diabase Opx
wt.-%			**core**	**rim**	**wt.-%**					
SiO2	68.79	53.66	51.86	55.67	SiO2	57.18	54.39	55.98	51.58	52.61
Al2O3	19.73	30.37	29.92	27.72	Al2O3	0.85	6.37	4.01	1.77	0.75
CaO	0.14	11.09	13.39	10.57	CaO	22.54	17.93	0.80	14.71	1.44
Na2O	11.24	3.90	3.63	5.11	Na2O	0.39	1.71	0.27	0.28	0.00
K2O	0.10	0.39	0.26	0.37	K2O	0.00	0.00	0.00	0.00	0.00
MgO	0.00	0.00	0.00	0.00	MgO	17.93	16.13	33.28	14.03	19.36
TiO2	0.00	0.00	0.00	0.00	TiO2	0.00	0.34	0.00	0.76	0.28
FeO	0.00	0.59	0.94	0.55	FeO	1.11	2.37	5.13	16.40	25.55
MnO	0.00	0.00	0.00	0.00	MnO	0.00	0.00	0.00	0.48	0.00
Cr2O3	0.00	0.00	0.00	0.00	Cr2O3	0.00	0.76	0.53	0.00	0.00
Total:	**100.00**	**100.00**	**100.00**	**99.99**	**Total:**	**100.00**	**100.00**	**100.00**	**100.01**	**99.99**
Atoms per 8 oxygen					**Atoms per 6 oxygen**					
Si	3.00	2.42	2.36	2.51	Si	2.04	1.94	1.92	1.95	1.99
Al	1.01	1.61	1.61	1.47	Al	0.04	0.27	0.16	0.08	0.03
Ca	0.01	0.54	0.65	0.51	Ca	0.86	0.68	0.03	0.60	0.06
Na	0.95	0.34	0.32	0.45	Na	0.03	0.12	0.02	0.02	0.00
K	0.01	0.02	0.02	0.02	K	0.00	0.00	0.00	0.00	0.00
Mg	0.00	0.00	0.00	0.00	Mg	0.95	0.86	1.70	0.79	1.09
Ti	0.00	0.00	0.00	0.00	Ti	0.00	0.01	0.00	0.02	0.01
Fe	0.00	0.02	0.04	0.02	Fe	0.03	0.07	0.15	0.52	0.81
Mn	0.00	0.00	0.00	0.00	**Mn**	0.00	0.00	0.00	0.02	0.00
Cr	0.00	0.00	0.00	0.00	**Cr**	0.00	0.02	0.01	0.00	0.00
Total	**4.97**	**4.96**	**5.00**	**4.97**	**Total**	**3.95**	**3.97**	**4.00**	**4.00**	**3.99**
An	0.01	0.60	0.66	0.52	En	0.52	0.53	0.91	0.42	0.56
Ab	0.99	0.38	0.32	0.46	Fe	0.02	0.04	0.08	0.27	0.41
Or	0.01	0.02	0.02	0.02	Wo	0.47	0.42	0.02	0.31	0.03

(± 3). Some of the Cpx grains show a Mg-enriched core and Cpx grains generally show Opx exsollution lamellae.

Cranberry Lake Diopside was kindly provided by Jacques Précigout (Université d'Orléans) and Damaping Enstatite and Diopside were kindly provided by Holger Stünitz (University of Tromsø). The diopside and enstatite material was provided in the form of mineral powder, with grain sizes of 40 - 125 μm for Cranberry Lake Diopside, 40 - 180 μm for Damaping Enstatite and $\leq$ 125 μm for Damaping Diopside. Damaping Enstatite and Diopside are derived from a peridotite xenolithe, the Cranberry Lake Diopside from a calc-silicate rock.

The albite material is extracted from an albite-quartz vein formed along a joint from the Alpe Rischuna area, Switzerland. Sonora Labradorite are labradorite megacrysts formed in basaltic deposits from the Pinacate volcanic field, Sonora, Mexico. From both, Sonora Labradorite and Alpe Rischuna Albite, a powder (grain size fraction $\leq$ 125 μm) was produced in the same manner as described for the Maryland Diabase powder. As the

Sonora Labradorite material showed some accessory calcite, the powder was cleaned with HCl_{aq} (10%). Subsequently, the powder was placed in a funnel with a grade 602 h qualitative filter paper with a pore size of 2 μm and rinsed thoroughly with distilled water. The powder retained by the filter was then dried in an oven at $\sim$ 110 °C. After this treatment, no calcite was observed anymore in the material. However, the initial grain size fraction of $\leq$ 125 μm, is expected to have been altered to $\sim$ 2 μm $\leq$ x $\leq$ 125 μm.
Synthetic Pl - Px powders are mixed with a phase distribution of vol.-% $\approx$ 57% Pl to 43% Px. To produce the synthetic mixtures, the powders were put in a 5 ml glass beaker with acetone and mixed using an ultrasonic stirrer. When most of the acetone was evaporated, the slurry was dried in an oven at 110 °C. This procedure prevented grain size and density sorting of the minerals.

2.1.3.2 Sample setup

Except for one, all experiments were performed using the previously described general shear setup with the 45° pre-cut forcing blocks (Figure 2.2b). In this setup, the sample is composed of a thin 'shear zone' formed by placing 0.11 g of rock powder + either 0.18 or 0.11 wt.-% (0.20 or 0.12 μl) H_2O between the Al_2O_3 forcing blocks.
One experiment was performed as an axial shortening experiment on a MD whole cylinder rock core. 0.18 wt.-% H_2O was added to the sample, which then was encapsulated in a Pt-jacket with an outer Ni-foil wrap. The Ni-foil wrap in this case was on the outside due to the larger cylinder diameter of the rock core (6.55 mm compared to the 6.33 mm of the Al_2O_3 forcing blocks) and the Ni-foil did not fit into the Pt-jacket together with the rock core.
In the case of the general shear experiments, some problems of coupling the forcing blocks with the rock material occurred at higher temperatures (700 and 800 °C). 800 °C experiments were therefore performed using forcing blocks with regular grooves cut into the 45°-inclined forcing block surfaces. 6 grooves, $\approx$ 300 μm wide and 150 μm deep, were cut at regular spacing on both, the upper and lower forcing block.

2.1.4 Experimental conditions

Experiments were run at confining pressures (Pc) of $\approx$ 0.5, 1.0, and 1.5 GPa, at temperatures (T) of 300, 500, 600, 700 and 800 °C , and constant displacement rates of $\approx$ 2 x 10^{-7}, 2 x 10^{-8} and 2 x 10^{-9} m s^{-1} (resulting in shear strain rates of $\approx$ 3 x 10^{-4}, 3 x 10^{-5} and 3 x 10^{-6} s^{-1} if homogeneous sample deformation is achieved).
To bring the sample to the desired Pc-T conditions, increments of advancing the Pc-

and load pistons are alternated with increments of heating (e.g. after every 200 MPa of pressure increase, a T increase of 100 °C is executed) (Figure 2.4). During heating steps, T is increased by 20 °C/min. The pressure vessel, base plate and the oil cylinder in the Rig are water cooled during the full length of the pressurisation, deformation run and de-pressurisation. The water cooling is needed to prevent excessive heating and distortion of the machine and pressure vessel.
Pressurisation is usually achieved within 5 to 8 h, depending on the Pc (duration is longer for higher Pc experiments). During constant displacement rate experiment, only the load piston is advanced. At the end of the experiment, samples are quenched to 200 °C within 2 min. During subsequent decompression, the load piston is simultaneously retreated to reduce the load on the sample (Figure 2.4). During de-pressurisation, the load is kept approximately 100 to 150 MPa above the Pc to prevent excessive cracking upon unloading. The 100 - 150 MPa differential stress imposed on the sample in this manner are far below the sample strength at the T = 200 °C after quenching and no sample showed a late brittle overprint due to this procedure.

2.2 Mechanical data processing

The mechanical data is mainly evaluated for the following parameters: σ_3, σ_1, strain and strain rate. For this, the following assumptions are made:

(i) σ_3 is assumed to be equal to Pc (σ_3 = Pc).

(ii) σ_1 can be calculated from the measured load as load per area. The globally imposed orientation of σ_1 is equal to the load axis.

(iii) The initial friction at the start of the lead run-in is not recovered during the experiment and can be subtracted from the applied load.

and the following corrections are applied to the mechanical data:

(i) correcting Pc for increasing volume in the sample assembly due to load piston advancement (see 'elastic salt correction', section 2.2.1 and Appendix C).

(ii) The effective area over which the applied load is supported is expected to decrease due to decreasing forcing block overlap with increasing shear displacement (see section 'area correction').

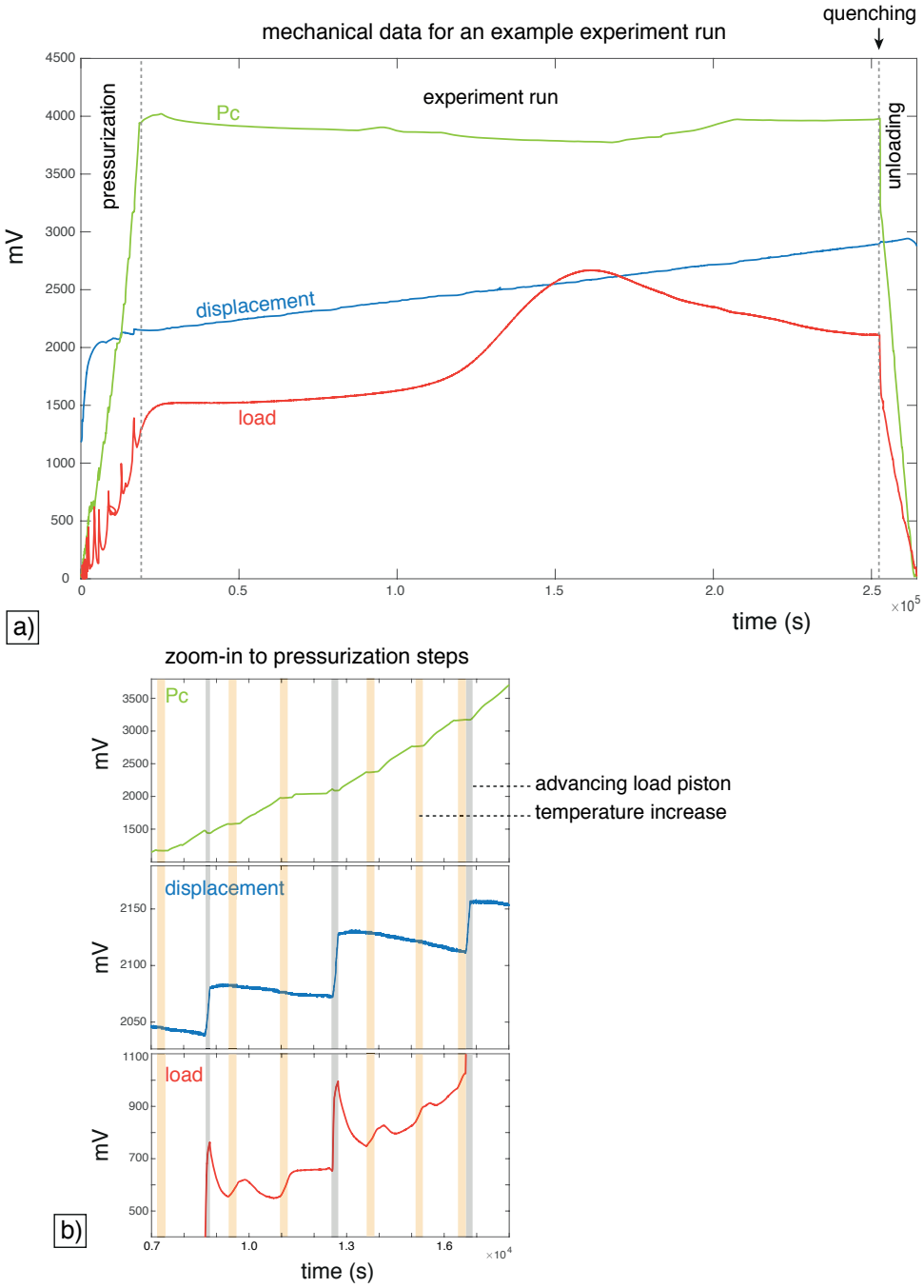

Figure 2.4: *Raw mechanical data as millivolts (mV) versus time (s). During 'pressurisation', the sample is brought step-wise to the desired Pc-T conditions. 'Displacement' is the axial displacement of the load piston. The Pc piston is not moved during the experiment run. Variations in Pc during the experiment run are mainly caused by friction between load- and Pc piston and variations in oil density (in the hydraulic system of the pressure ram), influenced by cooling water and room temperature fluctuations. The zoom-in view in b) shows a close-up on the pressurisation steps of Pc increase alternated with heating steps and load piston advancement. Spikes in the load curve are due to friction, which decays as soon as the load piston advancement is stopped.*

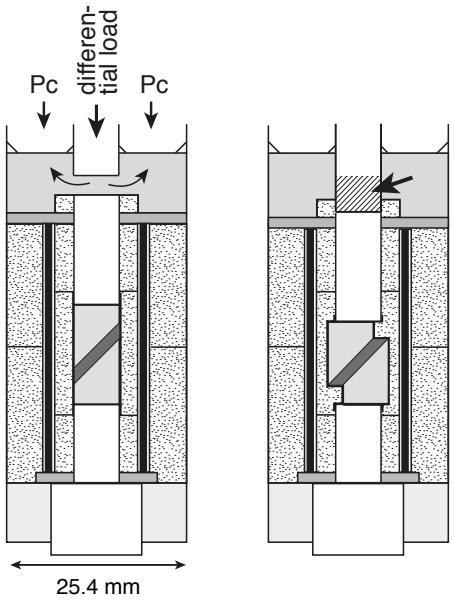

Figure 2.5: *Sketch of sample assembly, illustrating the volume increase within the assembly as the load piston is advanced during an experiment. The shaded area (black arrow) on the load piston in the right pictogram shows the additional area (in this 2D section) due to piston advancement.*

(iii) Piston friction seen at the onset of the lead run-in is subtracted from the load by defining a hit-point (see section 'New hit-point definition').

(iv) The displacement is corrected for elastic distortion of the Rig, caused by the effectuated load on the sample during an experiment. The displacement correction factor has been newly determined, with the procedure and results described in Appendix B.

The experimental setup, procedure and data treatment is also described in detail in Pec (2014). However, since then, a variety of changes to the data treatment were introduced, which will be emphasised in the following sections.

2.2.1 'Elastic salt correction' for confining pressure

During an experiment run, the load piston is advanced into the sample assembly, increasing the total volume within the assembly (Figure 2.5). This volume increase is expected to lead to an increase in confining pressure with increasing advancement of the load piston. The amount of confining pressure increase is depending on the compressibility of the materials within the assembly (salt, lead, alumina etc.). Up until today, as a first approximation, the increase in confining pressure is calculated considering only the salt confining medium. The procedure and calculations used for the 'elastic salt correction' are listed in Appendix C.

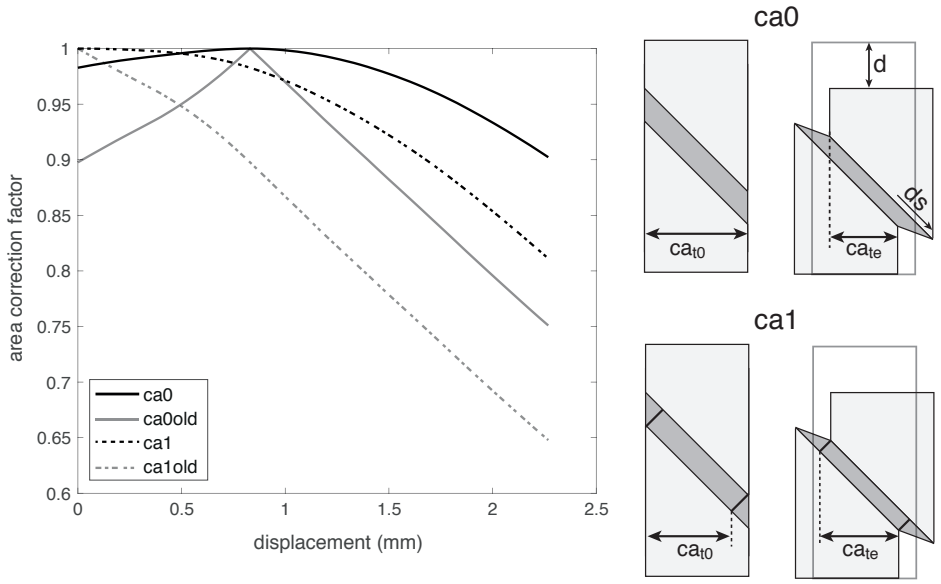

Figure 2.6: *Comparison of new and old area correction routines. Plot on the left shows the differences between the previously used area correction routine (ca0old, ca1old) and the new ones (ca0, ca1). ca = contact area. ca_{t0} = contact area at experiment start, ca_{te} = contact area at experiment end. d = axial displacement, ds = shear displacement parallel to the sample - forcing block interface. 'ca0' assumes that the force acts on the cross-sectional area of the sample seen when looking along the load axis (vertical). 'ca1' assumes the cross-sectional area of the sample when looking parallel the normal on the 45° inclined shear zone boundaries. 'ca1' has a maximum overlapping area at a shear displacement equal to the initial sample thickness.*

2.2.2 Area correction

A new area correction routine was introduced to correct for changing overlapping area of the forcing blocks during the shear experiments. The new routine is a cosine-square approximation to the ACF (the ACF approach had previously been used). The new area correction factor (AC) is calculated as:

$$AC(i) = cos^2\left(\frac{(ds(i) - Ls_x) \cdot 90^\circ}{Ls_0}\right) \tag{2.1a}$$

with *ds(i)* = shear displacement [mm] at each point i during the experiment, Ls_0 = maximum possible shear displacement = diameter of forcing blocks (6.33 mm / cos(45°)) = 8.95 mm.

$Ls_x = 0$, for the area correction routine ca0. And

$$Ls_x = \frac{th0}{tan(45^\circ)} \tag{2.1b}$$

for the area correction routine ca1 (Figure 2.6). *th0* = shear zone thickness at experiment start.
The area corrected differential stress then is calculated as:

$$\Delta\sigma_{AC}(i) = \Delta\sigma(i)/AC(i) \tag{2.1c}$$

with $\Delta\sigma_{AC}$: area corrected $\Delta\sigma$.

The differences between the previously used area correction routines and the new one are shown in Figure 2.6. The previous 'ca1' routine ('ca1old' in Figure 2.6) has a sharp inflection point when reaching maximum overlapping area (after a shear displacement equal the initial shear zone thickness). The new 'ca1' correction is a softer correction function. In general, the new area correction routines have a smaller influence on the differential stress than the previous ones.

2.2.3 New hit-point definition

The Grigs rig sample assembly is usually fabricated with a top lead piece, protecting the sample during pressurisation. At the start of the deformation experiment, the load piston thus has to be advanced through the top lead (lead run-in), before contact with the sample column is attained at the hit-point (Figure 2.5; Figure 2.7).
At the onset of a deformation experiment (beginning with the lead run-in), the load curve shows an initial steep increase and tapers off into an almost horizontal curve shortly thereafter (Figure 2.7b). The initial load increase is interpreted to be caused by friction in the load- and sample- column. The relatively shallow slope in the lead run-in increases as the load piston is driven through the lead piece and the lead run-in curve grades into the loading curve of the sample around the area of the hit point. So far, the routine of determining the hit-point, was by the intersection of the tangent to the initial stretch of the lead run-in section and the tangent to the linear part of the sample loading curve (HPo in Figure 2.7c). All the load attained prior to the hit point was considered to be due to non-recovering friction in the machine and sample assembly, and was subtracted from the load curve. However, it is not clear if the slow increase in load during the lead run-in is due to friction or due to increasing strain rate in the residual lead between sample column and load piston as the lead is being pushed aside by the advancing load piston (see e.g. Figure 2.5).
A new hit-point definition is introduced, which assumes only the initial load increase at the very start of the experiment as friction (HPn in Figure 2.7c). The slow load increase

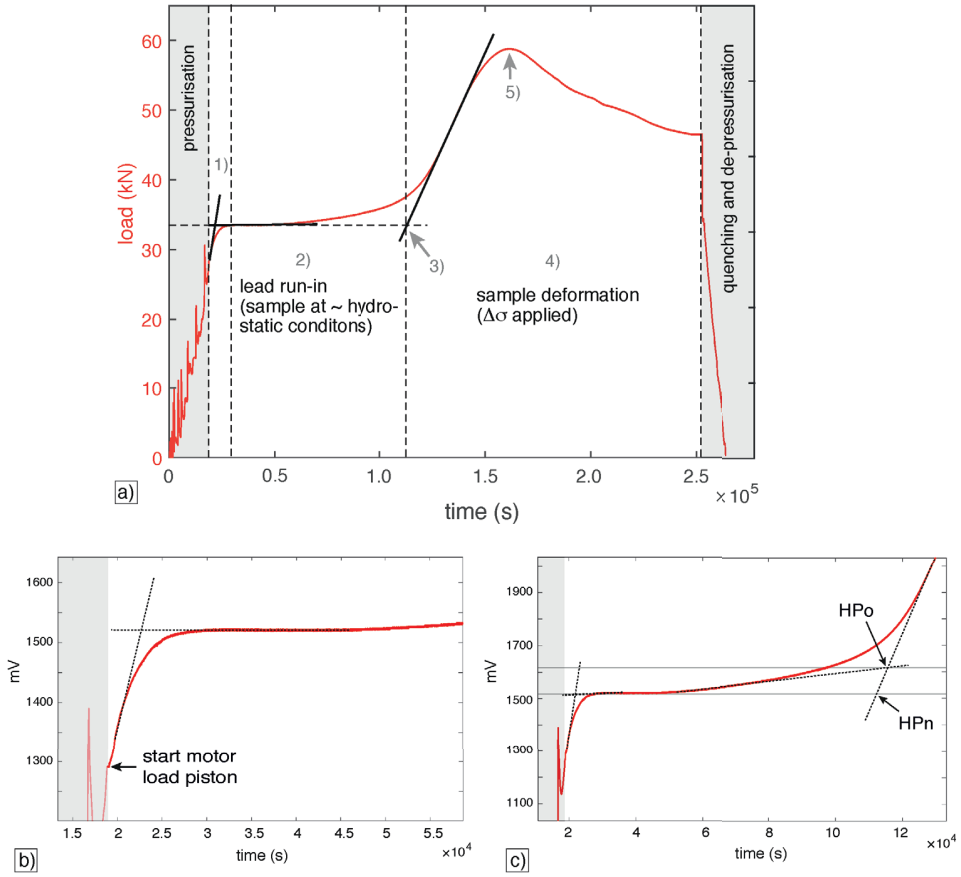

Figure 2.7: *Load curve and procedure of hit-point determination. a) (1) Initial force increase due to piston friction at the beginning of the lead run-in. (2) lead run-in, (3) hit-point, (4) sample loading and deformation, (5) peak stress. b) A tangent to the initial steep force increase and a tangent to the subsequent ~ horizontal force progression are determined. The y-value of the intersection is used as y-value of the new hit-point. c) A tangent to the linear part of the initial sample loading is determined. The x-value of the hit-point will be the x-value of this tangent at the y-value of the new hit-point (HPn). The procedure of determining the old hit-point is labeled with HPo.*

during the lead run-in then is considered to be transferred to the sample, inducing a differential load. The new hit-point is defined as the point where the tangent to the linear part of the initial sample loading has the load value attained at the plateau after the initial load increase at experiment start (Figure 2.7b and c).

2.2.4 Strain calculations

In the 45° pre-cut setup, general shear type of flow is effectuated. That is, strain has both shear and flattening components. The thinning of the shear zone during an experiment is unknown but can be approximated by comparing the shear zone thickness in experiments performed to different amounts of axial displacement (Figure 2.8). It was recognised from

this data, that experiments performed at T $\leq$ 700 °C show similar behaviour (Figure 2.8) and expected starting thickness of the shear zone at the hit point is $\approx$ 0.82 mm. 800 °C experiments show a smaller shear zone thickness at the hit point, with an initial expected thickness of $\approx$ 0.75 mm. The smaller values for shear zone thickness at 800 °C is attributed to a significant contribution of solution-mass transport to compaction during the lead run-in, leading to increased porosity reduction compared to lower T experiments. For both data sets presented in Figure 2.8, a linear fit was chosen.

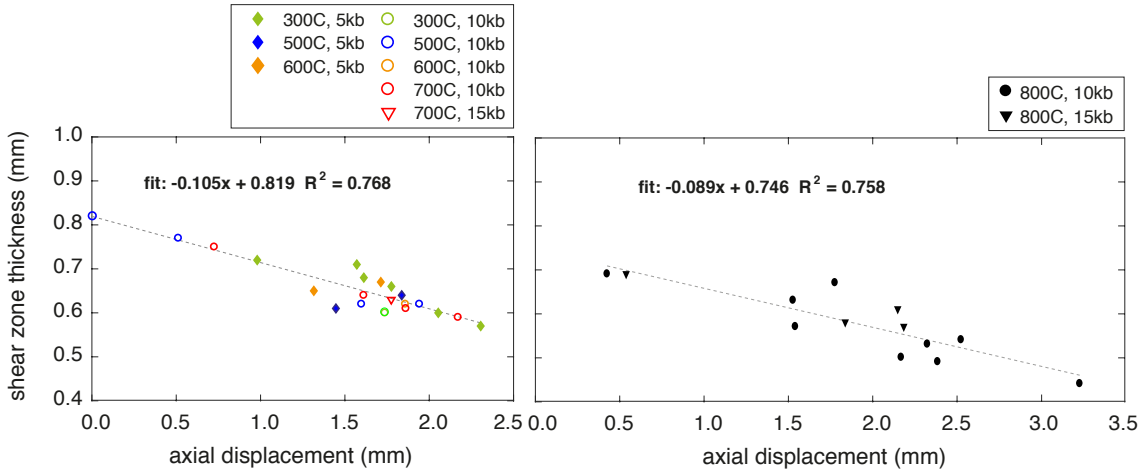

Figure 2.8: *Shear zone thickness as a function of axial displacement for experiments with different amounts of axial displacement for experiments performed at T $\leq$ 700 °C and for experiments performed at T = 800 °C respectively. In both cases, a linear fit to the data is chosen.*

As the shear zone thinning with displacement is approximately known, the axial displacement can be sub-divided into a shear and a shortening component, parallel and perpendicular to the shear zone boundaries. From the shear component, shear strain was previously calculated and presented as what could be called 'apparent instantaneous shear strain' (γ_i):

$$\gamma_i(i) = \frac{ds(i)}{th(i)} \tag{2.2}$$

with *ds(i)*: shear displacement at each measuring point i during an experiment, *th(i)*: shear zone thickness at each measuring point i.

An alternative way of shear strain calculation was introduced, that could be described as 'sum of incremental apparent shear strains' (γ_a):

$$\gamma_a = \sum_{k=2}^{i} \frac{ds(k) - ds(k-1)}{th(k)} \tag{2.3}$$

i : number of recorded measurements during the experiment, ds : shear displacement, th : shear zone thickness.

Unlike γ_i, γ_a has a memory of the strain history of foregoing incremental deformation steps at larger shear zone thicknesses. Apparent strains given in the following chapters will always be the 'incremental apparent shear strain' γ_a.

γ_i and γ_a are only approximate and not true measures for simple shear strain, thus are termed 'apparent' shear strains.
The flattening and simple shear components can be derived from the 'effective shear strain, Γ' (after Fossen and Tikoff (1993)), which is calculated as:

$$\Gamma = k^{-1} \cdot tan(\psi) = k^{-1} \cdot \frac{dsF}{thF} \tag{2.1}$$

with

$$k = th0/thF \tag{2.2}$$

where $th0$ = starting thickness of the shear zone, thF = shear zone thickness at experiment end (Figure 2.9), dsF = total shear displacement at experiment end, k = pure shear component.
The simple shear component (γ) of the general shear experiments is calculated after Fossen and Tikoff (1993) as:

$$\gamma = \Gamma \cdot \frac{2\ ln(k)}{k - k^{-1}} \tag{2.3}$$

2.3 Analytical methods

2.3.1 Microscopy

After the experiments, samples are impregnated with epoxy, cut parallel to the shear direction (in some cases also normal to it), and prepared to doubly polished thin sections. Light microscope, scanning electron microscope (SEM) and transmission electron microscope (TEM) are used for sample analysis.

2.3.1.1 Scanning electron microscopy

SEM analyses are performed either with the Zeiss Merlin SEM at Tromsø University, or with a Philips XL30 ESEM at the center of microscopy (SNI) at Basel University. Images

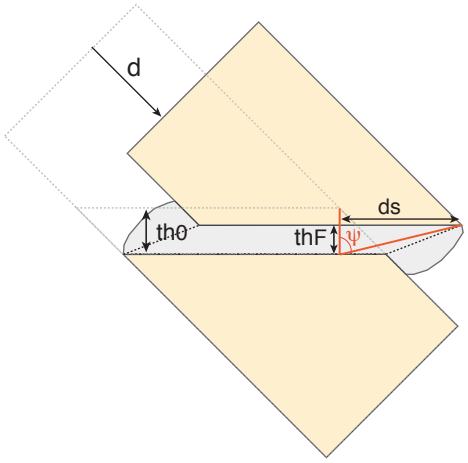

Figure 2.9: *General shear setup within initial state and shear zone thickness, th0, and state at end of experiment and final shear zone thickness, thF. d = axial displacement induced by the load piston, ds = shear displacement parallel to the forcing block - sample interface.*

are recorded either in secondary electron (SE) mode, or in back scattered electron (BSE) mode. Chemical analyses are performed using energy dispersive X-ray Spectroscopy (EDS), at 15 kV acceleration voltage and using a ZAF correction for quantification.

2.3.1.2 Transmission electron microscopy and Focused ion beam

TEM analyses are carried out at Utrecht University (Netherlands) using a FEI Talos 200FX equipped with a high-sensitivity Super-EDX system, and at the University of Minnesota (Minneapolis, USA) with a FEI-TECNAI T12. TEM images are recorded in bright field (BF), high angular annual dark field (HAADF) and bright field scanning TEM (BF-STEM) modes. BF images are highly sensitive on crystallographic orientation, whereas contrasts in HAADF images are sensitive to average atomic number (Z-contrast) of the material.
Focused ion beam (FIB) foils for TEM investigations are prepared in a FEI Helios NanoLab 3G at the University of Utrecht.

2.3.2 Image analysis

2.3.2.1 Segmentation

Mineral phase segmentations are performed on BSE SEM images. Phases are differentiated by their different Z-contrast using grey-level slicing. Prior to segmentation, the BSE images were processed with the freeware Fiji (link at: http://fiji.sc/Fiji). Preprocessing mainly involved noise filtering and enhancing contrast. The plugin *Statistical Region Merger* was used for automatic pre-segmentation from which phases then could be segmented by using grey-level thresholding. All automatically segmented maps were manually checked and corrected/cleaned where necessary.

2.3.2.2 Shape and orientation of fault zones

Shear bands and larger shear fractures are digitised manually on BSE SEM images or light microscope image. The x-y coordinates of the outlines are measured, smoothed (to remove digitising artifacts) and exported using the program Fiji and a modified version of the macro *Jazy_XY_export.ijm* by Rüdiger Kilian (University of Basel). The shape analysis was performed using the SURFOR program (Panozzo Heilbronner, 1984; Heilbronner and Barrett, 2014). SURFOR results yield an orientation distribution function (ODF) of boundary segments of the analysed structures and the SURFOR results are presented as rose diagrams.

2.3.2.3 Grain size and shape

Grain boundaries are traced manually on SE- and BSE- SEM images or on BF TEM images. The resulting grain maps are analysed with Fiji to derive the grain areas and the x-y coordinates of grain boundaries.
Grain size distributions are derived by calculating area equivalent diameters (dequ) from the measured grain areas. Grain size distributions will be presented as histograms and as a continuous kernel density estimate fit. The kernel density estimate fit is derived using the MATLAB function 'ksdensity'. From the fit, the mode of the distribution is determined.
Grain shape analyses are performed using the SURFOR program.

2.4 Reference frames and term definitions

If not stated otherwise, micrographs are oriented with the shear zone boundaries horizontal and with a dextral sense of shear (Figure 2.10a). In this representation, the load axis is at 45° (where σ_1 direction assumed to be = load axis) .
Rose diagrams are usually presented with black dots at the rim indicating the preferred orientation of the displayed data. Angles at rose diagram rims give the angle θ between the preferred orientation of the displayed data and the load axis (i.e. σ_1) (Figure 2.10b). Terminology used to describe stress-strain curves is given in Figure 2.10c. 'Yield' is used to describe the point of highest curvature after the initial sample loading. The 'yield' usually coincides with peak stress but does not have to.
Cataclasitic flow: We use the term *cataclastic flow* according to the defined in Schmid and Handy (1991) as "a deformational process involving initial granulation of grains by microcracking, leading to frictional sliding, dilatancy, and rigid-body rotation among

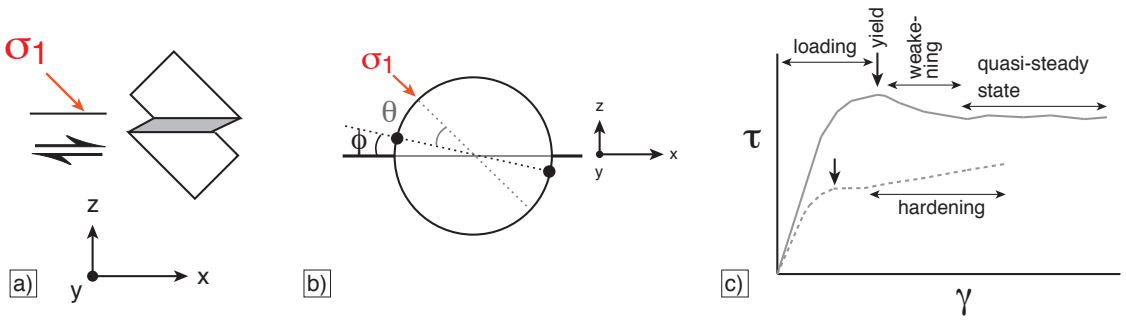

Figure 2.10: *Reference frame and terminology. a) Micrographs are oriented with the shear zone boundaries parallel to the x-direction with a dextral sense of shear. b) In rose diagrams, preferred orientations are marked with black dots; θ = angle between orientation and load axis (σ_1 direction); ϕ = angle between orientation and shear plane (shear zone boundaries). c) Stresses are usually plotted as shear stress τ versus apparent shear strain γ_a. The terms used to describe different stages in the stress-strain curves are labeled.*

grain fragments, grains or groups of grains."

Shear band: The term *shear band* is used to refer to a zone (with a certain thickness) of high shear strain accommodation. As opposite to a shear fracture, which is accommodating displacement along a plane without any obvious distribution of strain within a volume (at SEM resolution). The term *shear band* is used without implying any specific deformation mechanism or deformation regime (e.g. brittle or viscous).

Fault zone/fault network: The term *fault zone* or *fault network* is used to refer to zones of localised accommodation of displacement, happening along shear bands, shear fractures or a combination of both. The terms are used without implying a brittle or viscous regime.

Shear zone: The term *shear zone* in our particular case is simply used to refer to the layer of rock material put between the 45° pre-cut forcing block. The term thus is not used to imply any specific deformation mechanism.

Chapter 3

The brittle-viscous transition, from fracturing to diffusion creep

---

Pbulished as: ***Marti, S.*** *, Stünitz, H., Heilbronner, R., Plümper, O., and Drury, M. (2017). Experimental investigation of the brittle-viscous transition in mafic rocks - interplay between fracturing, reaction and viscous deformation. Journal of Structural Geology, 105, 62-79*

Abstract:

Rock deformation experiments are performed on 'synthetic' fault gouge fabricated from 'Maryland Diabase' rock powder to investigate the transition from dominant brittle to dominant viscous behaviour. At the imposed strain rates of $\dot{\gamma} \sim 3\ 10^{-5}$ - $3\ 10^{-6}$ s^{-1}, the transition is observed in the temperature range of (600 °C $<$ T $<$ 800 °C) at confining pressures of (0.5 GPa $\leq$ Pc $\leq$ 1.5 GPa). From microstructural observations, the transition is effected by a switch from brittle fracturing and cataclastic flow, to viscous dissolution-precipitation creep and grain boundary sliding. Mineral reactions and resulting grain size refinement by nucleation are observed to be critical processes for the switch to viscous deformation, i.e., grain size sensitive creep. In the transitional regime, the mechanical response of the sample is a mixed-mode between brittle and viscous

rheology and microstructures associated with both brittle and viscous deformation are observed. As grain size reduction by reaction and nucleation is a time dependent process, the brittle-viscous transition is not only a function of T but to a large extent also of microstructural evolution.

3.1 Introduction

Our knowledge about rock strength is largely based on laboratory-derived data. Given the condition that the strength of the rock cannot be greater than that of the constituting minerals, laboratory data for individual minerals have been used to construct 'strength envelopes', where the maximum strength is plotted versus depth (e.g. Brace and Kohlstedt, 1980; Kohlstedt et al., 1995; Burov, 2011, and references therein). Following the general consensus that the upper crust deforms dominantly by fracturing and the lower crust and upper mantle by viscous creep, the common strength envelopes are constructed using a constant strain rate, two-mechanism model. Frictional rock strength (Byerlee, 1978) is plotted against depth to the temperature and pressure conditions, where viscous deformation becomes dominant and results in a lower rock strength than frictional sliding. The intersection of the two rheological relationships forms a discontinuity in the strength envelope, corresponding to the transition from frictional deformation to viscous flow (here referred to as the 'brittle-viscous' transition, BVT).
At lower pressures and temperatures (shallower depth) than the BVT, the brittle-ductile transition (BDT) is defined as the intersection of the Mohr-Coulomb fracture envelope with the Byerlee relationship (Kohlstedt et al., 1995, e.g.). The region between the BDT and the BVT is commonly termed *semi-brittle* field of deformation. Thus, near the BVT, there are several competing processes active in rock deformation over a range of pressures and temperatures (combined as depth): fracturing, frictional sliding, crystal plasticity, and diffusive mass transfer. Given the number of parameters controlling the deformation, the BVT, where both, time dependent viscous processes and relatively time independent brittle and frictional processes significantly contribute to the deformation, is a complex system where temperature, pressure, fluid availability, grain size, strain rate, microstructure, rock composition (i.e. mineral assemblage), and chemical environment control the rheology. As a consequence, it is not surprising that there is a lack of laboratory data characterising the BVT in detail, despite pioneering seminal works by, e.g., Griggs et al. (1960); Heard (1960); Handin (1966); Byerlee (1967, 1968); Tullis and Yund (1977); Brace and Kohlstedt (1980); Carter and Tsenn (1987), and review in Paterson and Wong (2005) and references therein.

Currently, it is widely accepted within the tectonics community that fault zones bear their highest strengths at the BVT. It is also expected to mark the lower depth limit of the seismogenic zone (e.g. Sibson, 1982, 1984). The elevated rock strength at the BVT may explain the potential for high-magnitude earthquakes and represents a key-zone determining the dynamics of a fault-zone system. Therefore, it appears timely to return to experimental studies of the BVT to provide data on this important transition in rock deformation. In the absence of flow laws for other crustal minerals, the viscous strength of the continental crust was first estimated using a dislocation creep flow law for quartz (Brace and Kohlstedt, 1980; Kohlstedt et al., 1995). However, large proportions of the lower continental crust, and most of the oceanic crust are of mafic composition and quartz is virtually absent. Strength estimates for these crustal parts could only be assessed since flow law parameters for plagioclase and pyroxene became available (e.g. Mackwell, 1991; Raterron and Jaoul, 1991; Mauler et al., 2000; Bystricky and Mackwell, 2001; Rybacki and Dresen, 2000; Dimanov et al., 2003; Dimanov and Dresen, 2005; Rybacki et al., 2006; Chen et al., 2006; Dimanov et al., 2007). Most of the data, however, is applicable to high temperature deformation and experimental studies for mafic rocks at lower temperatures are scarce (Kronenberg and Shelton, 1980; Rutter et al., 1985; Hacker and Christie, 1991; Tullis and Yund, 1987; Getsinger and Hirth, 2014). Therefore, there is a need for more experimental studies on the BVT in mafic rocks to assess the rheology and deformation behavior of oceanic and lower continental crust.

One important aspect of the BVT - not represented in the strength envelope plots - is the development of the rheology of sheared rock over time or during a strain history. Fault- and shear zones may show a strain-dependent microstructural evolution, which, in turn, may cause a strain-dependent strength evolution. One of the consequences of such a strain-history-dependent evolution is that fault/shear zones are unlikely to initiate with their final steady state strength. It is frequently seen from natural examples that brittle and viscous deformation can occur cyclically (e.g. Gratier et al., 2011) or sequentially in time (e.g. Simpson, 1986; Fitz Gerald and Stünitz, 1993; Stünitz and Fitz Gerald, 1993; Trepmann and Stöckert, 2003; Mancktelow and Pennacchioni, 2005; Pennacchioni and Mancktelow, 2007; Fusseis and Handy, 2008; Goncalves et al., 2016; Bukovská et al., 2016). In order to address this question in our study, experiments have been performed to various amounts of strain to observe strain dependent microstructural changes during fault-/shear- zone formation. The aim of this study is to gain insights into the deformation processes active over the BVT in a mafic rock and how initiation and maintenance of fault/shear zones are achieved. Mechanical response is measured and deformation mechanisms are identified in the brittle, the semi-brittle and the viscous field.

3.2 Methods

3.2.1 Experimental setup and sample assembly

The experiments which will be presented in this chapter were performed on water added (0.18 wt.-% H_2O) Maryland Diabase powder, with a grain size fraction of $\leq$ 125 mum. The 45° pre-cut setup is used for all experiments.
Experiments performed at confining pressures of $\sim$ 0.5, 1.0 and 1.5 GPa, at temperatures of T = 300, 500, 600, 700 and 800 °C will be presented. Displacement rates are of $\sim 10^{-8}$ to 10^{-9} m s^{-1} (resulting in strain rates of $\sim 3{\cdot}10^{-5}$ to $3{\cdot}10^{-6}$ s^{-1} under the assumption of homogenous sample deformation). See Table 3.1 for a list of experiments and conditions.

3.2.2 Stress exponent

Combining constant displacement rate and displacement rate stepping tests, a stress exponent n is determined for the relationship $\tau = \gamma^{1/n}$. There is some uncertainty about the stress state in the sample assembly and over the years, different ways of data-treatment and -corrections have been applied (as well as differences between individual laboratories). To assess the influence of different data correction routines on calculated stress exponents n, the data of the 300 °C at 0.5 GPa Pc, and the 800 °C at 1.0 GPa Pc experiments are calculated and plotted with the following corrections:

(1) 'R16': Data correction described in Richter et al. (2016). This procedure of data correction is followed in this paper for stress calculations.

(2) 'R16 + H&K10': Data correction after Richter et al. (2016) with the stress correction for the solid-salt assembly after Holyoke III and Kronenberg (2010).

(3) 'P12': Data correction described in Pec et al. (2012a).

(4) 'P12 + H&K10': Data correction after Pec et al. (2012a) with the stress correction for the solid-salt assembly after Holyoke III and Kronenberg (2010).

3.2.3 FFT analyses of HR-TEM images

In high-resolution (HR) TEM images where lattice planes of individual crystals are resolved, Fast Fourier Transformations can be used to obtain the reciprocal space information akin to a direct diffraction pattern. Lattice fringes are only revealed when the crystal satisfies the diffraction condition. One single HRTEM image of a polycrystalline sample is not likely to reveal lattice fringes in all crystals. Therefore, FFT analysis used

Table 3.1: *List of experiments and experimental conditions.*

Exp. Nr	T [°C]	Pc [MPa]	Peak τ [Mpa]	Flow τ [Mpa]	γa	strain rate ýa [s-1]	
375	300	549	1022	951	2.6	3.3E-05	1
418	300	551	978	872	3.4	3.4E-05	1
442	300	530		876		3.4E-05	2
			963	959	3.9	3.3E-04	2
444	300	558	937	899		2.9E-05	2
				777	2.9	3.5E-06	2
446	500	1007	875	746		2.3E 05	2
				853		2.7E-04	2
				771	3.2	3.5E-05	2
367	600	587	620	451	2.0	3.2E-05	1
373	600	538	614	429	2.8	3.1E-05	1
399	600	1027	930	743	3.0	3.2E-05	1
501	600	1041	903	659	3.1	3.7E-05	1
393	700	572	606	288	2.4	3.1E-05	1
413	700	604	541	-	3.6	3.3E-05	1
365	700	1097	759	658	2.6	2.8E-05	1
416	700	1038	722	624	3.1	3.0E-05	1
531	700	1093	798	732		2.4E-05	2
				636		8.3E-06	2
				460		2.7E-06	2
				609	4.5	9.2E-06	2
473	700	1556	872	872	2.9	3.1E-05	1
436	700	1515	846	846	1.9	2.8E-05	1
414	800	1045	407	192	4.2	3.7E-05	1
468*	800	1061	348	348	0.7	-	1
484	800	1041	371	316		2.8E 05	2
				234	2.0	1.3E-05	2
489	800	1080	428	286	2.8	3.0E-05	1
490	800	1059	350	297		3.5E-05	2
				245		1.9E-05	2
				130	4.5	4.1E-06	2
492	800	1077	468	197	6.8	4.8E-05	1
449	800	1504	479	337	4.1	3.5E-05	1
470*	800	1477	446	-	0.9	-	1

T = Temperature. Pc = Confining pressure, averaged between γ_a = 1.5 to end of experiment; (∗) denotes peak stress experiments where average Pc is calculated between beginning and end of experiment. Peak τ = Maximum shear stress. Flow τ = Shear stress during quasi steady state or at end of experiment. γ_a = Apparent shear strain. $\dot{\gamma}_a$ = Apparent shear strain rate: (1) for constant displacement rate experiments calculated as the average value between γ_a = 1.5 and end of experiment; (2) for displacement rate stepping experiments as average value for each setting. (*) Experiment terminated at peak stress. All experiments have 0.2 µl = 0.18 wt% H_2O added.

to detect diffractions on three HR-TEM images from the same area, with different tilt angles.

3.2.4 EDS profiles

Element concentrations along a line-profile are prepared using the software Fiji (https://fiji.sc/). A line-profile of 10 px width is defined, where the value at each point along the profile is an average over these 10 px. In this manner, the noise is reduced.

The values are then normalized to the maximum count value (from the whole EDS map) of each element.

3.3 Results

Samples at T $\leq$ 600 °C develop similar microstructures and we therefore focus in this paper on the evolution from 600 - 800 °C. Reference frames of image orientation and angles are explained in Figure 2a, b; terminology used when describing stress-strain curves is shown in Figure 2c. Shear strain is always given as apparent shear strain γ_a (for calculation, see Appendix).

3.3.1 Mechanical data

3.3.1.1 Stress-strain curves

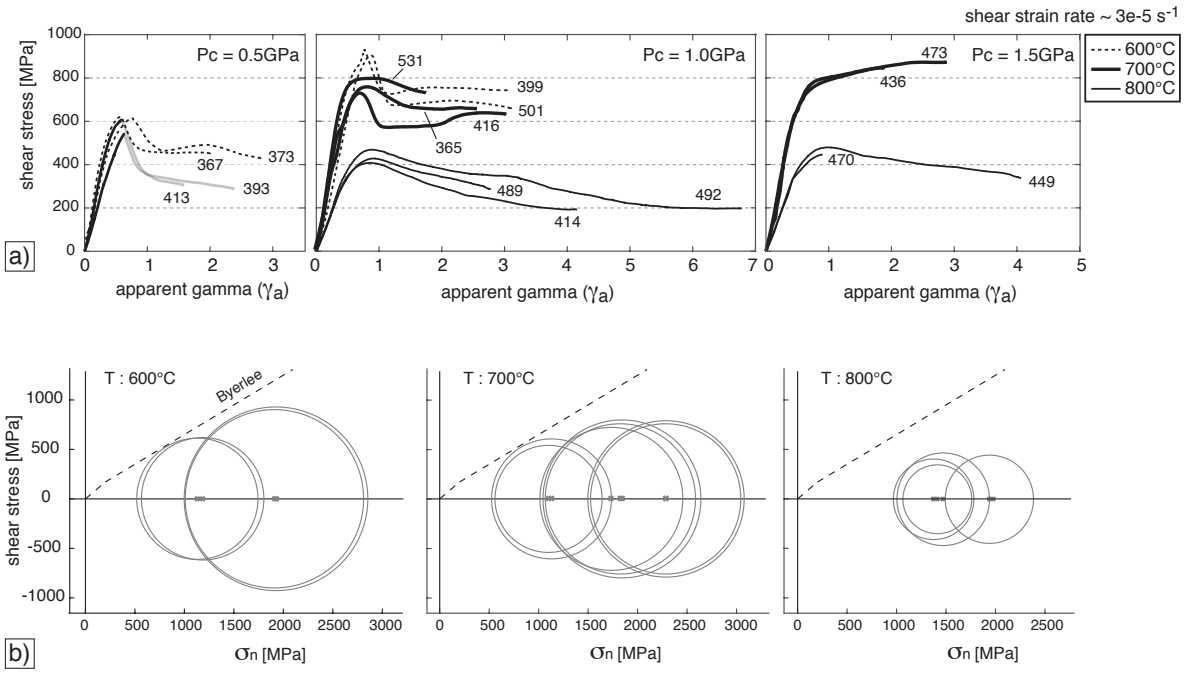

Figure 3.1: *Presentation of mechanical data. a) Shear stress vs. apparent shear strain for experiments performed at 600 °C, 700 °C and 800 °C, using confining pressures of ~ 0.5GPa, 1.0GPa and 1.5GPa. Shear strain rate for all experiments is ~ 3 x 10^{-5} s^{-1}. b) Mohr diagrams for same experiments. σ_3 = confining pressure; σ_1 = yield stress.*

Shear stress vs. apparent shear strain curves are shown for T of 600 °C, 700 °C and 800 °C and Pc of 0.5, 1.0 and 1.5 GPa (Figure 3.1a). Samples deformed at T = 700 °C and Pc = 0.5 GPa all showed severe slip at one sample-forcing block interface after

reaching peak stress. The part of the stress-strain curve after peak stress in 700 °C experiments at Pc = 0.5 GPa is therefore plotted in grey. The samples at 600 and 700 °C are markedly stronger at 1.0 GPa than at 0.5 GPa Pc. That is, they show a positive dependence of τ on Pc. 600 °C experiments show a pronounced weakening after peak stress, whereas the 700 °C experiments are more gradually weakening. Samples at 600 °C and 700 °C, and 1.0 GPa reach similar sample strength after the weakening, with slightly lower strengths for 700 °C experiments (3.1a).
Comparing the stress-strain data for 700 °C experiments at 1.0 and 1.5 GPa Pc, it is seen that the yield point occurs at relatively similar values. The 1.5 GPa Pc experiments however, unlike all other experiments, show hardening at 700 °C until $\gamma_a \sim 2.3$ where stresses stay at approximately constant levels thereafter.
At 800 °C, sample strength is significantly lower than in lower T experiments and within the variability between individual runs, no strength dependence on Pc is detected. 800 °C experiments show a gradual weakening after peak stress and reach a quasi-steady state at a $\gamma_a \sim 4$ onwards (3.1a). Note also the lower slope of the initial loading part of the stress-strain curve at 800 °C compared to the lower T experiments.
Samples at 800 °C deform at stresses below the Goetze criterion (the condition of $\Delta\sigma$ = Pc, which is taken as the upper $\Delta\sigma$-limit of plastic or viscous deformation; (Kohlstedt et al., 1995). At lower temperatures, all sample deform at $\Delta\sigma$ clearly above the Goetze criterion.

3.3.1.2 Mohr Circle construction

Morh circles for the stress state at the yield-point are constructed for 600, 700 and 800°C (Figure 3.1b). It is seen that experiments performed at Pc = 0.5 GPa reach shear stress values predicted by Byerlees (1978) relationship for frictional sliding at peak stress. At higher Pc, shear stresses stay below it. The shear stresses are pressure insensitive for samples at T $\geq$ 700 °C and Pc $\geq$ 1.0 GPa.

3.3.1.3 Stress exponents

A stress exponent n is determined for experiments performed at T = 300 °C, Pc = 0.5 GPa; T = 500 °C, Pc = 1.0 GPa; T = 700 °C, Pc = 1.0 GPa and T = 800 °C, Pc = 1.0 GPa (Figure 3.2). For T $\leq$ 500 °C n is large with values $>$ 19. n for 700 °C experiments is significantly lower with a value of 5.6 and n for at 800 °C experiments is as low as 1.9. The n values determined from different data treatment routines vary by 16 - 27% from the ones determined with the data treatment routine used in this study (Figure 3.2b).

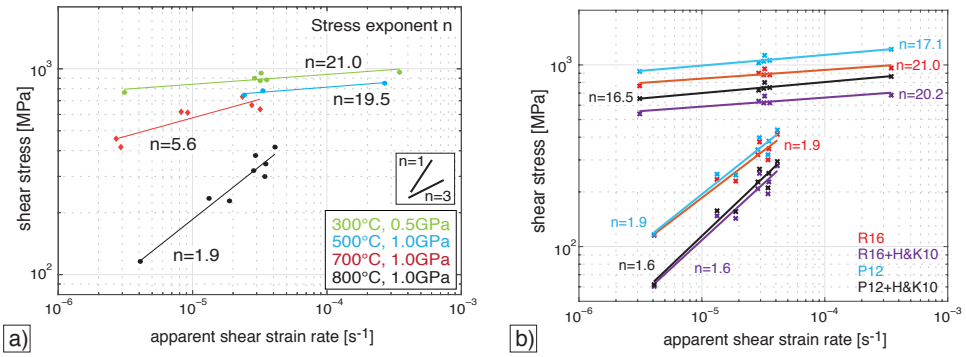

Figure 3.2: *Derivation of stress exponents. a) Shear stress vs. apparent shear strain rate, with calculated stress exponent n; slope of linear fit is 1/n. b) Different stress exponents calculated for different data-correction routines shown for two experiments performed at T = 800 °C, Pc = 1.0 GPa and T = 300 °C, Pc = 0.5GPa. R16 = after Richter et al., 2016; H&K10 = after Holyoke & Kronenberg, 2010; P12= after Pec et al, 2012.*

For example for the T = 800 °C, Pc = 1.0 GPa experiments, a range of n values from 1.6 - 1.9 arises from different data treatment.

3.3.2 Microstructures

3.3.2.1 Overview

Strain in experiments at all Pc-T conditions localizes into a network of shear fractures and/or shear bands. The term 'shear band' is used to refer to a zone (with a certain thickness) of high strain accumulation, without any implication of a specific deformation mechanism. As opposite to a 'shear fracture', which is accommodating displacement along a plane without any obvious distribution of strain within a volume (at SEM resolution).

The microstructures developed at different temperatures are systematically different (Figure 3.3). At 600 °C, the microstructure is dominated by brittle deformation. Fracturing is extensive and a foliation (S), defined by elongated aggregate shapes, develops due to cataclastic flow (Figure 3.3a, b). Larger shear displacements are accommodated along shear fractures and shear bands, usually in Riedel shear (R) orientation. Grain size reduction occurs via pervasive micro-fracturing (Figure 3.3b). No obvious strength difference between Pl and Px is observed. In rare occasions, delicate pore trails are seen where fractures are partially healed, indicating a limited amount of solution mass transfer (Figure 3.3c).

The microstructures in 700 °C experiments are discussed for the case of Pc = 1.0 and 1.5 GPa. At 700 °C, fracturing of (especially Px-) porphyroclasts is still observed and a

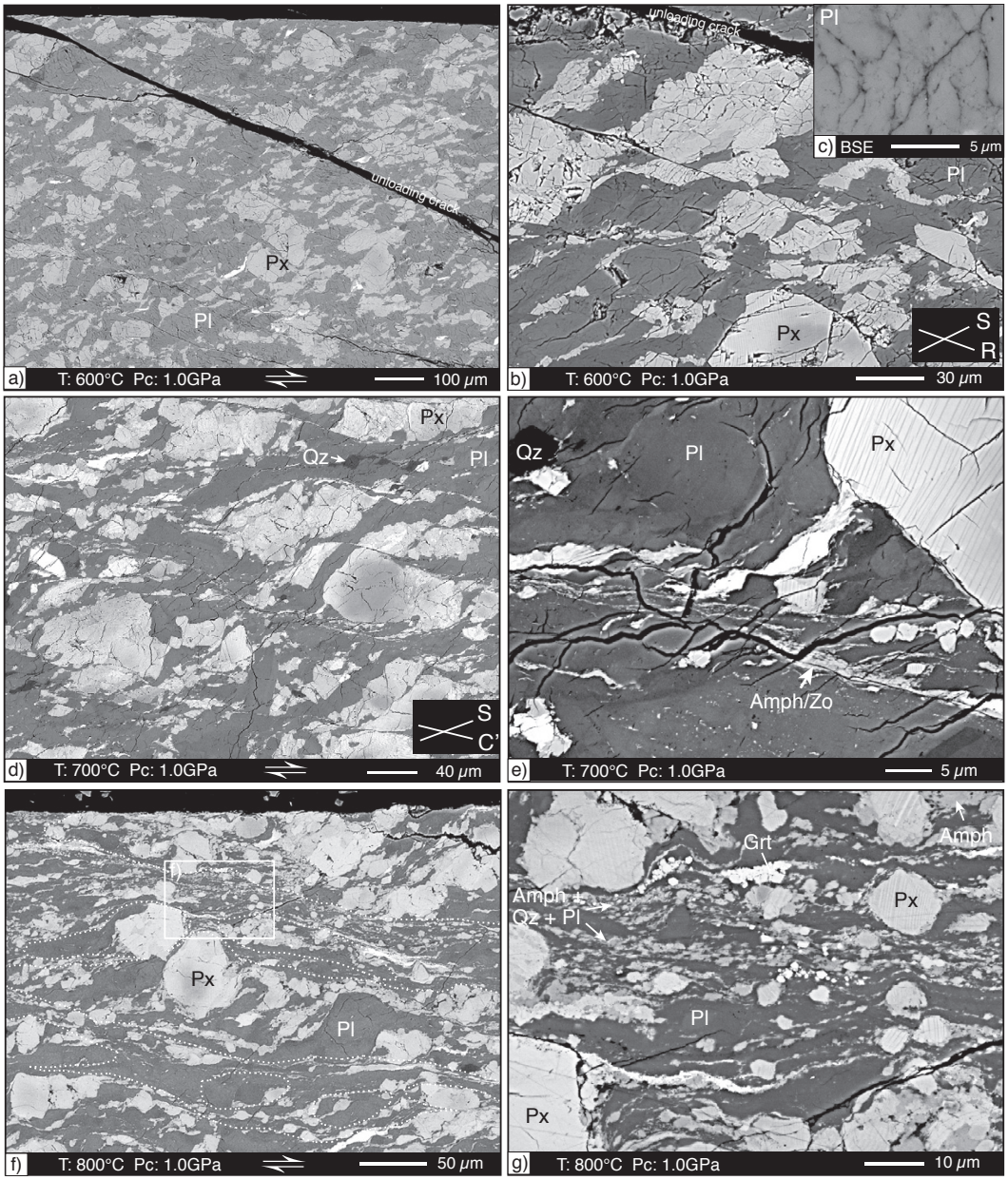

Figure 3.3: *Microstructure development across the Brittle-Viscous transition. Experimental conditions are indicated, dextral shear sense applies to all. a) and b) At T = 600 °C, fracturing is extensive; a foliation (S) is developed by cataclastic flow; shear displacement is accommodated along shear bands and shear fractures in Riedel shear (R) orientations. c) Pore trails along fractures indicate partial healing. d) and e) At T=700 °C, fracturing is extensive in Px porphyroclasts; a foliation (S) is developed partly by cataclastic flow. e) Shear bands are recognized by a fine-scale compositional layering and intense grain size reduction; hydrous reaction products Amph and Zo are beginning to form. f) and g) At T = 800 °C, broad shear bands (white stippled lines) anastomose around low strain lenses; they are characterized by grain size reduction and the formation of a foliation parallel to the shear band boundaries; hydrous reactions products Amph and (to a lower extent) Zo are formed.*

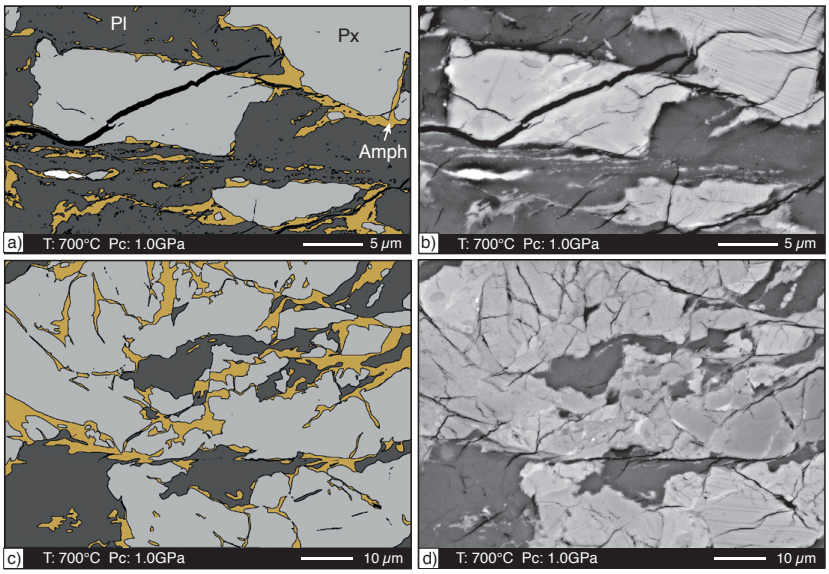

Figure 3.4: *Hydrous reactions at 700 °C. Left: digitally produced phase maps, right, BSE image of the same area. Dark grey = Pl; orange = Amph; bright grey = Px ; sample deformed at T = 700 °C, Pc = 1.0 GPa. Amph follows zones of high strain such as shear bands, or fractures within Px clasts.*

weak foliation (defined by elongated aggregate shapes) forms partly by cataclastic flow (Figure 3.3d). Strain is localized in a network of thin ($\sim$ 5 - 15 μm wide) shear bands in C' orientations, cross-cutting the foliation (Figure 3.3d, e). These shear bands consist of small ($\ll$ 1 μm) grains of mainly Pl, Amph and Zo (Figure 3.3e). The reaction to Amph occurs preferentially along zones of localized deformation such as fractures within Px clasts and along shear bands (Figure 3.4). The reaction to Zo and more albitic Pl occurs throughout the samples, but small Zo needles predominantly occur in shear bands. Both, the Amph and Zo forming reactions are observed at Pc = 1.0 and 1.5 GPa, but occur more extensively at 1.5 GPa.

At 800 °C broad shear bands form, separating low strain lenses between them (Figure 3.3f). Shear bands are recognized by small grain sizes and a fine-scale compositional layering, defining a foliation (Figure 3.3g). Fracturing is only minor represented in the microstructure but can still be observed. Mineral reactions occur pervasively throughout the sample (i.e. are not restricted to high strain zones) but are more abundant in shear bands compared to low strain lenses. Amph either grows as coronas around Px grains or as aggregates within shear bands (Figure 3.3g). Zo grains occur as small needles within Pl clasts or within shear bands. Grain sizes within shear bands are small, usually $<$ 1 μm. Experiments at 800 °C and 1.5 GPa Pc show very similar microstructures but the Amph and especially Zo reaction are more abundant at the higher Pc conditions.

At 800 °C, some melting is observed (melt vol.-% of total sample vol. $\leq$ 2), where the melt is mainly seen to form small pockets situated in extensional sites between larger porphyroclasts. No melt bands or shear-parallel melt layers are observed.

The geometry of strain localization changes over the temperature range from 600 - 800 °C

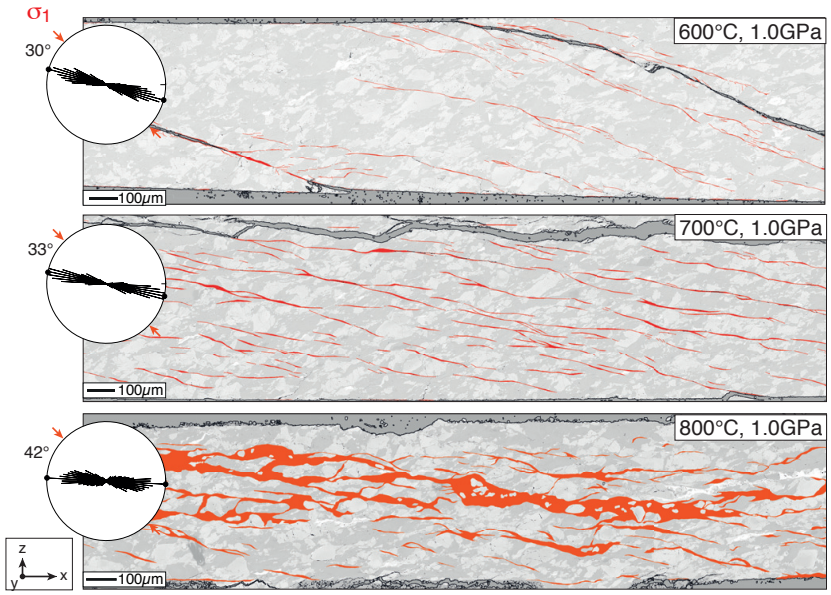

Figure 3.5: *Shear band morphology as a function of temperature. Shear bands and shear fractures are traced in red. Light background layer are BSE contrast images of the shear zones. Rose diagrams (surface ODFs) show orientation of boundary segments of the traced structures. Horizontal shear bands developed at the forcing block-shear zone interface are omitted from the analysis.*

(Figure 3.5). Shear bands and shear fractures at 600 °C tend to be few, with large displacements. At 700 °C, shear bands are more abundant, shorter and more anastomosing compared to the lower T experiments. Shear fractures with larger displacements are less abundant but still observed. At 800 °C, shear bands are broad and form an anastomosing network. Generally no shear fractures with any significant amount of displacement are observed at 800 °C.

The preferred orientations of shear bands and shear fractures with respect to the load axis increases from 30° at 600 °C (or 15° towards the shear zone boundaries) to 42° at 800 °C (or 3° towards the shear zone boundaries) (Figure 3.5).

3.3.2.2 Shear bands formed in low T experiments

Shear bands at 600 °C usually have a thickness of $\sim$ 2 to 10 μm and occur both, along parts of the sample-forcing block interface and traversing the sample (Figure 3.5). The shear bands are either formed by ultra-cataclasites (*type-I* shear bands) or by a material that shows flow structures, seen by perturbation of a micron- to sub-micron scale compositional layering (*type II* shear bands) (Figure 3.6a). There is a clear and relatively abrupt grain size gradient over a few microns from host material into the *type-II* shear bands. Whereas the host material is usually pervasively fractured, no fractures or grain fragments are resolved within shear bands (at SEM resolution). A *type II* shear band as shown in Figure 3.6a has been studied in more detail by TEM. The host material bordering the shear band, consists of larger ($\gg$ 100 nm) angular Pl fragments and the boundary to the shear band material is sharp (Figure 3.6b). The shear band itself is

composed of nano-crystalline and amorphous material in lenticular aggregates and layers, both with fairly sharp boundaries. Some crystals, identifiable by their darker appearance due to diffraction, are observed within the amorphous layers (Figure 3.6b - d). HAADF contrast images show that the crystalline domains are mainly formed from Px crystals. Lattice planes, seen in high-resolution BF TEM images and detected in FFT images show that the amorphously appearing layers still contain nano-crystals (Figure 3.6d).

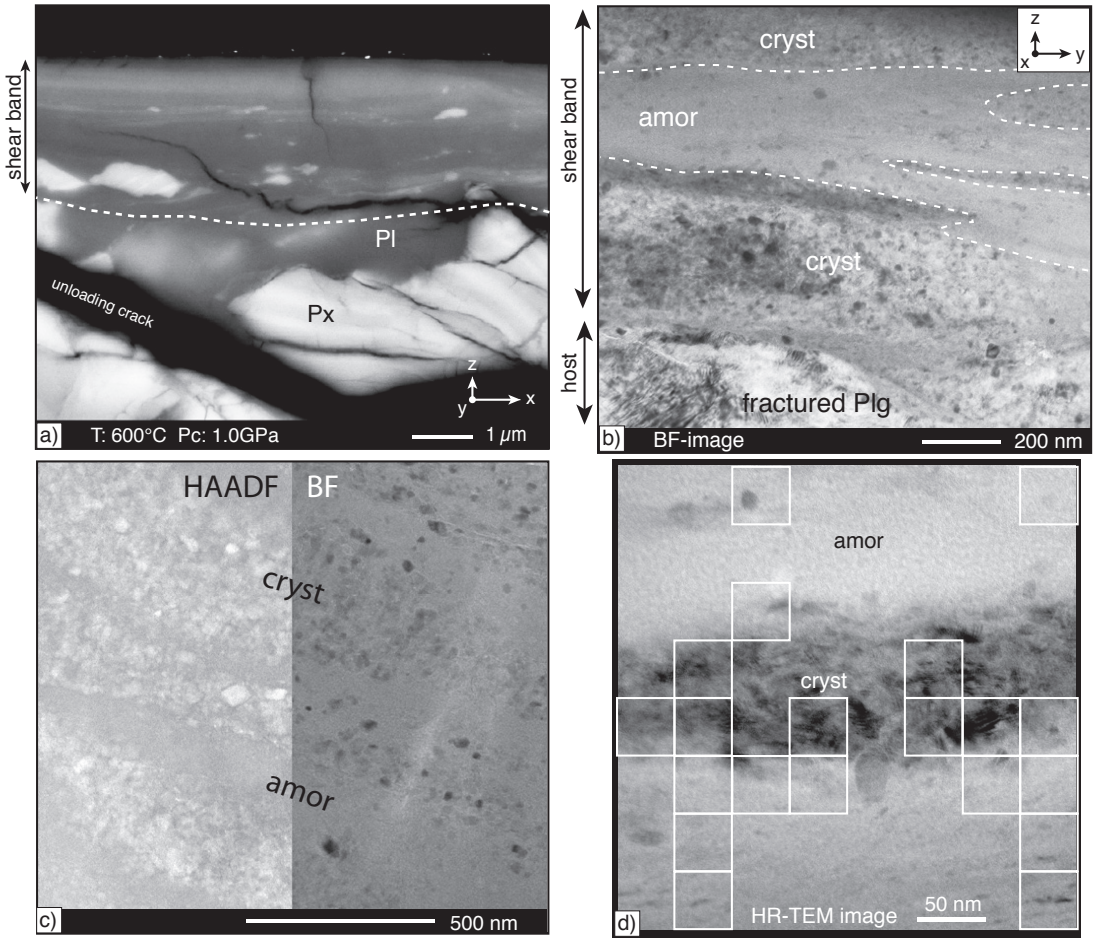

Figure 3.6: *Micro- to nanostructures of shear bands developed at 600 °C. a) SEM BSE image of a shear band formed in the sample near interface with the forcing block; shear sense is dextral. b) - d) TEM images of a shear band similar to the one shown in a). Kinematic reference frame for images b) - d) is given in upper right corner in b). b) BF TEM image. Increasing grain size refinement from top to lower half of the image; cryst = crystalline; amor = amorphous. Note few remaining crystals (darker) within amorphous layers. c) HAADF (left) and BF TEM image (right) of nano-crystals mainly formed by Px; amorphous layers correlate with the typical darker grey-value of Pl. d) High-resolution BF image from a central part of the shear band; nano-crystalline layer enclosed between amorphous domains. White squares denote areas where diffraction spots are detected in FFT analyses (see Methods); locally, amorphous layers contain nano-crystals, identified both from diffraction spots in FFT images and from their dark appearance in the BF image.*

3.3.2.3 Shear bands formed in intermediate T experiments

3.7 presents microstructures from shear bands developed at 700°C, 1.0GPa Pc. At these 700 °C and Pc of 1.0 and 1.5 GPa conditions, shear bands are fully crystalline and mainly composed of fine-grained Pl and Amph (Figure 3.7c). Pl grain sizes are on the order of $\sim$ 0.10 - 0.20 μm in diameter (Figure 3.7b, 3.10). Figure 3.7e shows the result of TEM EDS analysis over an area containing a small Pl porphyroclast surrounded by fine-grained Pl in the shear band. Plotting element count densities of Si, Ca and Al along a profile from the porphyroclast into the fine-grained matrix shows slightly higher Al and Ca contents and lower Si content in the porphyroclast compared to the Pl within the shear band. The differences are small but the coupled Al+Ca decrease with a Si increase from the clast to the shear band is consistent with a change towards lower anorthite component in the matrix Pl of the shear band.

3.3.2.4 Shear bands formed in high T experiments

Shear bands in samples deformed at 800 °C (Pc = 1.0 and 1.5 GPa) are fully crystalline. HAADF TEM and BF-STEM (STEM=scanning TEM) images at low magnification of a whole FIB-foil (Figure 3.8) show the typical shear band microstructure at these conditions. Fine-grained Pl is interlayered with Amph (+Qz) aggregates and a close-up on the Pl grains shows 'diamond shaped', largely defect-free grains with a weak shape preferred orientation (Figure 3.8b; 3.9). The mean axial ratio of grains is b/a = 0.64 and the grain size is $\sim$ 0.15 - 0.50 μm (Figure 3.10). Porosity along grain boundaries is almost absent and grain boundaries are tight (Figure 3.8b; 3.9a). Pl grain boundaries are aligned and show a strong preferred orientation in two maxima $\sim$ 10 - 30° away from the shear plane in both directions (Figure 3.9). Aligned grain boundaries are frequently observed, where relatively straight grain boundaries can be traced continuous over several neighbouring grains (Figure 3.9c). The ODF of grain boundary segments is weakly anisotropic with a monoclinic shape towards the upper right-lower left, consistent with the global dextral sense of shear.

3.3.2.5 Grain size distribution of plagioclase in shear bands formed in intermediate to high T experiments

Figure 3.10 presents grain size distributions (GSD) measured from Pl grains within shear bands formed at 700 and 800 °C. Due to the small grain sizes in shear bands at 700 °C, it is difficult to distinguish individual grains. The best results were obtained from SE SEM images of broken surface as shown in Figure 3.7b. For the 800 °C experiments, grain

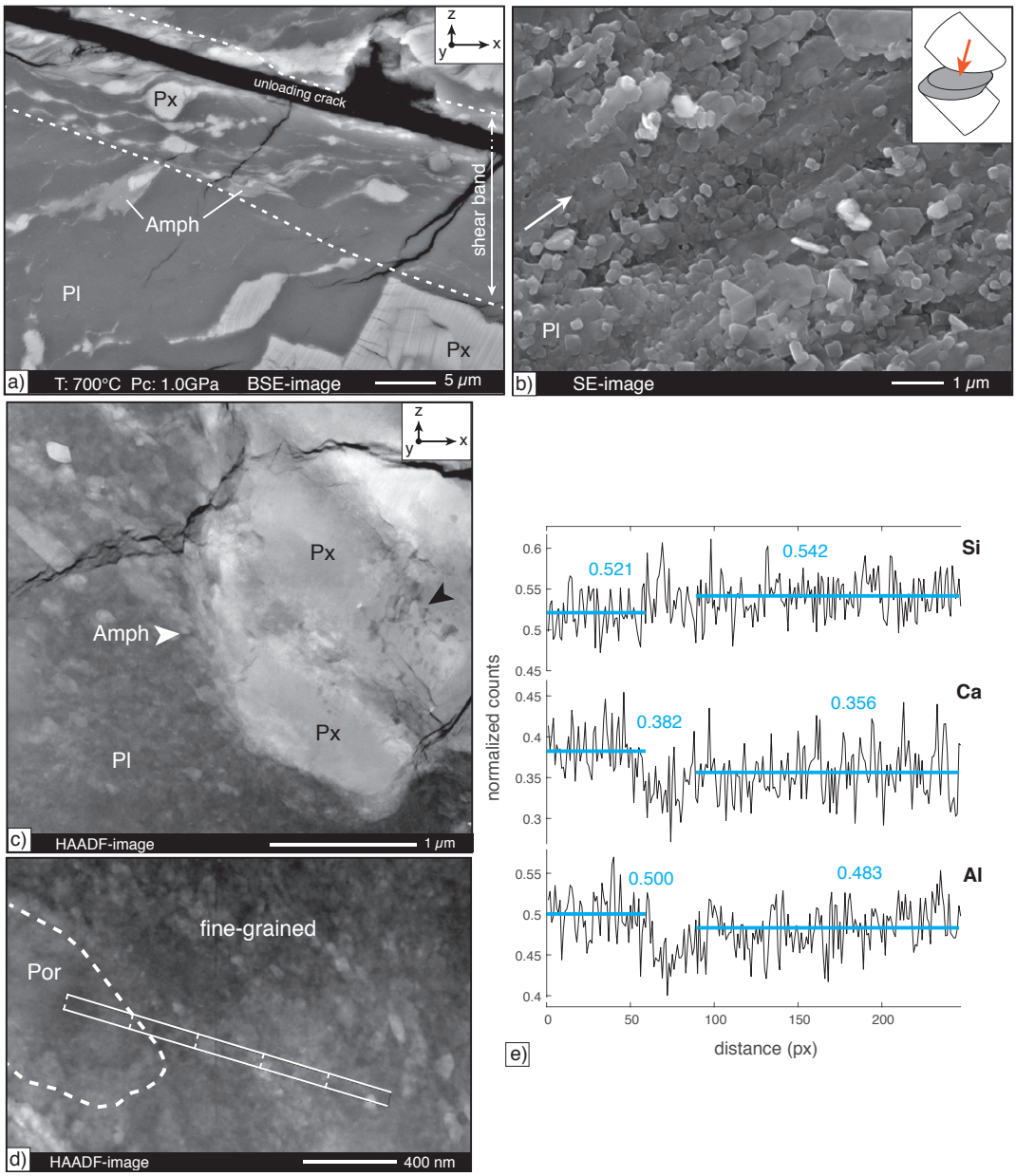

Figure 3.7: *Micro- to nanostructures of shear bands developed at 700 °C. a) SEM BSE image of a shear band. b) SEM SE SEM image of the surface of a shear band; mostly Pl grains are visible; white arrow indicates shear direction, with top to the upper right. c) HAADF TEM image showing a Px porphyroclast adjacent to a fine grained shear band formed by Pl + Amph; the Px porphyroclast shows a thin reaction corona of Amph; black arrow points to porosity within the Px clast. d) HAADF TEM image of a Pl porphyroclast with surrounding fine-grained Pl in a shear band; the trace of an EDX profile is marked. e) Element counts of Si, Ca and Al (normalized to max. count value of the respective element) versus distance (pixel) along the profile marked in d); mean values (blue) are indicated for the porphyroclast and the Pl of the shear band. Kinematic reference frame is the same as in d).*

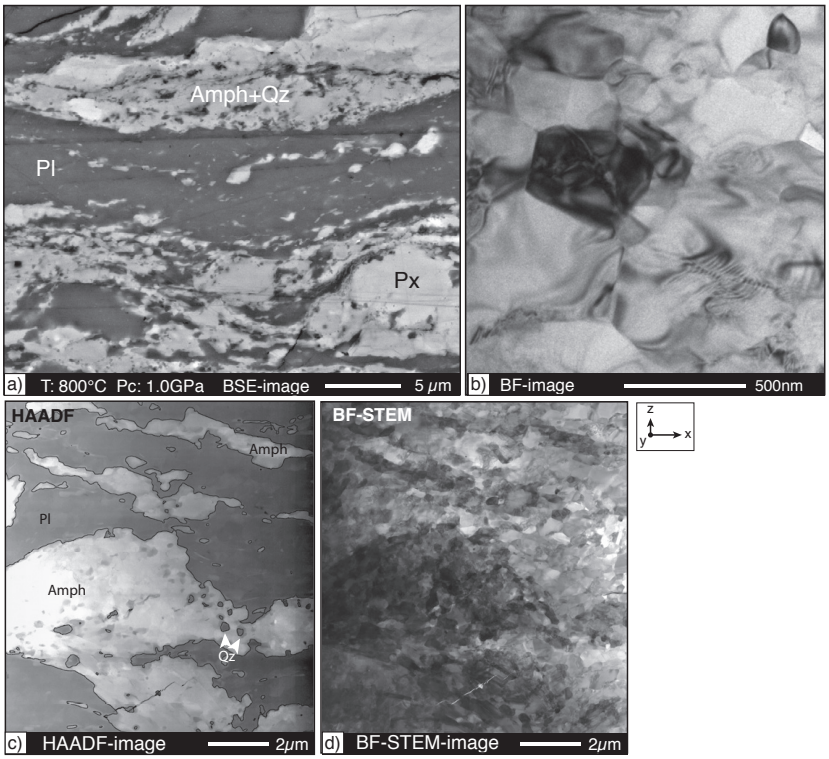

Figure 3.8: *Micro- to nanostructures of shear bands developed at 800 °C. a) SE BSE image of a shear band with typical compositional layering of Pl dominated layers alternating with Amph+Qz(+Pl) mixed layers. b) BF TEM image of Pl grains within a shear band; grains show a low defect density; porosity is low and grain boundaries are tight. c) HAADF TEM image showing the typical compositional layering of Pl dominated layers alternating with Amph+Qz aggregates. d) BF-STEM image of the same area as in c).*

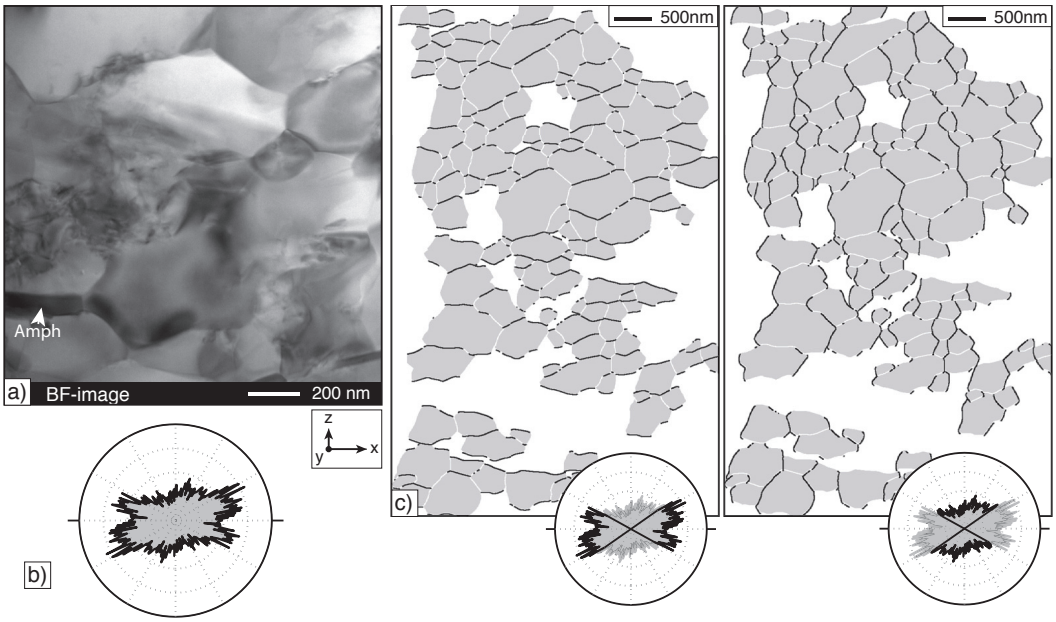

Figure 3.9: *Shape of plagioclase grains in shear bands at 800 °C. a) BF TEM image of diamond-shaped Pl grains with a weak shape preferred orientation. b) Rose diagram (surface ODF) of Pl grain boundaries preferentially oriented at ϕ = 10-30 °. The ODF shows a weak anisotropy consistent with the dextral sense of shear. c) Grain boundary segments are visualized separately for horizontal (-30 ° < ϕ < 30 °) and vertical (30 ° < ϕ < 150 °) orientations (marked black in rose diagrams).*

maps were produced from both TEM and SEM images. Size distributions obtained from TEM and SEM images are similar and the GSD presented in Figure 3.10b is measured on Pl grains from the TEM images shown in Figure 3.8. The GSD in Figure 3.10a is measured from grains segmented on SEM images of broken surfaces of a shear band top-view (Figure 3.7b), thus from an $\sim$ a quasi-3D view, whereas the GSD in Figure 3.10b is from the 2D section of grains measured from a FIB foil in the TEM. Consequently, the two GSD are not fully comparable but yield a semi-quantitative measure of the grain size differences in shear bands between 700 and 800 °C experiments. The size distribution developed at 700 °C is narrow and $>$ 80% of all grains are within 0.11 - 0.25 μm. The mode of the calculated kernel density estimate fit lies at 0.17 μm. The GSD at 800 °C is somewhat broader and $>$ 80% of all grains are within 0.15 - 0.50 μm with a mode of the kernel density estimate fit at 0.30 μm.

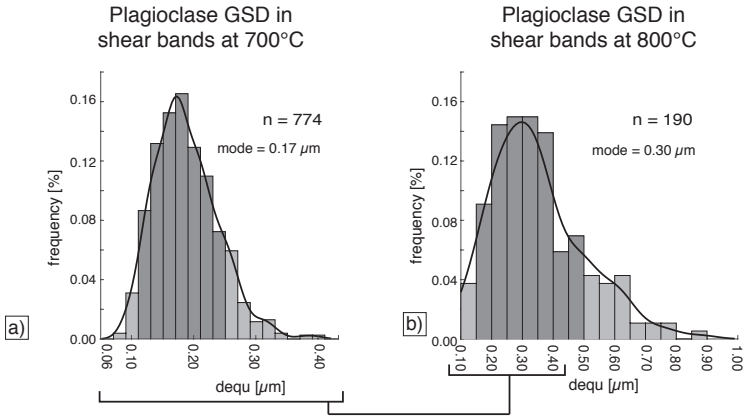

Figure 3.10: *Grain size distribution of plagioclase in shear bands. a) Sample 416 deformed at T = 700 °C, Pc = 1.0 GPa; area equivalent grain diameters, dequ, were determined from SE images as shown in Figure 9b. b) Sample 414 deformed at T = 800 °C, Pc = 1.0 GPa; area equivalent grain diameters, dequ, were determined from TEM images of the FIB-foil shown in Figure 10. Dark grey bars represent >80% of all grains; black line = kernel density estimate fit, number of grains, n, and mode of curve fit are indicated.*

3.3.2.6 Shear band evolution with strain in high T experiments

Figure 3.11 presents the evolution of shear bands in experiments at 800 °C and 1.0 GPa Pc, from peak stress ($\gamma_a \sim 0.7$) to increasing amounts of strain until a max of $\gamma_a \sim 6.8$. At peak stress, initial shear localization occurs mainly along favourably oriented grain- and phase boundaries. These initial zones are short ($\sim$ 100 - 200 μm), distributed (not interconnected) and make an angle of $\sim 27°$ with the load axis. From the microstructure it is apparent that these structures are often dilatant: minor melt segregations,

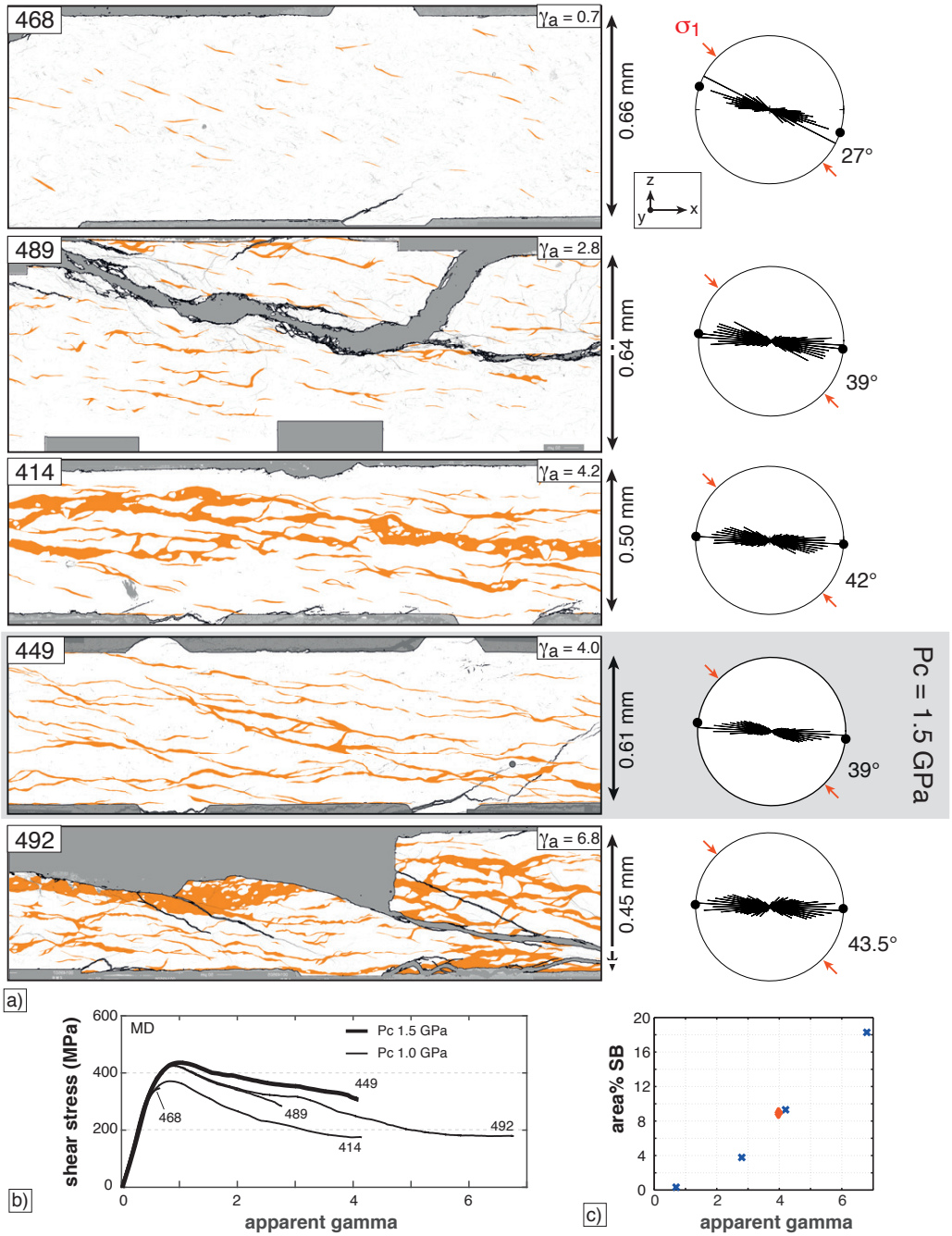

Figure 3.11: *Evolution of shear bands with increasing strain. a) Central parts of shear zones deformed at T = 800 °C and Pc = 1.0 GPa to increasing apparent shear strains; sample 449 (Pc = 1.5G Pa) is included for comparison. Shear bands are shown in orange; rose diagrams with surface ODF of shear band boundary segments on right. b) Stress - strain curves for samples shown in a). c) Increase of area fraction of shear bands with increasing shear strain; sample 449 is marked in orange.*

microfracturing and nucleation of new grains/phases such as Amph and Pl are observed (Figure 3.12). With increasing strain, the initial shear bands start to connect by the

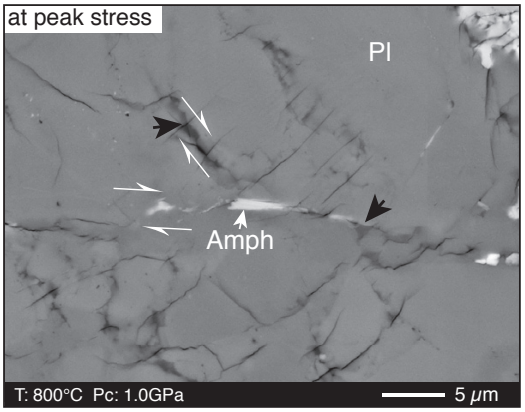

Figure 3.12: *Zones of initial shear localization. BSE SEM image of sample 460 deformed at T = 800 °C, Pc = 1.0 GPa. Black arrows point to minute segregation of melt; nucleation of new Amph (white arrow) and Pl grains is observed.*

formation of interconnected zones of fine-grained material. These zones make a smaller angle to the shear zone boundaries (or $\sim 39°$ with respect to the load axis) and have a width of $\sim$ 10 - 20 μm. At a shear strain of $\gamma_a \sim 4$, a network of anastomosing shear bands has formed, with $\sim 3°$ with respect to the shear zone boundaries (i.e. 42° to the load axis). The main shear band strand has a thickness of 50 - 150 μm. This microstructure coincides with the attainment of a quasi-steady state in the mechanical data (Figure 3.11a, b). With increasing strain, the vol.-% of shear bands increases (Figure 3.11c). Irrespective, sample strength varies only slightly between $\gamma_a \sim 4$ to 6.8 despite the significant increase in vol.-% of shear bands (Figure 3.11b, c). At $\gamma_a \sim 4$ in samples deformed at Pc = 1.5 GPa, shear bands are thinner and have a somewhat smaller angle towards the load axis than at Pc = 1.0 GPa. The shear band vol.-%, however, is the same at both Pc (Figure 3.11c).

3.3.2.7 Shear band orientation from peak stress to higher strains

3.13 shows the difference of shear band orientation at peak stress ($\sim$ coinciding with initiation of localization) and at higher strains (where stresses stay relatively constant), as a function of temperature. Initial shear bands at all temperatures show the same preferred orientation, with 27° towards the load axis. This orientation stays relatively constant at $\sim 30°$ in 600 °C experiment, but angles increase to 33° in the case of the 700 °C experiments, and to 42° for the 800 °C experiments.

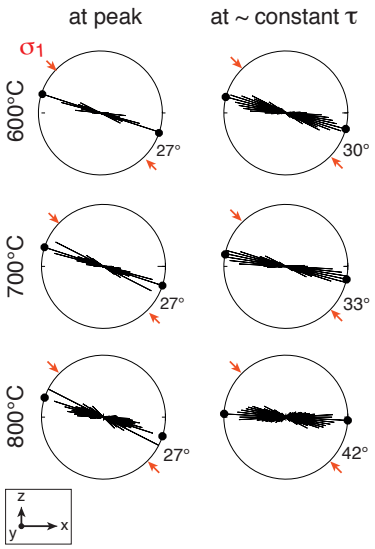

Figure 3.13: *Orientation of shear bands at peak stress and high strain. Comparison of shear band orientation formed at peak stress (left) and at higher strains at quasi steady state. Rose diagrams are surface ODFs of shear zone boundary segments.*

3.4 Discussion

3.4.1 Deformation mechanisms

3.4.1.1 low T experiments

At 600°C, both mechanical data and microstructures are characteristic for brittle deformation. The mechanical data shows a clear dependence of sample strength on Pc, with higher strengths at higher Pc (Figure 3.1a, b) and high stress exponent values (Figure 3.2) are consistent with brittle deformation and frictional sliding during cataclastic flow, as it is observed from the microstructure (Figure 3.3b). Some limited solution-mass transport is indicated by the presence of pore trails along healed fractures in 600°C experiments (Figure 3.3c) and is possibly (subordinately) contributing to strain accommodation.

Displacement in 600 °C experiments is localized in a network of shear fractures and fine-grained shear bands (Figure 3.3a, b; 3.5), some of which contain amorphous material (Figure 3.6). The angles of shear bands and shear fractures to the load axis (∼27° - 30°, Figure 3.13) are in accordance with brittle Riedel (R1) structures.
The area-% of shear bands in the thin section is about 1 - 2%. As an upper-bound estimate, if all displacement were to be accommodated by the shear bands, the strain rate $\dot{\gamma}$ within them would be on the order of

$$\dot{\gamma} = 1 \cdot 10^{-5} mms^{-1} / (0.64mm \cdot 0.02) \simeq 8 \cdot 10^{-4} s^{-1} \tag{3.1}$$

which is the induced displacement rate divided by 2% of the approximate shear zone

thickness. Although the strain rate within the shear bands is likely to be high, it stays well below seismic rates.

Partly amorphous shear bands as we observe them during aseismic brittle faulting have previously been described (Yund et al., 1990; Goldsby and Tullis, 2002; Janssen et al., 2010; Pec et al., 2012b, 2016, e.g.). TEM analyses of shear bands formed in our experiments show that they consist of amorphous material, with layers and lenses of nanocrystalline material (Figure 3.6). A clear material difference is seen between Pl and Px, where Pl preferentially becomes amorphous and Px remains largely crystalline, with very small sizes ($<$ 50 nm, Figure 3.6c). This is similar to the results of Pec et al. (2012b, 2016) or Yund et al. (1990): In their granitoid sample material amorphous shear bands form extensively within the feldspatic material.

The boundaries between shear bands and host rock in our samples are sharp, even on the nano-scale (Figure 3.6b). It appears from the microstructure that crystalline material is comminuted to a certain grain size ($<$ 50 nm) and below that, amorphization (mainly of the Pl) is effective. Consequently, grains smaller than this threshold are scarcely preserved in the microstructure. Pec et al. (2012b, 2016) discuss different possible formation mechanism for their amorphous material and conclude that the most likely mechanism is a type of mechanical amorphization, i.e. high defect densities until crystallinity is lost. Feldspars appear to be particularly susceptible to this process, as also supported by this study. The rheology of these (partly-)amorphous shear bands, however remains yet unclear.

3.4.1.2 High T experiments

At 800 °C, there is a significant difference in rheology compared with lower T experiments: differential stresses at 800 °C are half as high as at 700 °C and stay always below the Goetze criterion (Table 3.1; Figure 3.1a). Initial stress increase during sample loading (before peak stress) shows lower slopes at 800 °C compared to the lower T experiments (Figure 3.1a). This lower slope indicates a higher component of viscous deformation early on in the experiment.

The microstructure at 800 °C is dominated by mineral reactions and strong grain size refinement by nucleation (Figure 3.3f, g; 3.8). The grain size within shear bands ranges mainly between 0.15 - 0.50 μm for Pl (Figure 3.10b), with similar sizes for Amph and Zo. The small grain sizes facilitate a grain size sensitive creep mechanism, where the strain rate is proportional to d^{-m} (e.g. Ashby and Verrall, 1973; Coble, 1963; Rutter, 1976), where d is the grain size and m the grain size exponent. Diffusion creep and grain boundary sliding (GBS) are known to only leave few microstructural traces of their ac-

tivity. However, aligned grain boundaries, equant to weakly anisotropic grain shapes, and low internal defect densities of grains are microstructures characteristic of GBS and diffusion creep (e.g. Elliott, 1973; Boullier and Geugen, 1975; Gifkins, 1976; Drury and Humphreys, 1988; Kilian et al., 2011; Drury et al., 2011). The shear bands consist of small, elongated hexagonal grains, whose grain boundaries do not only have a similar orientation but can also be contiguous over several grain diameters (Figure 3.9). These contiguous grain boundaries are well orientated for sliding in all orientations. Grains in the shear bands are often defect free and with a low to medium shape anisotropy. These microstructures are consistent with diffusion creep and GBS. As the experiments are performed with H2O present, dissolution-precipitation creep is interpreted to be the dominant form of diffusion creep. The activation of solution-mass transport processes is indicated by the vast amount of reaction products formed. Dissolution-precipitation creep as a dominant deformation mechanism is in accordance with the low observed stress exponents of $n \sim 1.9$. Usually, stress exponents for diffusion creep are expected to be close or equal to 1 (e.g. Ashby and Verrall, 1973; Coble, 1963; Rutter, 1976; Karato, 2008; Paterson, 2013; Kohlstedt and Hansen, 2015), but higher n values have been suggested for dissolution-precipitation creep, depending on the driving potentials or chemical potential gradients along the grain contact area (e.g. Gratier et al., 2009, 2013). In addition, some frictional processes may be active (although not dominant) during 800 °C experiments, contributing to an increase of the stress exponent to values above = 1.
Diffusion creep as viscous deformation mechanism has previously been suggested for experimentally deformed basaltic material (under water added conditions) by e.g. Rutter et al. (1985); Getsinger and Hirth (2014), whereas Rutter et al. (1985) state more in detail, that they interpret dissolution-precipitation creep together with GBS to be the dominant deformation mechanism.

3.4.1.3 Intermediate temperature experiments

At 700 °C, sample strength as seen from the stress-strain curves are comparable to the 600 °C experiments (Figure 3.1a). However, the stress sensitivity on strain rate (1/n) is significantly higher ($n = 5.6$ at 700 °C, $n > 19$ at T < 600 °C; Figure 3.2a). The stress exponent of 5.6 is just slightly higher than what would be typical for dislocation creep ($n = 3$ to 5; Karato (2008); Paterson (2013); Kohlstedt and Hansen (2015)), but none of the microstructures indicate evidence for extensive crystal plasticity. Therefore, the intermediate n-values are interpreted as a combination of frictional (high n-values of 19.5 and higher) and viscous process ($n \sim 1.9$), marking a transition between frictional and viscous deformation at 700°C.

Although microfracturing and cataclastic flow are contributing to accommodate displacement within low strain lenses at 700 °C (Figure 3.3d; 3.4), strain is localized in an anastomosing network of shear bands with a microstructure similar to that formed in shear bands at 800 °C, where shear bands are formed by a fine-grained mixture of the reaction products Pl and Amph (Figure 3.3e; 3.7a - c). The GSD of Pl grains within these shear bands is narrow (Figure 3.10a) and grain shapes are equidimensional (Figure 3.7b), indicating neocrystallized grains. Fracturing is subordinate within shear bands. Fracturing and cataclasis are expected to produce a wide range of grain sizes with angular grain shapes (e.g. Stel, 1981; Storti et al., 2003; Keulen et al., 2007), unlike the observed microstructure. TEM-EDS mapping also reveals a small, but consistent compositional difference between Pl porphyroclast and fine-grained shear band Pl (Figure 3.7), which is further evidence that the plagioclase grains within the shear bands are not a result of fracturing but rather result from nucleation of grains with a different (more albitic) composition.

As the microstructure of shear bands in experiments at 700 and 800°C are comparable, dissolution-precipitation creep + GBS are interpreted to be the dominating deformation mechanisms in shear bands at both temperatures. The measured change in Pl chemistry between porphyroclasts and fine-grained shear band Pl excludes subgrain rotation recrystallization and instead points to nucleation as means of grain size reduction. However, a brittle precursor to the shear bands at 700 °C is possible, interpreted from the initiation of shear bands with the same low angle towards the load axis as in the brittle dominated 600 °C experiments (Figure 3.13), as well as by the similar sample strengths for 600 and 700 °C experiments. Due to the low strains at shear band initiation ($\sim$ at peak stress) it is, however, difficult to identify from the microstructure if and in which proportions viscous or brittle processes contribute at the point of initiation of strain localization.

3.4.1.4 Summary of deformation mechanisms

The dominance of viscous deformation at 800 °C, and of brittle deformation at 600 °C is evident, both from the mechanical data and the microstructure. Samples deformed at 700 °C are an intermediate case, where strain is localized into shear bands which are interpreted to deform with a viscous deformation mechanism but with stress-strain curves and strengths more like the brittle-dominated 600 °C samples (Figure 3a). Shear bands formed in 700 °C experiments, like the shear bands at 800 °C, are interpreted to accommodate strain mainly by dissolution-precipitation creep and GBS. However, low strain lenses at 700 °C show abundant microfracturing and a contribution of cataclastic flow to deformation. The stress exponent is considerably lower at 700 °C than for lower

T experiments (Figure 3.2a), indicating an increased viscous component to the rheology at 700 °C. The stress exponent of $n = 5.6$ for 700 °C experiments is interpreted to as a mixed mechanical response from determined by the rheology of viscously deforming shear bands and partly frictional/cataclastic low strain lenses.
The transition from dominantly brittle deformation to dominantly viscous flow in our experiments is seen to initiate with the dominance of solution-mass transport. Mineral reactions and nucleation lead to intense grain size reduction and thus strongly enhance the strain rate of grain size sensitive creep mechanisms. For our imposed experimental displacement rates, the transition occurs around 700 °C (although not fully Pc insensitive). In deformation experiments on whole-rock cores of Maryland Diabase at conditions similar to ours, Kronenberg and Shelton (1980) observed a brittle-viscous transition in their samples around 700 °C for a Pc = 1.0 GPa, comparable to our observations. However their strain rate was approximately one order of magnitude lower.
In our experiments, the influence of Pc is less pronounced compared to that of the temperature. Increasing the Pc at, e.g., 600 °C does not lead to a transition to more viscous behaviour. At 700 and 800 °C, the main effect of increasing the Pc is the formation of a higher abundance of reaction products. This indicates a rate-enhancing effect of increasing Pc on solution-mass transport processes and/or reaction kinetics, e.g., by a greater overstepping of reaction boundaries for pressure sensitive reactions.

3.4.2 Microstructural evolution and its influence on bulk rheology

3.4.2.1 Shear band evolution

As seen from 800 °C experiments, shear bands are widening and increase in volume percent with increasing strain (Figure 3.11). Shear band widening takes place by the on-going process of mineral reactions and nucleation, leading to the replacement of old, coarser-grained porphyroclasts by new, sub-micron sized grains. Shear band volume percentage stays relatively low in 700 °C experiments for the strains achieved, and interconnectivity is much lower than at 800°C (e.g. Figure 3.5). From the mechanical data it is seen that 700 °C experiments still show a large influence of brittle deformation, which is attributed to the low volume percentage, unfavourable orientation (not parallel to shear zone boundary but inclined against it with $\sim 7°$), and poor interconnectivity of shear bands. With increasing shear band widening, the viscous rheology of the shear bands at 700 °C is expected to eventually become more dominant.
As reaction and diffusion rates are lower at lower T, more time (or equivalently strain)

is needed in the case of the 700 °C experiment to attain a connected network of shear bands as it is observed at 800 °C. However, the positive feedback between fracturing and reaction kinetics (as seen from extensive mineral reactions along microfractures in 700 °C experiments, Figure 3.4) aids the microstructural change, i.e. grain size reduction by reaction and nucleation, and appears to be an important mechanism in switching from dominant brittle to more viscous rheology.
Comparing the orientations of shear bands formed at different T (Figure 3.5) it is apparent that the orientations are less favourable for bulk shear displacement in 600 and 700 °C compared to 800 °C experiments, due to the higher inclination of shear bands to the shear zone boundaries. Thus, shear band orientation is an additional factor determining how the weak phase controls the rheology (cf. Gerbi et al., 2016).

3.4.2.2 Shear band influence on bulk rheology in high-T experiments - estimating flow stresses in shear bands from plagioclase diffusion creep flow law

The shear band evolution in 800 °C experiments shows an increasing dominance in shear band orientations (sub-)parallel to the shear zone boundaries (Figure 3.11) with increasing shear band widening and interconnection. That is, the shear band network evolves into geometrically more favourable orientations. Sample strengths, however, remain relatively high, with shear stress values of $\tau > 190$ MPa (Table 3.1; Figure 3.1a). Additionally, a quasi-steady state in the stress-strain curves at $\gamma_a \geq 4$ is reached, disregarding a still increasing shear band vol.-%. These observations suggest that the bulk sample rheology is not simply determined by the rheology of the shear bands.
For our experimental samples, the imposed displacement rate, temperature and the grain size within shear bands are known. At 800°C, where dissolution precipitation creep is interpreted to dominate the deformation, we can attempt to calculate expected stresses within the shear bands for the given conditions. The rate of dissolution-precipitation creep depends on the following parameters (e.g. Paterson, 2013):

$$\dot{\varepsilon} = A \cdot \frac{D\ \omega\ c\ \nu_s\ \Delta\sigma^n}{R\ T\ d^m} \tag{3.1}$$

with A : constant, D : diffusion coefficient, ω : mean thickness of the intergranular fluid film, c : molar concentration, ν_s : molar volume of the material in solution, $\Delta\sigma$: differential stress, n : stress exponent (usually ~ 1), d : grain size, m : grain size exponent, Q : activation energy, R : universal gas constant, T : temperature.

At present, however, the lack of e.g. mineral solubility data and properties of grain boundary fluid films does not allow to calculate the dissolution-precipitation creep strain rates using Eq. (3.1). In the presence of the feldspar-dominated shear bands of our samples, we use a simplified approach to estimate the shear band rheology by using the flow law of Rybacki and Dresen (2000) for diffusion creep in feldspars, as has been done previously by e.g. Getsinger and Hirth (2014); Viegas et al. (2016). The flow law of Rybacki and Dresen (2000) has the form:

$$\dot{\varepsilon} = A \cdot \Delta\sigma^n \cdot d^{-m} \cdot exp(-\frac{Q}{RT}) \tag{3.2}$$

with A : constant, $\Delta\sigma$: differential stress, n : stress exponent, d : grain size, m : grain size exponent, Q : activation energy, R : universal gas constant, T : temperature.
Under the assumption that the shear bands accommodate the majority of the deformation, a shear strain rate of $\sim$ 1 x 10^{-4} s^{-1} is assumed for them. This is derived from the imposed displacement rate, $\sim$ 1 x 10^{-5} mm s^{-1} divided by the cumulative shear band thickness, $\sim$ 8 x 10^{-2} mm (which is 10 - 20% of the total sample thickness at quasi-steady state in the mechanical data, e.g. Figure 3.11). Using the Rybacki and Dresen (2000) flow law for diffusion creep in a wet plagioclase aggregate, we use a strain rate of 1 x 10textsuperscript-4 s^{-1}, a grain size range of 0.15 - 0.50 μm and T = 800 °C. To compare our shear strain rates to the axial shortening strain rates of the flow law, we use the conversion from axial shortening to simple shear strain rates after Schmid et al. (1987). Eq. (3.2) is thus reformulated to :

$$\dot{\gamma} = A \cdot \sqrt{3}^{(n+1)} \cdot \tau^n \cdot d^{-m} \cdot exp(-\frac{Q}{RT}) \tag{3.3}$$

$\dot{\gamma}$: shear strain rate, A: constant, n: stress exponent, τ: shear stress, d: grain size, m: grain size exponent, Q: activation energy, R: universal gas constant, T: temperature.

Solving equation (3.3) for shear stresses, they are calculated as:

$$\tau = exp\left(log(\frac{\dot{\gamma}}{A \cdot \sqrt{3}^{(n+1)} \cdot d^{-m}}) - (\frac{-Q}{R \cdot T})\right) \tag{3.4}$$

Resulting shear stresses are between 0.4 - 16 MPa. That is one to almost three orders of magnitude lower than measured in the mechanical data. Or conversely, if Eq. (3.3) would be used to calculate the strain rate for the given T and d, with τ = 200 MPa, strain rates of 1 x 10^{-3} to 5 x 10^{-2} s^{-1} would be predicted).
Our experimental samples contain significantly higher wt.-% of H_20 compared to the

samples of Rybacki and Dresen (2000), which is likely to have a marked effect on the rate of dissolution-precipitation creep. Despite some uncertainties in the application of the Rybacki and Dresen (2000) flow law the results are expected to yield values within the expected order of magnitude for dissolution-precipitation creep. The calculated stresses for the shear bands thus suggest that the elevated bulk sample strengths of $\tau \approx 200$ MPa at the given bulk strain rate of 10^{-5} s^{-1} cannot be explained by representing the fine-grained material within shear bands. Rather, an effect by a load-bearing framework of low strain lenses due to insufficient connectivity and unfavourable orientation of shear bands is suggested to explain the observed bulk sample strengths in the 800 °C experiments. Bulk sample strength is interpreted to be determined by the combined rate of dissolution-precipitation creep and GBS in the coarse-grained low strain lenses and the fine-grained shear bands. The onset of dissolution-precipitation creep does not depend on the occurrence of shear bands but because diffusion lengths are proportional to the grain size, the rate of strain accommodation by dissolution-precipitation creep will vary strongly between fine grained shear bands compared to low strain lenses which largely preserve the coarse initial grain sizes. Delocalized viscous processes relaxing some of the imposed stress, prior to shear band formation is also indicated by the low initial slope of the loading curve in the mechanical data (Figure 3.1a), which indicates a more viscous component of sample deformation from the very start of the experiment and dissolution-precipitation creep is speculated to cause this viscous relaxation.

3.4.2.3 The influence of strain on reaction rate as seen from the microstructures

At 700 °C, fractures in Px porphyroclasts are extensively decorated by Amph overgrowths (3.4), where Amph is forming by the reaction:

$$Px + Pl + H_20 \longrightarrow Amph + Qz \tag{3.5}$$

Amph is seen to grow along Px-internal fractures with no phase boundary towards Pl, indicating that element transport along the fractures occurred over several μm. It is described in the literature that fracturing can lead to high dislocation densities in the host crystal and is frequently associated with porosity (Fitz Gerald et al., 1991; Fitz Gerald and Stünitz, 1993; de Ronde et al., 2005). Fitz Gerald and Stünitz (1993) interpret from their observations that permeability along the microfractures must have been greatly enhanced, allowing for solution mass transport and mineral reactions along the fracture. Also from our observations, there is a clear positive feedback between deformation and

reaction. This seems especially important in the 700 °C experiments, where the positive contribution of deformation on reaction rate is seen more strongly in the microstructure compared to 800 °C experiments. This is not unexpected, as reaction and diffusion rates will increase with increasing temperature and the rate-enhancing effects of deformation on reaction and diffusion may become subordinate.

3.4.3 Sample strength in the brittle field at mid-crustal conditions

The brittle dominated 600 °C experiments just about reach the Byerlee (1978) relationship for frictional sliding at peak stress (Figure 3.1b). The differential peak stress reached in our experiments represents the stress needed for the initiation of shear localization under the imposed constant displacement boundary condition. With on-going deformation, shear bands and shear fractures develop, coinciding with sample weakening and resulting stresses below the Byerlee (1978) relationship. Nonetheless, high differential stresses are retained during semi-brittle deformation of the bulk sample. It is expected that with higher strains, the shear bands eventually interconnect in a more favourable orientation for shear and sample strength will be reduced further.
Extrapolation of the Byerlee (1978) relationship to mid-crustal conditions, as it is frequently done for the construction of stress envelopes to model strengths of lithospheric fault/shear zones (at steady state), will overestimate rock strengths as concluded from our findings. However, for non-steady state cases, e.g. during increased strain rate events or for the case of an initiating fault zone, the Byerlee (1978) relationship may be reached for short temporal scales as deep as mid-crustal levels.

3.5 Summary and conclusions

At the imposed experimental displacement rates, a transition from dominantly brittle to brittle-viscous to dominantly viscous is observed between the temperatures 600, 700 and 800 °C. The brittle-viscous transition in our study is observed to occur via a switch from fracturing to diffusion creep (in the sense of dissolution-precipitation creep) and grain boundary sliding as dominant viscous deformation mechanisms.
Viscous deformation in our experiments starts with the onset of diffusive mass transport and starts to dominate the rheology when fine-grained, interconnected zones have formed.
The important processes enabling viscous rheology are 1) efficient solution-mass trans-

port, 2) grain size refinement, which in our case as a result of reaction and nucleation, and 3) shear band interconnection.

We observe a brittle-viscous transition not only as a result of increasing temperatures but also via a microstructural evolution. Especially as the brittle-viscous transition is approached in terms of temperature (in our case at 700 °C), more evolved microstructure in shear bands allows for viscous deformation, whereas low strain lenses still show largely brittle deformation. This leads to a likely transient, mixed mechanical response of brittle and viscous rheology. For constant syn-kinematic conditions (i.e. strain rate, P and T, fluid availability, etc.) the syn-kinematic microstructural evolution with strain (and time) is expected to change the relative importance of brittle and viscous deformation in favour of the viscous processes.

Chapter 4

The viscous field

Published as: ***Marti, S.*** *, Stünitz, H., Heilbronner, R., Plümper, O., and Kilian, R., (2018). Syn-kinematic hydration reactions, grain size reduction and dissolution-precipitation creep in experimentally deformed plagioclase - pyroxene mixtures. Solid Earth, 9, 985-1009*

Abstract:

This chapter focuses on the deformation of a polyphase mafic rock, deforming in the dominant viscous field. Mechanical data and microstructures are presented from experiments on 'wet' plagioclase-pyroxene mixtures at temperatures of 800 °C and confining pressures of $\sim$ 1.0 and 1.5 GPa. The susceptibility of mafic rocks to mineral reactions in the presence of a hydrous fluid allows to incorporate the interplay between reaction and deformation in the experiments. Syn-kinematic mineral reactions lead to grain size reduction and phase mixing by heterogeneous nucleation. Strain is localised into a network of shear bands, formed by mainly fine-grained (< 1 μm) plagioclase and the new reaction product amphibole. Dissolution-precipitation creep accompanied by grain boundary sliding are interpreted to be the dominant deformation mechanism, likely for both, plagioclase and amphibole. Comparing our experimental samples to a naturally deformed hornblende pegmatite, it will be discussed how the experiments compare to the natural sample and under which conditions extrapolation to nature is likely feasible.

4.1 Introduction

Viscous deformation of crustal rocks is dominated by either the intra-crystalline deformation mechanisms dislocation glide and creep, or a grain size sensitive creep such as grain boundary sliding and diffusion creep. Apart from being rate and temperature sensitive, the rheology of viscous deformation is observed to be strongly material dependent (for a comprehensive list of flow law parameters for different rock types see e.g. Kohlstedt et al. (1995); Shaocheng and Bin (2002); Bürgmann and Dresen (2008); Burov (2011) and references therein). Derived from rock deformation experiments, flow laws for viscous creep exist for different types of rocks, where the majority of these flow laws are determined for monomineralic materials. Viscous deformation in monomineralic aggregates at mid- to lower crustal conditions is often described as being dominated by dislocation creep. Although differential stresses are expected to be low and therefore in favour of diffusion creep, grain growth in monomineralic aggregates at the elevated T of the mid- to lower crust is extensive and the large grain size is expected to render diffusion creep less efficient than dislocation creep.

A relatively comprehensive dataset exists for high-temperature experimental deformation of monomineralic polycrystalline plagioclase (e.g. Tullis and Yund, 1985; Shaocheng and Mainprice, 1987; Tullis and Yund, 1991; Dimanov et al., 1999; Rybacki and Dresen, 2000; Stünitz and Tullis, 2001; Stünitz et al., 2003; Ji et al., 2004; Barreiro et al., 2007) and pyroxene (e.g. Lallemant, 1978; Kolle and Blacic, 1982; Raterron and Jaoul, 1991; Mauler et al., 2000; Bystricky and Mackwell, 2001; Hier-Majumder et al., 2005; Chen et al., 2006; Zhang et al., 2006) and flow law parameters are described for dislocation creep and diffusion creep (e.g. Dimanov et al., 1999; Rybacki and Dresen, 2000; Rybacki et al., 2006; Bystricky and Mackwell, 2001). For polyphase mixtures of $\sim$ gabbroic composition, data on high-temperature deformation experiments is published by Dimanov et al. (2003); Dimanov and Dresen (2005); Dimanov et al. (2007). Depending on the grain size, the differential stress and the volume fraction of pyroxene (as the stronger phase in their pyroxene-plagioclase mixtures), the dominant deformation mechanism described by the author is either diffusion creep or dislocation creep. No mineral reactions were observed in these experiments. The strain rate of the two-phase aggregates is suggested to be a composite between the strain rates of the individual phases (e.g. Dimanov et al., 2003).

In somewhat lower-T experiments and under hydrous conditions, Rutter et al. (1985); Getsinger and Hirth (2014) and Stünitz and Tullis (2001) performed deformation experiments with syn-kinematic hydration reactions. Phase mixing thereby occurs (partly)

due to heterogeneous nucleation. The authors of these studies suggest grain size sensitive creep by a mix of diffusion creep and grain boundary sliding to be the dominant deformation mechanism. Rutter et al. (1985) thereby state more in detail, that they interpret diffusion creep in the sense of dissolution-precipitation creep.
Several processes are known to act in polymineralic mixtures that take influence the deformability and the dominating deformation mechanism. The occurrence of mineral reactions and nucleation entail grain size reduction (e.g. Brodie and Rutter, 1987; Fitz Gerald and Stünitz, 1993; Newman et al., 1999; de Ronde et al., 2005), grain pinning due to secondary phases will impede grain growth (e.g. Olgaard and Evans, 1986; Berger and Herwegh, 2004; Linckens et al., 2011), and diffusion is expected to be faster along phase boundaries compared to grain boundaries (e.g. Hickman and Evans, 1991; Wheeler, 1992; Sundberg and Cooper, 2008). Factors, which will enhance diffusion creep rates and can thus possibly lead to a switch in dominant deformation mechanism from dislocation creep in monomineralic layers, to diffusion creep in polymineralic layers (Etheridge and Wilkie, 1979; Mehl and Hirth, 2008; Linckens et al., 2011; Kilian et al., 2011).
Despite facing the difficulties of an increasingly complex system when performing experiments on polyphase aggregates, focusing only on monomineralic materials potentially leads to a biased view, overrating the importance of processes typical for the deformation of monomineralic aggregates. The observation that high strain zones such as ultramylonites are usually formed by a phase mixture, shows their ability to deform at higher strain rates (or equivalently, lower stresses) than monomineralic aggregates and emphasises their importance to rock deformation.

4.2 Methods

4.2.1 Sample Material

Experiments presented in this chapter were performed on the following starting materials:
(1) MD : Maryland Diabase powder, grain size fraction ≤ 125 μm.
(2) An60+En: Synthetic mixture of Sonora Labradorite (Pl(An_{60})) + Enstatiete (Damaping Enstatie) powder. Grain size fraction of $\sim 2 \leq x \leq 125$ μm, and 40 - 180 μm respectively.
(3) An60+Di(D): Synthetic mixture of Sonora Labradorite (Pl(An_{60})) + Damaping Diopside powder. Grain size fraction of $\sim 2 \leq x \leq 125$ μm, and ≤ 125 μm respectively.
(4) An60+Di(CrL): Synthetic mixture of Sonora Labradorite (Pl(An_{60})) + Cranberry

Lake Diopside powder. Grain size fraction of $\sim 2 \leq x \leq 125$ μm, and 40 - 125 μm respectively.
(5) Ab+En: Synthetic mixture of Alpe Rischuna albite + Enstatiete (Damaping Enstatie) powder. Grain size fraction of ≤ 125 μm, and 40 - 180 μm respectively.

To all samples, either 0.18 or 0.11 wt.-% H_2O was added. The procedure of sample preparation as well as phase composition and mineral chemistry of the different starting materials are described in section 2.1.3.1. All presented samples are deformed in the 45° pre-cut sample setup (see section 2.1.3).

4.2.2 Amphibole corona thickness determination

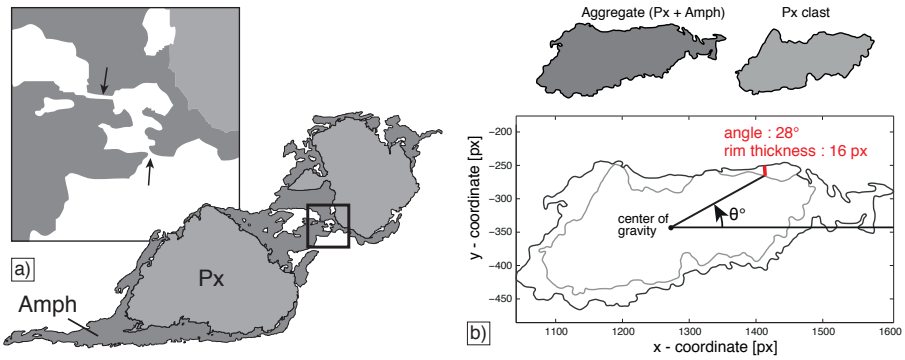

Figure 4.1: *Amphibole corona thickness analysis. a) Digital phase map of segmented Px clasts and associated Amph coronas. When adjacent Amph coronas are in contact, they have to be separated manually (Close-up, black arrows). b) Corona thickness is determined as the shortest distance from the aggregate (Px+Amph) outline to the Px clast outline. For each point along the clast boundary, the angle is determined CCW from the horizontal, with the clast center of gravity as rotation axis.*

In some experiments, Amph growth coronas on Px porpyhroclasts are observed and corona thicknesses were measured as a function of orientation around the clasts (Figure 4.1; Figure 4.12). To do so, Px and Amph phases were first segmented to derive digital phase maps. Where Amph coronas of neighbouring Px clasts are in contact, individual Px - Amph pairs had to be manually separated (Figure 4.1a). Clean phase maps contain segmented Px and Amph phases, and each Px grain is in contact to only its own Amph corona. x-y coordinates of the clast (Px) and the aggregate (Amph+Px) outlines are measured and exported using Fiji and a modified version of the *Jazy XY export* macro (by Rüdiger Kilian, available at https://earth.unibas.ch/micro/index.html). A MATLAB script was written which imports the x-y coordinates of clasts and aggregate outlines and determines corona thickness at each point along the Px clast as the shortest distance

between the clast to the aggregate outline (Figure 4.1b, Appendix D). This approach yields good results where coronas follow the clast shape, but tends to underestimate corona thickness where the corona becomes very elongated as e.g. in 'tails' around the clasts. The angle around the clast is determined counter clock wise (CCW) from the horizontal, with the clasts center of gravity as rotation axis.
For each experiment, the amount of thinning is approximately known (section 2.2.4). The total sample strain (assuming homogeneous deformation of the whole shear zone) is determined using the approach of Fossen and Tikoff (1993). From this, the orientation of the finite stretching and shortening axes, the orientation of the finite stretching direction and the kinematic vorticity number are calculated after Fossen and Tikoff (1993); Tikoff (1995) for a 2D plane strain case.

4.2.3 Electron backscatter diffraction

For Electron backscatter diffraction (EBSD) measurements, thin sections were polished with colloidal silica suspension and subsequently coated with a thin layer of carbon. Samples were analysed in the Zeiss Merlin SEM at the University of Tromsø, with a Nordlys nano camera in high vacuum at 15 keV acceleration voltage and probe currents of $\sim$ 14 - 18 nA. Data is acquired with the Oxford AZtec software and processed with Channel 5 and the MATLAB toolbox MTEX (available at https://mtex-toolbox.github.io; Bachmann et al. (2010)).
Polefigures are plotted using MTEX. For Polefigure contouring, the *de la Vallée Poussin* kernel with a half-width of 9.4° and a bandwidth of 30 is used. Polefigure J-index (PFJ; e.g. Bunge (1982); Mainprice and Silver (1993)) are given as a measure of texture strength. The index has a value of 1 for a random distribution and is infinite for a single orientation.

4.3 Results

4.3.1 Mechanical data

Figure 4.2 present the mechanical data as shear stress (τ) vs. apparent shear strain (γ_a) plots, of constant displacement rate runs and displacement rate stepping tests. Experiments and experimental conditions are listed in Table 4.1. For all experiments, the mechanical data shows a curve with an initial steep increase of shear stress, reaching a peak value usually after $\sim \gamma_a = 0.8$ - 1.0 (Figure 4.2a, b). Peak stress is followed by a shear stress decrease, often approaching a quasi-steady state stress value from a $\gamma_a \approx 4$

Table 4.1: *List of experiments.*

Exp. Nr.	Material	mean Pc [Mpa]	peak τ	τ at end	incremental apparent γ	mean strain rate [s-1]	added H2O [µl]	th0 [mm]	thF [mm]	d [mm]	thin section thF/ds	effective Γ	simple shear component γ	flattening component k
414	MD	1045	407	192	4.2	3.7E-05	0.20	0.75 ± 0.3	0.50	2.165	na	na	na	1.50
449	MD	1504	479	337	4.1	3.5E-05	0.20	0.75 ± 0.3	0.61	2.146	5.0	4.07	4.04	1.23
468*	MD	1061	348		0.7	1.7E-05	0.20	0.75 ± 0.3	0.69	0.426	1.2	1.10	1.10	1.09
470*	MD	1477	446		0.9	1.7E-05	0.20	0.75 ± 0.3	0.69	0.544	1.3	1.20	1.20	1.09
489	MD	1073	428	286	2.8	3.0E-05	0.20	0.75 ± 0.3	0.63	1.523	na	na	na	1.19
490	MD	1059	350			3.5E-05	0.20	0.75 ± 0.3						
						1.9E-05								
				130	4.5	4.1E-06			0.53	2.322	5.4	3.82	3.74	1.42
491	MD	1535	388			1.8E-05	0.20	0.75 ± 0.3						
						6.5E-06								
				82	3.2	1.9E-06			0.54	2.195	na	na	na	1.39
492	MD	1069	468	197	6.8	4.7E-05	0.20	0.75 ± 0.3	0.44	3.223	na	na	na	1.70
502	MD	1542	391			2.0E-05	0.20	0.75 ± 0.3						
						6.0E-06								
				33	3.4	1.5E-06			0.58	1.838	4.1	3.17	3.14	1.29
503	Slab + En	1089	530	367	5.6	4.1E-05	0.12	0.75 ± 0.3	0.55	2.83	na	na	na	1.36
505	Slab + Di (CrLk)	1072	460	253	5.3	4.0E-05	0.12	0.75 ± 0.3	0.55	2.683	5.7	4.18	4.11	1.36
507	MD	1073	479	191	4.7	4.1E-05	0.12	0.75 ± 0.3	0.49	2.383	na	na	na	1.53
518	Ab + En	1061	511	263	4.9	3.8E-05	0.12	0.75 ± 0.3	0.54	2.523	5.6	4.03	3.96	1.39
519	Slab + Di (D)	1076	517	289	4.7	3.6E-05	0.12	0.75 ± 0.3	0.54	2.435	4.8	3.46	3.40	1.39

MD = Maryland Diabase, Slab = Sonora Labradorite, En = Damaping Enstatite, Di (CL) = Cranberry lake Diopside, Di(D) = Damaping Diopside, Ab = Alpe Rischuna Albite. strain rate is given as average strain rate. For displacement rate stepping tests (grey-shaded columns), average strain rates are given for the individual displacement rate steps. th0 = shear zone thickness at experiment start, thF = shear zone thickness at experiment end. d = axial displacement of the load piston. ds = shear displacement parallel to the forcing block - sample interface. thin section thF/ds = final shear zone thickness and shear displacement as measured in the thin section. Γ, γ and k are determined as described in Fossen and Tikoff (1993). n.a. = no data available.

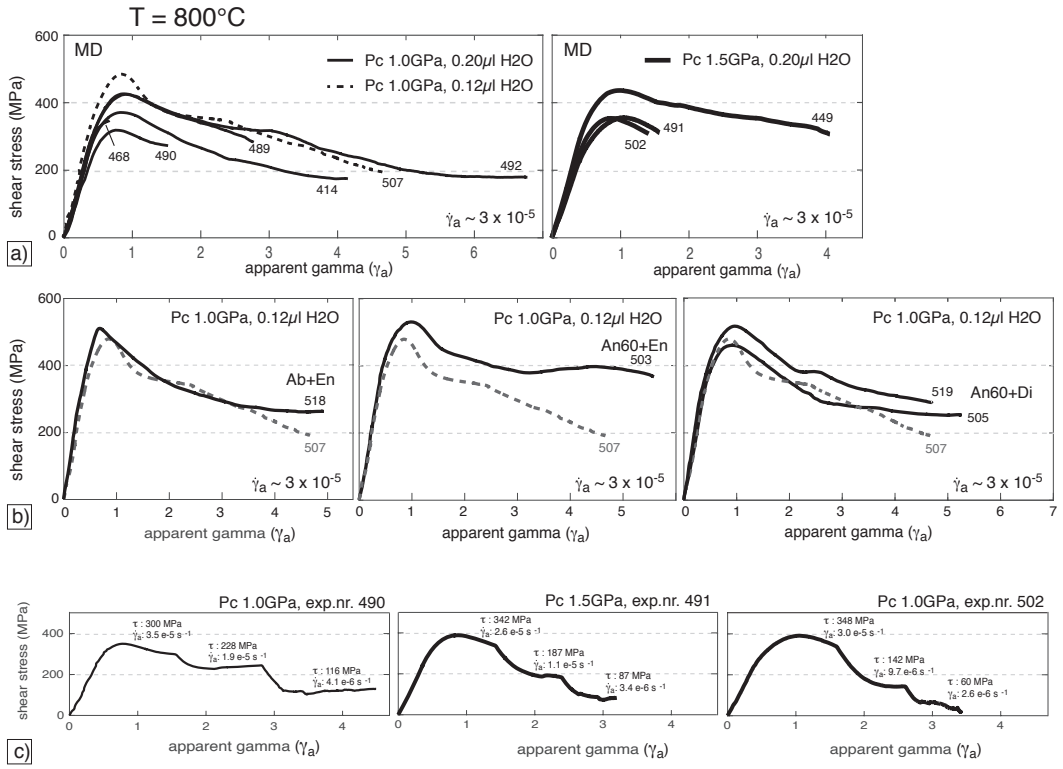

Figure 4.2: *Mechanical data. a) and b) Shear stress (MPa) vs. apparent shear strain plots. a) Maryland Diabase (MD) experiments. Pc is either 1.0 or 1.5 GPa. b) Experiments on synthetic Pl-Px mixtures. In each diagram, exp.nr. 507 (MD) is plotted as a reference. Pc ≈ 1.0 GPa c) Displacement-rate stepping tests on MD sample material. Experiment nr. 490 performed at Pc ≈ 1.0 GPa and experiment nr. 491 and 502 at Pc ≈ 1.5GPa.*

onwards. The samples with 0.12 μl H_2O added show higher stresses at peak and a more rapid shear stress decrease thereafter, compared to samples with 0.20 μm H_2O added. For the Maryland Diabase samples at Pc ≈ 1.0 GPa, the sample with 0.12 μl H_2O has a higher peak stress, however after an additional ∼ 0.5 γ_a, reaches shear stress values comparable to the samples with 0.20 μl H_2O. Within the variation, sample strength of Maryland Diabase at 1.0 and 1.5 GPa are the same at peak stress, however the 1.0 GPa experiments weaken more and reach a quasi-steady state flow stress at a γ_a ≈ 4 - 6 onwards (Figure 4.2a).

The synthetic Pl-Px mixtures (Figure 4.2b) show similar values for peak stress (460 - 530 MPa) and all but the An60+En mixture reach very similar flow stresses. The synthetic mixtures generally support ∼ 60 - 110 MPa more shear stress than the Maryland Diabase samples (Figure 4.2a, b; Table 4.1). At peak stress, the synthetic mixtures (samples 503, 518 and 519) reach differential stress values a few MPa above the Goetze criterion (Table 4.1). Due to the significant weakening subsequent to peak stress they however quickly fall below the Goetze criterion. The Goetze criterion is an empirical observation,

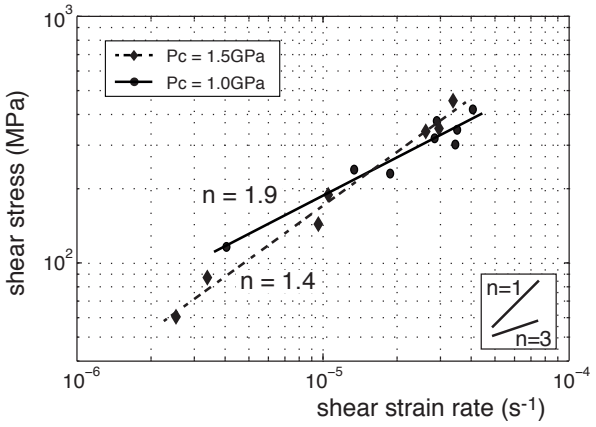

Figure 4.3: *Stress exponents. Stress exponent n is derived from data points from single-displacement rate and displacement rate stepping tests, for experiments performed at Pc ≈ 1.0 and 1.5 GPa respectively.*

that rocks which deform at $\Delta\sigma \leq$ Pc, usually deform plastically (Kohlstedt et al., 1995) (with plastic not necessarily $\equiv$ viscous). The Maryland Diabase samples all stay below the Goetze criterion during the experiments.

Figure 4.3 plot shear stress vs. apparent shear strain rate ($\dot{\gamma}_a$) from single-displacement rate experiments and displacement rate stepping tests on Maryland Diabase sample material at Pc $\approx$ 1.0 and 1.5 GPa. Linear fits are 1$^{\text{st}}$ degree polynomial fits used to determine stress exponents n, for a relationship $\tau = \dot{\gamma_a}^{(1/n)}$. Stress exponents are n = 1.9 and n = 1.4 for experiments at Pc $\approx$ 1.0 and 1.5 GPa respectively. There is some uncertainty about the stress state in the sample assembly and over the years, different ways of data treatment and data corrections have been applied (as well as differences between individual laboratories). The variation in calculated n due to different stress calculation routines is expected to be on the order of 16 - 27% (see section 3.3.1.3).

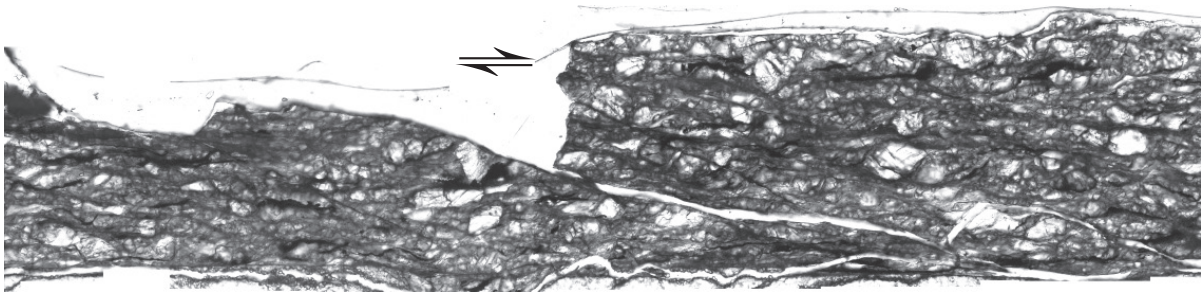

Figure 4.4: *Shear zone overview, sample 492. Light microscope image, plane polarised light. Strain in all samples localises into a network of shear bands, anastomosing around low strain lenses. The latter are indicated in this image by the large preserved porphyroclasts.*

4.3.2 Overview microstructures

In all experiments strain localises into a network of shear bands (Figure 4.4; Figure 4.5). Their thickness is variable but the main shear band strands usually have a thickness on the order of 40 - 150 μm (e.g. Figure 4.5d, h, j) and are characterised by strong grain size reduction (Figure 4.5e, k).
The following hydration reactions are observed, within shear bands as well as low strain lenses:

$$Px + Pl + H_20 \longrightarrow Amph + Qz \tag{4.1}$$

and

$$Pl_1 + H_20 \longrightarrow Pl_2 + Zo + Qz + Ky \tag{4.2}$$

where Pl_2 has a lower anorthite component than Pl_1.
Maryland Diabase samples:
In Maryland Diabase samples, both reaction (4.1) and (4.2) occur penetratively, however reaction (4.1) is more abundant. Amph is observed to grow as reaction coronas on Px clasts and as aggregates (often mixed with Qz) within shear bands (Figure 4.5b; Figure 4.6a). Vol.-% of hydrous reaction products reach about 15 - 25% for experiments with a duration of $\sim$ 60 - 70 h (lead run-in and subsequent deformation to $\gamma_a \approx 4$ to 6). Shear bands in Maryland Diabase experiments are broad and relatively shear zone parallel (Figure 4.5c), with a preferred angle ϕ of 3° towards the shear zone boundaries (or conversely, angle θ of 42° towards σ_1, see image 2.10 for reference frames). Shear bands are mainly formed by grains $<$ 1 μm diameter and a compositional layering between Pl dominated and Amph dominated layers is frequently developed (Figure 4.5a, b). Pl layers are either monomineralic or show mixing with Zo. In Amph dominated layers, Amph is frequently occurring together with Qz. Mixing between Amph and Pl is subordinate.

Synthetic mixtures:
In An60+En and An60+Di mixtures (Figure 4.5d - i), reaction (4.2) is the dominant hydration reaction. Vol.-% of hydrous reaction products reach 1 - 9%. In the An60+En mixture, shear bands are somewhat narrower and more anastomosing. With 9° between preferred angle of shear bands and shear zone boundaries (Figure 4.5f), shear bands are also more strongly inclined compared to the other samples. Shear bands in both, An60+En and An60+Di mixtures are mainly formed by fine-grained ($< 1\mu$m) Pl and Zo.

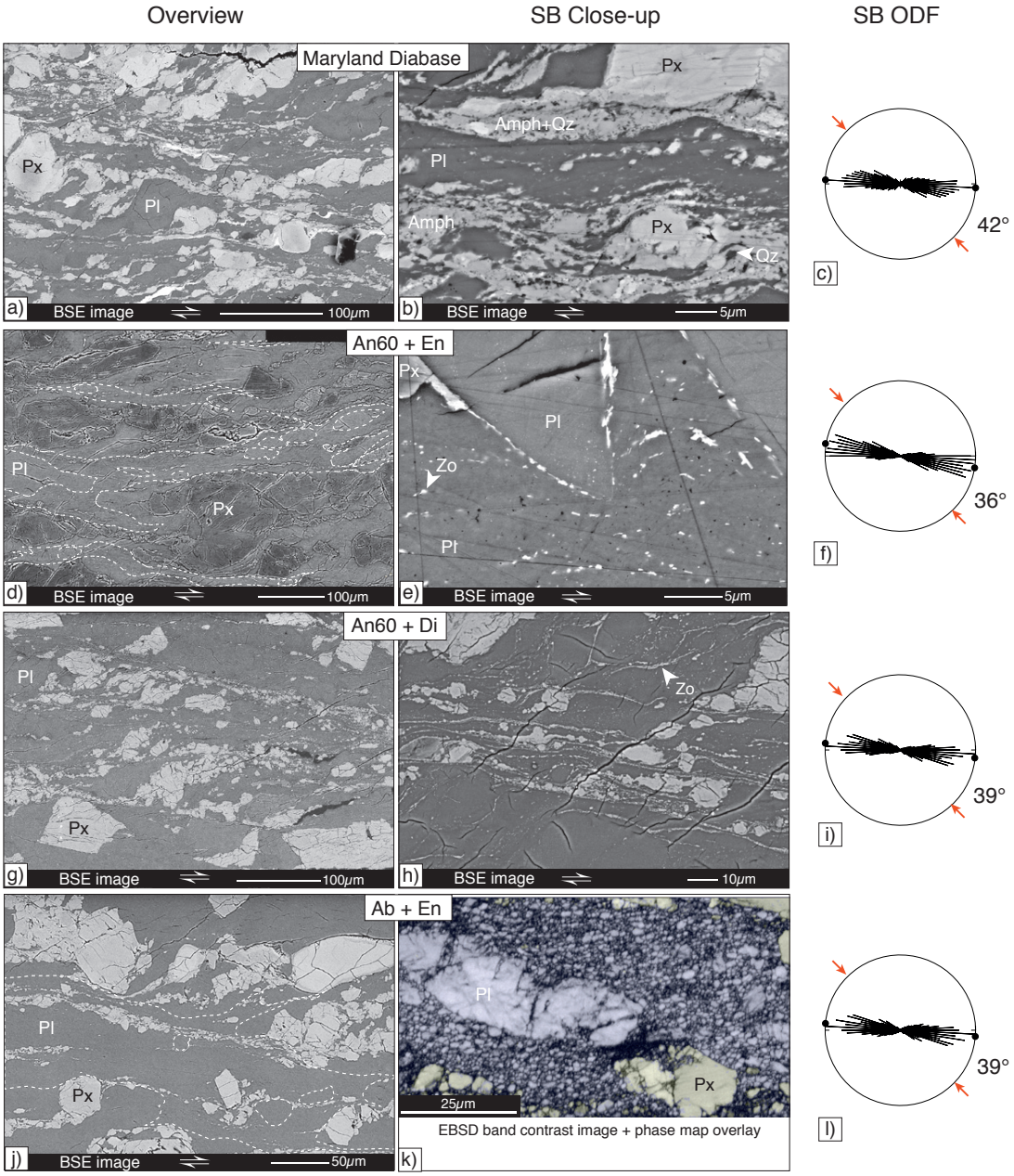

Figure 4.5: *Overview microstructures for experiments at Pc ≈ 1.0GPa. In d) and j), shear bands are traced with white dotted lines for better visibility. a) - c) Maryland Diabase sample material. d) - f) An60+En sample material. Due to the almost absence of iron, pyroxene appears darker than the plagioclase in BSE SEM images. g) - i) An60+Di sample material. j) - l) Ab+En sample material. h) EBSD band contrast image with transparent phase map overlay. Blue = Pl, Yellow = Px. Rose diagrams show orientation distribution function (ODF) of shear band boundary orientations of shear bands formed in the respective samples. Black dots indicate preferred orientation of shear bands. Red arrows indicate orientation of the globally imposed σ_1 direction. Nr. in degree gives the angle θ between σ_1 and preferred orientation of shear bands. SB = shear band.*

The Zo reaction predicts the formation of a new Pl with a lower anorthite component. The fine grain size within shear bands doesn't allow for quantitative EDS measurements. However, BSE SEM images reveal somewhat darker grey values for Pl within shear bands compared to Pl porphyroclasts (Figure 4.5e). Qualitative EDS measurements yield a decrease in anorthite component from An60 (starting composition) to $\sim$ An52 of Pl within shear bands.
In the Ab+En sample, shear bands are broad and sub-parallel (with a preferred orientation of 6°) to the shear zone boundaries (Figure 4.5l). Shear bands are pre-dominantly composed of fine-grained Pl (Figure 4.5k) with sizes $< 2\mu$m. No difference in composition between Pl porphyroclasts and shear band Pl was detected. In high-resolution BSE images, a fine-grained phase with a Z-contrast similar to enstatite is observed. Due to the small grain size it was however not possible to determine if these grains are new Px or Amph grains.

In all experiments (Maryland Diabase and synthetic mixtures), Pl shows extensive grain size refinement, whereas clasts are replaced by fine-grained Pl along their rims and along internal straight trails, which are interpreted to be former fractures (Figure 4.5k). Px grain size reduction in the synthetic mixtures is mainly observed to happen by fracturing (Figure 4.5d, g, h, j, k). In Maryland Diabase experiments, Px grains are far less affected by fracturing, and grain size reduction is mainly observed to be caused by the Px-consuming reaction to Amph (Figure 4.5a, b; Figure 4.6).

4.3.2.1 Influence of confining pressure on microstructure

The main difference between the microstructure developed at 1.0 and 1.5 GPa Pc is the increased amount of reaction products at the higher Pc (Figure 4.6). Zo and Amph form far more abundantly at the higher Pc and Amph corona surround Px porphyroclasts early on in the experiments. Additionally, shear bands are somewhat narrower and more inclined to the shear zone boundaries in the higher Pc experiments. Shear bands at Pc $\approx$ 1.0 GPa are mainly composed of a fine-grained mixture of Pl+Amph+Qz+Zo (in order of abundance). At Pc $\approx$ 1.5 GPa, shear bands are formed of a fine-grained mixture of Amph+Qz+Zo+Pl (again in order of abundance; Figure 4.6).

4.3.2.2 Amphibole chemistry

Qualitative EDS measurements reveal variability in the Amph chemical composition of Amph grown in Maryland Diabase experiments performed at Pc $\approx$ 1.0 GPa (Figure 4.7,

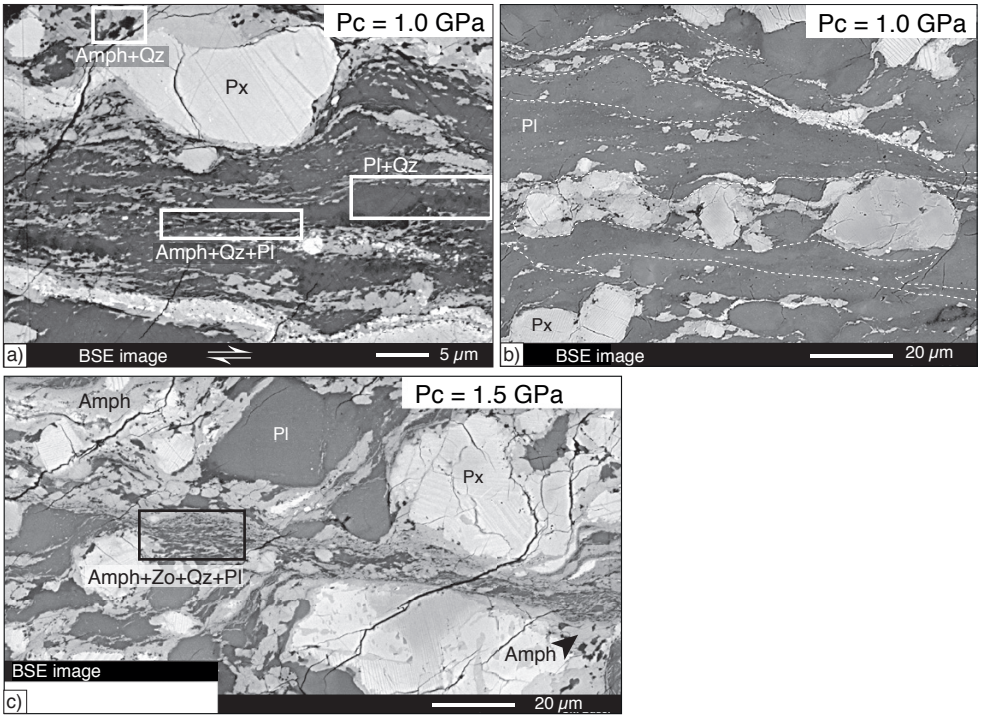

Figure 4.6: *Phase distribution at 1.0 (a and b) and 1.5 GPa (c) Pc, Maryland Diabase sample material. a) Extensive phase mixing in a shear band: Mixing of Pl+Qz or Pl+Zo and ordered mixing of Amph+Qz. Mixing between Amph and Pl is less frequent. Px clasts show Amph coronas and asymmetric Amph tails. b) Shear bands are predominantly composed of polycrystalline Pl. c) Extensive phase mixing between Amph+Zo+Qz(+Pl) within shear bands. Px clasts show Amph coronas and asymmetric Amph tails.*

Table 4.2): Seemingly two groups of Amph, differing in their Al (total) per formula unit (p.f.u.) to Mg p.f.u. ratio are present (Figure 4.7a). Furthermore, there are two sets of measurements differing in their Na p.f.u. to Al (total) p.f.u. ratio (Figure 4.7c, d). The Amph measurements are labeled according to their 2D neighbourhood observed in the thin section (Px-Px : Amph surrounded only by Px, Px-Pl : Amph grown between plagioclase and pyroxene grains, Pl-Pl : Amph grown in plagioclase dominated area). Looking at the Al to Mg ratio, there seems to be a consistent signal that high Al - low Mg Amph grow in plagioclase dominated areas. It is argued that this signal is not caused from 'plagioclase contaminated' measurements, on the basis that the Ca p.f.u. stays constant in all measurements (Figure 4.7b). If the higher Al contents would be the result of contaminated measurement caused by partly including plagioclase, then Ca contents would be expected to be elevated too.

Plagioclase in the Maryland Diabase starting material has an anorthite component of $\sim$ 65 - 70% (Table 2.1), its Na to Al ratio thus is $\sim$ 0.18 - 0.21. Plagioclase is the sole provider for Na and Al in Amph as pyroxene in the starting material shows only trace

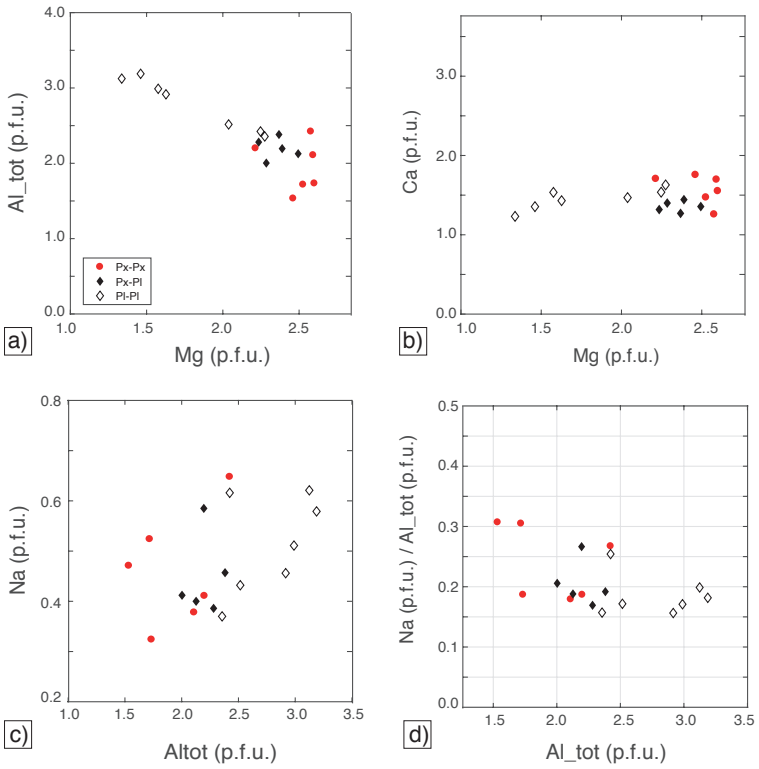

Figure 4.7: *Amph chemistry. Amph grains are measured in Maryland Diabase experiments performed at Pc ≈ 1.0 GPa. Measurements are classified by their 2D neighbourhood. Px-Px = pyroxene dominated neighbourhood; Px-Pl = Amph grown between Px and Pl grains; Pl-Pl = plagioclase dominated neighbourhood. a) total Al (p.f.u.) vs. Mg (p.f.u.) b) Ca (p.f.u.) vs. Mg (p.f.u.) c) Na (p.f.u.) vs. total Al (p.f.u.) d) Na to total Al ratio (p.f.u.) vs. total Al (p.f.u.).*

amounts of these elements. Most Amph measurements show an Na:Al-ratio of 0.16 - 0.21 (Figure 4.7c), consistent with reaction (4.1) and the consumption of a plagioclase with a composition of ∼ An(65-70). The second set, with Na:Al-ratios in Amph > 0.25 is comparable to the Na:Al-ratio of the starting plagioclase rim composition of ∼ An(50-55) (Table 2.1; resulting Na:Al-ratios of ∼ 0.29 - 0.33) and thus again would be compatible with the plagioclase-consuming, Amph forming reaction (4.1).

4.3.3 Shear bands

4.3.3.1 Nanostructure of plagioclase within shear bands

TEM images are presented from shear bands formed within the Ab+En sample 518 (Figure 4.8) and the Maryland Diabase sample 414 (Figure 4.9). In both figures, the section portrayed is normal to the shear zone boundaries and parallel to the shear direction.
Figure 4.8a shows the interface between an albite porphyroclast and the fine-grained albite matrix of an adjacent shear band. The albite clast has a high internal defect density, seen from the diffracting defects as well as from smeared-out diffraction spots in the diffraction pattern (Figure 4.8a, b). No sub-cell structures are identified, which would indicate subgrain rotation recrystallization. Furthermore, the interface between the clast and the shear band is sharp and no bulges are observed (Figure 4.8a). Within

Table 4.2: *EDS measurements of Amph chemical compositions from samples deformed at Pc ≈ 1.0GPa. Amphibole classification after Hawthorne et al. (2012).*

Sample	414	414	492	490	490
Amph class.:	Tschermak.	Mg Hornbl	Mg Hornbl	Mg Hornbl	Tschermak.
wt.-%, normalized to 98%					
SiO2	45.18	45.72	48.03	47.76	47.31
Al2O3	17.13	14.13	14.99	13.06	17.73
CaO	9.24	8.92	9.63	9.45	10.02
Na2O	1.63	1.74	1.56	2.12	1.84
K2O	1.26	0.86	0.74	0.89	0.90
MgO	7.56	9.95	9.59	11.24	7.39
TiO2	0.00	1.78	0.00	0.00	0.00
FeO	15.99	14.90	13.47	13.48	12.81
MnO	0.00	0.00	0.00	0.00	0.00
Cr2O3	0.00	0.00	0.00	0.00	0.00
Total:	**97.99**	**98.00**	**98.00**	**97.99**	**98.00**
Formula per 23 oxygen					
Si	6.59	6.76	6.89	6.89	6.77
Ti	0.00	0.00	0.00	0.00	0.00
Al	2.95	2.46	2.53	2.22	2.99
Fe3+	0.00	0.00	0.00	0.00	0.00
Cr	0.00	0.00	0.00	0.00	0.00
Mg	1.65	2.19	2.05	2.42	1.58
Ca	1.45	1.41	1.48	1.46	1.54
Mn	0.00	0.00	0.00	0.00	0.00
Fe2+	1.95	1.84	1.63	1.63	1.53
Na	0.46	0.50	0.43	0.59	0.51
K	0.23	0.16	0.14	0.16	0.16
Total	**15.28**	**15.34**	**15.15**	**15.38**	**15.08**

Tschermak = Tschermakite, Mg Hornbl = Magnesium Hornblende. All Fe is taken as Fe^{2+} due to the reducing conditions in the sample assembly.

the shear band, porosity is seen along few grain boundaries, either as open grain boundaries or as pore trails (Figure 4.8c - e). Pore trails in Figure 4.8c and d follow several aligned grain boundaries and the trace of the pore trail is oriented at a small angle to the globally imposed σ_1 direction. The pore system shown in Figure 4.8e is also suggested to represent syn-kinematic porosity and not an artifact from sample unloading or FIB-foil preparation: The porosity is confined to a single grain boundary segment - porosity from unloading is expected to produce misfit and resulting porosity along several sites along the grain boundary of a grain. The geometry of the pore system in Figure 4.8e can be explained by local grain boundary sliding with clockwise rotation of grain nr. 2. Black arrow points to a grain boundary bulge, coinciding with a twin formed in grain nr. 3. Many of the open grain boundaries (Figure 4.8c, white arrows) however cannot beyond

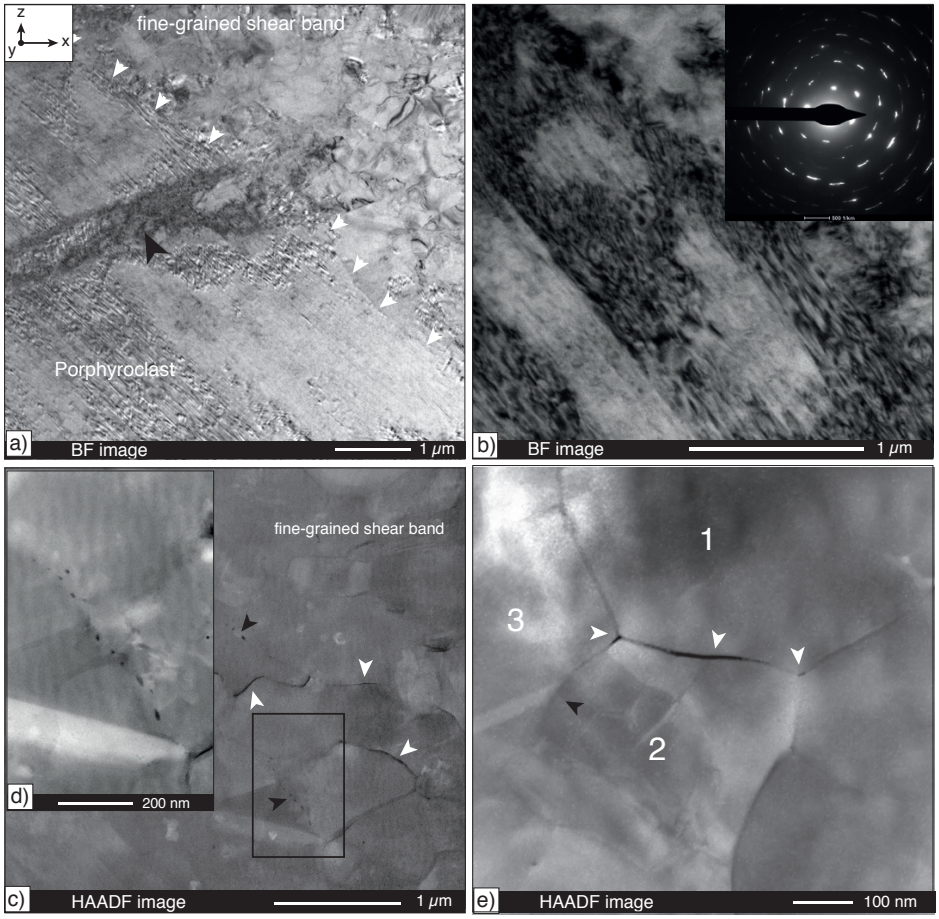

Figure 4.8: *Nano structures in shear bands, Ab+En sample material (exp.nr. 518). Shear zone boundaries are horizontal, shear sense is dextral. a) BF TEM image showing a Pl porphyroclasts adjacent to a fine grained shear band. White arrows mark the porphyroclast - shear band interface. Black arrow points to a high defect density band within the clast. b) BF TEM image. Detail of porphyroclast internal structure. Twin lamellae can be recognised. Defect density is high, which is also seen from the smeared out diffraction spots in the diffraction pattern. c) HAADF image showing the fine-grained shear band Pl. Porosity appears in black. White arrows point to some of the open grain boundaries, black arrows indicate pore-trails along grain boundaries. Black rectangle marks close-up view in d). d) HAADF image of a pore-trail following several aligned grain boundaries. e) HAADF image. White arrows point to porosity/opening sites developed along two triple-junctions and a grain boundary. The geometry of the pores is consistent with grain boundary sliding with a relative sinistral shear movement for this site, or a clockwise rotation of grain nr. 2. Black arrow points to a grain boundary bulge, coinciding with a twin formed in grain nr. 3.*

doubt be interpreted as syn-kinematic porosity. Opening could have happened during sample unloading at the end of the experiment. Nonetheless, even if the opening of grain boundaries happened during unloading, it might be an indicator for a possible low degree of congruency between the lattices of the neighbouring grains during deformation.

The shear band formed in the Maryland Diabase sample shows the typical compositional

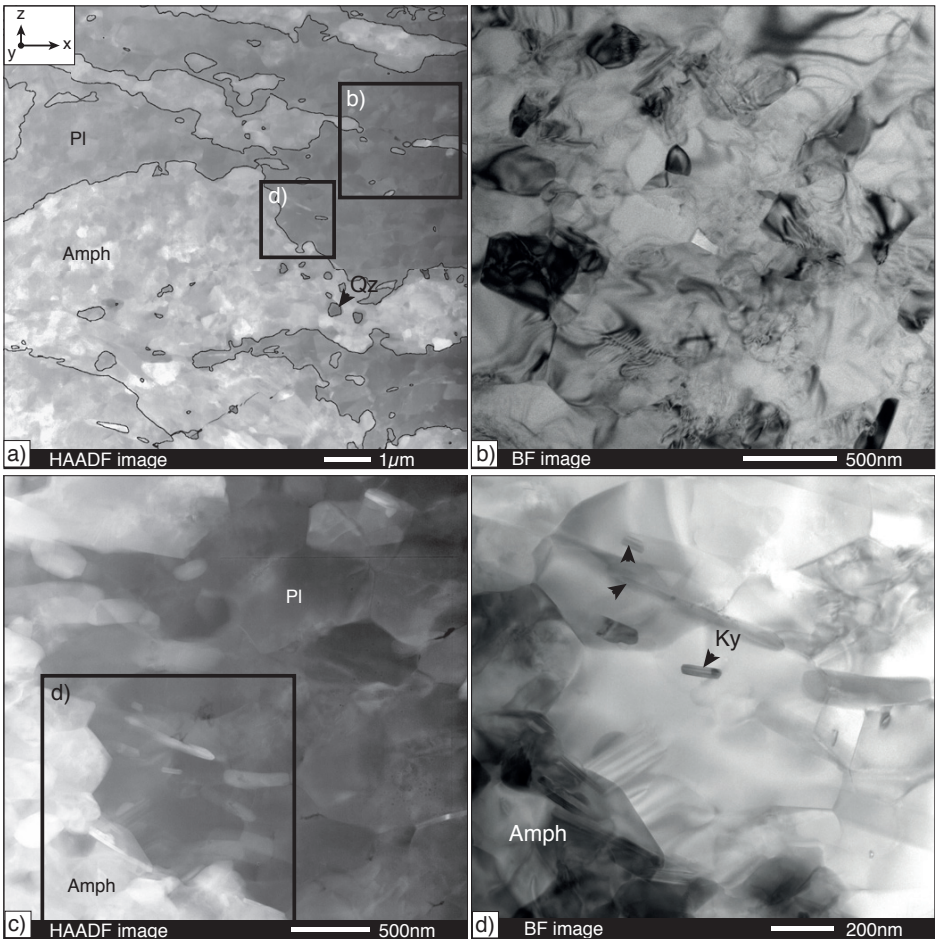

Figure 4.9: *Nano structure in shear bands, Maryland Diabase sample (experiment nr. 414). Shear zone boundaries are horizontal, shear sense is dextral. a) HAADF image, overview. Amph aggregates are traced with black lines for better visibility. Rectangle indicate areas shown in b) and d). b) BF TEM image, showing small (usually $\leq$ 600 nm) Pl grains with low internal defect density. Grain boundaries are tight and porosity is scarce. c) HAADF image, black rectangle indicates area shown in d). d) BF TEM image. Few Ky and Amph grains can be seen to grow between Pl grains. Sizes of all phases are of a few 100 nm and grains have a low internal defect density. Grain boundaries are tight, porosity is largely absent.*

layering between Pl dominated layers and Amph (+Qz) aggregates (Figure 4.9a). Bright field TEM images reveal largely defect free grains (Figure 4.9b, d) and grain sizes are similar for Amph and Pl. Grain and phase boundaries are tight and porosity is scarce (Figure 4.9b - d). Pl grains are weakly anisotropic in shape (not perfectly equant) and show a shape preferred orientation sub-parallel to the shear zone boundaries (Figure 4.9b - d).

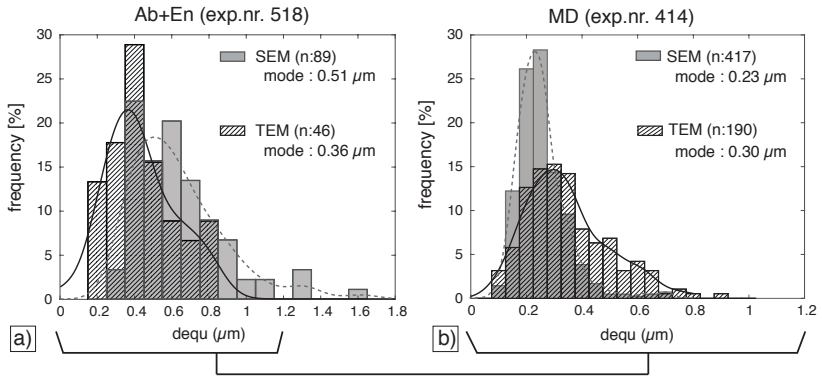

Figure 4.10: *2D grain size distributions of Pl within shear bands of a) Ab+En experiment 518, and b) the Maryland Diabase experiment 414. Grain sizes in both samples were determined on BSE SEM images and TEM images separately. n = number of grains analysed. Solid black and dashed grey lines are kernel density estimate fits to the TEM and SEM determined grain size distributions respectively.*

4.3.3.2 Plagioclase grain size distributions

2D grain size distributions (GSD) are presented for Pl within shear bands of the Ab+En experiment nr. 518 and the MD experiment 414 (Figure 4.10). The distributions in the two samples are similar with somewhat higher frequencies in bins > 1 μm for albite compared to the labradorites of the Maryland Diabase sample. Due to the small grain sizes and extremely narrow grain boundaries, grains are difficult to identify (especially in SEM images) and there is some uncertainty to the measured grain size distribution inherent from the grain segmentation. Nonetheless, grains segmented from TEM and SEM images correlate relatively well for the highest frequency bins. The GSD from sample 518 have modes at 0.51 and 0.36 μm. In sample 414, the GSD have modes at 0.23 and 0.30 μm (for grains segmented from SEM and TEM images respectively).

4.3.3.3 Albite textures

Three EBSD maps were collected along one shear band in the Ab+En sample 518 (Figure 4.11). Orientation data of Pl grains with < 2 μm equivalent diameter are plotted in pole figures for [a]-, [b]-, and [c]-axes ([100], [010] and [001]), as well as poles to (010)-planes. Orientation data of porphyroclasts and their fractured fragments is excluded. Although the textures are weak (PFJ values are not far from random), they show similar distributions in all three sites. Poles to (010) planes tend to agglomerate at the peripheries with a large angle towards the trace of the shear band orientation. [100] axes show peripheral and central maxima, $\sim$ along the trace of the shear band plane. The EBSD map in site7 contains a large Pl porphyroclast and the orientation data of this clast is plotted with

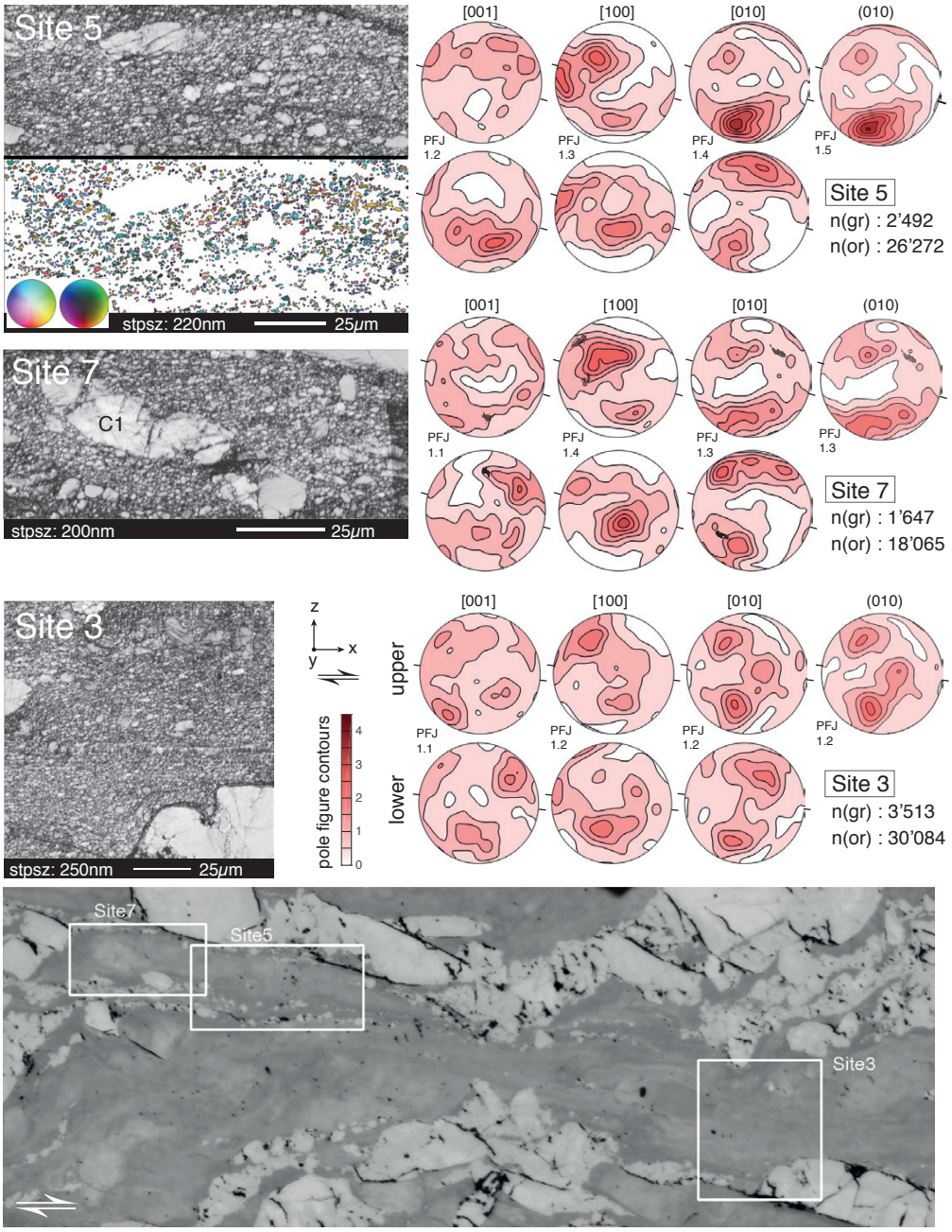

Figure 4.11: *Crystallographic orientation of fine-grained plagioclase within shear bands. Ab+En sample, exp. nr. 518. Band contrast images and contoured polefigures are given for three different sites along one shear band. For site 5, the EBSD map (inverse pole figure color coding) is additionally shown. Pole figures are upper hemisphere equal angle plots of orientations from grains < 2 μm in diameter. For site7, the orientation data of the Pl porphyroclast (C1) is additionally plotted as black dots in polefigures. Contours are at 0.5x multiples of uniform distribution. Black lines at polefigure rims indicate local shear band orientation. stpsz = step size of EBSD data acquisition, n(or) = number of EBSD data points used in pole figures, and n(gr) = number of corresponding grains.*

black dots in the polefigures of this site. The porphyroclast orientation is not coinciding with the density maxima of the orientations measured from the < 2 μm shear band grains.

4.3.3.4 Amphibole corona analysis

Amph grows abundantly in experiments on Maryland Diabase, especially at the higher Pc (e.g. Figure 4.6), where Px clasts are surrounded by Amph coronas early on in the experiment run. Px clast - Amph rim pairs from experiments performed at Pc $\approx$ 1.5 GPa were analysed, studying the average Amph coronas thickness as a function of orientation around Px porphyroclasts (Figure 4.12). Three different cases are distinguished: a *hydrostatic* ($\sigma_1 = \sigma_3 = Pc$), a *peak stress* ($\gamma_a \sim 1$) and a *deformed* ($\gamma_a \sim 4$) case. The three cases are representative for the different evolutionary stages of a higher strain experiment. The *hydrostatic* case represents the microstructural state at the hit-point after the lead run-in (see e.g. section 2.2.3). The *peak stress* case shows the microstructural state at the beginning of sample yielding and the *deformed* case represents the microstructure evolved after higher sample strain.

At *hydrostatic* conditions, corona growth is symmetrical around the clasts, with an average thickness of 2.4 to 3.1 μm (Figure 4.12a). In the *deformed* case, the average corona thickness curve shows a monoclinic, sigmoidal shape. Corona thickness is reduced by $\sim$ 0.5 - 2μm in most orientations except between $\sim$ 346 - 53° and 186 - 232° compared to the *hydrostatic* case. That is, average corona thickness is reduced in orientations with a small angle to the globally imposed σ_1 direction, and increased in orientations with a high angle to the σ_1 direction. Interesting is the orthorhombic shape of the average Amph corona thickness curve at *peak stress*. Where the average Amph thickness in σ_1 direction is the same as in the *hydrostatic* case ($\sim$ 2.7μm), Amph corona thickness is increased in almost all other directions. Furthermore, despite the 23 h longer duration of the *hydrostatic* run compared to the *peak stress* run (Figure 4.12b), coronas did not grow to larger thicknesses in the former.

Instantaneous stretching and shortening axes (ISA), finite stretching direction and vorticity number are calculated for the *peak stress* and the *deformed* case (Figure 4.12c). The ISA and the finite stretching direction can be derived because the initial thickness of the shear zone is approximately known and the end-thickness and *effective shear strain (*Γ*)* can be measured after the experiment from the thin section. The starting thickness is known with an expected error of $\pm$ 0.03 mm. This error leads to some uncertainty on the amount of flattening strain, and therefore also to a certain range of values for ISA, finite stretching direction and vorticity number. The orthorhombic shape of the

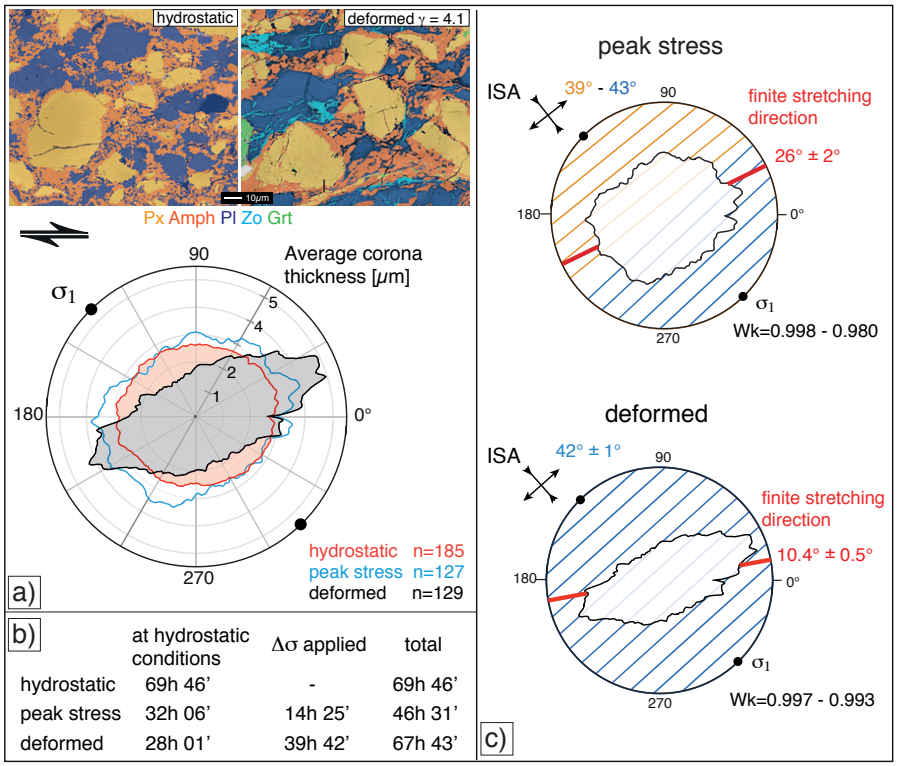

Figure 4.12: *Amph corona thickness as a function of orientation around Px porphyroclasts, analysed for Pc ≈ 1.5GPa Maryland Diabase experiments. a) Average Amph corona thickness presented as rose diagram. n = nr. of analysed Px clast - Amph rim pairs. Analysis for three different samples are presented, 'hydrostatic', 'peak stress' ($\gamma_a \sim 0.6$) and 'deformed' ($\gamma_a \sim 4$). b) Duration of experiments in hours (h) and minutes ('). c) same data as a), orange and blue lines indicate calculated instantaneous stretching directions. Due to some uncertainties in the amount of flattening strain, the calculated axis orientation ranges between 39-43° for the peak stress case. In red, calculated finite stretching direction. Wk = kinematic vorticity number.*

peak stress corona curve is well described by the ISA. The corona curve for the *deformed* case shows some possible relation to the ISA in orientations corresponding to the shortening sectors around the Px clasts. The finite stretching direction (10.4°, i.e. 190.4°) has a more shallow orientation than the orientation of maximum average amph corona thickness.

4.3.4 Comparison to nature

We compare our experimental results to a naturally deformed Hornblende pegmatite (Figure 4.13), collected on the island of Arnøya, Northern Norway (outcrop coordinates: 70°02'39" N, 20°43'54" E). The syn-kinematic P-T conditions are estimated to ∼ 0.7 - 0.9 GPa and 610 - 710 °C (Getsinger et al., 2013) and thus are close to our experimental

Pc-T conditions. The initial pegmatite contained Amph, Pl and Qz, with grain sizes > 1 mm. Deformation lead to mylonitisation defined by strong grain size reduction and partial re-distribution of phases. Phase assemblage within the mylonite remained largely the same, except for Zo, which is syn-kinematically appearing as a new phase.
Two types of domains are distinguished: (i) domains of distinct compositional layering between layers dominated by Pl (+Zo) and layers dominated by Amph+Qz (Figure 4.13b). Mixing between Pl+Amph is scarce. (ii) Domain of intense phase mixing, including the phases Pl+Amph+Qz+Zo (Figure 4.13c). Pl grain sizes within the two domains are on the order of ~ 170 μm in the Pl dominated layers, and ~ 50 μm in the polyphase mixture (Figure 4.13d, e). The chemistry of Amph grown in the phase mixture and as tails around Amph porphyroclasts differs from the chemistry of the Amph porphyroclasts (Table 4.3). The lower Si p.f.u. of the syn-kinematically grown Amph in tails and the polyphase mixture is consistent with the observation of abundant Qz nucleation (Figure 4.13b, c).
The microstructure and phase assemblage of the natural sample is strikingly similar to our Maryland Diabase experiments. That is, intense syn-kinematic grain size reduction and the formation of either a compositional layering between Amph(+Qz) and Pl(+Zo) dominated layers (Figure 4.13b; Figure 4.6; Figure 4.9a), or formation of a phase mixture including the phases Amph+Qz+Pl(+Zo) (Figure 4.13c; Figure 4.6a). The most significant difference in the microstructure between the natural and the experimental rock is the difference in grain size, which is on the order of $\sim 1 \cdot 10^2$ to $5 \cdot 10^2$ (compare Figure 4.10; Figure 4.13d, e).

4.4 Discussion

4.4.1 Identification of dominant deformation mechanism

Strain in all samples is localized into a network of shear bands, formed by fine-grained Pl+Amph+Qz+Zo, where the relative phase percentages are somewhat depending on the imposed Pc. TEM observations from these shear bands reveal relatively equant, strain free grains. The small grain size of grains within shear bands (Figure 4.10) clearly favours a grain size sensitive deformation mechanism. The vast amounts of mineral reactions indicates the activity of solution-mass transport and dissolution-precipitation creep accompanied by grain boundary sliding (GBS) are interpreted to be the dominant deformation mechanisms in our experiments. The low stress exponents of $n < 2$ (Figure 4.3) are in accordance with such an interpretation. The morphology of pores presented

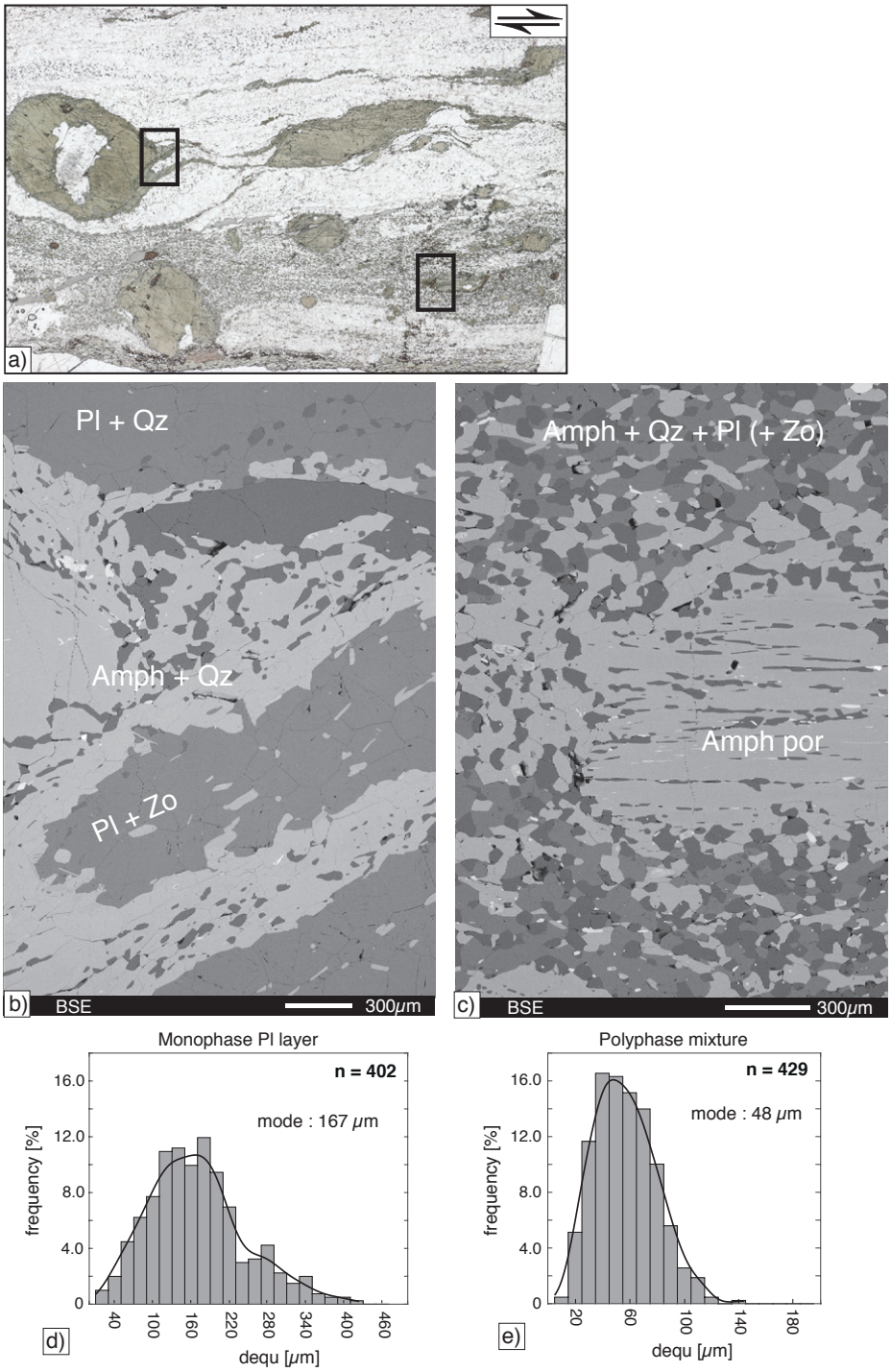

Figure 4.13: *Natural case, deformed hornblende pegmatite a) Thin section scan, plane polarised light. Black rectangles indicate location of micrographs in b) and c). b) Compositional layering and only limited phase mixing. c) Zone of extensive phase mixing. por = porphyroclast. d) and e) Grain size distributions of plagioclase d) in ∼ monomineralic Pl layers and e) in the phase mixture. n = number of grains, black solid lines = kernel density fit.*

Table 4.3: *Amph chemistry, natural sample, as normalised oxide wt.-% and as calculated stoichiometric mineral formula. porph = porphyroclast.*

	Amph porph	Amph porph tail	Amph poly-phase matrix
wt.-%, normalized to 98%			
SiO2	48.12	44.69	44.61
TiO2	0.66	0.77	0.83
Al2O3	8.91	13.78	14.00
FeO	12.38	13.54	12.58
MnO	0.37	0.00	0.25
MgO	14.28	11.47	11.93
CaO	11.74	11.60	11.66
Na2O	1.30	1.67	1.68
K2O	0.25	0.49	0.46
Total:	**98.01**	**98.00**	**98.00**
Formula per 23 Oxygen			
Si	6.87	6.46	6.42
Al	1.50	2.35	2.38
Ti	0.07	0.08	0.09
Fe3+	0.62	0.41	0.44
Fe2+	0.85	1.22	1.07
Mn	0.05	0.00	0.03
Mg	3.04	2.47	2.56
Ca	1.80	1.80	1.80
Na	0.36	0.47	0.47
K	0.05	0.09	0.08
Total:	**15.20**	**15.35**	**15.35**

in Figure 4.8c - e might be further supporting evidence; the pore trail in Figure 4.8d could be interpreted as to have formed by precipitation of Pl and entrapment of residual fluid along the grain boundaries at a small angle to the globally σ_1 direction. Figure 4.8e shows a pore system developed which would be consistent with grain boundary sliding (GBS) and rotation of grain nr. 2. The twin formed in the neighbouring grain 3 correlates with a possible high stress site induced by the convex grain boundary along grain 2 pushing into grain 3 due to rotation.

Intracrystalline deformation mechanisms such as dislocation glide or creep are excluded based on the following observations: porphyroclasts show extremely high dislocation densities (Figure 4.8a). Glide of dislocations is thus expected to be severely restricted due to entanglements amongst neighbouring dislocations. Furthermore, no sub-cell structures or bulges are observed which would be indicative for recovery controlled dislocation glide. Whereas Maryland Diabase experiments show vast amount of Amph and Zo growth, reactions in the synthetic mixtures are largely restricted to the Pl hydration reaction to Zo (Figure 4.5). Shear bands in the Maryland Diabase samples differ in their phase

proportions between Pl, Amph, Qz and Zo, depending on the imposed Pc (Figure 4.6). Disregarding, the resulting sample strength and stress exponents are similar for the different experimental conditions (Figure 4.2 and Figure 4.3). Dissolution-precipitation creep and GBS are interpreted to be the dominant deformation mechanisms in all experiments. Pl thereby is seen to be the most crucial phase enabling viscous deformation by its ability to undergo reaction, entailing nucleation and grain size reduction.

4.4.2 Grain size reduction

There is a drastic grain size decrease (down to sized < 1 μm) accompanied with the shear band formation, whereas this grain size reduction is observed to be caused by mineral reactions and heterogeneous nucleation. Grain size reduction (or synonymously, grain boundary area increase) is energetically unfavourable as it increases the amount of surface atoms with non-satisfied bonding sites. Dissolution-precipitation creep (which is interpreted to be one of the dominant strain accommodating mechanisms in our experiments) does not necessitate the formation of new grains, but precipitation could occur as overgrowth rims on existing porphyroclasts. The intense grain size reduction that we observe is suggested to be caused by high nucleation rates. If nucleation rates are high compared to growth rates, a material will become fine-grained (e.g. Rubie, 1998). High nucleation rates can e.g. be attained by (i) large overstepping of reaction boundaries (e.g. Rubie, 1998; Putnis, 1992) or, (ii) high grain internal defect densities might aid to speed-up reaction rates, as the elevated defect densities can have a rate enhancing effect on dissolution (e.g. Wintsch, 1985; Schott et al., 1989).
Our experiments clearly satisfy point (i): the starting materials + H_2O are not in equilibrium at the experimental Pc-T conditions and the duration of sample pressurisation and heating before the experiment start happens within 5 - 8h. Therefore, the sample material is brought very rapidly to out-of-equilibrium conditions, leading to large overstepping of reaction boundaries. Although this way of rapid change in P-T conditions is relatively unique to experiments, it is suggested that this should not pose a problem in extrapolation to nature. There is widespread evidence from observations on natural rocks that metastable mineral assemblages can be sustained even at high-grade conditions and to large overstepping of reaction boundaries, when rocks are dry (e.g. Rubie, 1986; Austrheim, 1987; Wayte et al., 1989; Krabbendam et al., 2000; Austrheim, 2013; Jamtveit et al., 2016). Where there is fluid influx, mineral reactions are enabled and equilibration can be attained, usually along the localised zones of fluid infiltration.
(ii) TEM analyses revealed high defect densities in plagioclase porphyroclasts (Figure

4.8). The defects are likely to be introduced either during sample preparation (preparation of the rock-powder by crushing rock fragments and mineral grains), during sample pressurisation or during sample deformation.
The low defect densities and the narrow grain size distribution for the fine-grained Pl within shear bands (Figure 4.8; Figure 4.9; Figure 4.10) are in accordance with the formation by nucleation. Grain size reduction by fracturing is generally observed to produce a wide range of fragment sizes and as fracturing is often observed to be accompanied by high dislocation densities (e.g. Fitz Gerald et al., 1991; Fitz Gerald and Stünitz, 1993; Stünitz et al., 2003; Trepmann et al., 2007). Fragments caused by fracturing are thus expected to (partly) show high dislocation densities (e.g. Stünitz et al., 2003). For Pl, fracturing is not seen to contribute in a significant manner to grain size reduction.
Fracturing as important means of grain size reduction is only observed for pyroxene grains in the synthetic mixtures (e.g. light microscope image in 4.10). In these samples, pyroxene is not seen to participate in any mineral reaction and reaction (4.2) is the only reaction observed. In contrast, Px grains in Maryland Diabase experiments show grain size reduction by dissolution during the Px-consuming reaction (4.1) to Amph.
For all other phases except Px, nucleation is seen as the main process leading to grain size reduction and (partial) phase mixing.

4.4.2.1 Grain size reduction in the special case of the Ab+En experiment

In the special case of the Ab+En experiment, Pl grain size reduction in shear bands occurs without a measurable change in Pl composition. That is, nucleation of new Pl grains seems to happen without the additional driving force of lowering Gibbs free energy. However, as discussed previously, no microstructural evidence for fracturing or dynamic recrystallization by subgrain rotation or bulging recrystallization is observed (see e.g. also Figure 4.8).
Due to the small grain size of plagioclase within shear bands (Figure 4.10), quantitative EDS measurements are not feasible - that is, small changes in solid-solution composition won't be detected. In that case, nucleation could still be driven by chemical potential. The observation of abundant nucleation along what is interpreted as former fractures (Figure 4.5k) cannot simply be associated with the influence of strain energy (in the sense of high defect densities locally introduced by fracturing). As fracturing is always accompanied by some amount of dilatancy, fluid flow is expected to be enhanced along the fractures, leading to higher solution-mass transport rates and thus also to expected higher rates of nucleation (e.g. Fitz Gerald and Stünitz, 1993). The significance of strain energy as a possible rate-enhancing contributor to nucleation is thus difficult to keep

apart from the effects of enhanced fluid flow and it remains unclear if elevated defect densities in the albite porphyroclasts alone would be able to induce neo-crystallization.

4.4.3 Albite Texture

Dislocation creep and dynamic recrystallization by subgrain rotation recrystallization is unlikely for feldspars under our experimental conditions. The large Burgers vectors and cation ordering (coupled Al+Ca and Si+Na) in plagioclase are unfavourable for intracrystalline deformation. Dislocation glide and creep are described in plagioclase at both natural and experimental conditions (e.g. Tullis and Yund, 1985; Shaocheng and Mainprice, 1990; Yund and Tullis, 1991; Shigmeatsu and Tanaka, 2000; Kruse et al., 2001; Lapworth et al., 2002; Stünitz et al., 2003; Ji et al., 2004; Mehl and Hirth, 2008) but are often reported to do not accommodate significant amounts of strain. Recrystallization happens by bulging recrystallization and/or neo-crystallization (e.g. Fitz Gerald and Stünitz, 1993; Rosenberg and Stünitz, 2003; Brander et al., 2012; Fukuda and Okudaira, 2013; Mukai et al., 2014) or from fragments formed by fracturing (e.g. Stünitz et al., 2003; Viegas et al., 2016). Diffusion creep (in the broadest sense - often dissolution precipitation creep) in fine-grained aggregates is the main strain accommodating process described for polycrystalline Pl aggregates (e.g. Yund and Tullis, 1991; Fitz Gerald and Stünitz, 1993; Jiang et al., 2000; Lapworth et al., 2002; Rosenberg and Stünitz, 2003; Brander et al., 2012; Fukuda and Okudaira, 2013; Mukai et al., 2014; Viegas et al., 2016).

We find no microstructural evidence for significant strain accommodation by intracrystalline slip mechanisms such as dislocation glide or creep. However, there is a weak but consistent texture measured in a shear band of the Ab+En sample 518 (Figure 4.11). A tendency is seen, for aligning [001] axes within the shear plane and poles to the (010) planes at a high angle to it. PFJ values indicate close to random distributions of crystal orientations but the three independent sites 3, 5 and 7 show very similar textures. This similarity is evidence that these textures, although weak, are not random.

There are different mechanisms, which can lead to crystallographic preferred orientation of grains within an aggregate. Texture-forming mechanisms described in the literature are dislocation glide (e.g. Schmid and Boas, 1950), directed growth (possibly together with rigid body rotation, (e.g. Berger and Stünitz, 1996; Rosenberg and Stünitz, 2003; Viegas et al., 2016) and texture formation determined by interfacial energy, e.g. via host controlled nucleation (e.g. Jiang et al., 2000) or by interface controlled diffusion creep (e.g. Bons and den Brok, 2000; Sundberg and Cooper, 2008). Similar textures to the

ones we measured have previously been found within experimentally deformed anorthites (e.g. Ji et al., 2004), and in naturally deformed rocks (e.g. Mehl and Hirth, 2008; Viegas et al., 2016; Xie et al., 2003). Ji et al. (2004) and Mehl and Hirth (2008) interpret the textures to have formed due to dislocation creep within the monomineralic plagioclase layers. Viegas et al. (2016) observe no evidence for dislocation creep and suggest the textures to have formed due to directed growth and rigid body rotation during diffusion accommodated grain boundary sliding. In our case, we also argue that the weakly developed crystallographic preferred orientation is not due to dislocation creep, as we find no indicators for such. Rather, we see strong evidence that the weak texture formed during grain size sensitive creep in the largely monomineralic albite layer. The reason for the texture formation in our case could however not be further specified. Speculating, it is suggested that preferential growth and rigid body rotation are the most likely causes.

4.4.4 Evidence for dissolution precipitation creep of Amphibole

Amph growth coronas on Px porphyroclasts for the cases *hydrostatic*, *peak stress* and *deformed* were measured (Figure 4.12). During the prolonged ($\sim$ 40 h) time of deformation (i.e. duration of applied $\Delta\sigma > 0$) in the *deformed* case, average corona thickness is reduced by 0.5 - 2 μm around the compressional sites of porphyroclasts, while simultaneously growing around orientations corresponding to extensional sites (Figure 4.12). We interpret these results as indicating strain accommodation by dissolution-precipitation creep of Amph. The orientation of the shortening ISA lies within the orientation range of minimum average corona thickness. The orientation of the shortening ISA is expected to be equal to the direction of the instantaneous maximum principal stress (Mancktelow, 2011). A correlation between the shortening ISA and the minimum in average corona thickness is thus consistent with the interpretation of dissolution-precipitation creep, where material is preferentially dissolved along high stress sites and deposited along low stress sites.

The geometry of deformation by diffusion mass transport is irrotational (Karato, 2008), that is, as the principal stress axes are normal to each other, the resulting fabric due to diffusion mass transport should be orthorhombic. The *peak stress* case, where shear strain yet is small, shows an orthorhombic shape of the corona curve, well described by the ISAs (Figure 4.12). As the ISAs should indicate the minimum and maximum principle stress directions, the observation of the corona curve following the ISAs correlates well with the interpretation that dissolution-precipitation creep determines the Amph corona thickness evolution. The asymmetric shape of the corona curve in the *deformed*

case is suggested to be explained by a superposition of co-axial diffusional flow and rigid body rotation (induced by the rotational component of simple shear) of the clast - rim pairs.
The analysed clast - rim pairs are predominantly situated outside of shear bands in low strain lenses, where shear strains are lower than in shear bands (Figure 4.12). From microstructural observations we do not see evidence that the reduction in average corona thickness at clast compressional sites is due to 'shearing-off' of Amph from compressional to extensional sites by some sort of granular flow.
The amounts of Amph reaction in Maryland Diabase experiments, for the short experimental durations are astounding. The observation of variable Amph compositions (Figure 4.7, Table 4.3) could be evidence for local equilibria. Deformation is likely to alter fluid pathways, grain neighbourhoods (neighbour switching) and grain internal defect densities - continuously allowing for a change in local equilibrium and thus chemical potential to further drive reaction and nucleation (i.e., dissolution and reprecipitation).

4.4.5 Extrapolation to nature

One of the key-questions in experimental rock deformation is for the feasibility of extrapolation to nature. Often, the similarity between microstructures of naturally and experimentally deformed samples is taken as an argument that the same processes must have acted in experiment and nature.
In the viscous field, extrapolation from experiments to nature usually takes advantage of what sometimes is referred to as the *temperature - time - trade-off*. That is, since the rate ($\dot{r}$) of many viscous processes shows a proportionality of the form $\dot{r} \propto exp(-1/T)$, an increase in temperature will have a rate-enhancing effect on the process. In our case, where dissolution-precipitation creep is suggested as the main strain accommodating mechanism, the grain size sensitivity of the process can additionally be made advantage of, to extrapolate from experiment to nature. As seen from the comparison between the experimental samples and the naturally deformed hornblende pegmatite, grain size differences are on the order of $\sim 5 \cdot 10^2$ to $1 \cdot 10^2$.
Dissolution precipitation creep flow laws vary but as e.g. described by Paterson (2013), the rate of dissolution-precipitation depends on the parameters:

$$\dot{\varepsilon} = \frac{A\ D\ \omega\ c\ \upsilon_s\ \Delta\sigma^n}{R\ T\ d^m} \tag{4.3}$$

where, A = constant, D diffusion coefficient, ω grain boundary width, c solubility, υ_s molar volume, $\Delta\sigma$ = differential stress, n = stress exponent, R = universal gas constant,

T = temperature, d = grain size, m = grain size exponent

and

$$D = D_0 \cdot exp(-Q/RT) \tag{4.4}$$

where, Q = activation energy.

The stress exponent is generally described to be close to $n = 1$ (e.g. Elliott, 1973; Paterson, 2013). The grain size exponent varies depending on the rate limiting step. With $m = 3$, for the transport-limited case, and $m = 1$ where reaction is the rate limiting step (e.g. Shimizu, 1995; Paterson, 2013). Under the assumption that experiments and nature should only differ in T and grain size, reaction (4.3) can be simplified to

$$\dot{\varepsilon} \propto \frac{exp(-Q/RT)}{R\ T\ d^m} \tag{4.5}$$

We compare our experiments with the naturally deformed hornblende pegmatite. The experimental and natural P and especially T conditions are very similar and consequently extrapolation has to be made without a significant *temperature - time - trade-off*. Assuming a natural strain rate of $\sim 10^{-12}$ s^{-1}, the experimental strain rates at $\sim 10^{-5}$ s^{-1} are 10^7 times higher. The grain size difference between the natural and experimental samples are on the order of $\sim 5 \cdot 10^2$ to $1 \cdot 10^2$.
For the transport controlled case, with $m = 3$ and the aforementioned grain size difference between nature and experiment:

$\dot{\varepsilon} \propto d^{-m}$ with $\dot{\varepsilon} \propto d^{-3}$

$$\longrightarrow ((5 \cdot 10^2)^{-1})^{-3} = \text{increase in } \dot{\varepsilon} \text{ by a factor of } 1.3 \cdot 10^8$$

$$\longrightarrow ((1 \cdot 10^2)^{-1})^{-3} = \text{increase in } \dot{\varepsilon} \text{ by a factor of } 1.0 \cdot 10^6$$

For the reaction controlled case, with $m = 1$:
$\dot{\varepsilon} \propto d^{-1}$

$$\longrightarrow ((5 \cdot 10^2)^{-1})^{-1} = \text{increase in } \dot{\varepsilon} \text{ by a factor of } 5 \cdot 10^2$$

$$\longrightarrow ((1 \cdot 10^2)^{-1})^{-1} = \text{increase in } \dot{\varepsilon} \text{ by a factor of } 1.0 \cdot 10^2$$

Thus, for the grain sizes attained in the experiments, the strain rate is expected to be

2 to max. 8 orders of magnitude higher compared to the natural sample, depending if either reaction or transport is rate-limiting.

It is difficult to extrapolate the influence of increased T in the experiments to nature, because activation energies for most processes are poorly constraint. As a first approximation, a range of activation energies between 20 - 200 kJ/mole are considered, aimed to attain a rough estimate to which extent the strain rate will differ comparing 600 - 700°C (natural sample) to 800°C (experiments).

With Q = 20 and Q = 200 kJ/mole and $\dot{\varepsilon} \propto exp(-Q/RT)$:

$$\longrightarrow \text{From 600 °C to 800 °C} \longrightarrow \text{increase in } \dot{\varepsilon} \text{ of times} \sim 1.7 \cdot 10^0 \text{ to} \sim 1.7 \cdot 10^2$$

$$\longrightarrow \text{From 700 °C to 800 °C} \longrightarrow \text{increase in } \dot{\varepsilon} \text{ of times} \sim 1.3 \cdot 10^0 \text{ to} \sim 1.0 \cdot 10^1$$

The temperature effect on strain rate thus is likely relatively small, because T are similar for the natural and experimental case. A strain rate increase by a factor of max $1.7 \cdot 10^2$ might be expected due to the higher experimental T.

These estimates suggest, that for dissolution-precipitation creep as dominant strain accommodating mechanism, and in the transport-controlled case, extrapolation of experimentally derived parameters may be possible even to high-grade natural conditions. The small grain sizes (< 1 μm) attained in the experiments are expected to increase the strain rate 6 to 8 orders of magnitude, which is $\sim$ the order of magnitude difference between natural and our experimental strain rates. However, in the case of reaction-controlled diffusion creep, grain size reduction has a much smaller rate-enhancing effect on strain rate (on the order of $\sim$ maximum $5 \cdot 10^2$ times). Extrapolation in this case needs a significant contribution of e.g. a larger temperature-time trade off (i.e. comparing experiments to lower T natural conditions), higher stresses, higher solubility, and/or fracturing. In this case, it becomes increasingly complicate to assure that the rate limiting processes in experiments and nature are the same and extrapolation to nature remains feasible.
When extrapolating experiments to lower T natural conditions, so as to make use of a grater temperature-time trade off, problems might arise when dealing with reactions: The elevated experimental T will stabilise high-grade mineral assemblages, possibly unlike the lower-grade natural case the experiments are compared with. In this case, it depends on how strongly mineral type influences the rock strength. A factor in favour

of our case is the fact that the typical reaction products in our experiments, Amph, Pl, Qz and Zo, are phases stable over a broad range of T. Thus, mineral assemblages at experimental and natural T are likely to be similar, although solid solution compositions will vary.

As we observe in our experimental samples, fracturing still occurs in both plagioclase and pyroxene (e.g. Figure 4.5g, j, k; Figure 4.8a; light microscope image in Figure 4.11) and is seen to locally enhance nucleation rates (Figure 4.5k). Fracturing of plagioclase and pyroxene during dominantly viscous creep at high metamorphic grades is frequently observed in natural samples (e.g. Hanmer, 2000; Kruse et al., 2001; Rosenberg and Stünitz, 2003; Brander et al., 2012; Viegas et al., 2016) and does not seem to be restricted to lower grade, e.g. green schist facies conditions. The occurrence of fracturing and its possible rate-enhancing influence on dissolution-precipitation creep and nucleation might likely occur in the experiments and in nature at higher-grade conditions.

4.5 Summary and Conclusions

Viscous deformation in our experiments, at the temperatures of 800 °C and confining pressures of 1.0 and 1.5 GPa is dominantly achieved by dissolution-precipitation creep accompanied by grain boundary sliding (GBS). Strain is largely localised into shear bands, formed by a fine-grained mixture of neo-crystallized Pl and the syn-kinematic reaction products Amph, Qz and Zo.

Intense grain size reduction is evoked by high nucleation rates, likely caused by (i) large overstepping of reaction boundaries and (ii) energy minimisation by dissolving defect-rich porphyroclasts. Deformation and nucleation are localised in shear bands, implying a positive feedback between the two mechanisms.

We find no microstructural evidence for a contribution of dislocation glide or creep to strain accommodation for none of the mineral phases.

A weak but consistent crystallographic preferred orientation (CPO) of albite is seen to have formed within shear bands, interpreted to be associated with the dominant strain accommodating mechanisms dissolution-precipitation creep and GBS. The CPO is characterised by alignment of [001] axes along the trace of the shear plane, and poles to (010) at a high angle to it.

Amph is seen to accommodate displacement via dissolution-precipitation creep, as interpreted from the evolution and distribution of Amph coronas on Px grains.

The microstructure and active deformation mechanisms in our experiments compare well to what is frequently described for natural shear zones in mafic rocks. Extrapolation of

the experimental data to even high-grade natural conditions is likely feasible in the case of transport limited diffusion creep as dominant deformation mechanism.

Chapter 5

The semi-brittle field

---

in preparation as: ***Marti, S.*** *, Heilbronner, R., Stünitz, H.*
Low temperature deformation of mafic fault rock and the influence of amorphisation on fault rock strength
To be submitted in: ***Journal of Structural Geology***

Abstract:

Following the previous chapter which focused on the dominant viscous field, this chapter presents the results from a set of deformation experiments performed on Maryland Diabase in the semi-brittle regime. Experiments were performed at 300 - 600 °C, Pc of 0.5 and 1.0 GPa, and 'bulk' strain rates of 10^{-4} to 10^{-6} s^{-1}. At these conditions, the material deforms in a semi-brittle manner in the dominantly brittle field. However, beside a strong pressure dependence of strength, the mechanical data also shows a significant temperature dependence. The latter is usually indicating viscous deformation. The microstructure reveals that strain is highly localised in shear bands often composed of amorphous to nano-crystalline material. Flow-structures such as passive folding of a compositional layering indicate possible viscous deformation of this partly amorphous material. Efforts have been made to derive a first idea on the changing physical properties of this material at different temperatures, using Brillouin spectroscopy. We suggest that the occurrence of amorphous material within our samples causes the pronounced weak-

ening of sample strength for higher temperatures and suggest, that fault zones within the dominant brittle field can potentially show a temperature sensitive rheology where amorphous material is present. A finding with significant implications to our understanding of the rheological behaviour of faults within the semi-brittle field.

5.1 Introduction

At the elevated confining pressures of mid-crustal conditions within the continental crust, rocks are expected to deform in a semi-brittle manner (e.g. Kohlstedt et al., 1995). Rocks thereby achieve significant amounts of strain without abrupt and locaised failure, and deformation is accommodated by pervasive cataclastic flow. The change from localized brittle, to de-localized semi-brittle flow is attributed to the condition that frictional sliding at elevated pressures requires higher stresses than the stresses needed to form a new micro-crack.

Laboratory deformation rates are generally several orders of magnitude higher than natural ones. To overcome the large difference between natural and experimental deformation rates, rock deformation experiments aimed to study viscous deformation frequently take advantage of what might be termed a *temperature-time trade off*. That is, as viscous deformation mechanisms are temperature activated, their rate increases as temperature is increased. Thus, the relatively high experimental strain rates are 'compensated' by performing the experiments at higher temperatures than nature. In contrast, rock deformation experiments in the brittle field are usually performed at ambient temperatures up to $\sim$ 200 °C (e.g. Niemeijer et al., 2012; Brantut et al., 2013, and references therein). Brittle deformation is largely rate and temperature insensitive but highly pressure sensitive. However, there are processes associated with the brittle field that do show a temperature (and rate) dependence. Sub critical crack growth due to stress corrosion cracking is known to have a temperature and thus rate dependence (see e.g. the reviews of Anderson and Grew, 1977; Brantut et al., 2013). Additionally, brittle faulting is sometimes observed to be accompanied by solution-mass transport, activated by grain size reduction due to cataclasis (e.g. Gratier and Gueydan, 2008, and references therein). The occurrence of amorphous material in brittle fault zones (e.g. Yund et al., 1990; Goldsby and Tullis, 2002; Janssen et al., 2010; Pec et al., 2012b; Kirkpatrick et al., 2013; Hayward et al., 2016) may furthermore bear the potential to introduce a time and temperature sensitivity of fault strength.

The occurrence of amorphous material in seismically and aseismically sheared rocks has long been recognised and is reported from deformation experiments under a range of tem-

peratures and normal stresses (e.g. Spray, 1987; Yund et al., 1990; Goldsby and Tullis, 2002; Di Toro et al., 2006; Niemeijer et al., 2011; Pec et al., 2012b; Hayward et al., 2016). In nature, 'pseudotachylytes', which are interpreted to have formed during seismic rupture and melt generation due to frictional heating, are the most commonly described occurrence of amorphous material within fault zones (e.g. Sibson, 1975; Camacho et al., 1995; Obata and Karato, 1995; Curewitz and Karson, 1999; Austrheim and Andersen, 2004). Or understanding of the formation of amorphous material in fault zones and its rheological effect on aseismically creeping faults yet is marginal.
As amorphous materials are likely to deform in a viscous manner, their rheology is expected to be temperature and rate sensitive. Thus, to study their rheological effect in rock deformation studies, experiments should be performed in the intermediated temperature regime, considering temperature as a crucial parameter. At the high laboratory strain rates, time- and temperature- sensitive processes need a certain *temperature-time trade off* to be activated at rates high enough for them to influence the sample rheology. To study the influence of such processes on the rheology of fault zones in the dominant brittle field, it is seen as crucial to extend our dataset of laboratory experiments to higher temperature conditions.
In the following, a set of deformation experiments is presented, deforming a mafic fault rock within the semi-brittle regime at somewhat elevated temperatures of 300 - 600 °C. A significant decrease in sample strength at higher experimental temperatures is attributed to the syn-kinematic formation of nano-crystalline and amorphous material during otherwise dominant cataclastic flow. Based on microstructural observations, the formation mechanisms of the amorphous material will be discussed, as well as its influence on fault rock rheology in the experiments and nature.

5.2 Methods

5.2.1 Experimental conditions

Experiments are performed at temperatures (T) of 300, 500 and 600 °C, at confining pressures (Pc) of 0.5 and 1.0 GPa and constant displacement rates of $\dot{d} \sim 2 \times 10^{-7}$, 2×10^{-8} and 2×10^{-9} m/s (resulting in strain rates of $\sim 3 \times 10^{-4}$, 3×10^{-5} and 3×10^{-6} s^{-1} if homogeneous sample deformation would be attained, Table 5.1).

Table 5.1: *List of experiments and experimental conditions*

Exp. Nr.	T [°C]	average Pc [Mpa]	peak τ [MPa]	average τ at flow [MPa]	thF [mm]	th0 [mm]	total d [mm]	average d rate [m/s]
367	600	582	620	455	0.82	0.64	1.31	2.1E-08
369	500	546	738	680	0.82	0.65	1.44	2.0E-08
373	600	534	614	469	0.82	0.67	1.71	1.9E-08
374	300	562	1101	1012	0.82	0.68	1.60	1.9E-07
375	300	552	1022	954	0.82	0.71	1.56	2.0E-08
395	300	1016	1318	1059	0.82	0.60	1.72	2.2E-08
397	500	1014	1051	890	0.82	0.62	1.59	1.9E-08
399	600	1027	930	752	0.82	0.62	1.85	2.0E-08
401*	500	1012	928	na	0.82	0.75	0.50	7.1E-09
402**	500	~ 1000	na	na	0.82	0.82	0.00	-
418	300	551	978	894	0.82	0.60	2.04	1.9E-08
421	300	517	973	na	0.82	0.72	0.97	9.5E-09
442	300	530		877	0.82			1.9E-08
			963	961		0.59	2.28	1.6E-07
444	300	558	937	869	0.82			1.7E-08
				765		0.66	1.77	2.0E-09
483	500	549	792	665	0.82	0.64	1.83	2.0E-08
501	600	1037	903	688	0.82	0.57	1.86	2.4E-08
509	300	560	1069	957	0.82	na	1.72	2.2E-08
521	300	553	1065	935	0.82	na	1.38	2.2E-08

Exp. Nr.	T [°C]	Pc [Mpa] at peak	Δσ at end [MPa]	thF [mm]	th0 [mm]	total d [mm]	d rate [m/s]
475	300	582	1846	15.80	12.7	3.33	8.3E-09

th0 = shear zone thickness at experiment start, thF = shear zone thickness at experiment end, d = axial displacement of load piston. (∗) experiment terminated at peak stress, (∗∗) experiment terminated at hit-point.

5.2.2 Sample preparation

The starting material is produced from Maryland Diabase rock powder (grain size fraction $\leq$ 125 μm), where all but one experiment were performed with the 45° pre-cut sample setup (as described in section 2.1.3). One experiment (nr. 475) was performed on a cylinder of intact Maryland Diabase, with a cylinder diameter of 6.55 mm and a length of 15.80 mm. The cylinder ends were ground plane parallel (within a precision of 10 μm) and normal to the cylinder axis. 0.18 wt.-% H_2O was added to the sample. The sample was placed in a weld-sealed Pt-jacket with an outer Ni-foil wrap. Due to the slightly larger diameter of the rock core, the Ni-foil did not fit into the Pt-jacket. Otherwise, the sample assembly was equal to the one used in all other experiments.

5.2.3 Brillouin light scattering

Samples used for Brillouin spectroscopy were cut untreated (without epoxy immersion). This procedure was necessary as some of the Brillouin spectra were measured with the sample heated to ≥ 400 °C, which is above the stability of epoxy and most other resins. Polishing of these samples was achieved using the Leica EM TIC 3X Ion Beam Slope Cutter at the centre of nano imaging (SNI) at Basel University. The ion beam cutter was operated at 6 kV, with a sample tilt of 3° and a sample preparation time of 5 h.
Brillouin spectroscopic measurements were performed at the CEMHTI (Conditions Extrêmes et Matériaux : Haute Température et Irradiation) CNRS at the University of Orléans. A Brillouin interferometer JRS Scientific 'Tandem Interferometer' was used, equipped with an Olympus microscope with a 100x microscope objective. The laser is an Oxxius DPSS 532 nm single frequency laser (LCX-532S) with a 100 mW output on the sample when run at 100% capacity.
A first test spectra was acquired with 100% laser capacity but resulted in minor sample damage and some re-deposition of material on the sample surface. From the damaged spot on the sample, the laser spot-size could be measured to be ~ 18 μm in diameter. A second test run then was performed using only 10% of the lasers full capacity (~ 10 mW output on the sample) and no sample damage was observed from this test run. However, the reduction in laser intensity caused the need for longer spectra acquisition durations, which now ranged between 4, up to 16 h (overnight run).
The Brillouin setup is equipped with a Linkam THMS 600 heating stage and the rate of temperature increase during heating was at 20 °C/min. Spectra were attained at room pressure and at three different temperatures of T_B = room temperature (~ 20 °C), 400 and 500 °C.
Brillouin light scattering is the interaction between light (as an electromagnetic wave) and a density wave (phonon) in a material. Thermal motions of atoms in a material create acoustic vibrations, causing density variations and scattering of light. The scattering is inelastic (no energy conservation of the incident ray) and the photon either loses or gains energy by either negative or positive interference with a phonon. The change in the scattered light frequency is seen as a frequency shift (Brillouin shift). The frequency shift thereby is proportional to the wavelenght of the incident light in the material, the scattering angle, and the acoustic wave velocity in the material (Pecora, 1985). Generally said, the Brillouin peak position is a function of bulk material propperties and Brillouin spectroscopy can be used to analyse the elastic properties of a material. Changing physical properties of the material (e.g. due to heating) will be manifested by a shift in the Brillouin peak postition.

Brillouin spectres are presented as normalised intensity vs. frequency shift (cm^{-1}) of the scattered ray. The intensity is normalised to the maximum intensity value of the highest Brillouin peak from each individual spectra. Brillouin peaks by definition have to be symmetric around 0, that is, if a peak appears at a frequency of +20 cm^{-1}, it also has to appear at -20 cm^{-1}. Non-symmetric peaks are not Brillouin scattering and are measurement artifacts. The Brillouin spectra obtained here usually show two non-Brillouin peaks at around +19 and +25 cm^{-1}.

5.2.4 Strain estimates in shear bands

Smeared-out oxide grains on a shear band plane were used for strain estimates. For this, the length (l) and width (w) of the oxide aggregate was measured in BSE images. Under the assumption that the initial oxide grain was $\sim$ isotropic in shape, the length of the oxide aggregate caused by shearing (l_s) is calculated as the measured length minus the width of the aggregate ($l_s = l - w$). Shear strain is calculated by dividing l_s by an assumed shear band thickness of 10 μm. The assumed value for shear band thickness is derived from microstructural observations. As strain estimates are highly sensitive on the assumed shear band thickness, the reported strain values can only be considered to give approximate orders of magnitude in shear strain and not absolute numbers.

5.2.5 Fault zone orientation distribution

Fractures and shear bands were segmented by manual tracing them from BSE (for general shear experiments) and light microscope (for the axial shortening experiment) images. The orientation of shear bands and shear fractures was determined using the 'Analyze Particle' function in Fiji. As especially shear bands can show an anastomosing trend and significant variations in local orientations, they were manually separated into approximately straight segments so that the true orientation of the individual segments could be measured and not an intermediate mean angle derived from measuring an anastomosing shear band as a whole. The minimum length of a structure measured in the case of the general shear experiments was set to 50 μm.
To derive a mode orientation of the measured shear bands and shear fractures, a continuous kernel-density estimator function was fitted on the orientation distribution, using the MATLAB software and the MATLAB function 'ksdensity'.

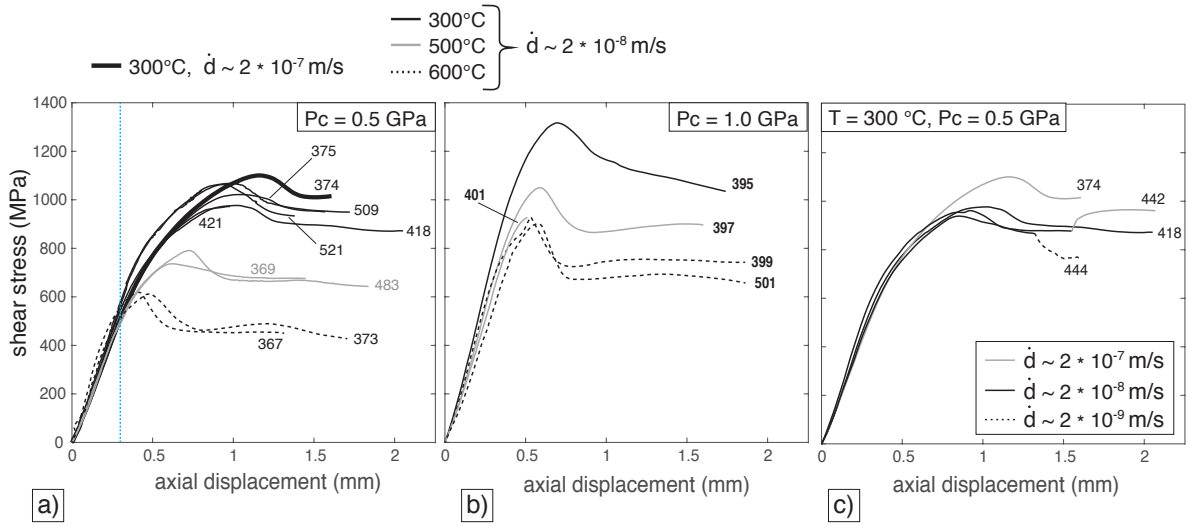

Figure 5.1: *Mechanical data, general shear experiments. Shear stress vs. axial displacement plots for experiments performed at 300, 500 and 600 °C, at confining pressures of 0.5 and 1.0 GPa. a) and b) constant displacement rate experiments. For all experimental temperatures, sample strengths are observed to be both pressure and temperature sensitive. Blue line in a) marks point of significant deviation of linearity in stress - displacement curve for all T. c) Constant displacement rate and displacement rate stepping tests, performed at T = 300 °C, Pc ≈ 0.5 GPa.*

5.3 Resutls

5.3.1 Mechanical data, general shear experiments

At all imposed Pc-T conditions, samples show initial loading to a peak differential stress and subsequent weakening which is often followed by a relatively constant stress value independent of increasing displacement (Figure 5.1a, b). Sample strengths are observed to depend on both, temperature and confining pressure. Pressure dependence is positive, with increasing sample strengths at higher Pc - a behaviour typically associated with dilatant, brittle deformation and frictional sliding. The temperature dependence is negative with lower sample strengths at higher temperatures - a behaviour typical for viscous flow by temperature-activated deformation mechanisms.

Significant amounts of permanent strain are accommodated in all experiments and although all samples show a weakening after peak stress, non experienced abrupt failure and full loss of shear resistance. Interestingly, peak stresses in experiments performed at different T are reached after different amount of displacements. The higher the experimental T, the earlier peak stress is reached (Figure 5.1a). This signal is more pronounced at the lower Pc of 0.5 GPa, than at 1.0 GPa (Figure 5.1a, b). At Pc ≈ 0.5 GPa, the initial part of the loading curves are congruent and approximately linear (for axial dis-

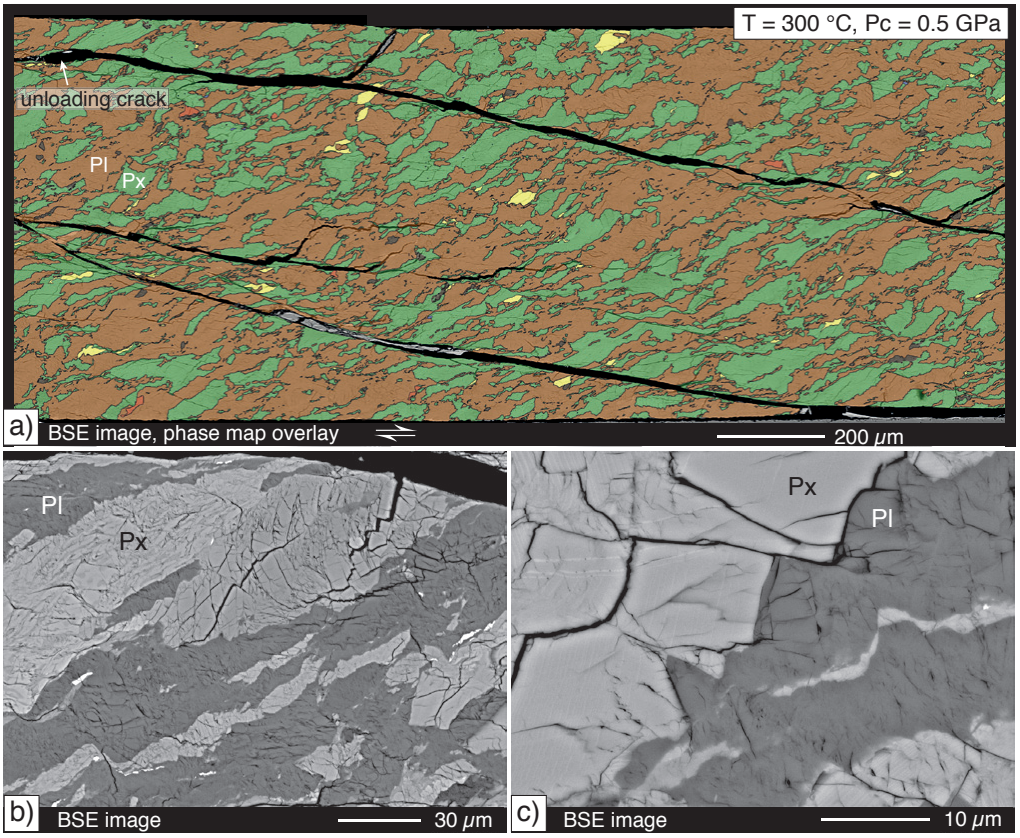

Figure 5.2: *Microstructural overview, general shear experiments, T = 300 °C. a) Central shear zone part of sample 375 deformed at 300 °C and 0.5 GPa Pc. Digital phase map overlay onto BSE SEM image. orange : Pl, green: Px, yellow : oxides, red : apatite, dark grey : Qz. b) The sample shows a foliation, defined by elongated aggregates of intensely fractured grains. c) Grain size reduction by fracturing down to sub-micron sized fragments. Plagioclase usually shows more intense fragmentation than pyroxene.*

placements approximately $\leq$ 0.3 mm, Figure 5.1a).

Figure 5.1c presents displacement rate stepping tests performed at T = 300 °C at Pc $\approx$ 0.5 GPa. Displacement rates were varied between $\sim$ 2 x 10^{-8} to 2 x 10^{-9} m/s, and $\sim$ 2 x 10^{-8} to 2 x 10^{-7} m/s. Sample strength is relatively insensitive to the imposed displacement rate, and stress exponents calculated from the data are on the order of n $\approx$ 21 (see chapter 3, section 3.3.1.3).

5.3.2 Microstructural overview - general shear experiments

The deformed samples show pervasive and intense grain size reduction by fracturing. A foliation, defined by elongated mineral aggregates, is formed due to cataclastic flow (Figure 5.2). Both, plagioclase and pyroxene are intensely fractured. However, by tendency, pyroxene grains more frequently show larger (longer through-going) fractures and larger

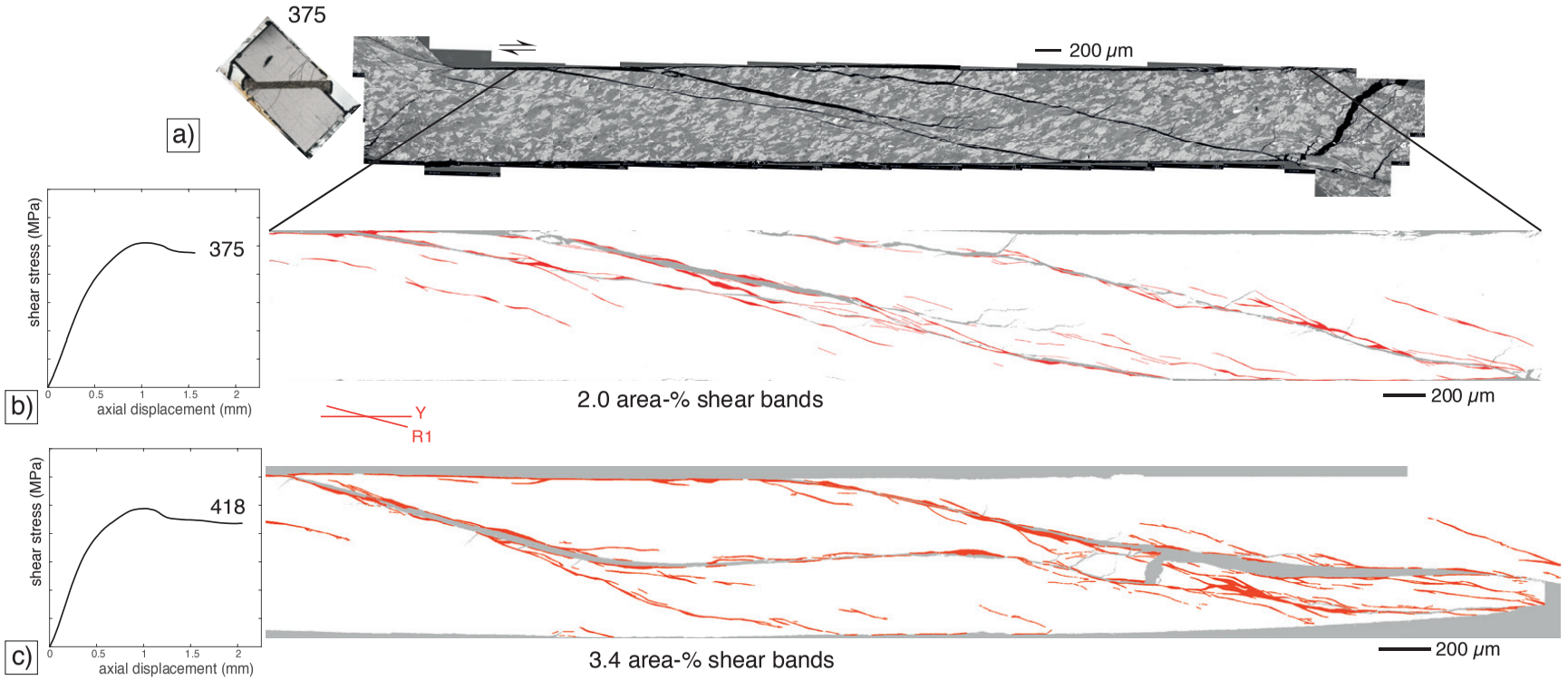

Figure 5.3: *Fault zone network in 300 °C experiments. Strain is localised into fault zones formed from segments of shear bands and shear fractures, traversing the sample usually in two to three main fault strands. a) thin section scan of sample 375 and BSE SEM image of the shear zone. b) and c) Mechanical data and segmented fault zones (red) for samples 375 (b) and 418 (c) respectively. In grey: unloading cracks or missing area. Area-% of shear bands are given for both samples. R1 = orientation of synthetically inclined Riedel shear, Y = orientation of Y-shear.*

non-fractured domains, whereas plagioclase fractures pervasively to fine fragments, without exploiting more dominant fractures (Figure 5.2c).
In all samples, strain localises into a network of shear bands and larger shear fractures. Usually, two to three bigger fault strands crosscut the sample, transferring displacement from one end of the sample to the other (Figure 5.3). For experiments at 300 °C, the amount of shear bands is seen to increase with increasing shear displacement, from ∼ 2.0 area-% in sample 375 (1.56 mm axial displacement) to ∼ 3.4 area-% in sample 418 (2.04 mm axial displacement).
Although pervasively fractured and deformed by cataclastic flow, the sample material is cohesive after the experiment, as was seen from samples that were cut without preceding epoxy immersion.

5.3.2.1 Shear bands

Shear bands are observed to either be ultra-cataclasites (thereafter referred to as *type I* shear bands) or from a material which is presumed to be of nano-crystalline or amorphous nature (in the following termed *type II* shear bands). The *type I* shear bands will be mentioned again in a later section (5.3.6) and in the following, we will focus first on the *type II* shear bands. They occur most ubiquitously at 300 °C, especially at the lower Pc of 0.5 GPa. They are recognised by a strong foliation deflection and the foliation within the shear bands is defined by a nano- to micrometer scale compositional layering of strongly elongated aggregates of the different mineral phases (Figure 5.4). *Type II* shear bands occur in variable thicknesses but vary mostly between ∼ 2 μm up to 20 μm in thickness. In 300 °C experiments, they appear to become wider with increasing displacement imposed on the sample (Figure 5.3). This behaviour is not so obviously observed for the higher T experiments at 500 and 600 °C.
The compositional layering within the *type II* shear bands is frequently perturbed in what appears like flow structures and no porosity by fractures is observed within them, in contrast to the surrounding host material (Figure 5.4b - d). The host material shows pervasive microfracturing and the transition from the fractured host to the homogeneously appearing shear band appears to be relatively abrupt (Figure 5.4b, c). Unloading cracks are localised within the *type II* shear bands, indicating a lesser amount of expansion upon unloading to room conditions at the experiment end, compared to the bordering host material.

Upon unloading to room conditions, some of the samples cracked apart along the forcing block interface and/or larger fault zones, giving the opportunity to examine the fault zone

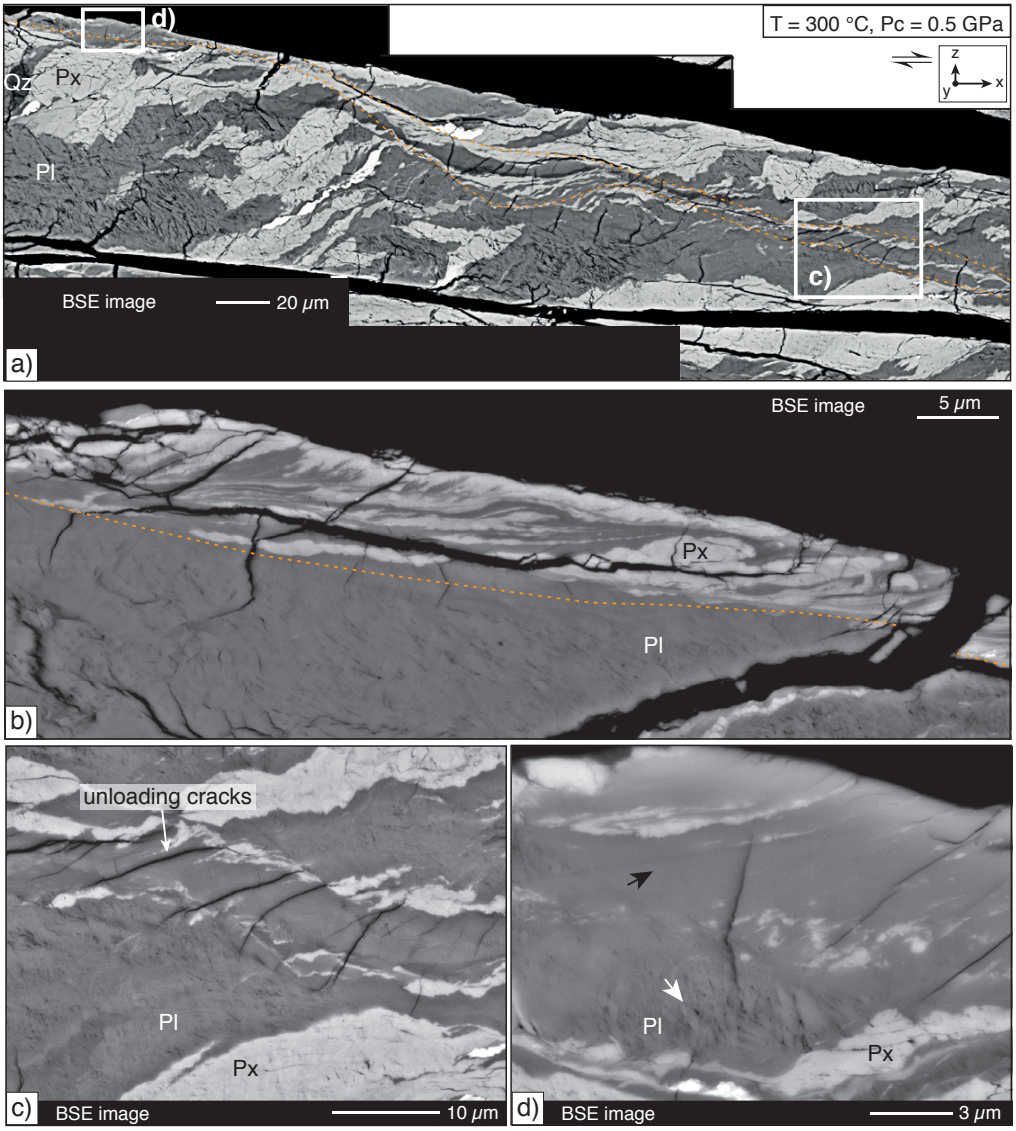

Figure 5.4: *Morphology of type II shear bands in 300 °C experiments. a) Shear band (traced in orange) crosscutting the sample in Riedel R1 orientation. b) Shear bands can be identified by a strong foliation deflection and a fine-scale compositional layering defining a foliation. The compositional layering can be laminar or perturbed in what appears like flow structures. c) Unloading cracks preferentially form within the shear band material. c) and d) A sharp transition between intensely fractured host and shear bands is seen. White arrow in (d) points to small pores in the fractured host material. The shear band material appears homogeneous and no porosity or fractures are visible.*

planes. Linear structures, parallel to the shear direction are observed and the exposed fault surface show alternating rougher and highly polished parts (Figure 5.5). From the sheared oxide grains, which are easily identified in BSE SEM images, approximate strain estimates are derived. The assumption is made, that the oxides are sheared within a shear band of a thickness of 10 μm. This is a conservative estimate of the width of the

shear bands which are ubiquitously occurring along the forcing block interface as seen from the thin section. With this procedure, strains in the range of 38 - 62 are estimated (Figure 5.6).

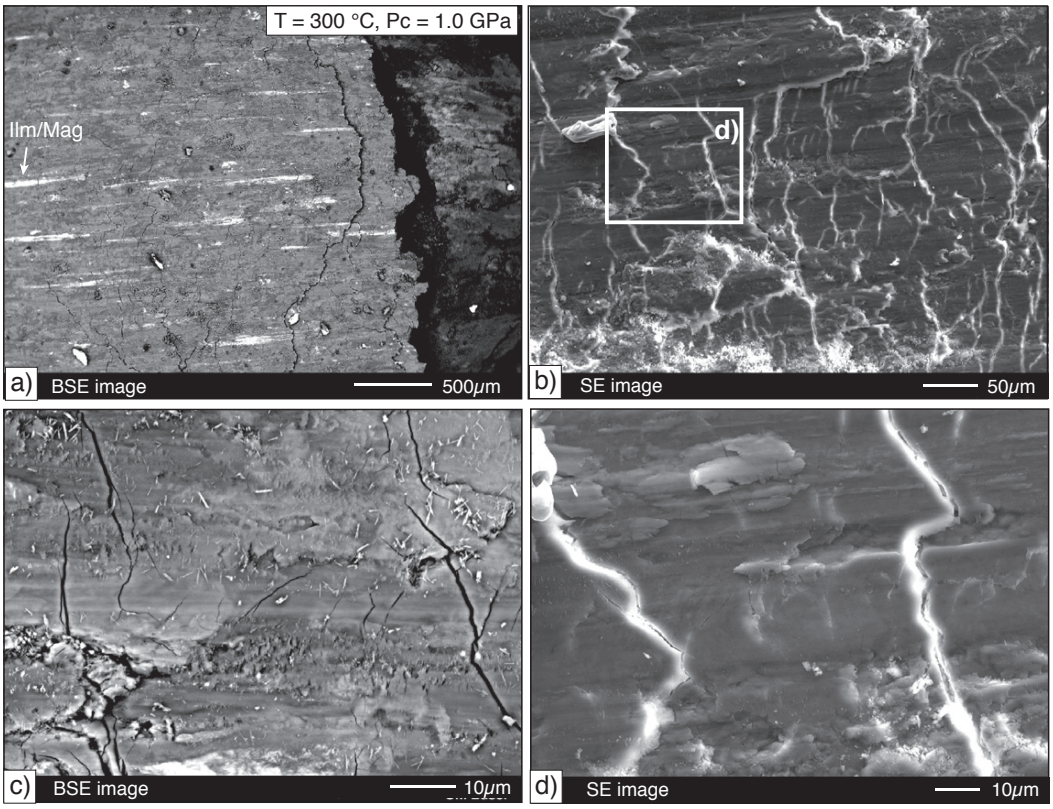

Figure 5.5: *Top-view onto a fault plane, shear sense is top to the right. Sample deformed at 300 °C, 1.0 GPa. a) BSE SEM image. White streaks are sheared oxide grains. b) SE SEM image showing variable roughness of the fault plane. Linear features indicate the shear direction. c) BSE SEM image. Variations in surface roughness are not systematically correlated with mineral phase (Px : light grey. Pl : dark grey). d) SE SEM image of area marked in b), showing a close-up on the mirror-surface like streaks.*

An experiment (T = 300 °C, Pc ≈ 0.5 GPa) terminated at peak stress shows the microstructure that formed during the loading part of the experiment. A pervasive, weak foliation caused by cataclastic flow and resulting aggregate elongation is already formed when reaching peak stress (Figure 5.7). Strain is yet only weakly localised but some zones of more intense grain size reduction by fracturing are observed, with minor localisation of shear displacement within them (Figure 5.7b, c).

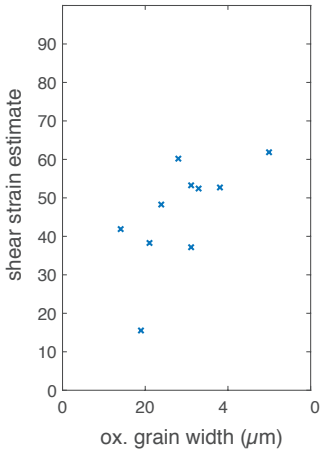

Figure 5.6: *Strain estimates from smeared-out oxides on fault surface shown in Figure 5.5. Most shear strain estimates range between ∼ 40 - 60. A weak correlation between width and shear strain estimate might indicate a weak bias of the method predicting higher strains for larger oxide particles.*

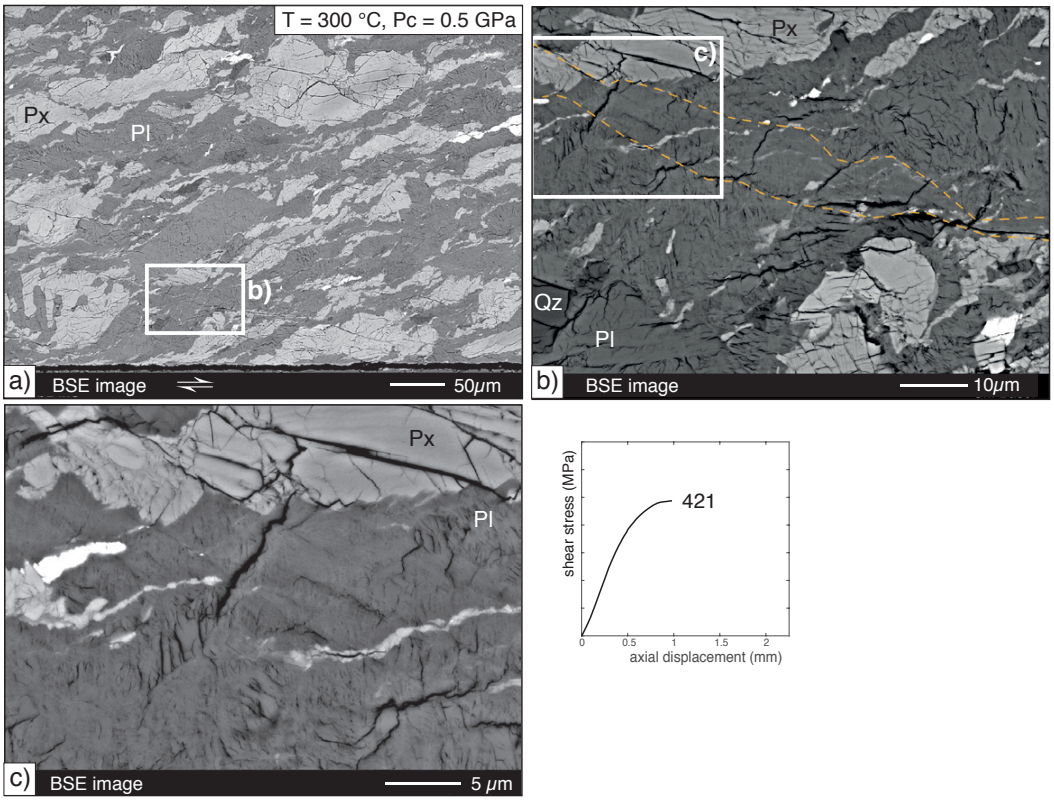

Figure 5.7: *Initial zones of shear localisation at peak stres. a) Overview shear zone in experiment 421 (300 °C, 0.5 GPa Pc), terminated at peak sterss. Localisation is only weakly developed and deformation is mainly accommodated by cataclastic flow of the bulk sample. b) Close-up on area marked in a). Ultra-cataclastic zone (traced in orange) with minor strain localisation as seen from the weak deflection of small Px aggregates. c) Close-up on area marked in b). The ultra-cataclasite is difficult to identify in the close-up view but shows a subtly stronger grain size refinement by more intense fracturing.*

5.3.3 Microstructures, axial shortening whole-rock core experiment vs. general shear experiments

With the 45° pre-cut set-up, the material is confined between the rigid alumina forcing blocks and the direction of shear is pre-defined. To examine the possible influence of this pre-defined geometry, a 'non-constraint' axial shortening experiment was run on a whole-rock core cylinder, at T = 300 °C and Pc ≈ 0.5 GPa (Figure 5.8). The displacement rate is ∼ 2 x 10^{-8} m/s, the same as for most of the shear experiments. Noting however, that the rock sample is much larger in the axial shortening case and thus, the resulting strain rate in case of homogenous deformation would be approximately one order of magnitude lower in the axial shortening than in the general shear set-up.
The mechanical data of the axial shortening experiment (nr. 475) and a general shear experiment (nr. 418) are compared as differential stress ($\Delta\sigma$) vs. axial displacement (Figure 5.8d). Although the shear experiment is performed on a pre-crushed rock powder and the axial shortening experiment on a whole rock sample, the initial loading curves of sample 418 and 475 are congruent. The axial shortening sample 475 then deviates to lower stresses for equal amounts of axial displacement. Whereas 'yield' occurs in both samples at approximately the same amounts of axial displacements, stresses are 227 MPa higher in experiment 418. Experiment 418 shows a pronounced weakening whereas experiment 475 shows a weak but steady hardening. The fault pattern developed in experiment 475 shows multiple conjugated faults, interfering, i.e. crosscutting each other (Figure 5.8c). Additionally, the major faults at the bottom of the sample interfere with the lower alumina piston. This interference is thought to be causing the continuing hardening.
The thin section of sample 475 was fabricated from a section as close as possible to be parallel to the dip direction of the major fault zone marked in red in Figure 5.8a. Zooming into the major fault shows strikingly similar microstructures to the ones observed in the general shear experiments. A weak foliation formed in the close vicinity of the main fault zones (Figure 5.8e - g) and the narrow, ∼ 10 - 20 μm wide main fault shows the same structures as *type II* shear bands found in the general shear experiments: that is, strong foliation deflection and a compositional banding defining a foliation parallel to the shear band boundaries, flow structures, no resolvable syn-kinematic porosity and an accumulation of unloading cracks (compare e.g. with Figure 5.4).

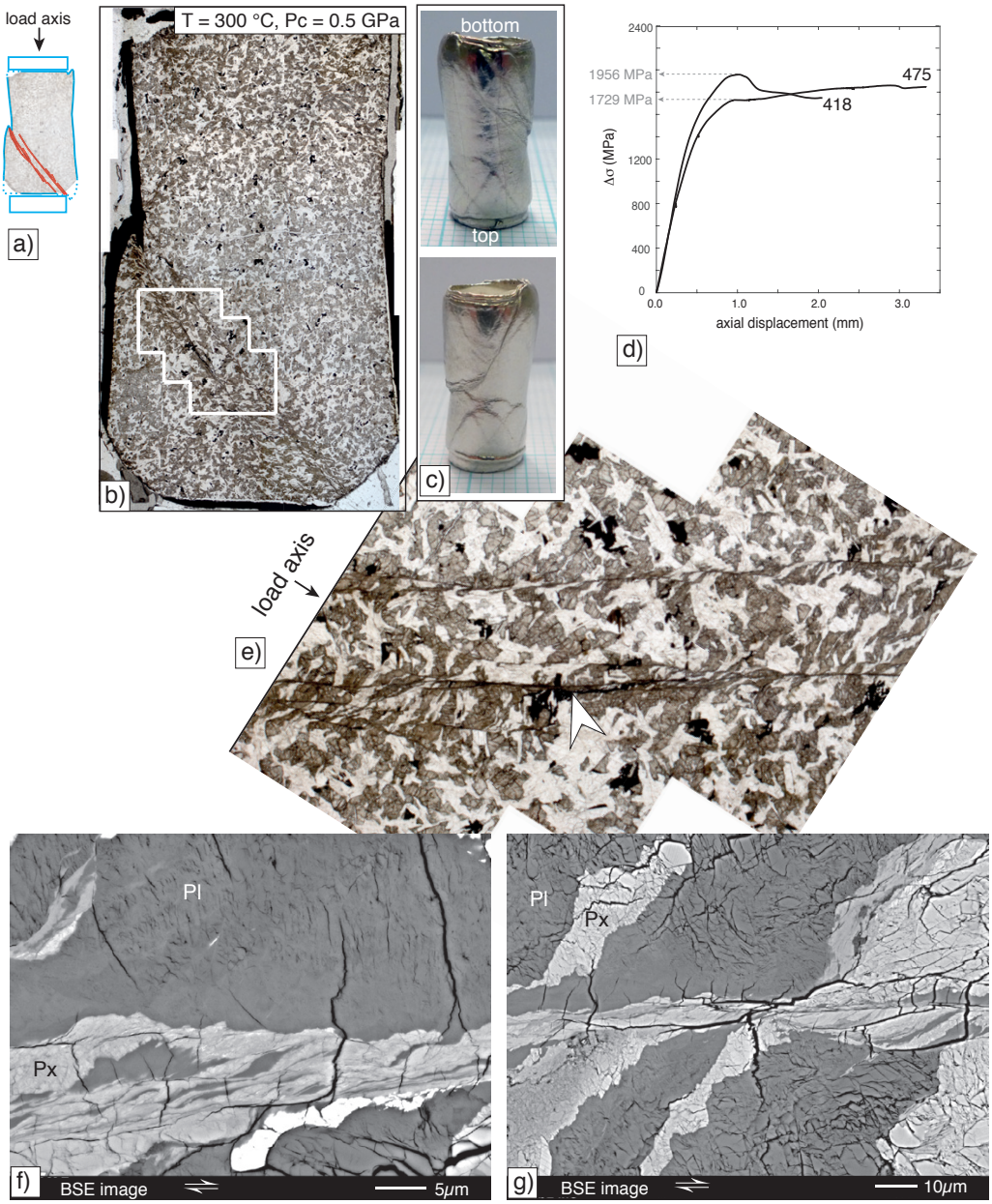

Figure 5.8: *Whole rock core axial shortening experiment (300 °C, 0.5 GPa Pc). a) Sketch of sample 475 with the main fault zone traced in red. b) Thin section scan, plane polarized light. Marked area is shown in e). c) Sample just after the experiment still sealed in the metal jacket. Conjugated faults are seen to crosscut the sample. d) Mechanical data (differential stress vs. displacement) of the axial shortening experiment 475 and the general shear experiment 418. Differential stress values at yield are indicated in grey. e) Light microscope image, plane polarized light. Two fault strands are seen, with a foliation formed in the adjacent host rock. White arrow marks location of image f). f) and g) BSE SEM image close-up view on a fault strand. The same microstructure as in the general shear experiments is observed within and around fault zones. I.e. thoroughly fractured host rock and amorphously appearing shear bands with flow structures.*

5.3.3.1 Fault orientations

Figure 5.9 shows the orientations of fault strands (shear bands and shear fractures) towards the load axis, for the major fault in the axial shortening experiment 475 (Figure 5.8a), and the fault network in two general shear experiments (375 and 418, Figure 5.3). The general shear experiments differ in total amount of axial displacement, with 1.57 mm for sample 375 and 2.05 mm for sample 418. Axial displacement of sample 475 is 3.33 mm.

As the dominant mode of failure is brittle, unconstraint faults are expected to show orientations around 30° away from the load axis. Sample 475 shows 79% of all fault orientations between 20 - 40° from the load axis (Figure 5.9a). Mainly shorter (< 0.3 mm) fault strands show a broader scatter in orientation. In the general shear experiments, the rock material is constraint by the 45° pre-cut alumina forcing blocks. Disregarding, for smaller axial displacements (sample 375) most faults (85%) are oriented with 20 - 40° towards the load axis and thus faults are not parallel to the boundaries imposed by the forcing blocks. With increasing displacement (sample 418), faults with orientations $> 40°$ to the load axis increase in number, while 66% of all measured fault segments remain with orientations of 20 - 40° to the load axis. The frequency distributions of fault orientations for the different experiments all show similar modes (in the range of 32 - 34°) (Figure 5.9b). The distributions however vary somewhat with a narrow distribution of fault orientations for sample 375 and a broader distribution for the larger displacement experiment 418. The axial shortening experiment shows a narrow range of high frequency bins with some low-frequency bins broadening the distribution.

5.3.4 Shear bands structures observed in TEM

Type II shear bands formed in general shear experiments at T = 300 °C, Pc = 0.5 GPa and T = 600 °C, Pc = 1.0 GPa were studied in more detail by preparing FIB foil cuts and analysing the foils using TEM. The analysed shear bands from both temperatures are composed of nano crystalline and amorphous material in lenses and layers (Figure 5.10). The amorphous nature can be confirmed by lack of diffraction spots in diffraction patterns, lack of beam diffraction in bright field images disregarding of the tilt angle, and the uniform grey value, intermediate between bright diffracting and dark non-diffracting crystals, in DF images. Within the amorphous layers, few dispersed nano crystals are observed and amorphous layers alternate with elongated lenses of nano crystalline aggregates (Figure 5.10b, c). The latter are mostly observed to be formed by pyroxene. Pyroxene nano crystals are observed to have an elongated shape with a shape preferred

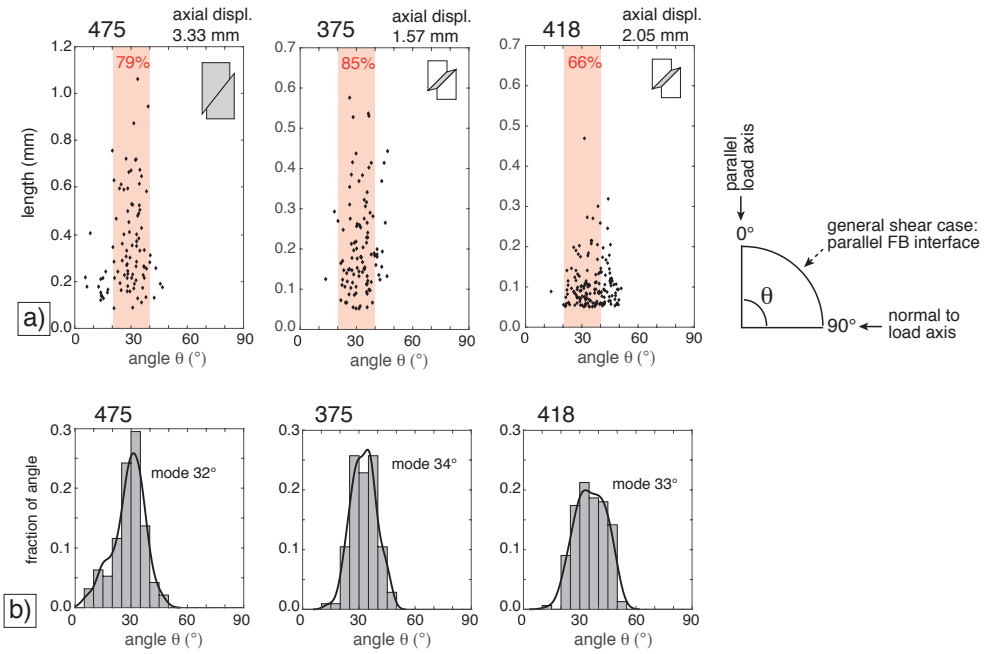

Figure 5.9: *Fault-orientation measurements comparing the axial shortening experiment 475 to the two general shear experiments 375 and 418. a) Fault segment length vs. fault segment angle plots. Reference frame on the outer right. FB = forcing block. Total axial displacement achieved during the experiments is given above each plot. Red-shaded area marks angles between 20 - 40° and number in red gives the frequency-% of faults within this range. b) Frequency distribution of fault orientations as histogram (grey bars) and continuous kernel density estimate fit (black line).*

orientation parallel to the shear direction (Figure 5.10b). The border between nano crystalline aggregates and adjacent amorphous layers is seen to be relatively sharp.
The area shown in Figure 5.10e was mapped with TEM EDS and element densities were obtained from sites on three different materials, the amorphous shear band, a nanocrystalline pyroxene aggregate and a highly fractured plagioclase aggregate in the host (Figure 5.10f). The element distribution of the shear band is similar to the plagioclase material, with similar Al, Ca, and Si contents. Na is depleted in the shear band but this could be caused by the susceptibility of Na to evaporate from the material under the electron beam, particularly in the amorphous zones. Some Mg and Fe are detected within the shear band, indicating the presence of Px derived material.

5.3.5 Brillouin spectroscopy

Brillouin peaks are a measure of the elastic properties of a material. For amorphous material, the elastic modulus (amongst other physical properties) is observed to change measurably with changing temperature as the glass transition temperature (T_g) is crossed.

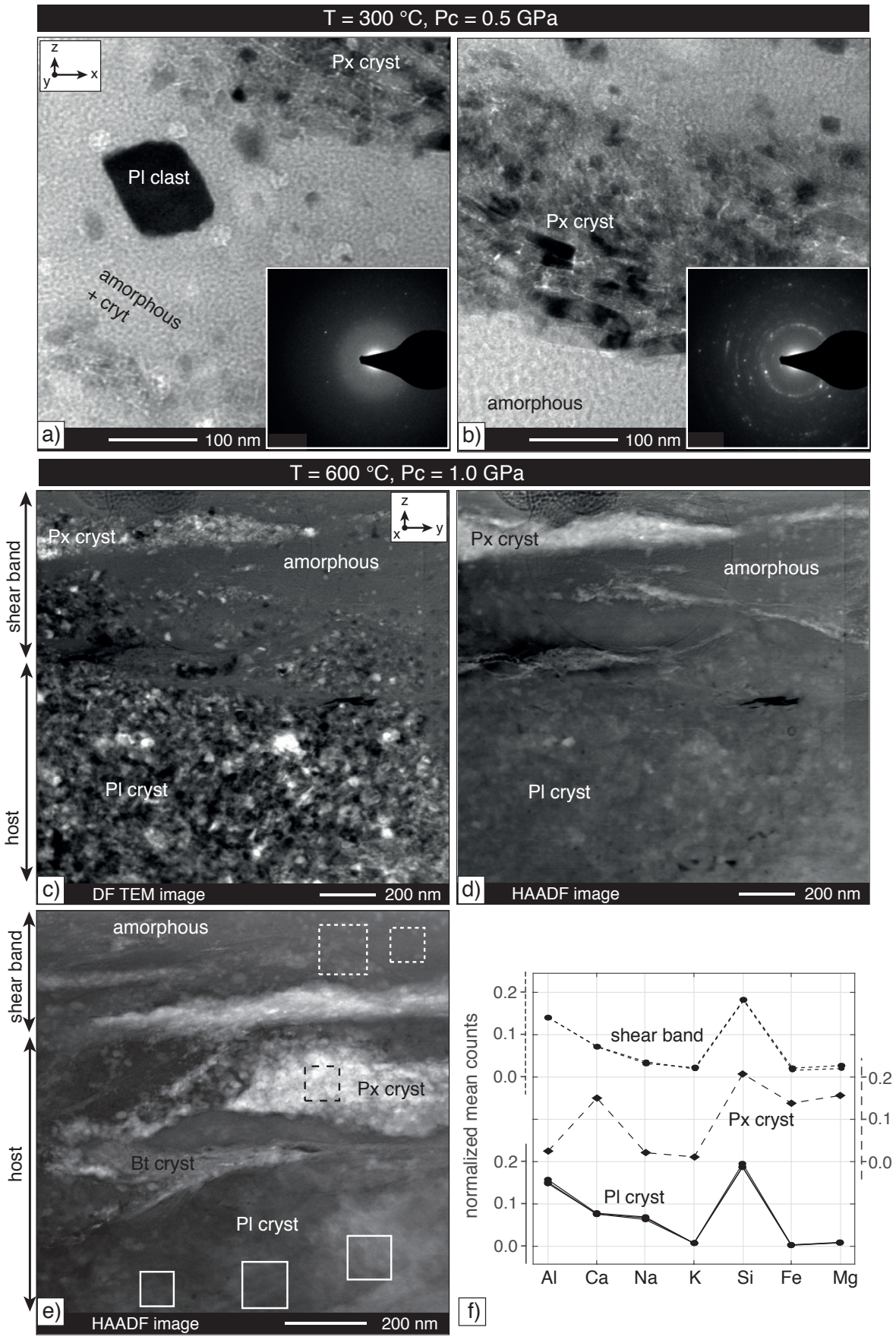
T = 300 °C, Pc = 0.5 GPa
Px cryst
Pl clast
amorphous
+ cryt
a)
100 nm
Px cryst
amorphous
b)
100 nm
T = 600 °C, Pc = 1.0 GPa
shear band
host
Px cryst
amorphous
Pl cryst
c)
DF TEM image
200 nm
Px cryst
amorphous
Pl cryst
d)
HAADF image
200 nm
shear band
host
amorphous
Px cryst
Bt cryst
Pl cryst
e)
HAADF image
200 nm
normalized mean counts
shear band
Px cryst
Pl cryst
Al
Ca
Na
K
Si
Fe
Mg
f)

Figure 5.10

Figure 5.10: *Nano-structure of type II shear bands from 300 and 600 °C experiments. a) and b) BF TEM image and diffraction pattern from a shear band formed at 300 °C, 0.5 GPa Pc. Section portrayed is parallel to shear direction and normal to the shear zone boundaries a) Amorphous layer, with few remaining nano-crystals, bordered at the upper right by a layer of pyroxene nano-crystals. b) Polycrystalline, nano-meter sized Px aggregate (middle) bordered by largely amorphous zones. c) - e) TEM images from a shear band formed towards the forcing block interface at 600 °C, 1.0 GPa Pc. Section portrayed is normal to both shear direction and shear zone boundaries c) and d), same area, recorded in DF and HAADF mode respectively. e) HAADF image of an area which was mapped with EDX in the TEM. The sites indicated are quantified for their element distribution shown in f). f) Normalised element counts for the elements Al, Ca, Na, K, Si, Fe and Mg. Two sites are evaluated from the amorphous part of the shear band, one site from a nano-crystalline Px aggregate and three individual sites from a Pl aggregate. cryst = crystalline*

In the Brillouin spectra, such a change in is indicated by a shift in peak position.
Brillouin spectra were obtained from the area of a *type II* (partly amorphous) shear band, formed in a T = 300 °C, Pc ≈ 0.5 GPa experiment. Obtaining Brillouin spectra with the sample heated to different temperatures, a first idea of the changing physical properties of this material as a function of T could be obtained. The spot size of the laser in the Brillouin setup is somewhat larger than the width of the shear band, and the bulk measured material will both contain the amorphous shear band as well as the fractured but crystalline host material.
Due to the difficult sample preparation that had to be achieved without resin impregnation, much of the amorphous material was lost during preparation and only one sample was successfully prepared for Brillouin spectroscopy. The difficulty of the sample preparation and the long durations of spectra acquisition determine the scarce data. Nonetheless, successful runs of Brillouin spectra measurements were obtained from one sample, and with the sample heated to three different temperatures (T_B) during Brillouin spectra measurement. The temperature of sample deformation during the deformation experiment should not be confused with the temperature to which the sample was heated during the Brillouin measurements. The latter therefore is referred to as T_B. Brillouin spectra were obtained with the sample heated to T_B = room temperature (∼ 20 °C), 400 and 500 °C. In the spectra, three distinct Brillouin peaks are recognised (Figure 5.11a, b) and the middle one is observed to shift its position with increasing T_B. Plotting the peak position vs. T_B shows that the peak shift between room-T to 400 °C is smaller than between 400 to 500 °C (Figure 5.11c). Furthermore, with increasing T_B, the intensity-ratio of the shifting peak with respect to the prominent stationary peak (positioned at ∼ ± 27 cm^{-1}) changes with increasing dominance of the shifting peak.

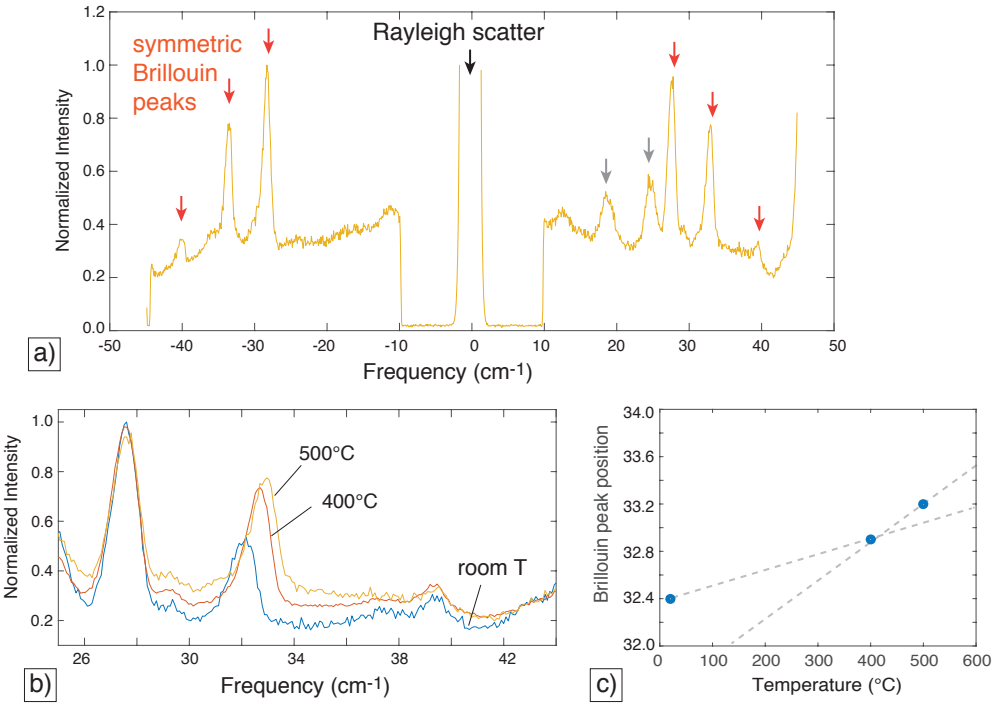

Figure 5.11: *Brillouin light scattering analysis. a) Full length of the spectra obtained at T_B 500° C. Only symmetrical peaks are considered (red arrows). The two non-symmetrical peaks (grey arrows) are a machine internal artifact and don't represent Brillouin scattering. b) Normalised intensity vs frequency shift plot of three different Brillouin spectra collected at different temperatures T_B: room T, 400 and 500 °C. A shift of the middle peak (at around 32 to 33 cm^{-1}) is observed with increasing temperature. c) Brillouin peak position vs temperature of the shifting peak. Blue dots represent measured peak position, grey lines are line fits through the points at room-T and 400 °C and 400 °C and 500 °C respectively.*

5.3.6 Microstructural comparison between 300, 500 and 600 °C experiments

Shear bands are not always composed of amorphous material but can also form within fine-grained cataclastic bands (*type I* shear bands, Figure 5.12). The amorphous *type II* shear bands are most ubiquitous in 300 °C experiments, whereas the cataclastic *type I* shear bands occur more commonly at 500 and especially 600 °C, as well as more common in the lower Pc experiments. However, shear bands formed at the interface to the forcing block, at all temperatures and confining pressures, are dominantly of *type II*.

Type I shear bands usually are narrow ($<$ 10 μm in width) and are formed from sub-micron sized, angular grains (Figure 5.12a, b). At 600 °C and Pc $\approx$ 0.5 GPa, uniquely, up to 20 μm wide cataclastic *type I* shear bands form from relatively rounded grains with a broad grain size distribution (Figure 5.12c, d). In 600 °C at both 0.5 and 1.0 GPa Pc, pore trails are ubiquitous (Figure 5.12e), indicating limited solution mass transport

and partial fault healing.
Figure 5.13 presents a comparison of the fault networks formed within 300 and 600 °C experiments, at Pc of 0.5 and 1.0 GPa. 300 °C experiments show displacement transfer traversing the sample in a network of mainly amorphous shear bands and discrete shear fractures. 600 °C experiments often show strong strain localisation at the forcing block - sample interface in amorphous *type II* shear bands. Some displacement is accommodated along a fault network traversing the sample, where the fault segments are formed by *type I* and *type II* shear bands and shear fractures. At the higher confining pressure of 1.0 GPa (Figure 5.11c, d), shear fractures become more dominant, *type II* shear bands tend to be thinner and *type I* shear bands are scarce, even at 600 °C. The microstructure of 500 °C experiments is not shown but is intermediate between the 300 and 600 °C experiments.

5.4 Discussion

5.4.1 Overview

At all temperatures the microstructure is defined by pervasive fracturing (brecciation), leading to grain size reduction, and cataclastic flow. The observed significant amounts of displacement accommodated without abrupt failure are typical for semi-brittle deformation (Figure 5.1a, b). However displacement in all samples becomes highly localised at around peak stress, partitioning into a fault network of thin shear bands and shear fractures (e.g. Figure 5.3, Figure 5.13).

Low strain lenses
The material in low strain lenses (referring to the material outside of shear bands) shows intense grain size refinement by fracturing (Figure 5.2). Both pyroxene and plagioclase fracture extensively but plagioclase shows a higher susceptibility to fragmentation (Figure 5.2). Only small amounts of displacement are needed to pervasively fracture the sample (see e.g. sample 421, terminated at peak stress after an axial displacement of $\sim$ 1 mm, Figure 5.7). As the initial sample material is fabricated from a rock powder, the sample contains some residual porosity after pressurisation and prior to the start of the experiment. During the initial loading of the sample, this porosity is closed by grain crushing and compaction. The small amounts of displacement needed for pervasive fracturing is likely caused by high stresses around pores and the susceptibility to fracturing of plagioclase and pyroxene attributed to their cleavage planes.

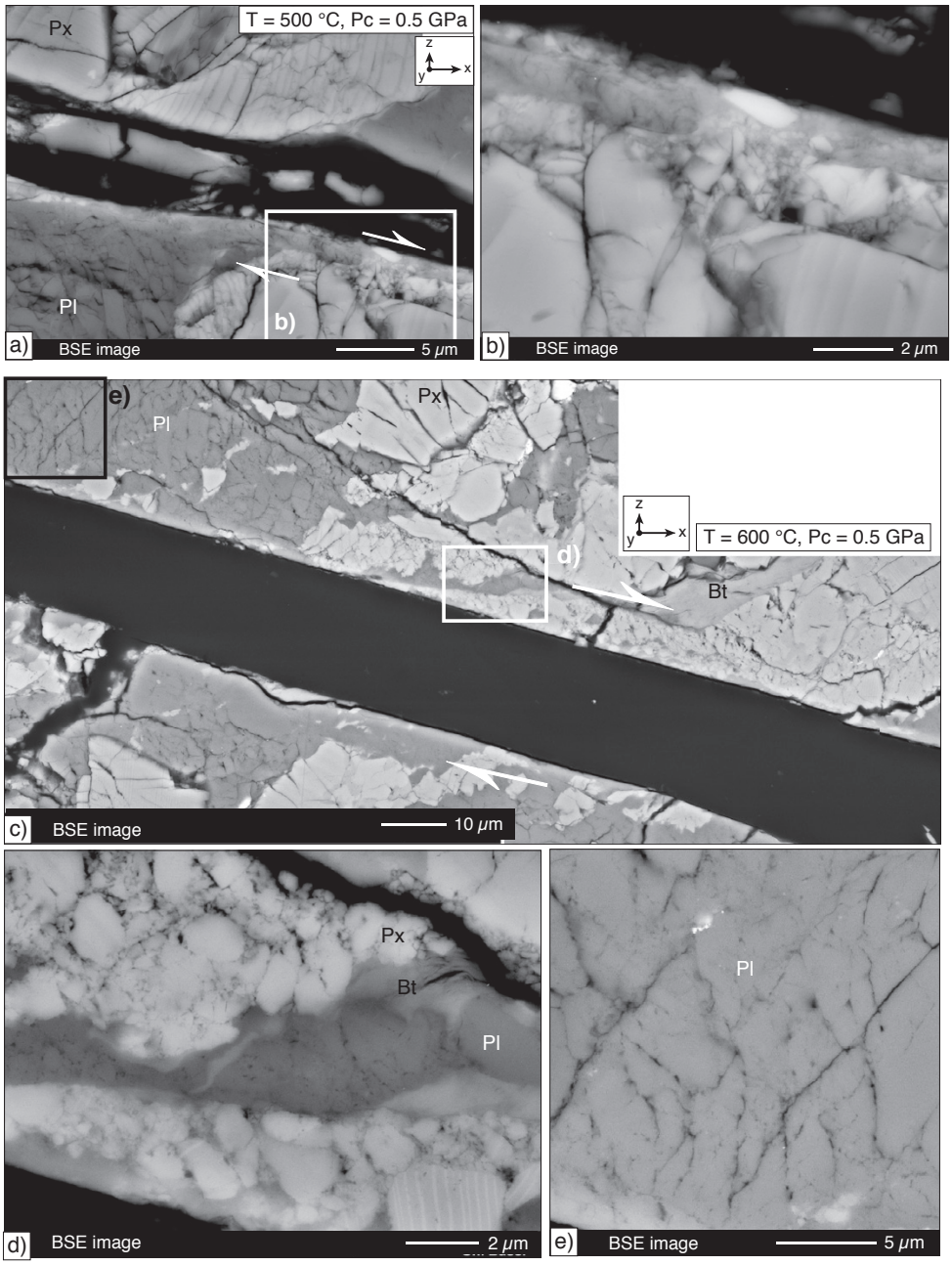

Figure 5.12: *Microstructure of (ultra-)cataclastic shear bands. a) Shear is accommodated in a very narrow (∼ 2 µm) wide, ultra-cataclastic zone. Sample deformed at 500 °C, 0.5 GPa Pc. b) Close-up of area marked in a). The ultra-cataclastic zone consists of sub-micron sized angular fragments. c) and d) Unique cataclastic shear bands only formed in 600 °C, 0.5 GPa Pc experiment. Shear bands are composed of rounded grains with a broad size distribution. e) At 600 °C, fractures are frequently decorated with pore trails, indicating limited healing.*

Shear bands

Strain in all samples is localised in fault zones formed by segments of shear bands and

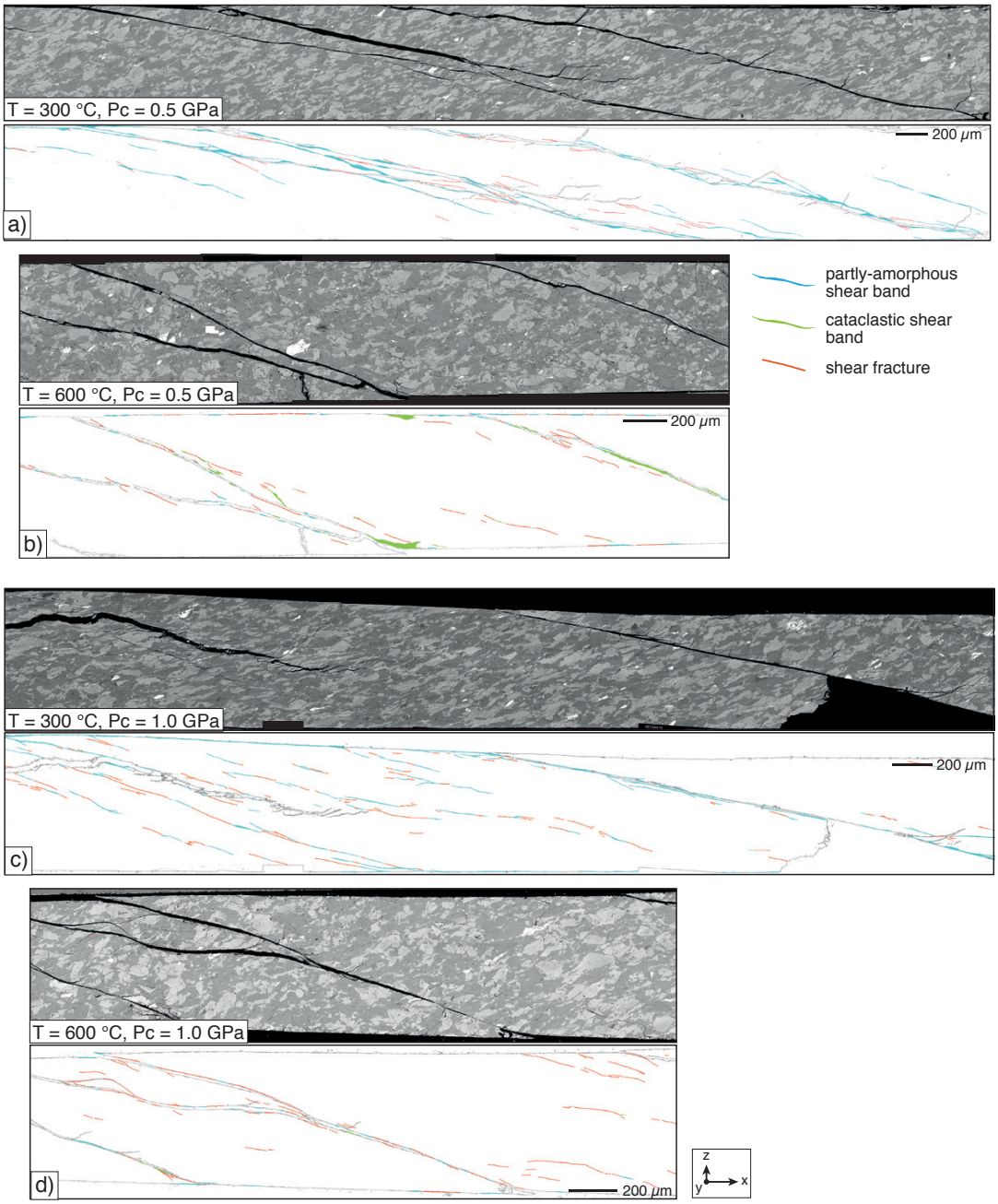

Figure 5.13: *Microstructural overview and segmented fault zones formed at 300 and 600 °C, Pc of 0.5 and 1.0 GPa. BSE images (top) show central parts of each sample. Underneath, the same area is shown with segmented fault zones. Blue: amorphous type shear bands, green: cataclastic type shear bands, red: shear fractures.*

shear fractures. Two types of shear bands are distinguished, *type I* shear bands, formed by (ultra-)cataclasites (Figure 5.12), and *type II* shear bands, formed by partly amorphous material (Figure 5.4; Figure 5.10). *Type I* shear bands are most frequently occurring at the higher experimental T of 500 and 600 °C and the lower Pc of 0.5 GPa. At the

higher Pc, the formation of *type I* shear bands seem to be suppressed and shear fractures dominate (Figure 5.13d). This observation suggests, that at the high Pc, the dilatancy necessitated from granular flow by shearing in a cataclastic shear band is increasingly impeded.
300 °C, Pc ≈ 0.5 GPa experiments at low displacements also show frequent *type I* shear bands (Figure 5.7), whereas such ultra-cataclastic shear bands are lacking in the microstructure at higher displacements. There, *type II* shear bands are ubiquitous (Figure 5.13a). Although the direct transition is not clearly observed, we interpret from the microstructure that the partly amorphous *type II* shear bands develop with increasing displacement from the ultra-cataclastic *type I* shear bands.
Type II shear bands are made of a cohesive, non-porous material, with only few resolvable grains at SEM resolution, and a nano- to micro scale compositional layering, either laminar or perturbed in flow structures (Figure 5.4). From TEM observations, *type II* shear bands are seen to be partly amorphous, with amorphous and nano-crystalline material in layers and lenses (Figure 5.10).

5.4.2 Mechanical data vs. microstrucutre

In accordance with the dominant brittle deformation (as interpreted from the microstructure) the mechanical data shows a positive pressure dependence of strength at all experimental temperatures (Figure 5.1a, b). As fracturing is a process accompanied by dilatancy, it demands work against the confining pressure, hence increasing confining pressure impedes fracturing. Unexpectedly however, the temperature sensitivity is observed to be as pronounced, with significantly weaker samples at higher experimental temperatures. This behaviour is typically associated with temperature activated viscous processes.
Based on microstructural observations, two possible causes for the temperature dependence of strength are seen: (i) Solution-mass transport is indicated at 600 °C by the observation of pore trails along healed fractures (Figure 5.12e). (ii) Partly amorphous shear bands form in all experiments, exhibiting flow structures and are seen to accommodate large amounts of displacement.
The effect of solution mass transport to the sample rheology is considered to be subordinate. The amount of transported material appears to be small and no indicators for significant strain accommodation by solution-mass transport are observed in the microstructure. Conversely, the amorphous type shear bands are seen to accommodate the major part of the displacement and thus are more likely to be influencing the bulk

rheology.
Amorphous material is found along fault zones in nature as well as in experiments, whereas many of these observations are attributed to frictional melting during seismic slip rates (e.g. Philpotts, 1964; Sibson, 1975; Mc Kenzie and Brune, 1972; Di Toro et al., 2005; Spray, 1987; Hirose and Shimamoto, 2005; Del Gaudio et al., 2009; Niemeijer et al., 2011; Hayward et al., 2016). However, also from aseismically creeping faults, amorphous material has been reported, both from nature (e.g. Janssen et al., 2010) and experiments (e.g. Yund et al., 1990; Goldsby and Tullis, 2002; Pec et al., 2012a,b; Hayward et al., 2016). Pec et al. (2012b) and Yund et al. (1990) attribute the formation of amorphous material to mechanical wear and resultant loss of crystallinity during deformation of their samples. An effect also observed from ball-milling (e.g. Sanchez et al., 2004). We agree with the interpretations of these authors and also suggest that the amorphous zones in our samples formed from mechanical wear during deformation.
In the granitoid samples of Pec et al. (2012b) and Yund et al. (1990), feldspars are seen to readily become amorphous, whereas quartz is often preserved (nano-)crystalline. The high susceptibility of plagioclase to amorphisation is supported by our study, where the amorphous material is mainly originating from plagioclase, while pyroxene remains (nano-)crystalline within the shear bands (Figure 5.10).
An interesting point arising from this is a likely possibility to distinguish between crush-origin and melt-origin 'pseudotachylyte' (that is, amorphous material) found in fault zones. As the feldspars are observed to get readily amorphizised, a crush-origin pseudotachylyte would be expected to show a negligible amount of feldspar clasts. In contrast to a melt origin pseudotachylyte, which might be likely to preserve plagioclase clasts due to incomplete melting.

Whereas the amorphous shear bands are ubiquitous at 300 °C, they are dominantly confined to the forcing block - sample interface in 600 °C experiments (500 °C experiments have an intermediate microstructure) (Figure 5.13). Under the assumption that the amorphous material forms from mechanical wear, the amount of amorphisation should be a function of the work performed on the system. That is, the integral of the stress - strain curve. As samples deformed at 600 °C show markedly lower stresses, higher amounts of strain are needed to reach the same amount of work. Two causes for the localisation of amorphous type shear bands at the sample - forcing block interface are suggested: (i) the favourable orientation of these shear bands with respect to the shear direction, allowing for high strain accommodation, and/or (ii) stress concentrations due to a strength contrast between rigid alumina forcing block and deforming rock sample,

leading to more intense crushing and amorphisation at this interface.

5.4.3 Rheology of amorphous shear bands

Despite the frequent observation of amorphous material in fault zones, their rheological behaviour is poorly understood. The deformability of amorphous materials is usually described by the timescale of structural relaxation, which determines the transition from liquid (relaxed) to glassy (i.e. solid, unrelaxed) behaviour (e.g. Dingwell and Webb, 1989). The transition from the solid glassy form to the liquid state occurs at the glass transition temperature (T_g) and is accompanied by a marked change in physical properties such as viscosity, shear modulus, heat capacity etc. (Ojovan, 2008).
The ways in which a glassy (solid amorphous) material is achieving deformation are relatively complicated - unlike crystalline materials, amorphous materials lack such structures as a long-range ordered crystal lattice for e.g. dislocation creep, or grain boundaries for boundary diffusion processes. Amorphous materials in the glassy state therefore are not expected to be per se weak. However, when heated above the glass transition temperature, their viscosity significantly decreases.
The flow structures and high strain accommodation in the amorphous shear bands of our experiments rose the question if the material could be already above its glass transition temperature at such low temperatures as the 300 °C of our low-T experiments. The Brillouin spectra obtained give a first indication towards the physical changes of this amorphous material in the temperature range of our experiments (Figure 5.11). Due to major problems with sample preparation, our data set of Brillouin spectra at different temperatures T_B of spectra acquisition is limited to three data points. The peak shift with increasing T_B shows a change in physical properties of the analysed material. That the change in peak position per °C is smaller between the T_B-range of room-T to 400°C than between 400 to 500 °C could point to approaching a 'phase transition' or 'glass transition' towards higher T_B. With the limited dataset this can however not be proved and clearly more measurements and further quantifications are needed to make any founded statements.
Under the assumption that the partly amorphous material is causing the temperature dependence of sample strength, the lower strengths for experiments performed at $T \geq 500$ °C (Figure 5.1a, b) would indicate significantly lower viscosities for the partly amorphous material than at 300 °C. With increasing experimental T, the partly amorphous shear bands are observed to decrease in width and become more localised into few boundary shears. This behaviour would be consistent with a decreasing viscosity of these partly

amorphous shear bands, allowing for stronger strain localisation.

5.4.3.1 Influence of amorphous shear bands on bulk sample strength

Based on microstructural observations, shear bands are expected to be weak. Although all samples exhibit a pronounced weakening in the stress vs. displacement curve after a peak stress, residual sample strength remain always high (Figure 5.1a, b). Three possible explanations are suggested: (i) Shear bands often show orientations between 20 - 40° away from the load axis (Figure 5.9), and therefore are inclined against the forcing block interface with 5 - 25°. Due to this angular relation, displacement along the shear bands necessitates deformation of the low strain lenses in-between. The resulting sample strength is then partly determined by the rheology of the material in low strain lenses and not representative for the strength of the shear band material. (ii) As seen from the variable smoothness of the fault zone surfaces (Figure 5.5), fault zones appear to have segments that are likely to deform more easily than others. That is, there might be segments that are more 'locking' and others that are creeping. (iii) Shear bands are only a few μm wide (usually between 2 - 20 μm), and their vol.-% of the total sample stays below 4 % for the displacements attained in our experiments. If most of the displacement is accommodated in shear bands, the strain rate within them could rise up to $\sim 5 \times 10^{-3}$ s^{-1}. At these high strain rates, even a viscously flowing amorphous material could likely support high differential stresses.

5.4.4 Formation of Amorphous material by frictional melting?

Our experiments were performed at displacement rates far from seismic slip rates and as demonstrated from very similar experiments by Pec et al. (2012b), melting by frictional heating is unlikely at the low displacement rates and can be ruled out as the cause for amoprhisation. Supporting this interpretation, the trend of shear bands formed in our experiments is seldom straight but irregular with many 'wavy' segments (e.g. Figure 5.4a, c). Pseudotachylytes that are interpreted to have originated from frictional melting during seismic rupture, are generally seen to follow a relatively straight trend (even if the pseudotachylyte boarders may be wavy). The undulatory trend of shear bands in our samples is not favouring them for fast slip.

The amorphous type shear bands are interpreted to initiate from a cataclastic origin, as indicated by the microstructure. This is best seen in the 300 °C, 0.5 GPa Pc experiments: initial shear localisation occurs in ultra-cataclastic *type I* shear bands at peak stress. With increasing sample displacements, *type II* shear bands become domi-

nant and *type I* shear bands are now only rarely observed. Furthermore, at higher Pc, both ultra-cataclastic and amorphous type shear bands form less extensively and less frequently, at all experimental T (Figure 5.13). Increased Pc suppress the formation of ultra-cataclasites, as cataclastic flow necessitates a certain degree of dilatancy. Suppressing the formation of ultra-cataclasites will then also cause a decreased occurrence of amorphous type shear bands in case where the latter are evolving out of the former.

5.4.5 Axial shortening experiment

The pre-defined boundary conditions of the 45° pre-cut geometry was observed to interfere with the geometrical arrangement of fault zones. That is, shear bands and shear fractures frequently form in orientations inclined against the forcing block interfaces. The axial shortening experiment was performed with the aim of deforming the material without a pre-defined shear geometry. Unfortunately, the developed fault geometry in the axial shortening experiment was complex, with several interfering conjugated sets of faults and with a major fault that interfered with the bottom alumina piston (Figure 5.8a, c). The hardening in the mechanical data indicates that the measured strength cannot represent the fault zone strength, as the localisation into the fault should lead to a weakening rather than a hardening. Rather, the mechanical data obtained from the axial shortening experiment is thought to represent a mixed rheology of weakened fault zones and stronger low strain domains, which have to deform in order to overcome fault interaction with conjugated faults and the bottom alumina piston.
However, interesting are the similarities between the general shear and the axial shortening experiment, which are (i) the more or less exact same amount of displacement needed until yield is reached (Figure 5.8d). And (ii) the similarity in microstructure of shear bands formed: Fault orientation is measured to be mainly between 20 - 40° away from the load axis (Figure 5.9), pervasive fracturing and cataclastic flow lead to a foliation in the wall rock adjacent to the faults and the faults are in most parts formed from shear bands with the microstructural characteristics of *type II* shear bands (Figure 5.8f, g). The significantly smaller sample volume in the general shear compared to the axial shortening sample seems not to have an influence on the bulk sample strength, as indicated by the similar differential stresses attained in the two cases (Figure 5.8).

5.4.6 Comparison to nature

The question arises what conclusions we can draw concerning the strength of amorphous material in natural fault zones, on the basis of the collected laboratory data.

The occurrence of amorphous material within brittle fault zones is interesting as it bears the potential to introduce a temperature dependency to fault rock rheology. However, significant temperature effects on sample strengths in our experiments are observed at temperatures between 300 - 600 °C. These are much higher temperatures than generally assumed to be found in brittle fault zones at natural conditions (usually around T < 300 °C). For natural slow slipping fault zones where temperatures are low, the presence of an amorphous material, similar to the one observed in our study, might thus not cause a significant strength drop. The viscosity of the amorphous material is potentially not low enough at the low natural temperatures.
It has been reported from several studies, that pseudotachylytes that are interpreted to have formed during seismic rupture, are likely to have initiated from a cataclastic stage (e.g. Magloughlin, 1992; Hetztel et al., 1996; Curewitz and Karson, 1999). As seen from our experiments, there is only a few mm of displacement needed (at the high experimental differential stresses) to form amorphous material from plagioclase. Such amorphisation due to mechanical wear could likely also occur co-seismic from an ultra-cataclastic pre-stage. As long as the amorphous material is below its glass transition, it will remain strong and frictional heating can occur. However, upon reaching the glass transition temperature, the amorphous material will significantly weaken the fault, impeding any further frictional heating. The resulting temperatures reached along the fault in that case would likely stay way below the typical assumed temperatures for frictional melting of around ≥ 1000 °C.

5.5 Summary and Conclusions

Our experiments performed between 300 and 600 °C all deform within the dominant brittle field. However, the mechanical data shows a significant negative strength dependence on temperature. It is suggested that this temperature sensitivity is caused by the occurrence of amorphous material, formed during the experiments. The amorphous material is interpreted to form due to intense fragmentation of the material by fracturing and mechanical wear until crystallinity is lost. Thus, the formation mechanism is a brittle one and not classical melting. Once the amorphous material is formed, it deforms in a viscous manner if the temperatures are high enough (or strain rates low enough). The significantly lower supported sample strengths at T ≥ 500 °C indicate a viscosity decrease of the amorphous material. A change in physical properties around these temperatures is also indicated by the Brillouin scattering analyses (Figure 5.11c).

From our experiments we conclude that:
Amorphous material can form after few millimeters of bulk sample displacement, within the aseismically sheared mafic fault rock. Most parts of the sample deform by cataclastic flow, where however strain is localised into a network of ultra-cataclastic and/or (partly) amorphous shear bands and shear fractures.
Microstructural observations indicate that the amorphous material originates from an ultra-cataclastic pre-stage, and amorphisation is interpreted to be induced by mechanical wear.
Plagioclase is the more susceptible phase to this and amorphous zones show a composition close to that of the starting plagioclase.
The observed negative temperature dependence of 'bulk' sample strength is suggested to be caused by viscous (temperature activated) flow within the partly amorphous shear bands. A first effort to try and quantify the material properties of the amorphous material using Brillouin light scattering indicates a likely change in physical properties for temperatures around 500 °C. This is in accordance with the significant sample weakening at experimental T of $\geq$ 500 °C.
The occurrence of amorphous material in fault zones in the brittle field bears the potential to introduce a marked temperature dependence to rheology, under the condition that the amorphous material achieves viscous flow. This would have important implications on the way we model the rheology of brittle-dominated fault rocks within the earths lithosphere.

Chapter 6

General Discussion and Conclusions

6.1 The brittle-viscous transition in mafic rocks

In the course of this thesis, the rheological behaviour and microstructural evolution of a mafic fault rock was studied, over a range of conditions where a transition from brittle to viscous deformation was observed. Chapter 3 presented the results on how this transition is achieved, with the main conclusions:

- At the experimentally imposed strain rates of $\sim 10^{-5}$ s^{-1}, the brittle-viscous transition is observed in the temperature range 600 °C $<$ T $<$ 800 °C, at confining pressures $0.5 \leq$ Pc ≤ 1.5 GPa.
- The transition is effected by a switch from brittle fracturing and cataclastic flow, to viscous dissolution-precipitation creep and grain boundary sliding. Mineral reactions leading to grain size refinement are seen as a crucial process enabling viscous deformation, i.e., grain size sensitive creep.
- In the transitional regime, the mechanical response of the sample is a mixed-mode between brittle and viscous rheology.
- And following up on the previous point: The mixed-mode rheology is likely only transient, as with the evolving microstructure viscous processes are expected to become more dominant. That is, the brittle-viscous transition is not only a function of T but to a large extent also of microstructural evolution.

Strain in our samples is largely accommodated by plagioclase. A transition from brittle to viscous deformation by grain size sensitive creep mechanisms, like it is observed in

our experiments, compares well with observations from natural feldspar-rich fault rocks (e.g. Fitz Gerald and Stünitz, 1993; Jiang et al., 2000; Lapworth et al., 2002; Rosenberg and Stünitz, 2003; Brander et al., 2012; Fukuda and Okudaira, 2013; Mukai et al., 2014; Viegas et al., 2016). In contrast, many previous experimental studies on similar rock types have suggested a transition from brittle deformation to viscous flow accommodated by intracrystalline deformation mechanisms such as dislocation glide or -creep, or twinning (e.g. Kirby and Kronenberg, 1984; Boland and Tullis, 1986; Tullis and Yund, 1987; Tullis et al., 1987; McLaren and Pryer, 2001). Furthermore, from observations on natural examples and our experiments likewise, a history-dependent transition from an initial brittle state followed by subsequently more viscous deformation can be observed for certain conditions.

From the similarities between the microstructures and active processes in our experiments and nature, we are confident that the experimentally derived mechanical data can be used to make assumptions on the rheology of natural fault zones. As the strains in our experiments remain small ($\gamma_a \leq 6$), our results are mainly relevant to the initiation and early stages of fault/shear zone formation and maintenance. Amongst the most significant findings thereby is the strong influence of microstructural evolution on the bulk sample rheology, and the resulting transient various contributions from brittle and viscous deformation. These findings should be of particular interest to the modeling community, indicating that fault zone initiation is most certainly not showing a steady-state rheology but an evolving one, as the fault zone is maturing.

6.2 The viscous field

In experiments performed within the dominant viscous field, mineral reactions are the most obvious indicator for the activity of solution-mass transport. The fine-grained plagioclase within shear bands is generally observed to show a different composition than the starting plagioclase, indicating newly nucleated grains. No indicators for subgrain rotation or bulging recrystallization of porphyroclasts is observed, and fracturing as means of grain size reduction is excluded on the basis of the morphology of these grains (diamond-shaped grains with minor internal defect density and a narrow grain size distribution). The main deformation mechanism leading to viscous deformation was suggested to be dissolution-precipitation creep accompanied by grain boundary sliding (GBS).

A method was developed to measure the thickness of amphibole growth coronas around pyroxene porphyroclasts, determining the average corona thickness as a function of orientation around the clasts. The results of this analysis indicated that amphibole - like

plagioclase - is likely accommodating strain by dissolution-precipitation creep.
Dissolution-precipitation creep as a viscous deformation mechanism is often recognized in natural examples of shear zones within mafic rocks. Contrarily, experimental studies on similar rock types frequently report the activity of dislocation glide or creep. The latter usually base their interpretations on the observations of elevated stress exponents > 1, undulatory extinction or sub-cell structures as seen in the light microscope and sometimes on the observation of a crystallographic preferred orientation. As seen in this study, elevated stress exponents can be achieved for example by a mixture of newtonian viscous deformation accompanied by brittle deformation. Additionally, a weak crystallographic preferred orientation within shear bands formed from fine-grained albite was measured, attributed to have formed by/during deformation accommodated by dissolution-precipitation creep.
The knowledge and understanding of texture-forming mechanisms in geological materials is still incomplete. And the possibility of activating several mechanisms in parallel during experimental deformation greatly complicates the interpretations of the mechanical responses measured in the laboratory. Clearly further research is needed to advance in our knowledge on these topics. Studying microstructures of experimentally deformed rocks thereby appears crucial and extremely helpful to the interpretation of laboratory derived rock rheology.

An interesting point, which hasn't been discussed so far, is the astounding rates at which mineral reactions proceed at such relatively low experimental T as 800 °C. Vast amounts of amphibole, zoisite, quartz and new plagioclase form within as little as 20 h of the presented experiments. This behaviour might be explained by the likely high driving force for reaction in the experiments. During sample pressurization and heating (5 - 8 h), the rock sample is brought to out-of-equilibrium conditions without sufficient time to equilibrate, and at the start of an experiment, reaction boundaries are highly overstepped. This is not per se a problem as observations from nature suggest that mineral assemblages can be preserved metastable for long periods of time, under the condition that no hydrous fluid is available for enhanced reaction and transport rates (e.g. Rubie, 1986; Austrheim, 1987; Wayte et al., 1989; Krabbendam et al., 2000; Austrheim, 2013; Jamtveit et al., 2016). However, it might be a factor that needs attention when determining the rate limiting step in diffusion creep comparing nature and experiments. If a high driving force for reaction is sustained in the experiments due to large reaction boundary overstepping, the rate limiting step for diffusion creep might be transport. In nature, where mineral assemblages are closer to equilibrium and driving force for reaction

is smaller, diffusion might be transport-limited.
The implications of the rate limiting step for diffusion creep on how the experimental results might be extrapolated to nature was discussed in chapter 4. Owing to the intense grain size reduction in the experiments, extrapolation to even high grade natural conditions might likely be possible in the case where diffusion creep is the dominant deformation mechanism with transport as the rate limiting step. However, so far there are still major unknowns concerning the parameters controlling dissolution-precipitation creep rates at the pressures and temperatures relevant for mid- to lower crustal deformation. As dissolution-precipitation creep is often observed to occur during syn-kinematic mineral reactions, the driving forces for deformation and mineral reactions are likely to be interdependent. Understanding such a system is far from trivial and clearly represents a field with great need and possibilities for future work.

6.2.1 A short tale about the struggles of thermodynamic modeling - or, a potential evidence that reaction kinetics may be dominating over attaining phase equilibrium

During this thesis, I attempted to use the thermodynamic modeling software Theriak-Domino (by C. de Capitani) to predict the stable phase assemblage at the chosen experimental conditions. The Maryland Diabase starting material showed abundant reaction to amphibole, quartz, zoisite and a new plagioclase (with a lower anorthite component than the initial plagioclase in the starting material) in 800 ° experiments. Predicted by the thermodynamic models however would be abundant growth of pyroxene, garnet and only minor amphibole. Zoisite was never stable in any of the calculated pseudosections. I was aware that full equilibrium under my experimental conditions is unlikely, but that at least element transport should not be the limiting factor along areas where plagioclase and pyroxene grains are in contact. My approach for the input chemistry into the thermodynamic model therefore was a 'model phase boundary', i.e. a theoretic contact area between a plagioclase and a pyroxene grain, assuming water to be present in excess. However, also this approach did not yield comparable assemblages between the calculated and the observed ones. Only by suppressing garnet and pyroxene growth, the vast and dominant occurrence of amphibole could be reproduced. A fact that could be interpreted as showing the ability of amphibole to nucleate and grow, and the failure of garnet and pyroxene nucleation/growth. Thus, a potential indicator that reaction kinetics are dominating over attaining the energetically most stable mineral assemblage.

However, as the existing solution models for especially amphibole are not too well constraint, a different interpretation of the discrepancy between modeled and observed assemblage was, that the solution models used were not appropriate for the Maryland Diabase composition. For amphibole, the best solution models exist for the magnesium end-members. I therefore went about to try a set of experiments with synthetic mixtures of plagioclase and the Mg-end member pyroxenes Enstatite and Diopside. The aim was, that the chemistry of that system would be appropriate for the available solution models. The results from this were better than with the Maryland Diabase, but the reaction extent was significantly less and the pyroxenes did hardly participate in any mineral reaction. This could be interpreted that a chemically more versatile system (such as the Maryland Diabase material) is easier to react, probably again showing the dominance of reaction kinetics over energy minimisation by attaining phase equilibrium.
Due to the above described difficulties with the thermodynamic modeling, none of it was shown in this thesis, as it always raised more questions than it answered. Although the approach with the synthetic mixtures using Mg-end member pyroxenes was in a way promising, the complexity of the system makes it hard to formulate any sound interpretations at present state.

6.3 The semi-brittle field

A negative temperature dependence on sample strenght had been observed over the whole experimentally imposed temperature range from 300 - 700 °C of this study. Disregarding, the results were grouped in a brittle dominated range of 300 - 600 °C, and the transition from brittle-to-viscous at T $\geq$ 600 °C. This might raise the question why the brittle-viscous transition was not considered to occur within the broad T range from 300 - 700 °C. The distinction had been made on the basis of microstructural observations, whereas at T $\leq$ 600°C, brittle processes are dominating the deformation. The temperature sensitivity in these samples was attributed to the syn-kinematic formation of amorphous material, caused by ongoing intense brecciation and mechanical wear from a previous ultra-cataclastic stage. The formation of the amorphous material is thus seen as being confined to the brittle regime. Unlike what is typically thought of as 'brittle-viscous-transition', where the relative rates of the typical viscous deformation mechanisms for rocks (either intra- or intercrystalline mechanisms) become increasingly dominant over the rate of brittle deformation.
The observations of amorphous material forming during aseismic shearing of fault gouge material had previously been observed in a similar study on granitoid fault gouge by Pec

(2014), (see also Pec et al., 2012a,b, 2016). This syn-kinematically formed amorphous material in 'low'-T experiments had likewise been observed in this study. In accordance with the interpretation of Pec (2014), the amorphous material in this study is also thought to originate from intense brecciation and mechanical wear, where feldspar seem to be particularly susceptible to this.
It is clearly seen from the mechanical data that the occurrence of amorphous material leads to a temperature dependence of fault rock strength. An observation with significant impact on our ways of modeling brittle fault zones, which are usually reduced to a mere pressure sensitive behaviour. Therefore, it is of great interest to assess how frequently such amorphous material forms within aseismically creeping natural fault zones. It is seen to form ubiquitously in experimental samples, likely favoured by the high experimental differential stresses. Where stresses are lower in nature, strains must be higher to perform the same amount of work on the material and thus allowing for amorphizatino by mechanical wear. At lower natural strain rates and in the presence of fluids, mineral reactions will probably lead to retrograde hydration reactions and strain be accommodation by solution-mass transport. Amorphous material might not be expected to form under these conditions. However, in the transient stages of enhanced aseismic slip rates or during post-seismic relaxation, the rates of alteration reactions and solution-mass transport are likely to not be able to keep up with the rate of slip and amorphization might take place.

6.4 Concluding remarks

This study presented results spanning a wide range of pressure-temperature conditions including the transition from dominant brittle to dominant viscous deformation. Our knowledge about the acting processes in each field remain incomplete and further studies are needed. From the experience gained during the course of this study, there are many challenges to meet in performing rock deformation experiments of the likes from this study: amongst others, this are difficulties to analyse the newly nucleated small grains within shear bands, the limited temperature range available for the experiments due to melting at higher T, and strain localization. However there are also many insights to be gained from the experiments, as we have controls over the imposed parameters such as temperature, pressure, strain rate etc., mechanical response can be measured and overprinting by e.g. exhumation, as it is the case for many natural rocks, is not affecting the microstructures of the experimental samples. As seen in this study, in-depth microstructural observations proved to be extremely helpful in understanding the active

processes during deformation and in making interpretations concerning the mechanical data.

6.5 Suggestions for future work

From the experience gained during this study, suggestions for future work are presented in the following, being subdivided into suggested (i) improvements to the sample setup, (ii) improvement of the starting materials and ideas for future experiments, and (iii) promotion for following the approach of using Brillouin spectroscopy to characterize the amorphous material forming in the aseismically sheared low-T experiments.

(i) Sample setup:

- Introduction of a $\sim$ 34° pre-cut setup: As was seen in the low-T experiments (300 - 600 °C), fault zones usually form at orientations between 20 - 40° from the load axis, with modes at 32 - 34°. Using a 45° pre-cut setup for low-T experiments appears not to be the most appropriate geometry. Performing the same experiments with a $\sim$ 34° pre-cut geometry is suggested to likely allow for a fault zone network to form parallel to the forcing block interfaces. In the ideal case, this would result in the ability to extract the mechanical response of the weakened fault zone material. In the 45° pre-cut setup with the fault zone network forming inclined against the rigid forcing blocks, the bulk measured mechanical response is believed to be a mixed mode between weakened faults and the remaining 'strong' material in low strain lenses.
From the problems met in the low-T axial shortening experiment, it had been recognized that using a pre-cut geometry is principally a good approach. However for low-T experiments, the angle to the load axis should be smaller than 45°, likely ideally $\sim$ 34°.

- Introduction of *direct shear* sample setup: The general shear setup used for the experiments in this thesis allows to attain higher strains than in axial shortening experiments. Furthermore, simple shear dominated type of flow is of more relevance in natural fault zones than pure shear flow. However, there are some disadvantages of the 45° pre-cut setup: (I) the problem of decreasing forcing block overlap, generating the need for an 'area correction' in the calculation of σ_1. And (II), the normal stress, σ_n, acting on the shear zone increases with increasing sample strength. Although the effect of tectonic stresses on thermodynamic equilibrium in metamorphic reactions is not well understood, it has been observed that minerals do show phase transformations accord-

ing to the magnitude of imposed stresses. From fluid dynamics, it is usually assumed that the mean stress is controlling volume change and thus should be considered as the thermodynamic pressure for metamorphic equilibrium calculations. As the mean stress in the 45° pre-cut setup is determined by the evolution of the sample strength, it complicates the system when performing experiments with syn-kinematic mineral reactions. To overcome the problems outlined as (I) and (II), it is suggested that efforts should be taken to introduction the L-shaped *direct shear* assembly to the Griggs rig sample assembly. In the *direct shear* setup, σ_n is equal to the imposed confining pressure and shear stress, τ, is equal to the applied axial load.

(ii) Improvement to starting material and ideas for future experiments:

- Reducing the variability in starting material grain size fraction: As has been seen in the high-T experiments of this thesis, grain size sensitive creep mechanisms are dominating viscous deformation. Strain thereby is localized into shear bands with a grain size largely < 1 μm. It was however argued in this thesis, that the material within shear bands never fully controlled the rheology, largely likely due to geometric constraints. It would therefore be of great interest to fabricate a starting material (in the best case a Pl - Px mixture), with a relatively small grain size ($\sim$ 1 - 5 μm) and a narrow grain size distribution, to determine the strength of such a fine grained material. Experiments on such fine grained plagioclase and plagioclase - pyroxene mixtures have previously been run by e.g. Rybacki and Dresen (2000) or Dimanov et al. (2003), but never in the temperature - pressure range achievable with the Griggs rig deformation apparatus. The procedure followed by e.g. Rybacki and Dresen (2000), by hot isostatically press the starting material from a glass powder seems to be a reliable method to produce narrow grain size distributions with a small (on the order of a few μm) grain size mode.
The fine grained material might likely be weak enough to reach the strength resolution limit of the Griggs rig apparatus. In that case, constant load (instead of constant displacement rate experiments) might be a good approach to characterize the material. If promising results arise, the setup might be used to gain some insights on the controlling parameters of dissolution-precipitation creep rates at elevated P and T.

- Strontium (Sr) doping to trace plagioclase precipitation: The amount of reacted and re-precipitated plagioclase in the fine-grained experimental samples is difficult to detect and thus estimates on overall reaction rates were not possible. As plagioclase is known to incorporate Sr as a trace element (e.g. Butler and Skiba, 1962), providing a

Sr reservoir in the sample could potentially lead to Sr incorporation of syn-kinematically grown plagioclase. Due to the high atomic weight of Sr, the newly grown plagioclase would ideally have a distinct Z-contrast in BSE and/or CL SEM images and could thus be easily identified and quantified.

- Annealing experiments on amorphous material formed in low-T experiments: Amorphous material in shear bands formed reproducible in large quantities during deformation experiments at 300 °C, 0.5 GPa Pc. Annealing experiments are suggested, following low-T deformation and formation of the amorphous shear bands. The experiments would be aimed to study the stability of the amorphous material to devitrification and mineral reactions, also in comparison to the surrounding fractured host rock. Although amorphous materials should be prone to reaction, the lack of grain boundaries for fast diffusional transport could likely render them more stable to reaction than the surrounding host material. From the preservation of 'pseudotachylytes' in nature it might be expected that amorphous material is not per se susceptible to overprinting by static 'annealing' and experiments in this direction could help to gain insight into this.

(iii) Brillouin scattering analyses on amorphous shear bands:

- The Brillouin scattering spectra measured in this thesis were obtained with the aim of eventually determining the glass transition temperature for the amorphous material that forms in the low-T experiments. To do so, knowledge of material parameters such as density are needed to calculate elastic modulus from the Brillouin signal. Although sample preparation for the Brillouin scattering measurements posed some problems, the Brillouin measurements themselves are simple to undertake. A challenge arising will be the derivation of the density of the amorphous material. However so far, the approach in quantifying rheological parameters of the fault-related amorphous material using the Brillouin scattering technique appeared promising. To my knowledge there is no data available for the rheological behaviour of such materials other than the observed weakening due to melt-lubrication during frictional melting in high velocity friction experiments. The rheological significance of amorphous material in slow (aseismically) slipping fault zones until today is only poorly understood.

As a generally final remark, from my personal experience gained during this thesis, I would strongly support the promotion of low strain rate deformation experiments (if the results should be extrapolated to low strain rate natural conditions). The closer we

come to natural rates, the less problems we are expected to face in achieving extrapolation to nature. Any improvements in this direction will be helpful. This could be e.g. improvements on machine stability, necessitated for long duration runs at low strain rates. Or the fabrication of a starting material as close as possible to the 'steady state' microstructure for the respective conditions during deformation. In the best case this would reduce the amount of time needed for microstructural evolution and shorten the amount of strain needed to extract the rheological parameters wanted from the experiments. Of course undidsputable, there are obvious limits to how much time we can be spent on a deformation experiment. But keeping an open mind and being aware of the problems we face surely are the best pre-requisites to come up with solutions.

Bibliography

Anderson, O. L. and Grew, P. C. (1977). Stress corrosion theory of crack propagation with applications to geophysics. *Reviews of Geophysics and Space Physics*, 15(1):77 – 104.

Ashby, M. F. and Verrall, R. A. (1973). Diffusion-accommodated Flow and Superplasticity. *Acta Metallurgica*, 21:149 – 163.

Austrheim, H. (1987). Eclogitization of lower crustal granulites by fluid migration through shear zones. *Earth and Planetary Science Letters*, 81:221 – 232.

Austrheim, H. (2013). Fluid and deformation induced metamorphic processes around Moho beneath continent collision zones: Examples from the exposed root zone of the Caledonian mountain belt, W-Norway. *Tectonophysics*, 609:620 – 635.

Austrheim, H. and Andersen, T. B. (2004). Pseudotachylytes from Corsica: fossil earthquakes from a subduction complex. *Terra Nova*, 16:193 – 197.

Bachmann, F., Hielscher, R., and Schaeben, H. (2010). Texture analysis with mtex - free and open source software toolbox. *Solid State Phenomena*, 160:63 – 68.

Barreiro, J. G., Lonardelli, I., Wenk, H., Dresen, G., Rybacki, E., Ren, Y., and Tome, C. (2007). Preferred orientation of anorthite deformed experimentally in newtonian creep. *Earth and Planetary Science Letters*, 264:188 – 207.

Beeler, N. M., Tullis, T. E., and Weeks, J. D. (1994). The role of time and displacement in the evolution effect in rock friction. *Geophysical Research Letters*, 21(18):1987 – 1990.

Berger, A. and Herwegh, M. (2004). Grain coarsening in contact metamorphic carbonates: effects of second-phase particles, fluid flow and thermal pertubations. *Journal of Metamorphic Geology*, 22(5):459 – 474.

Berger, A. and Stünitz, H. (1996). Deformation mechanisms and reaction of hornblende: examples from the Bergell tonalite (Central Alps). *Tectonophysics*, 257:149 – 174.

Berman, R. G. (1988). Internally-consistent thermodynamic data for minerals in the system na2o-k2o-cao-mgo-feo-fe2o3-al2o3-sio2-tio2-h2o-co2. *Journal of Petrology*, 29:445–522.

Boland, J. N. and Tullis, T. E. (1986). Deformation behavior of wet and dry clinopyroxenite in the brittle to ductile transition region. In Hobbs, B. E. and Heard, H. C., editors, *Mineral and Rock Deformation: Laboratory Studies: The Paterson Volume*, volume 36 of *Geophys. Monogr. Ser.*, pages 35 – 50. AGU.

Bons, P. D. and den Brok, B. (2000). Crystallographic preferred orientation development by dissolution-precipitation creep. *Journal of Structural Geology*, 22:1713 – 1722.

Boullier, A. M. and Geugen, Y. (1975). SP-Mylonites: Origin of Some Mylonites by Superplastic Flow. *Contribution to Mineralogy and Petrology*, 50:93 – 104.

Brace, W. F. and Kohlstedt, D. (1980). Limits of lithospheric stress imposed by laboratory experiments. *Journal of Geophysical Research*, 85(B11):6248 – 6252.

Brander, L., Svahnberg, H., and Piazolo, S. (2012). Brittle-plastic deformation in initially dry rocks at fluid-present conditions: transient behaviour of feldspar at mid-crustal levels. *Contribution to Mineralogy and Petrology*, 163:403 – 425.

Brantut, N., Heap, M. J., Meredith, P. G., and Baud, P. (2013). Time-dependent cracking and brittle creep in crustal rocks: A review. *Journal of Structural Geology*, 52:17 – 43.

Brodie, K. H. and Rutter, E. H. (1987). The role of transiently fine-grained reaction prodcuts in syntectonic metamorphism: natural and experimental examples. *Canadian Journal of Earth Sciences*, 24:556 – 564.

Bukovská, Z., Jerábek, P., and Morales, L. F. G. (2016). Major softening at brittle-ductile transition due to interplay between chemical and deformation processes: An insight from evolution of shear bands in the South Armorican Shear Zone. *Journal of Geophysical Research - Solid Earth*, 121:1158 – 1182.

Bunge, H. J. (1982). *Texture Analysis in Materials Sciences*. Buttleworth, London.

Bürgmann, R. and Dresen, G. (2008). Rheology of the lower crust and upper mantle: Evidence from rock mechanics, geodesy, and field observations. *Annu. Rev. Earth Planet. Sci.*, 36:531 – 567.

Burov, E. B. (2011). Rheology and strength of the lithosphere. *Marine and Petroleum Geology*, 28:1402 – 1443.

Butler, J. R. and Skiba, W. (1962). Strontium in plagioclase feldspars from four layered basic masses in somalia. *MM*, pages 213 – 225.

Byerlee, J. (1978). Friction of Rocks. *Pure and Applied Geophysics*, 116:615 – 626.

Byerlee, J. D. (1967). Frictional characteristics of granite under high confining pressure. *Journal of Geophysical Research*, 72(14):3639 – 3648.

Byerlee, J. D. (1968). Brittle-ductile transition in rocks. *Journal of Geophysical Research*, 73(14):4741 – 4750.

Bystricky, M. and Mackwell, S. (2001). Creep of dry clinopyroxene aggregates. *Journal of Geophysical Research*, 106(B7):13443 – 13454.

Camacho, A., Vernon, R. H., and Fitz Gerald, J. D. (1995). Large volumes of anhydrous pseudotachylyte in the Woodroffe Thrust, eastern Musgrave Ranges, Australia. *Journal of Structural Geology*, 17(3):371 – 383.

Caristan, Y. (1982). The transition from high temperature creep to fracture in maryland diabase. *Journal of Geophysical Research*, 87(B8):6781 – 6790.

Carter, N. L. and Tsenn, M. C. (1987). Flow properties of continental lithosphere. *Tectonophysics*, 136:27 – 63.

Chen, S., Hiraga, T., and Kohlstedt, D. L. (2006). Water weakening of clinopyroxene in the dislocation creep regime. *Journal of Geophysical Research*, 111:B08203.

Coble, R. L. (1963). A Model for Boundary Diffusion Controlled Creep in Polycrystalline Materials. *Journal of Applied Physics*, 34(6):1679 – 1682.

Curewitz, D. and Karson, J. A. (1999). Ultracataclasis, sintering, and frictional melting in pseudotachylytes from East Greenland. *Journal of Structural Geology*, 21:1693 – 1731.

de Capitani, C. and Petrakakis, K. (2010). The computation of equilibrium assemblage diagrams with theriak/domino software. *American Mineralogist*, 95:1006–1016.

de Ronde, A. A., Stunitz, H., Tullis, J., and Heilbronner, R. (2005). Reaction-induced weakening of plagioclase-olivine composites. *Tectonophysics*, 409:85 – 106.

Del Gaudio, P., Di Toro, G., Han, R., Hirose, T., Nielsen, S., Shimamoto, T., and Cavallo, A. (2009). Frictional melting of peridotite and seismic slip. *Journal of Geophysical Research*, 114(B06306).

Di Toro, G., Hirose, T., Nielsen, S., and Shimamoto, T. (2006). Relating High-Velocity Rock-Friction Experiments to Coseismic Slip in the Presence of Melts. In Abercrombie, R., McGarr, A., Di Toro, G., and Kanamori, H., editors, *Radiated Energy and the Physics of Faulting*, volume 170 of *Geophysical Monograph*, pages 121 – 134. AGU.

Di Toro, G., Nielsen, S., and Pennacchioni, G. (2005). Earthquake rupture dynamics frozen in exhumed ancient faults. *Nature*, 436:1009 – 1012.

Dietrich, J. H. (1978). Time-dependent friction and the mechanics of stick-slip. *Pageoph*, 116:790 – 806.

Dimanov, A. and Dresen, G. (2005). Rheology of synthetic anorthite-diopside aggregates: Implications for ductile shear zones. *Journal of Geophysical Research*, 110:B07203.

Dimanov, A., Dresen, G., Xiao, X., and Wirth, R. (1999). Grain boundary diffusion creep of synthetic anorthite aggregates: The effect of water. *Journal of Geophysical Research*, 104(B5):10483 – 10497.

Dimanov, A., Lavie, M. P., Dresen, G., Ingrin, J., and Jaoul, O. (2003). Creep of polycrystalline anorthite and diopside. *Journal of Geophysical Research*, 108(B1):B001815.

Dimanov, A. E., Rybacki, E., Wirth, R., and Dresen, G. (2007). Creep and strain-dependent microstructures of synthetic anorthite-diopside aggre-gates. *Journal of Structural Geology*, 29:1049 – 1069.

Dingwell, D. B. and Webb, S. L. (1989). Structural Relaxation in Silicate Melts and Non-Newtonian Melt Rheology in Geologic Processes. *Physics and chemistry of minerals*, 16:508 – 516.

Drury, M. R., , Avé Lallemant, H. G., Pennock, G. M., and Palasse, L. N. (2011). Crystal preferred orientation in peridotite ultramylonites deformed by grain size sensitive creep, Étang de lers, pyrenees, france. *Journal of Geophysical Research*, 33:1776 – 1789.

Drury, M. R. and Humphreys, F. (1988). Microstructural shear criteria associated with grain-boundary sliding during ductile deformation. *Journal of Structural Geology*, 10(1):83 – 89.

Elliott, D. (1973). Diffusion Flow Laws in Metamorphic Rocks. *Geological Society of America Bulletin*, 84:2645 – 2664.

Etheridge, M. A. and Wilkie, J. C. (1979). Grainsize reduction, grain boundary sliding and the flow strength of mylonites. *Tectonophysics*, 58:159 – 178.

Fitz Gerald, J. D., Boland, J. N., McLaren, A. C., Ord, A., and Hobbs, B. (1991). Microstructures in water-weakened single crystals of quartz. *Journal of Geophysical Research - Solid Earth*, 96(B2):2139 – 2155.

Fitz Gerald, J. D. and Stünitz, H. (1993). Deformation of Granitoids at low Metamorphic Grade. 1. Reactions and Grain-size Reduction. *Tectonophysics*, 221(3-4):269 – 297.

Fossen, H. and Tikoff, B. (1993). The deformation matrix for simultaneous simple shearing, pure shearing and volume change, and its application to transpression-transtension tectonics. *Journal of Structural Geology*, 15:413 – 422.

Fukuda, J.-I. and Okudaira, T. (2013). Grain-size-sensitive Creep of Plagioclase accompanied by Solution-Precipitation and Mass Transfer under Mid-crustal Conditions. *Journal of Structural Geology*, 51:61 – 73.

Fusseis, F. and Handy, M. R. (2008). Micromechanisms of shear zone propagation at the brittle-viscous transition. *Journal of Structural Geology*, 30(10):1242 – 1253.

Gerbi, C., Johnson, S. E., Shulman, D., and Klepeis, K. (2016). Influence of microscale weak zones on bulk strength. *Geochemistry Geophysics Geosystems*, 17:4064 – 4077.

Getsinger, A. J. and Hirth, G. (2014). Amphibole fabric formation during diffusion creep and the rheology of shear zones. *Geology*, 42(6):535 – 538.

Getsinger, A. J., Hirth, G., Stünitz, H., and Goergen, E. T. (2013). The influence of water on rheology and strain localization in the lower continental crust. *Geochemistry Geophysics Geosystems*, 14(7):2247 – 2264.

Gifkins, R. C. (1976). Grain-boundary sliding and its accommodation during creep and superplasticity. *Metallurgica Transactions*, 7A:1225 – 1232.

Gleason, G. C. and Tullis, J. (1995). A flow law for dislocation creep of quartz aggregates determined with the molten salt cell. *Tectonophysics*, 247:1 – 23.

Glen, J. W. (1955). The creep of polycrystalline ice. *Proc. R. Soc. London, Ser. A*, 228:519 – 538.

Goldsby, D. and Tullis, T. E. (2002). Low frictional strength of quartz rocks at subseismic slip rates. *Geophysical Research Letters*, 29(17):L015240.

Goncalves, P., Poilvet, J.-C., Oliot, E., and Trap, P. (2016). How does shear zone nucleate? An example from the Suretta nappe (Swiss Eastern Alps). *Tectonophysics*, 86:166 – 180.

Gratier, J.-P., Dysthe, D. K., and Francois, R. (2013). The Role of Pressure Solution Creep in the Ductility of the Earth's Upper Crust. volume 54 of *Advances in Geophysics*, pages 47 – 179.

Gratier, J.-P. and Gueydan, F. (2008). *Deformation in the Presence of Fluids and Mineral Reactions: Effect of Fracturing and Fluid-rock Interaction on Seismic Cycles*. The Dynamics of Fault Zones, edited by M. R. Handy, G. Hirth, N. Hovius. The MIT Press, Mass., USA.

Gratier, J.-P., Guiget, R., Renard, F., Jenatton, L., and Bernard, D. (2009). A pressure solution creep law for quartz from indentation experiments. *Journal of Geophysical Research*, 114:B03403.

Gratier, J.-P., Richard, J., Renard, F., Mittempergher, S., Doan, M.-L., Di Toro, G., Hadizadeh, J., and Boullier, A.-M. (2011). Aseismic sliding of active faults by pressure solution creep: Evidence from the San Andreas Fault Observatory at Depth. *Geology*, 39(12):1131 – 1134.

Griggs, D. T., Turner, F. J., and Heard, H. C. (1960). Deformation of rocks at 500 to 800c. *Geol. Soc. Am. Mem.*, 79:39 – 105.

Hacker, B. R. and Christie, J. M. (1991). Experimental deformation of a glassy basalt. *Tectonophysics*, 200:79 – 96.

Handin, J. (1966). Strength and ductility. In Clark, S. P., editor, *Handbook of Physical Constants*, number 97 in Geol. Soc. Am. Mem., pages 223 – 289.

Handy, M. R., Babist, J., Wagner, R., Rosenberg, C., and Konrad, M. (2005). Decoupling and its relation to strain partitioning in continental litosphere: insight from the periadriatic fault system (european alps). *Geol. Soc. Lond., Spec. Pub.*, 243:249 – 276.

Hanmer, S. (2000). Matrix mosaics, brittle deformation, and elongate porphyroclasts: granulite facies microstructures in the Striding-Athabasca mylonite zone, western Canada. *Journal of Structural Geology*, 22:947 – 967.

Hawthorne, F. C., Oberti, R., Harlow, G. E., Maresch, W. V., Martin, R. F., Schumacher, J. C., and Welch, M. D. (2012). Nomenclature of the amphibole supergroup. *American Mineralogist*, 97:2031 – 2048.

Hayward, K. S., Cox, S. F., Fitz Gerald, J. D., Slagmolen, J. J., Shaddock, D. A., Forsyth, P. W. F., Salmon, M. L., and Hawkins, R. (2016). Mechanical amorphization, flash heating, and frictional melting: Dramatic changes to fault surfaces during the first millisecond of earthquake slip. *Geology*, 44(12):1043 – 1046.

Heard, H. C. (1960). Transition from brittle fractur to ductile flow in solnhofen limestone as a function of temperature, confining pressure and interstitial fluid pressure. In Griggs, D. T. and Handin, J., editors, *Rock Deformation (A Symposium)*, volume 79 of *Rock Deformation, Mem. Geol. Soc. Am.*, pages 193 – 226. GSA Memoir.

Heilbronner, R. and Barrett, S. (2014). *Image Analysis in Earth Sciences - Microstructures and Textures of Earth Materials*. Springer-Verlag, Berlin.

Hetztel, R., Altenberger, U., and Strecker, M. R. (1996). Structural and chemical evolution of pseudotachylytes during seismic events. *Mineralogy and Petrology*, 58:33 – 50.

Hickman, S. H. and Evans, B. (1991). Experimental pressure solution in halite: the effect of grain/interphase boundary structure. *Journal of the Geological Society, London*, 148:549 – 560.

Hier-Majumder, S., Mei, S., and Kohlstedt, D. L. (2005). Water weakening of clinopyroxenite in diffusin creep. *Journal of Geophysical Research*, 110:B07406.

Hirose, T. and Shimamoto, T. (2005). Growth of molten zone as a mechanism of slip weakening of simulated faults in gabbro during frictional melting. *Journal of Geophysical Research*, 110:B05202.

Holland, T. and Powell, R. (1998). An internally consistent thermodynamic data set for phases of petrological interest. *J. metamorphic Geol.*, 16:309–343.

Holyoke III, C. W. and Kronenberg, A. K. (2010). Accurate differential stress measurement using the molten salt cell and solid salt assemblies in the Griggs apparatus with applications to strength, piezometers and rheology. *Tectonophysics*, 494:17 – 31.

Jamtveit, B., Austrheim, H., and Putnis, A. (2016). Disequilibrium metamorphism of stressed lithosphere. *Earth-Science Reviews*, 154:1 – 13.

Janssen, C., Wirth, R., Rybacki, E., Naumann, R., Kemnitz, H., Wenk, H.-R., and Dresen, G. (2010). Amorphous material in SAFOD core samples (San Andreas Fault): Evidence for crush-origin pseudotachylytes? *Geophysical Research Letters*, 37:L01303.

Ji, S., Jiang, Z., Rybacki, E., Wirth, R., Prior, D. J., and Xia, B. (2004). Strain softening and microstructural evolution of anorthite aggregates and quartz-anorthite layered composites deformed in torsion. *Earth and Planetary Science Letters*, 222:377 – 390.

Jiang, Z., Prior, D. J., and Wheeler, J. (2000). Albite crystallographic preferred orientation and grain misorientation distribution in a low-grade mylonite: implications for granular flow. *Journal of Structural Geology*, 22:1663 – 1674.

Karato, S.-I. (2008). *Deformation of Earth Materials - an introduction to the rheology of solid earth*. Cambridge University Press, Cambridge.

Karman, T. v. (1911). Festigkeitsversuche unter allseitigem druck. *Zeitschrift des Vereines Deutscher Ingenieure*, 55(42):1749 – 1757.

Keulen, N., Heilbronner, R., Stünitz, H., Boullier, A.-M., and Ito, H. (2007). Grain size distributions of fault rocks: A comparison between experimentally and natrually deformed granitoids. *Journal of Structural Geology*, 29:1282 – 1300.

Kilian, R., Heilbronner, R., and Stünitz, H. (2011). Quartz grain size reduction in a granitoid rock and the transition from dislocation to diffusion creep. *Journal of Structural Geology*, 33:1265 – 1284.

Kirby, S. H. and Kronenberg, A. K. (1984). Deformation of clynopyroxenite : Evidence for a transition in flow mechanisms and semibrittle behaviour. *Journal of Geophysical Research*, 89:3177 – 3192.

Kirkpatrick, J. D., Rowie, C. D., White, J. C., and Brodsky, E. E. (2013). Silica gel formation during fault slip: Evidence from the rock record. *Geology*, 41(9):1015 – 1018.

Kohlstedt, D. L., Evans, B., and Mackwell, S. J. (1995). Strength of the Litosphere: Constraints imposed by laboratory experimetns. *Journal of Geophysical Research - Solid Earth*, 100(B9):517 – 587.

Kohlstedt, D. L. and Hansen, L. N. (2015). Constitutive equations, rheological behavior, and viscosity of rocks. In Schubert, G., editor, *Treatise on Geophysics*, pages 441 – 472. Elsevier.

Kolle, J. J. and Blacic, J. D. (1982). Deformation of single-crystal clinopyroxenes: Mechanical twinning in diopside and hedenbergite. *Journal of Geophysical Research*, 87(B5):4019 – 4034.

Krabbendam, M., Wain, A., and Andersen, T. B. (2000). Pre-Caledonian granulite and gabbro enclaves in the Western Gneiss Region, Norway: indications of incomplete transition at high pressure. *Geological Magazine*, 137(3):235 – 255.

Kronenberg, A. K. and Shelton, G. L. (1980). Deformation microstructures in experimentally deformed Maryland Diabase. *Journal of Structural Geology*, 2(3):341 – 353.

Kruse, R., Stünitz, H., and Kunze, K. (2001). Dynamic recrystallization processes in plagioclase porphyroclasts. *Journal of Structural Geology*, 23:1781 – 1802.

Lallemant, H. A. (1978). Experimental deformation of diopside and websterite. *Tectonophysics*, 48:1 – 27.

Langdon, T. G. (2006). Grain boundary sliding revisited: Developments in sliding over four decades. *Journal of Material Science*, 41:597 – 609.

Lapworth, T., Wheeler, J., and Prior, D. J. (2002). The Deformation of Plagioclase investigated using Electron Backscatter Diffraction Crystallographic Preferred Orientation Data. *Journal of Structural Geology*, 24:387 – 399.

Linckens, J., Herwegh, M., Müntener, O., and Mercolli, I. (2011). Evolution of a polymineralic mantle shear zone and the role of second phases in the localization of deformation. *Journal of Geophysical Research*, 116(B6):B06210.

Mackwell, S. J. (1991). High-temperature creep of enstatite single crystals. *Journal of Geophysical Research*, 18:2027 – 2030.

Magloughlin, J. F. (1992). Microstructural and chemical changes associated with cataclasis and frictional melting at shallow crustal levels: the cataclasite - pseudotachylyte connection. *Tectonophysics*, 204(3-4):243 – 260.

Mainprice, D. and Silver, P. G. (1993). Interpretation of SKS-waves using samples from the subcontinental lithosphere. *Physics of the Earth and Planetary Interiors*, 78:257 – 280.

Mancktelow, N. S. (1985). The simplon line: a major displacement zone in the western lepontine alps. *Eclogae geol. Helv.*, 78:73 – 96.

Mancktelow, N. S. (2011). Deformation of an elliptical inclusion in two-dimensional incompressible power-law viscous flow. *Journal of Structural Geology*, 33:1378 – 1393.

Mancktelow, N. S. and Pennacchioni, G. (2005). The control of precursor brittle fracture and fluid-rock interaction on the development of single and paired ductile shear zones. *Journal of Structural Geology*, 27:645 – 661.

Marone, C., Raleigh, B., and Scholz, C. H. (1990). Frictional behavior and constitutive modeling of simulated fault gouge. *Journal of Geophysical Research*, 95(B5):7007 – 7025.

Mauler, A., Bystricky, M., Kunze, K., and Mackwell, S. (2000). Microstructures and lattice preferred orientations in experimentally deformed clinopyroxene aggregates. *Journal of Structural Geology*, 22:1633 – 1648.

Mc Kenzie, D. and Brune, J. N. (1972). Melting on Fault Planes During Large Earthquakes. *Geophys. J. R. austr. Soc.*, 29:65 – 78.

McLaren, A. C. and Pryer, L. L. (2001). Microstructural investigation of the interaction and interdependence of cataclastic and plastic mechanisms in feldspar crystals deformed in the semi-brittle field. *Tectonophysics*, 335:1– 15.

Mehl, L. and Hirth, G. (2008). Plagioclase preferred orientation in layered mylonites: Evaluation of flow laws for the lower crust. *Journal of Geophysical Research - Solid Earth*, 113(B5):B05202.

Meredith, P. G. (1990). Fracture and failure of brittle polycrystals: an overview. In Barber, D. J. and Meredith, P. G., editors, *Deformation Processes in Minerals, Ceramics and Rocks*, pages 5 – 41. Springer.

Mukai, H., Austrheim, H., Putnis, C. V., and Putnis, A. (2014). Textural Evolution of Plagioclase Feldspar across a Shear Zone: Implications for Deformation Mechanism and Rock Strength. *Journal of Petrology*, 55(8):1457 – 1477.

Newman, J., Lamb, W. M., Drury, M. R., and Vissers, R. L. M. (1999). Deformation processes in a peridotite shear zone: reaction-softening by an H2O-deficient, continuous net transfer reaction. *Tectonophysics*, 303:193 – 222.

Niemeijer, A., Di Toro, G., Griffith, W. A., Bistacchi, A., Smith, S. A., and Nielsen, S. (2012). Inferring earthquake physics and chemistry using an integrated field and laboratory approach. *Journal of Structural Geology*, 39:2 – 36.

Niemeijer, A., Di Toro, G., Nielsen, S., and Di Felice, F. (2011). Frictional melting of gabbro under extreme experimental conditions of normal stress, acceleration, and sliding velocity. *Journal of Geophysical Research*, 116:B07404.

Obata, M. and Karato, S.-I. (1995). Ultramafic pseudotachylite from the Balmuccia peridotite, Ivrea-Verbano zone, northern Italy. *Tectonophysics*, 242:313 – 328.

Ojovan, M. I. (2008). Viscosity and Glass Transition in Amorphous Oxides. *Advances in Condensed Matter Physics*, 2008.

Okudaira, T., Jerabek, P., H., S., and Fusseis, F. (2015). High-temperature fracturing and subsequent grain-size-sensitive creep in lower crustal gabbros: Evidence for coseismic loading followed by creep during decaying stress in the lower crust? *Journal of Geophysical Research - Solid Earth*, 120:3119 – 3141.

Olgaard, D. L. and Evans, B. (1986). Effect of second-phase particles on grain growth in calcite. *Journal of the American Ceramic Society*, 69:272 – 277.

Panozzo Heilbronner, R. (1984). Two-dimensional strain from the orientation of lines in a plane. *Journal of Structural Geology*, 6(1-2):215 – 221.

Paterson, M. S. (2013). *Materials Science for Structural Geology*. Springer, Dordrecht.

Paterson, M. S. and Wong, T.-F. (2005). *Experimental Rock Deformation - The Brittle Field*. Springer, 2 edition.

Pec, M. (2014). *Experimental investigation on the rheology of fault rocks*. PhD thesis, University of Basel.

Pec, M., Stünitz, H., and Heilbronner, R. (2012a). Semi-brittle deformation of granitoid gouges in shear experiments at elevated pressures and temperatures. *Journal of Structural Geology*, 38:200 – 221.

Pec, M., Stünitz, H., Heilbronner, R., and Drury, M. (2016). Semi-brittle flow of granitoid fault rocks in experiments. *Journal of Geophysical Research - Solid Earth*, 121:JB012513.

Pec, M., Stünitz, H., Heilbronner, R., Drury, M., and de Capitani, C. (2012b). Origin of pseudotachylites in slow creep experiments. *Earth and Planetary Science Letters*, 355 - 356:299 – 310.

Pecora, R. (1985). In Pecora, R., editor, *Dynamic light scattering - applications of photon correlation spectroscopy*, pages 1 – 6. Plenum Press.

Pennacchioni, G. and Mancktelow, N. (2007). Nucleation and initial growth of a shear zone network within compositionally and tructurally heterogeneous granitoids under amphibolite facies conditions. *Journal of Structural Geology*, 29:1757 – 1780.

Philpotts, A. R. (1964). Origin of Pseudotachylites. *American Journal of Science*, 262:1008 – 1035.

Putnis, A. (1992). *Introduction to mineral sciences*. Cambridge University Press, New York.

Raterron, P. and Jaoul, O. (1991). High-temperature deformation of diopside single crystal, 1. mechanical data. *Journal of Geophysical Research*, 96:14277 – 14286.

Richter, B., Stünitz, H., and Heilbronner, R. (2016). Stresses and pressures at the quartz-to-coesite phase transformation in shear- deformation experiments. *Journal of Geophysical Research - Solid Earth*, 121:JB013084.

Rosenberg, C. L. and Stünitz, H. (2003). Deformation and recrystallization of plagioclase along a temperature gradient: an example from the Bergell tonalite. *Journal of Structural Geology*, 25:389 – 408.

Rubie, D. C. (1986). The catalysis of mineral reaction by water and restrictions of the presence of aqueous fluid during metamorphism. *Mineralogical Magazine*, 50:399 – 415.

Rubie, D. C. (1998). Disequilibrium during metamorphism: the role of nucleation kinetics. *Geological Society Special Publication*, 138:199 – 214.

Rutter, E. H. (1976). The kinetics of rock deformation by pressure solution. *Philosophical Transactions of the Royal Society of London*, 283:203 – 219.

Rutter, E. H., Peach, C. J., White, S. H., and Johnston, D. (1985). Experimental 'syntectonic' hydration of basalt. *Journal of Structural Geology*, 7(2):251 – 266.

Rybacki, E. and Dresen, G. (2000). Dislocation and diffusion creep of synthetic anorthithe aggregates. *Journal of Geophysical Research - Solid Earth*, 105(B11):26017 – 26036.

Rybacki, E., Gottschalk, M., Wirth, R., and Dresen, G. (2006). Influence of water fugacity and activation volume on the flow properties of fine-grained anorthite aggregates. *Journal of Geophysical Research - Solid Earth*, 111:B03203.

Sanchez, E. C., Torres, E. M., Diaz, C., and Saito, F. (2004). Effects of grinding of the feldspar in the sintering using a planetary ball mill. *Journal of Materials Processing Technology*, 152:284 – 290.

Schmid, E. and Boas, W. (1950). *Plasticity of Crystals with Special Reference to Metals*. F. A. Hughes, London.

Schmid, S., Panozzo, R., and Bauer, S. (1987). Simple shear experiments on calcite rocks: rheology and microfabric. *Journal of Structural Geology*, 9(5/6):747 – 778.

Schmid, S. M. and Handy, M. R. (1991). Towards a genetic classification of fault rocks: geological usage and tectonophysical implications. In Müller, D. W., Mc Kenzie, J. A., and Weissert, H., editors, *Controversies in Modern Geology*. Academic Press, London.

Scholz, C. and Engelder, J. T. (1976). The role of asperity indentation and ploughing in rock friction - i: Asperity creep and stick-slip. *Int. J. Rock Mech. Men. and Geomech. Abstr.*, 13(5):149 – 154.

Scholz, C., Molnar, P., and Johnson, T. (1972). Detailed studies of frictional sliding of granite and implications for the earthquake mechanism. *Journal of Geophysical Research*, 77(32):6392 – 6406.

Scholz, C. H. (1998). Earthquakes and friction laws. *Nature*, 391:37 – 42.

Schott, J., Brantley, S., Crerar, D., Guy, C., Borcsik, M., and Willaime, C. (1989). Dissolution kinetics of strained calcite. *Geochemica et Cosmochimica Acta*, 53:373 – 382.

Shaocheng, J. and Bin, X. (2002). *Rheology of polyphase earth materials*. Polytechnic International Press, MontrÃľal.

Shaocheng, J. and Mainprice, D. (1987). Experimental deformation of sintered albite above and below the ordered-disorder transition. *Geodinamica Acta (Paris)*, 1(2):113 – 124.

Shaocheng, J. and Mainprice, D. (1990). Recrystallization and fabric development in plagioclase. *Journal of Geology*, 98(1):65 – 79.

Shigmeatsu, N. and Tanaka, H. (2000). Dislocation creep of fine-grained recrystallized plagioclase under low-temperature conditions. *Journal of Structural Geology*, 22:65 – 79.

Shimizu, I. (1995). Kinetics of pressure solution creep in quartz: theoretical considerations. *Tectonophysics*, 245:121 – 134.

Sibson, R. H. (1975). Generation of Pseudotachylyte by Ancient Seismic Faulting. *Geophysical Journal International*, 43(3):775 – 794.

Sibson, R. H. (1977). Fault rocks and fault mechanisms. *J. geol. Soc. Lond.*, 133:191 – 213.

Sibson, R. H. (1982). Fault zone models, heat flow, and the depth distribution of earthquakes in the continental crust of the United States. *Bulletin of the Seismological Society of America*, 72:151 – 163.

Sibson, R. H. (1984). Roughness at the Base of the Seismogenic Zone: Contributing Factors. *Journal of Geophysical Research - Solid Earth*, 89(B7):5791 – 5799.

Sibson, R. H., White, S. H., and Atkinson, B. K. (1981). Structure and distribution of fault rocks in the alpine fault zone, new zealand. *Geol. Soc. Lond., Spec. Pub.*, 9:197 – 210.

Simpson, C. (1986). Fabric Development in Brittle-to-Ductile Shear Zones. *Pure and Applied Geophysics*, 124(1/2):269 – 288.

Spray, J. G. (1987). Artificial generation of pseudotachylite using friction welding apparatus: Simulation of melting on a fault plane. *Journal of Structural Geology*, 9:49 – 60.

Stel, H. (1981). Crystal growth in cataclasites: Diagnostic microstructures and implications. *Tectonophysics*, 78(1-4):585 – 600.

Storti, F., Billi, A., and Salvini, F. (2003). Particle size distributions in natural carbonate fault rocks: insights for non-self-similar cataclasis. *Earth and Planetary Science Letters*, 206:173 – 186.

Stünitz, H. and Fitz Gerald, J. D. (1993). Deformation of granitoids at low metamorphic grade. II: Granular flow in albite-rich mylonites. *Tectonophysics*, 221:229 – 324.

Stünitz, H., Fitz Gerald, J. D., and Tullis, J. (2003). Dislocation generation, slip systems, and dynamic recrystallization in experimentally deformed plagioclase single crystals. *Tectonophysics*, 372:215 – 233.

Stünitz, H. and Tullis, J. (2001). Weakening and strain localization produced by syndeformational reaction of plagioclase. *International Journal of Earth Sciences*, 90:136 – 148.

Sundberg, M. and Cooper, R. F. (2008). Crystallographic preferred orientation produced by diffusional creep of harzburgite: Effects of chemical interactions among phases during plastic flow. *Journal of Geophysical Research*, 113:B12208.

Tarantola, A., Diamond, L. W., and Stünitz, H. (2010). Modification of fluid inclusions in quartz by deviatoric stress i: experimentally induced changes in inclusion shapes and microstructures. *Contributions to Mineralogy and Petrology*, 160:825 – 843.

Tikoff, B. (1995). The limitations of three-dimensional kinematic vorticity analysis. *Journal of Structural Geology*, 17:1771 – 1784.

Trepmann, C. A. and Stöckert, B. (2003). Quartz microstructures developed during non-steady state plastic flow at rapidly decaying stress and strain rate. *Journal of Structural Geology*, 25:2035 – 2051.

Trepmann, C. A., Stöckert, B., Dorner, D., Moghadam, R. H., Küster, M., and Röller, K. (2007). Simulating coseismic deformation of quartz in the middle crust and fabric evolution during postseismic stress relaxation - an experimental study. *Tectonopyhsics*, 442:83 – 104.

Tullis, J., Dell'Angelo, L., and Yund, A. (1987). Ductile shear zones from brittle precursors in feldspathic rocks: The role of dynamic recrystallization. *Geophysical Monograph*, 56:67 – 80.

Tullis, J. and Yund, A. (1985). Dynamic recrystallization of feldspar: A mechanism for ductile shear zone formation. *Geology*, 13:238 – 241.

Tullis, J. and Yund, A. (1987). Transitino from cataclastic flow to dislocation creep of feldspar: Mechanisms and microstructures. *Geology*, 15:606 – 609.

Tullis, J. and Yund, A. (1991). Diffusion creep in feldspar aggregates: experimental evidence. *Journal of Structural Geology*, 13(9):987 – 1000.

Tullis, J. and Yund, R. A. (1977). Experimental deformation of dry westerly granite. *Journal of Geophysical Research*, 82:5705 – 5718.

Viegas, G., Menegon, L., and Archanjo, C. (2016). Brittle grain-size reduction of feldspar, phase mixing and strain localization in granitoids at mid-crustal conditions (Pernambuco shear zone, NE Brazil). *Solid Earth*, 7:375 – 396.

Wang, Y. F., Zhang, J. F., Jin, Z. M., and Green II, H. W. (2012). Mafic granulite rheology: Implications for a weak continental crust. *Earth and Planetary Science Letters*, 353-354:99 – 107.

Wayte, G. J., Worden, R. H., Rubie, D. C., and Droop, G. T. R. (1989). A TEM study of disequilibrium plagioclase breakdown at high pressure: the role of infiltrating fluid. *Contribution to Mineralogy and Petrology*, 101:426 – 437.

Wheeler, J. (1992). Importance of Pressure Solution and Coble Creep in the Deformation of Polymineralic Rocks. *Journal of Geophysical Research*, 97(B4):4579 – 4586.

Whitney, D. and Evans, B. W. (2010). Abbrevations for names of rock-forming minerals. *American Mineralogist*, 95:185 – 187.

Wintsch, R. P. (1985). *The Possible Effects of Deformation on Chemical Processes in Metamorphic Fault Zones*. Advances in Physical Geochemistry, 4. Springer-Verlag, N.Y.

Xie, Y., Wenk, H.-R., and Matthies, S. (2003). Plagioclase preferred orientation by TOF neutron diffraction and SEM-EBSD. *Tectonophysics*, 370:269 – 286.

Yund, R. A., Blanpied, M. L., Tullis, T. E., and Weeks, J. D. (1990). Amorphous material in high strain experimental fault gauges. *Journal of Geophysical Research*, 95(B10):15589 – 15602.

Yund, R. A. and Tullis, J. (1991). Compositional change of minerals associated with dynamic recrystallization. *Contributions to Mineralogy and Petrology*, 108:346 – 355.

Zhang, J., Green, H. W., and Bozhilov, K. N. (2006). Rheology of omphacite at high temperature and pressure and significance of its lattice preferred orientations. *Earth and Planetary Science Letters*, 246:432 – 443.

Zhou, S., Rybacki, E., Wirth, R., He, C., and Dresen, G. (2012). Creep of partially molten fine-grained gabbro under dry conditions. *Journal of Geophysical Research*, 117:B05204.

Appendices

Appendix A

List of all experiments

Table A 1: *List of all experiments*

Exp. Nr	T [°C]	Pc [MPa]	Material	γa	strain rate ýa [s-1]	th0 [mm]	thF [mm]	d [mm]	axial d rate [m/s]	H2O added	comment
364	700	~ 500	MD	n.a.	~ 3E-04	n.a.	n.a.	n.a.	n.a.	0.20 µl	(1)
365	700	1088	MD	2.6	2.9E-05	0.83	0.62	1.601	1.7E-08	0.20 µl	
367	600	582	MD	2.0	3.4E-05	0.83	0.64	1.307	2.1E-08	0.20 µl	
369	500	546	MD	2.3	3.3E-05	0.83	0.65	1.437	2.0E-08	0.20 µl	
371	700	~ 500	MD	n.a.	~ 3E-05	n.a.	n.a.	n.a.	n.a.	0.20 µl	(2)
373	600	534	MD	2.8	3.2E-05	0.83	0.67	1.713	1.9E-08	0.20 µl	
374	300	562.1	MD	2.6	3.3E-04	0.83	0.68	1.597	1.9E-07	0.20 µl	
375	300	552	MD	2.6	3.4E-05	0.83	0.71	1.559	2.0E-08	0.20 µl	
393	700	561	MD	2.4	3.6E-05	0.83	0.71	1.466	2.2E-08	0.20 µl	
395	300	1016	MD	2.8	3.8E-05	0.83	0.6	1.724	2.2E-08	0.20 µl	
397	500	1014	MD	2.5	3.3E-05	0.83	0.62	1.588	1.9E-08	0.20 µl	
399	600	1027	MD	3.0	3.2E-05	0.83	0.62	1.848	2.0E-08	0.20 µl	
401	500	1012	MD	0.8	2.2E-05	0.83	0.78	0.499	7.1E-09	0.20 µl	
402**	500	1006	MD	0	n.a.	0.83	0.83	0	0.0E+00	0.20 µl	
413	700	604	MD	3.6	3.3E-05	0.83	0.67	2.103	2.0E-08	0.20 µl	
414	800	1045	MD	4.2	3.7E-05	0.75	0.50	2.165	1.8E-08	0.20 µl	
416	700	1038	MD	3.1	3.0E-05	0.83	0.61	1.853	1.8E-08	0.20 µl	
418	300	551	MD	3.4	3.4E-05	0.83	0.60	2.043	1.9E-08	0.20 µl	
420	800	1495	MD	0.5	1.6E-05	0.75	0.72	0.294	8.9E-09	0.20 µl	
421	300	517	MD	1.5	2.9E-05	0.83	0.72	0.967	1.8E-08	0.20 µl	
436	700	1515	MD	1.9	2.8E-05	0.83	0.73	1.187	2.0E-08	0.20 µl	
438	700	1002	MD	1.1	1.7E-05	0.83	0.75	0.718	1.1E-08	0.20 µl	
440	300	562	MD	3.1	2.7E-05	0.83	0.65	1.852	1.5E-08	0.20 µl	(3)
442	300	530	MD		3.4E-05	0.83			2.0E-08		
				3.9	3.3E-04		0.59	2.285	1.6E-07	0.20 µl	
444	300	558	MD		2.9E-05	0.83			1.7E-08	0.20 µl	
				2.9	3.5E-06		0.66	1.766	1.9E-09	0.20 µl	
446	500	1007	MD		2.3E-05	0.83			2.2E-08		
					2.7E-04				1.3E-07		
				3.2	3.5E-05		0.62	1.929	1.8E-08	0.20 µl	
449	800	1504	MD	4.1	3.5E-05	0.75	0.61	2.146	1.8E-08	0.20 µl	
451	700	1052	MD	3.4	3.2E-05	0.83	0.68	2.042	1.8E-08	0.20 µl	
468*	800	1061	MD	0.7	1.7E-05	0.75	0.69	0.426	1.1E-08	0.20 µl	
470*	800	1477	MD	0.9	1.7E-05	0.75	0.69	0.544	1.1E-08	0.20 µl	

continuing Table A 1.

Exp. Nr	T [°C]	Pc [MPa]	Material	γa	strain rate ýa [s-1]	th0 [mm]	thF [mm]	d [mm]	axial d rate [m/s]	H2O added	comment
473	700	1556	MD	2.9	3.1E-05	0.83	0.63	1.762	1.8E-08	0.20 µl	
475	300	582	MD	n.a.	n.a.	15.8	12.70	3.335	8.3E-09	???	(4)
477	800	1045	Ab + Di (D)	3.3	1.9E-05	0.75	0.67	1.774	1.0E-08	0.20 µl	
483	500	549	MD	3	3.4E-05	0.83	0.64	1.826	2.0E-08	0.20 µl	
484	800	1041	MD		2.8E-05	0.75			1.6E-08		
				2.0	1.3E-05		0.61	1.138	8.1E-09	0.20 µl	
486	700	1093	MD	3.7	8.00E-06	0.83	0.59	2.166	4.5E-09	0.20 µl	
489	800	1073	MD	2.8	3.0E-05	0.75	0.63	1.523	1.6E-08	0.20 µl	
490	800	1059	MD		3.5E-05	0.75			2.1E-08		
					1.9E-05				9.6E-09		
				4.5	4.1E-06		0.54	2.195	1.9E-09	0.20 µl	
491	800	1535	MD		1.8E-05	0.75			1.4E-08		
					6.5E-06				5.6E-09		
				3.2	1.9E-06		0.54	2.195	1.8E-09	0.20 µl	
492	800	1069	MD	6.8	4.7E-05	0.75	0.44	3.223	2.2E-08	0.20 µl	
501	600	1037	MD	3.1	4.1E-05	0.83	0.62	1.858	2.4E-08	0.20 µl	
502	800	1542	MD		2.0E-05				1.5E-08		
					6.0E-06				5.8E-09		
				3.2	1.5E-06	0.75	0.58	1.838	1.3E-09	0.20 µl	
503	800	1089	Slab + En	5.6	4.1E-05	0.75	0.55	2.83	2.0E-08	0.12 µl	
505	800	1072	Slab+Di (CrLk)	5.3	4.0E-05	0.75	0.55	2.683	2.0E-08	0.12 µl	
507	800	1073	MD	4.7	4.1E-05	0.75	0.49	2.383	2.0E-08	0.12 µl	
509	300	560	MD	2.9	3.80E-05	0.83	0.7	1.722	2.2E-08	0.20 µl	
510	800	1462	MD	0.0	0.0E+00	0.75	n.a.	0	0.0E+00	0.20 µl	(5)
514	900	1080	MD	4.3	3.90E-05	0.75	0.55	2.251	1.8E-08	0.12 µl	
515	800	1049	MD	5	3.80E-05	0.75	0.55	2.566	1.9E-08	0.12 µl	
517	800	1236	MD	9.7	8.20E-04	0.75	0.55	4.697	3.6E-07	0.12 µl	
518	800	1061	Ab + En	4.9	3.8E-05	0.75	0.54	2.523	1.9E-08	0.12 µl	
519	800	1076	Slab + Di (D)	4.7	3.6E-05	0.75	0.54	2.435	1.8E-08	0.12 µl	
520	800	995	MD	1.4	6.00E-06	0.75	0.7	0.917	4.0E-09	0.12 µl	(6)
521	300	553	MD	2.2	3.80E-05	0.83	0.65	1.381	2.3E-08	0.20 µl	
522	800	1032	MD	1.6	4.60E-06	0.75	0.64	1.072	3.1E-09	0.12 µl	(7)
523	800	1028	MD	0.7	1.20E-06	0.75	0.67	0.58	1.0E-09	0.12 µl	(8)
531	700	1093	MD		2.4E-05	0.83			1.4E-08		
					8.3E-06				5.0E-09		
					2.7E-06				1.7E-09		
				4.4	7.1E-06		0.60	2.527	3.5E-09	0.20 µl	

MD = Maryland Diabase, Ab = Albite, Di(D) = Damaping Enstatite, Slab = Sonora Labradorite, Di(CrLk) = Cranberry Lake Diopside, En = Damaping Enstatite; γa = apparent incremental shear strain, th0 = shear zone thickness at experiment start, thF = shear zone thickness at experiment End, d = axial displacement of load piston; comments: (1) and (2) Intense stress-drop after peak stress. Experiment was aborted thereafter. (3) MD whole rock used as forcing blocks. (4) Axial shortening experiment. (5) Hydrostatic experiment. (6) constant load experiment at $\tau \approx 215$ MPa. (7) constant load experiment at $\tau \approx 200$ MPa. (8) constant load experiment at $\tau \approx 190$ MPa.; (∗) peak stress experiment. (∗∗) experiment terminated at hit-point.

Appendix B

New calibration of displacement correction factor

The deformation apparatus are not perfectly stiff and thus extend elastically when building up confining pressure and differential load (e.g. (Pec, 2014) Fig. 2.25). Especially during deformation of a strong sample as high loads are applied, machine extension will be significant. Likewise, during sample weakening, the machine will contract because of the decrease in load. The machine extension during an experiment leads to the fact that not all of the axial displacement of the load piston will reach the sample, but will be partially 'lost' in accommodating machine extension. Thus, the measured displacement from the digital record must be corrected for machine extension to derive the axial displacement of the load piston into the sample assembly (enforcing sample shortening). The correction factor for the effect of machine extension on displacement is calibrated by using a tungsten carbide (WC) sample. The WC sample was loaded at three different confining pressures (Pc), Pc = 0.5, 1.0 and 1.5GPa, at room temperature. During the WC runs, confining pressure, load and displacement were recorded. From the applied load and the elastic moduli of WC, a theoretically expected displacement is calculated. The theoretical displacement is compared with the measured displacement, which, due to the machine extension, will be larger than the expected displacement. From the discrepancy of the measured and the theoretically expected displacement, a correction factor as mm/N is derived. The WC sample tests were performed, and data made available by courtesy of Leif Tokle.

The elastic modulus (E) of WC was taken as E = 600GPa. The WC sample is a cylindrical rod with a length l = 37mm and a diameter d = 6.33mm. In the calibration runs, the WC sample was loaded to maximum $\sim$ 115kN, which is calculated to result in $\sim$ 3.65GPa pressure on the WC sample (pressures are determined assuming a constant cross-sectional area of the WC rod). The maximum differential stress thus were $\sim$ 3.15 to 2.15GPa, depending on the confining pressure. The length change of the WC rod and the length change per Newton were calculated as the following:

length change of WC rod:

$$\begin{aligned} dL &= (\Delta\sigma / E_{WC}) * l \\ &= (3.15 * 10^9 Pa / 600 * 10^9 Pa) * 37mm = 0.1973mm \end{aligned} \tag{1}$$

length change of WC rod per Newton:

$$\begin{aligned} (dL/3.15 * 10^9 Pa)/area &= 6.2635 * 10^{-11}/(\pi * 3.165^2) = \\ &= 1.9903 * 10^{-12} mm/N \end{aligned} \tag{2}$$

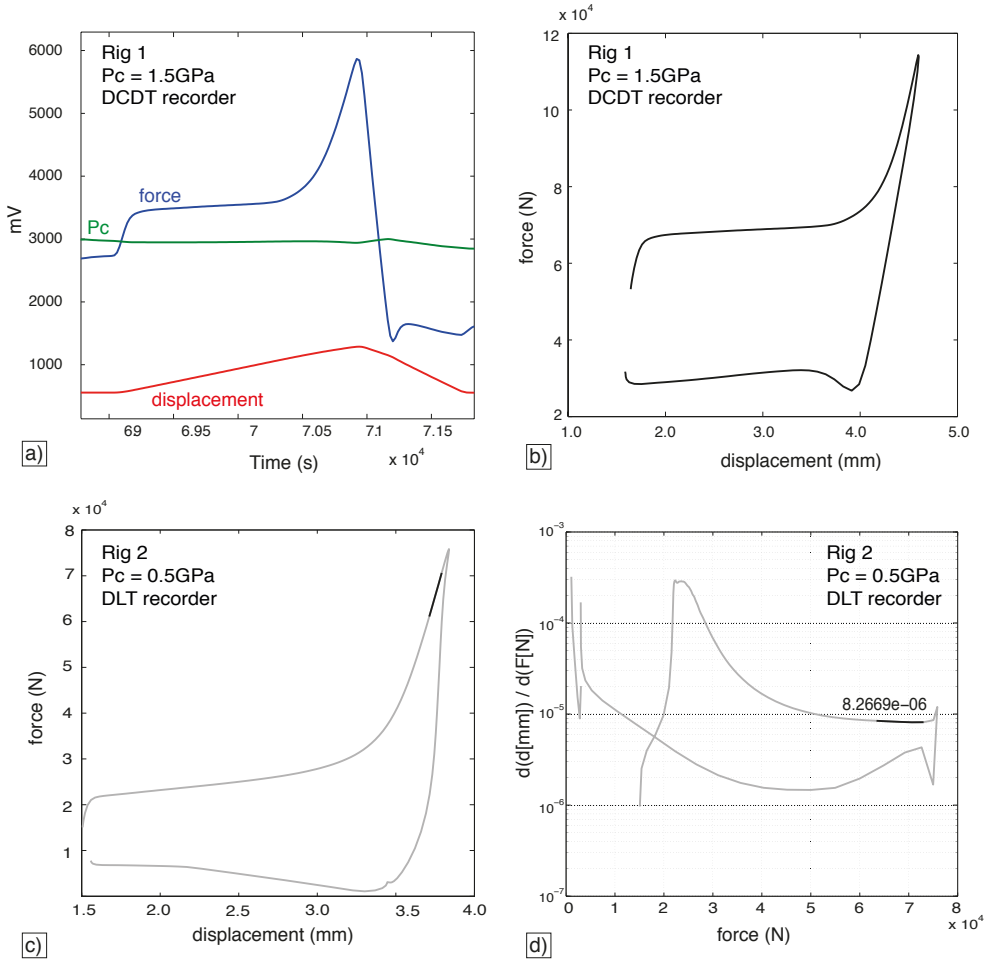

Figure 1: *Overview WC sample runs for machine extension determination. a) Example of a WC sample run using Rig 1 at a confining pressure (Pc) = 1.5GPa. b) Force vs. displacement curve for the data shown in a). c) Force vs. displacement curve for a WC sample run on Rig 2 at Pc = 0.5GPa and the displacement record from the DLT detector. d) Same data as in c), plotted as change in displacement per change in force vs. force. The black curve part in c) and d) marks the interval over which the change in displacement per change in force is measured (number given in plot).*

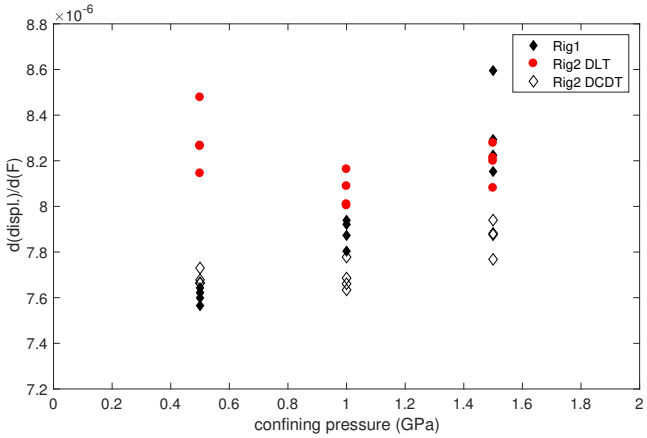

Figure 2: *Change in displacement per change in force (d(displ.)/d(F)) values determined for Rig 1 and Rig 2 and the three different confining pressures (Pc). For each Pc and Rig, d(displ.)/d(F) was measured four times using different intervals over the curve.*

A typical run on a WC rod sample is presented in Fig. 1a. Plotting displacement vs. force (Fig. 1b, c) shows the hysteresis in the machine, i.e. during unloading, force drops far below the value at experiment run start for the same load-piston position. This behavior is interpreted to be a combination of friction in the sample assembly and retarded machine contraction (note load-piston retreat was performed in ∼ half the time of load-piston advancement, Fig. 1a). The friction during WC rod experiments is expected to be much higher than in the usual sample assembly, because lead instead of salt is used as confining medium in the WC runs.

A change in displacement per change in force is determined (d(displacement)/d(F)), as an average over the linear part of the curve (curve parts marked in black in Fig. 1c and d). The d(displacement)/d(F) curves are rarely close to linear and thus determined values are sensitive on the selected interval over which they are calculated. There are furthermore differences between runs at different confining pressures, especially for Rig 1 (Fig. 2).

Values for d(displacement)/d(F) are on the order of 7.5 * 10^{-6} - 8.6* 10^{-6} mm/N. The expected displacement due to elastic deformation of the WC rod lies in the range of ∼ 2 * 10^{-12} mm/N, which is 6 orders of magnitude smaller than the measured one. The elastic deformation of the WC rod is negligible and is thus not considered, i.e. all displacement measured in the digital record is considered to be due to machine extension.

The correction factors for machine extension on displacement were previously set to 3.3156 * 10^{-6} mm/N for Rig 1, and 5.0486 * 10^{-6} mm/N for Rig 2. After the presented new evaluation, correction factors should be changed to ∼ 7.9 * 10^{-6} mm/N for the DCDT detector on Rig 1, and 7.8 * 10^{-6} mm/N and 8.2 * 10^{-6} mm/N for the DCDT and DLT detectors on Rig 2 respectively. For the DCDT detectors, there seems to be a ∼ linear relationship between the change in displacement per force as a function of

confining pressure. Especially for Rig 1, the values are significantly different, from $\sim$ 7.6 * 10^{-6} mm/N at 0.5GPa confining pressure, to 8.2 * 10^{-6} mm/N at 1.5GPa. It thus might be worth to consider applying a different correction factor to the displacement record, according to the confining pressure of a given experiment.

Appendix C

Matlab code, elastic salt correction

The *elastic salt correction* was developed by Renée Heilbronner (Basel University), with significant contributions from Bettina Richter (Basel University). The *elastic salt correction* procedure is listed in this thesis to allow for reconstruction of the corrections applied to the mechanical data. A fortran code for the Rig data treatment (including the *elastic salt correction*) is publicly available at https://earth.unibas.ch/micro/index.html. The MATLAB code presented here is my translation of the *elastic salt correction* fortran code to MATLAB.

```
% ------------------------------------------------------------
% ////////////////////// Salt correction \\\\\\\\\\\\\\\\\\\\\\
% ------------------------------------------------------------

%-------------------------------------------------------------------------
% Parameter for salt correction
fprintf('------------------------------------------------------ \n')
iMPa=input('Pc of experiment [MPa]: ');
fprintf('------------------------------------------------------ \n')
itempC=input('T of experiment [degree Celcius]: ');
fprintf('------------------------------------------------------ \n')
isalt1=input('inner salts ? NaCl (1), KI (2) : ');
fprintf('------------------------------------------------------ \n')
isalt2=input('outer salts ? NaCl (1), KI (2) : ');
fprintf('=================================== \n \n');

%-------------------------------------------------------------------------
% inner radius (R) defined by average diameter of stove (11.45-14.75mm) furnace
% material is neglected.
%
% *    sample size
% *    rs2= r outer = 25.4mm/2 = 12.7 mm
% *    rs1= r inner = ((11.45 + 14.75mm)/2)/2 = 13.1/2 = 6.55 mm
% *    rp=  r sig1 piston = sdia/2 = 6.35/2 = 3.175 mm
%
% Bulk modulus is calculated in GPa for homologous T
%-------------------------------------------------------------------------

xL = 36.0; % length of salt cilyinder
rp = 3.175; % rp=  r sig1 piston = sdia/2 = 6.35/2 = 3.175 mm
rs1 = 6.55; % [mm] outer radius inner salt (rs1= r inner = ((11.45 + 14.75mm)/2)/2 = 13.1/2
= 6.55 mm)
rs2 = 12.7; % [mm] outer radius outer salt (rs2= r outer = 25.4mm/2 = 12.7 mm)

bsi=(1:100); bso=(1:100);
iwhich= (10*isalt1)+isalt2; % isalt1 = NaCl, isalt2 = KI.
```

```
if isalt1==1 & isalt2==1
    [bsi] = profileNaCl(xL,itempC,iMPa);
    [bso] = profileNaCl(xL,itempC,iMPa);
elseif isalt1==2 & isalt2==2
    [bsi] = profileKI(xL,itempC,iMPa);
    [bso] = profileKI(xL,itempC,iMPa);
elseif isalt1==2 & isalt2==1
    [bsi] = profileKI(xL,itempC,iMPa);
    [bso] = profileNaCl(xL,itempC,iMPa);
else
    fprintf('\n ===================================== \n')
    fprintf('salt correction is not calculated for this \n combination of salts')
    fprintf('\n ===================================== \n')
end

iloop = xL+1;
half = (0.5*xL) +1;

bs=((rs1-rp)/(rs2-rp).*bsi) + ((rs2-rs1)/(rs2-rp).*bso);

bs_sum=sum(bs);
bs_mean=bs_sum/iloop;

pratio2 = (rp/rs2)^2; % area ratio (piston/salt) = vol ratio if d(piston)=xL
bs_exp = (pratio2/(1-pratio2))/xL;
deltaMPa = 1000 * bs_exp/bs_mean;
slope=deltaMPa;


% ---------------------------------------------------------------
% ////////////////////// function 'profileNaCl' \\\\\\\\\\\\\\\\\\
% ---------------------------------------------------------------

function [bs] = profileNaCl(xL,itempC,iMPa)

% * fit to data from Matej Pec Dissertation (2014)
cT0 = 0.00010511;
cT1 = -0.0014089;
cT2 = -0.00000071412;


% * fit to data from Akella et al. (1969)
cm0 = 802.48;
cm1 = 217.88;
cm2 = -18.815;

% * fit to data from Robertson et al. (1958)
ck0 = 21.907;
ck1 = 17.751;
ck2 = -9.8914;
ck3 = -143.02;
ck4 = 215.34;
ck5 = -87.2;

% *--- find TC and Th profile ------------------------------
% *    fit to data from Matej Pec Dissertation (2014)

xM2 = cT0 + (cT1* itempC) + (cT2*(itempC^2));

% *--- find z, T(z) profile -------------------------------

iloop = xL+1;
half = (0.5*xL) +1;
```

```
clear i
for i=1:iloop
    zi = i;
    z(i) = zi - half;
    TC(i) = itempC + (xM2 * z(i)) + (xM2 * (z(i)^2));
end

% *--- find melting T as f(Pressure) ------------------------------

iGPa = iMPa*0.001;
Tmelt = cm0 + (cm1*iGPa) + (cm2*(iGPa^2));


% *--- profiles -------------------------------

clear i
for i=1:iloop
    Th(i) = (TC(i)+273)/(Tmelt+273);

    if Th(i) < 0.25
        fprintf('\n ================================== \n')
        fprintf('Thom is too low, the salt correction should not be used')
        fprintf('\n ================================== \n')
    elseif Th(i) > 1
        fprintf('\n ================================== \n')
        fprintf('Thom > 1. Something cannot be right!')
        fprintf('\n ================================== \n')
    end

    % *--- bulk modulus
    % *    fit to data from Akella et al. 1969
    xK(i) = ck0 + (ck1*Th(i)) + (ck2*(Th(i)^2)) + (ck3*(Th(i)^3)) + (ck4*(Th(i)^4)) +
(ck5*(Th(i)^5));

    % *--- bulkstrain for 1GPa
    bs(i)= 1/xK(i);

end


% ---------------------------------------------------------------
% ////////////////// function 'profileKI' \\\\\\\\\\\\\\\\\\
% ---------------------------------------------------------------

function [bs] = profileKI(xL,itempC,iMPa)

% * fit to data from Matej Pec Dissertation (2014)
cT0 = 0.00010511;
cT1 = -0.0014089;
cT2 = -0.00000071412;

% * fit to data from Pistorius (1965)
cm0 = 684;
cm1 = 294;
cm2 = -86.58;

% * fit to data fitted such that K NaCl : K KI = 2.05 at 25?C (salt-from-scratch2.key)
ck0 = 10.865;
ck1 = 8.7887;
ck2 = -4.8586;
ck3 = -70.997;
ck4 = 106.84;
ck5 = -43.259;
```

```
% *--- find TC and Th profile -----------------------------
% *    fit to data from Matej Pec Dissertation (2014)

xM2 = cT0 + (cT1* itempC) + (cT2*(itempC^2));


% *--- find z, T(z) profile -----------------------------

iloop = xL+1;
half = (0.5*xL) +1;

clear i
for i=1:iloop
    zi = i;
    z(i) = zi - half;
    TC(i) = itempC + (xM2 * z(i)) + (xM2 * (z(i)^2));
end


% *--- find melting T as f(Pressure) -----------------------------

iGPa = iMPa*0.001;
Tmelt = cm0 + (cm1*iGPa) + (cm2*(iGPa^2));


% *--- profiles -----------------------------

clear i
for i=1:iloop
    Th(i) = (TC(i)+273)/(Tmelt+273);

    if Th(i) < 0.25
        fprintf('\n ================================== \n')
        fprintf('Thom is too low, the salt correction should not be used')
        fprintf('\n ================================== \n')
    elseif Th(i) > 1
        fprintf('\n ================================== \n')
        fprintf('Thom > 1. Something cannot be right!')
        fprintf('\n ================================== \n')
    end

    % *--- bulk modulus
    % *    fit to data from Akella et al. 1969
    xK(i) = ck0 + (ck1*Th(i)) + (ck2*(Th(i)^2)) + (ck3*(Th(i)^3)) + (ck4*(Th(i)^4)) +
(ck5*(Th(i)^5));

    % *--- bulkstrain for 1GPa
    bs(i)= 1/xK(i);

end
```

Appendix D

Matlab code, determining amphibole corona thickness as a function around pyroxene clasts.

```
% ---------------------------
% Sept. 2015
% MATLAB script to determines the thickness of an overgrowth corona as a
% function of orientation around the clast. The result is termed
% 'radius curve'
%
% Pre-requisites:
% (i) x-y coordinates of the aggregate (clasts + overgrowth rim)
% outlines
% (ii) x-y coordinates of the clast outlines
% (iii) center of mass of clasts


% Cx = list of x coordinate of the 'center of mass' of clasts
% Cy = list of y coordinate of the 'center of mass' of clasts
% cpx = x coordinates of clast outlines
% cpy = y coordinates of clast outlines
% aggregate X Y coords input data import
% agx = x coordinates of aggregate outlines
% agy = y coordinates of aggregate outlines
% ---------------------------
```

```
fprintf('\n============================================================ \n');
fprintf('ATENTION, y coords need to have zero in upper left \n');
fprintf('angles are taken counter clockwise \n');
fprintf('============================================================ \n');

% ---------------------------
l=1:1:numel(Cx);
% plot data to see if all is ok. Centroids should be inside grains
figure; subplot(1,2,1);
plot(cpx,cpy); hold on; scatter(Cx,Cy,'r')
labels = num2str((1:numel(Cx))','%d');
text(Cx, Cy, labels, 'horizontal','left', 'vertical','bottom')
title('clasts')
hold off

subplot(1,2,2);
plot(agx,agy); hold on; scatter(Cx,Cy,'r')
labels = num2str((1:numel(Cx))','%d');
text(Cx, Cy, labels, 'horizontal','left', 'vertical','bottom')
title('aggregates')
hold off

figure;
plot(cpx,cpy); hold on; scatter(Cx,Cy,'r')
labels = num2str((1:numel(Cx))','%d');
text(Cx, Cy, labels, 'horizontal','left', 'vertical','bottom')
title('clasts')

plot(agx,agy,'r'); scatter(Cx,Cy,'r')
labels = num2str((1:numel(Cx))','%d');
text(Cx, Cy, labels, 'horizontal','left', 'vertical','bottom')
title('aggregates')
hold off
axis equal
% ---------------------------

% ////////////////////////////////////////////////////////////
% ---------------------------
delim = input('delimiter ? ') % get delimiters
ddcp = find(cpx==delim); % find positions of delimiter for clasts
ddcp = ddcp';
dcp(1) = delim; dcp=[dcp ddcp];

ddag = find(agx==delim); % find positions of delimiter for aggregates
ddag = ddag';
dag(1) = delim; dag=[dag ddag];
```

```
for i=1:(numel(dcp)-1);
    % group individual clasts in cells
    jcpx{i}=(cpx((dcp(i)+1):(dcp(i+1)-1)))';
    jcpy{i}=(cpy((dcp(i)+1):(dcp(i+1)-1)))';

    % group individual aggregates in cells
    jagx{i}=(agx((dag(i)+1):(dag(i+1)-1)))';
    jagy{i}=(agy((dag(i)+1):(dag(i+1)-1)))';
end
% ---------------------------

% ////////////////////////////////////////////////////////////
% check if the clast centroids are in the according aggregate.

% centroid coordinates (Cx, Cy) should preferentially be derived in the
% order of the measured aggregate particles.

clear i
for i=1:numel(Cx)
    if  min(jcpy{i}) <= Cy(i) && Cy(i) <= max(jcpy{i}) && min(jcpx{i}) <= Cx(i)…
    && Cx(i) <= max(jcpx{i})
        test(i)=1;
    else
        test(i)=0;
    end
end
test

testN=find(test==0);

% ////////////////////////////////////////////////
%  Calc radius curve                                ////////////

% *----- approach ----------------------
% * Search along the aggregate outline for the closest
% * of the clast.                                    outline point
% * For each point along the clast outline, the shortest distance to the
% * aggregate outline is determined. The angle with respect to the
% * horizontal, with the clast center of gravity (centroid) as rotation
% * axis, is determined for each of the points along the clast outline.
% *-------------------------------------
tt=0;
clear i j
for i=1:numel(Cx)
    njag = numel(jagx{i}); % get number of aggregate
    njcp = numel(jcpy{i});                          outline points
    xc = Cx(i); yc = Cy(i); % x,y of centroid.
```

```
    for j=1:njag
        tt=tt+1;
        xo = jagx{i}(j); yo = jagy{i}(j); % outline x-y coordinate for the aggregate

        dx = abs(xo - jcpx{i}); % difference between the x
        % the aggregate outline point and the clast outline value of
        dy = abs(abs(yo) - abs(jcpy{i})); % difference between the
        % y-value of the aggreg. outline point and the clast
        % pionts.                                          outline

        mth = sqrt((dx.^2) + (dy.^2)); % calc thickness of rim for each pair
        mtmp=find(min(mth)==mth);
        m(j)=mtmp(1);
        th{i}(j)=mth(m(j));

       % ---------------------------------------
        %---- find angle of the line spanned by the centroid of the clast
        % and the determined outline point of the clast. 0 degree is
        % horizontal, angles increase CCW --------

        ddx(j) = abs(jcpx{i}(m(j)) - abs(xc)); % difference in x coord between the
        % clast outline point and the centroid
        ddy(j) = abs(abs(jcpy{i}(m(j))) - abs(yc)); % difference in y coord
        % between the clast outline point and the centroid

        ang{i}(j)=atan(ddy(j)/ddx(j))/degree; % Angle of calc radius. /degree
         % => convert to degree

        % The horizontal should be 0, angles increase CCW :

        if (jcpx{i}(m(j)) <= xc) && (jcpy{i}(m(j)) >= yc)
            ang{i}(j)= 180 - ang{i}(j);

        elseif (jcpx{i}(m(j)) < xc) && (jcpy{i}(m(j)) < yc)
            ang{i}(j)= 180 + ang{i}(j);

        elseif (jcpx{i}(m(j)) >= xc) && (jcpy{i}(m(j)) <= yc)
            ang{i}(j)= 360 - ang{i}(j);
        end

    end
    clear m a b dx dy xo yo

end
```

```
% ////////////////////////////////////////////////////////////
% Smooth curve

xx=0:360; % curve fit interpolation should be for every degree
clear i j

for j=1:numel(ma)
   xii=ma{j}; yii=mR{j};
   yy{j}= interp1(ma{j},mR{j},xx);

   clear xii yii
end


% ////////////////////////////////////////////////////////////
% Substract P (Px) rad.curve from C (comb Amph+Px) rad.curve

% ------------------------------------------------------------------------
% Plot the radius curve of a random grain to check if output looks ok
nr=1;

figure; plot(xx,yy{nr},'b')
xlabel('angle'); ylabel('length of radius')
legend('rad.curve of Px+Amph');
hold off
% ------------------------------------------------------------------------

% ------------------------------------------------------------------------
% Calculate sum curves, where rad.curves for each grain are summed up to one
% rad.curve. dyy and ryy, which can contain negative values will result in
% smaller to equal lengths of rad.curves compared to sdyyc and sryyc.
% Because in reality, there no negative values should exist for dyy and ryy,the
% cleaned curves dyyc and ryyc (here the sum curves sdyyc and sryyc) can be
% considered as the resulting data curves of interest. But if there are
% large deviations from the cleaned curves (dyyc, ryyc, dyycs, ryycs) to
% the uncleaned (dyy, ryy, sdyy, sryy), a closer look should be taken at
% the input grains.
```

```
clear i j

% initiate the arrays
syy(1:361)=0;

for i = 1:numel(yy)
   syy = yy{i} + syy; % sum of yy
end

% normalize to nr. of aggregates
syy=syy/numel(Cx);

figure; plot(xx,syy,'b')
xlabel('angle, CCW from east')
ylabel('length of radius curve [px]')
axis([0 360 0 50]);
set(gca,'XTick',[0:30:360])
grid on;
set(gcf,'renderer','painters')

sc_syy=syy*(unit/px); % convert to original unit (unit/px), set values for
% 'unit' and 'px'

% scaled radius curves
figure; plot(xx,sc_syy,'b')
xlabel('angle, CCW from east')
ylabel('length of radius curve [micrometer]')
axis([0 360 0 7]);
set(gca,'XTick',[0:30:360])
grid on;
set(gcf,'renderer','painters')
```

Appendix E

A short summary on the results from thermodynamic modeling

The thermodynamic modeling software *Theriak Domino* (de Capitani and Petrakakis, 2010) was used to calculate the theoretical stable mineral assemblage at the P-T conditions of the performed deformation experiments. The calculated mineral assemblages however did not compare well with the observed ones. This was interpreted to show that for the short duration of the experiments, chemical equilibrium could not be attained, even at the highest experimental T of 800 °C. Reasons why bulk equilibrium is not attained can be due to (i) diffusion rates being too low, preventing the transport of chemical compounds throughout the sample. (ii) reaction rates being too low, where either old meta-stable grains don't fully react, or new phases of the stable mineral assemblage don't succeed in nucleating. Or (iii), a combination of (i) and (ii).
Instead of using the bulk chemistry to calculate bulk equilibrium assemblage, an alternative approach was tested, using the theoretical element occurrence along a simulated (water present) phase boundary. The term *phase boundary* here refers to the contacting boundary between two grains of a different mineral phase, as opposite to a *grain boundary*, which is used to refer to a boundary between two grains of the same mineral phase. Along a phase boundary, where the reacting phases are in contact, diffusion should initially not be a limiting factor.

The input chemistry for the thermodynamic modeling following the 'phase boundary

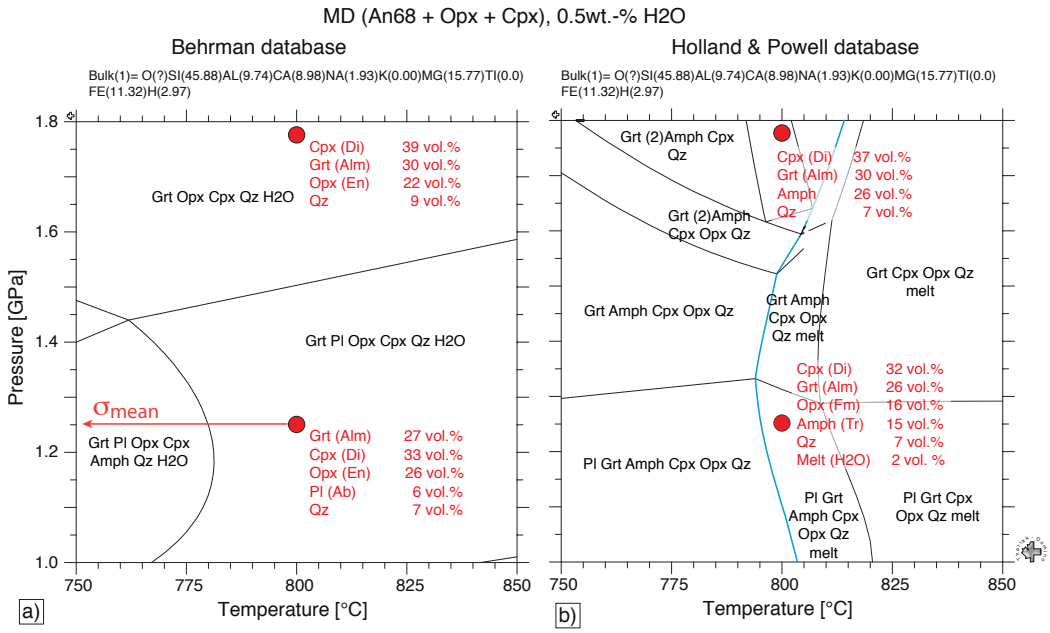

Figure 1: *Pseudosection for a modeled system Plagioclase-Orthopyroxene-Clynopyroxene (+H_2O) with mineral chemistries representative for the Maryland Diabase starting material. a) Pseudosection calculated using the Behrmann database. b) Pseudosection calculated using the Holland and Powell database. The blue line marks the melt-in boundary. Red dots indicate ∼ P-T conditions of the 800 °C experiments, where the pressure is not taken to be equal to Pc but to the mean stress (σ_{mean}) during deformation. For each red dot, the stable mineral assemblage is given, with indicated dominant solid-solution endmember in brackets.*

approach', is derived by calculating the element occurrences along a unit length of a modeled phase boundary between plagioclase and pyroxene, adding a given value of H_2O. Representative EDX chemical analyses for plagioclase and pyroxene from the starting material are used for this calculations. The amount of moles of each phase contributing to the input chemistry was determined by the different molar volumes of the phases, such that each phase occupies the same volume. Therefore, mineral phases with a higher atom density (such as pyroxenes) contribute with more moles to the input chemistry than mineral phases with a lower atom density (such as plagioclase). Using this approach, there is one crucial parameter that has to be set, which is the amount of water to be added to the input chemistry. The local H_2O occurrence along an actual phase boundary during the experiment is unknown. The amount of water in the input chemistry is especially taking influence when a melt phase is becoming stable in the calculated assemblage. This problem concerns only the Holland and Powell (Holland and Powell, 1998) database (H&P98), which, unlike the Behrman (Berman, 1988) database (B88), includes solution parameters for melt phases.

Figure 1 shows pseudosections for the model input chemistry of Maryland Diabase. As

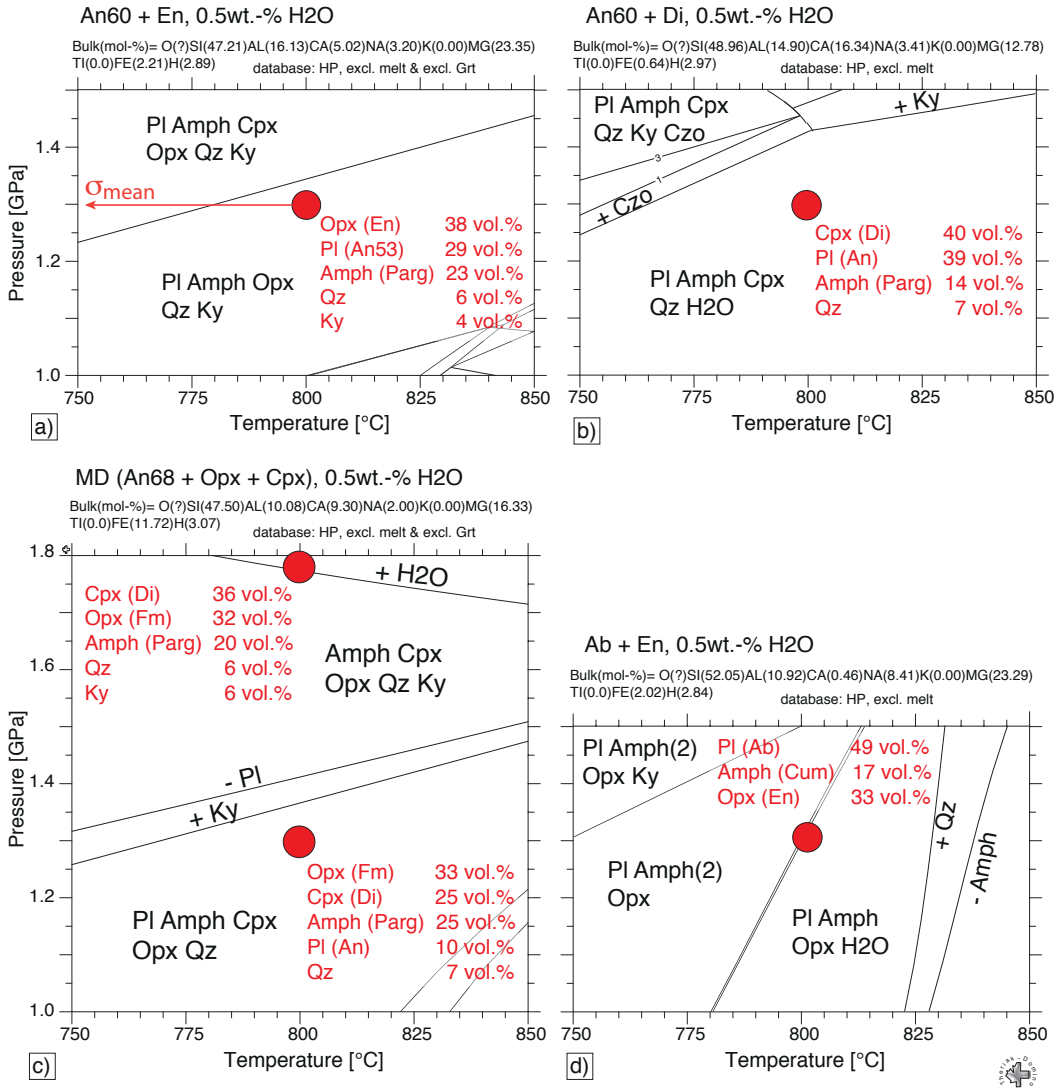

Figure 2: *Pseudosections for the four different starting materials, with calculated input chemistry after the described 'modeled phase boundary' approach (see text). a) An60+En = Sonora Labradorite + Damaping Enstatite; b) An60+Di = Sonora Labradorite + Cranberry Lake Diopside; c) MD = Maryland Diabase; d) Ab+En = Alpe Rischuna Albite + Damaping Enstatite. All pseudosections are calculated using the H&P98 database, excluding melt phase and, where indicated, garnet. A freely chosen amount of 0.5 wt.-% H_2O is added to the input chemistries. Red dots indicate the P-T conditions of the 800 °C experiments, where pressure is considered to be equal to mean stress (σ_{mean}) during deformation. For each red dot, the corresponding stable assemblage is given. Minerals with solid-solutions have the* ***dominant*** *solid-solution endmember indicated in brackets.*

the Diabase contains both ortho- and clynopyroxene, the chemistry is calculated from equal volumes of plagioclase, ortho- and clynopyroxene. Two pseudosections are calculated, each corresponding to a different thermodynamic database but both for the case of the 800 °C experiments at Pc=1.0 and Pc=1.5 GPa. Mean stress (calculated for the 2D

plain strain case) and not Pc is assumed to be the 'thermodynamic significant pressure'. The observed mineral reactions in the 800 °C experiments are:

(1) $Px + Pl + H_2O = Amph + Qz$

(2) $Pl(An_x) + H_2O = Zo + Pl(An_{x\text{-}m}) + Ky + Qz$

x and m are integers between 0 and 100, with $m \leq x$.
The H&P98 database determines Amph as a stable phase in the assemblage (Figure 1b), whereas with the B88 database, Amph is not seen to become stable (Figure 1a). Zo is not predicted by either of the pseudosections. Unlike the observed assemblage in the sample, the calculated pseudosections both predict large quantities of garnet to be present. The occurrence of melt as predicted by the pseudosection calculated with the H&P98 database is in accordance with the observation of small amounts of melt in the samples.

In the experimental samples, garnet is locally seen to be growing as coronas on ilmenite and magnetite grains, as well as within biotite grains. Ilmenite, magnetite and biotite occur as accessory minerals in Maryland Diabase. Garnet however is never observed to grow along Plagioclase-Pyroxene phase boundaries. Garnet is known for its difficulty to nucleate and the absence of garnet in our experimental samples is interpreted to be owing to this.
To take the absence of garnet into account, garnet was excluded from the database to suppress its formation in the pseudosection (Figure 2). The same was done for the melt phase. The occurrence and composition of melt in the pseudosection is highly sensitive on the water content in the input chemistry and thus is difficult to model. However, the observed melt content in the samples was usually less than 2%.

It was recognized, that the garnet stability in the thermodynamic modeling is mainly driven by the iron component in the input chemistry. For amphibole, the solution models are best defined for Mg-amphiboles but less so for Fe-amphiboles. In an attempt to simplify the chemical system with regard to the thermodynamic modeling, the sample materials fabricated from mixtures of plagioclase + Mg-endmember pyroxenes were introduced (An60+Di, An60+En and Ab+En).

Figure 2 presents pseudosections calculated for the four different starting materials Maryland Diabase (MD), Labradorite + Enstatite, Labradorite + Diopside (Cranberry Lake) and Albite + Enstatite. For the calculation of the presented pseudosections, the H&P98 database file was modified to exclude melt as a possible phase. Additionally, for pseudo-

sections in Figure 2 a) and c), garnet was additionally excluded from the database. The calculated mineral assemblages in Figure 2 are coming close to reproduce the observed mineral assemblages found in the experimentally deformed samples. However, there is one major differences between calculated and observed mineral assemblages: Zoisite is never predicted to appear as a stable mineral phase, whereas Zoisite is widely observed to grow as a reaction product in the experimental samples.

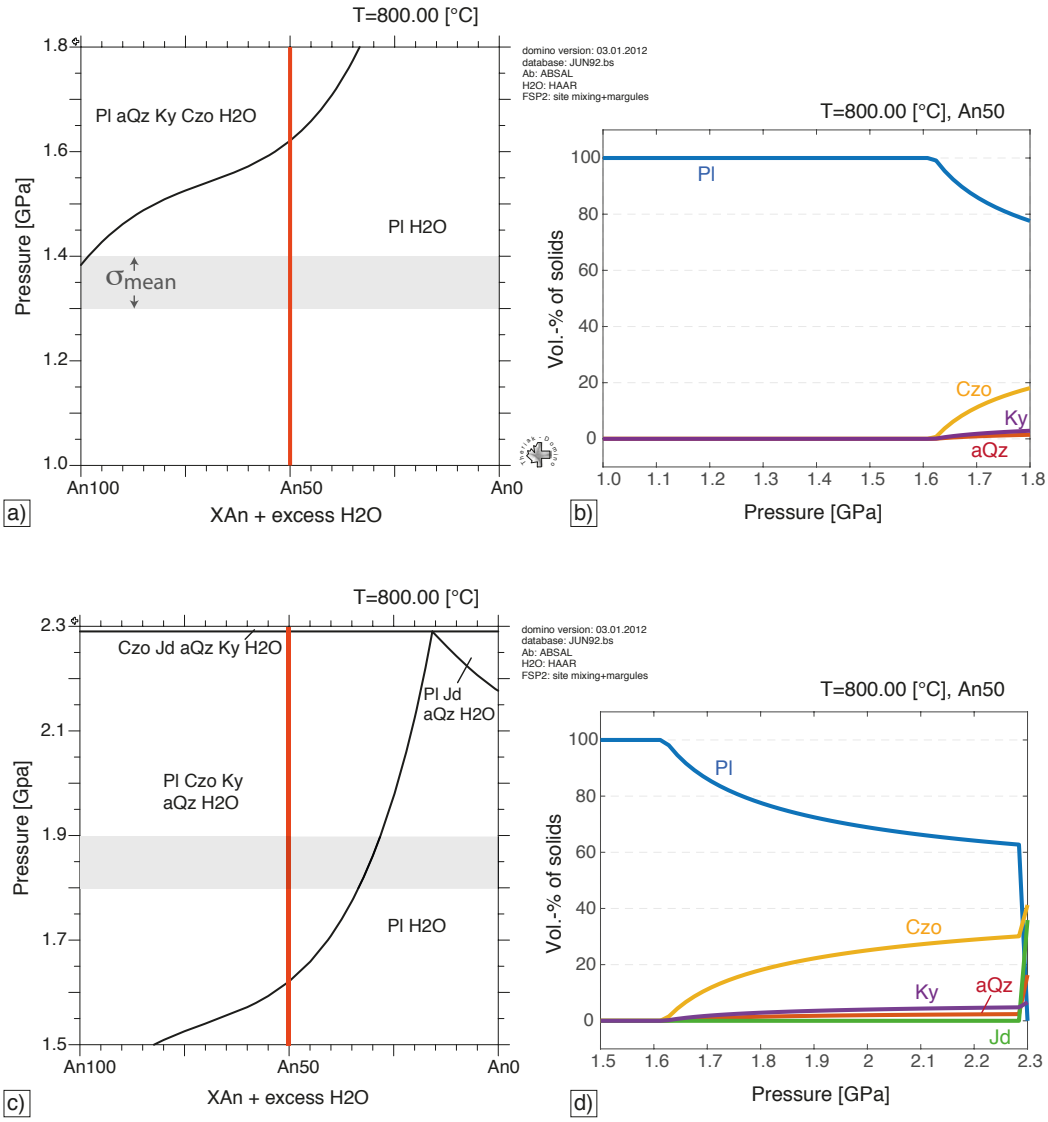

Figure 3: *a) and c) Pseudosections for pressure vs. Anorthite component in Plagioclse calculated at 800 °C. Grey bar indicates the ∼ mean stress range (considered as 'thermodynamic significant' pressure, rather than Pc) for the 1.0 GPa experiments (a) and the 1.5 GPa experiments (c). Red lines indicate section portrayed in pseudosections b) and d). b) and d) Pseudosections showing the stable mineral assemblage (vol.-% of solids) vs. Pressure, calculated for a T of 800 °C.*

Figure 3 shows plagioclase stability in the presence of water, at T = 800 °C and a pressure range from 1.0 - 1.8 GPa (Figure 3 a, b) and 1.5 - 2.3 GPa (Figure 3 c, d). Although Zoisite is observed to grow in samples deformed at Pc = 1.0 GPa, its formation is not predicted by the thermodynamic calculation, disregarding of the initial Plagioclase composition. For the higher Pc experiments deformed at Pc = 1.5 GPa, extensive Zoisite formation is observed in the samples and similarly predicted by the calculated pseudosection (if mean stress is considered).

Summary

During this study, it was recognized that using thermodynamic modeling to predict the stable mineral assemblage at the experimental P-T conditions was challenging. In the experimental samples, likely limited kinetics for both reaction and diffusion caused the formation and preservation of metastable mineral assemblages. The 'simplyfied' system of using plagioclase and Mg-endmember pyroxenes showed some promising results with better comparison between predicted and observed mineral assemblage (i.e. thermodynamic modeling and experimental result). The Maryland Diabase starting material is more complex as it shows a broad range of pyroxene and plagioclase compositions. However, reaction extent is much larger in experiments on Maryland Diabase material compared to the synthetic plagioclase-pyroxene mixtures.

All in all, it may be said that the studied system is relatively complicated for comparison with thermodynamic models and as it is, the results are difficult to interprete.